CRANFIELD UNIVERSITY

Defence Academy - College of Management and Technology

Department of Informatics & Systems Engineering,
Autonomous Systems Group

PhD
2011

Feng Wang

Robust Control of Quasi-Linear Parameter-Varying L_2 Point Formation Flying with Uncertain Parameters

Supervisor:
Professor Antonios Tsourdos

June 2011

Abstract

Robust high precision control of spacecraft formation flying is one of the most important techniques required for high-resolution interferometry missions in the complex deep-space environment. The thesis is focussed on the design of an invariant stringent performance controller for the Sun-Earth L_2 point formation flying system over a wide range of conditions while maintaining system robust stability in the presence of parametric uncertainties.

A Quasi-Linear Parameter-Varying (QLPV) model, generated without approximation from the exact nonlinear model, is developed in this study. With this QLPV form, the model preserves the transparency of linear controller design while reflecting the nonlinearity of the system dynamics.

The Polynomial Eigenstructure Assignment (PEA) approach used for Linear Time-Invariant (LTI) and Linear Parameter-Varying (LPV) models is extended to use the QLPV model to perform a form of dynamic inversion for a broader class of nonlinear systems which guarantees specific system performance. The resulting approach is applied to the formation flying QLPV model to design a PEA controller which ensures that the closed-loop performance is independent of the operating point.

Due to variation in system parameters, the performance of most closed-loop systems are subject to model uncertainties. This leads naturally to the need to assess the robust stability of nonlinear and uncertain systems. This thesis presents two approaches to this problem, in the first approach, a polynomial matrix method to analyse the robustness of Multiple-Input and Multiple-Output (MIMO) systems for an intersecting $\mathcal{D}$-region, which can cope with time-invariant uncertain systems is developed. In the second approach, an affine parameter-dependent Lyapunov function based Linear Matrix Inequality (LMI) condition is developed to check the robust $\mathcal{D}$-stability of QLPV uncertain systems.

To
my wife Xueqin Chen.

Acknowledgements

I would like to thank everyone who has knowingly and unknowingly helped me and encouraged me to accomplish this study.

I would like to express particular thanks to my supervisor, Professor Antonios Tsourdos, for his understanding, his persistent encouragement and his valuable guidance over the whole study. I would like to thank my dissertation committee members, Professor Brian A. White, and Professor Rafał Żbikowski, for their valuable help and discussions during the study.

I would like to thank the ESA (ESTEC) and EADS Astrium Ltd organizations for sponsoring this research over the past three years. I would like to thank Dr. Finn Ankersen, Dr. Alexander Cropp, Dr. Adrian Stanley, and Dr. Sean Hardacre, for sharing their knowledge and experiences with Darwin mission technology to help ensure practical relevance of this research.

Finally, I would like to thank all my family and friends whose support and wishes are essentially important over this entire study. Especially, I would like to thank Dr. YunHua Wu for his constructive discussions and selfless support during my study and life in UK.

Contents

List of Tables

List of Figures

Nomenclature

All units are in SI unless otherwise stated

Alphanumeric

$\boldsymbol{J}_i$ The inertia matrix of spacecraft i

$\boldsymbol{p}$ The time-varying parameter

$\boldsymbol{q}_e$ The error attitude quaternion

$\boldsymbol{r}_h = [X_h, Y_h, Z_h]^T$ The vector from L_2 to the mass centre of the hub

$\boldsymbol{f}_d$ The disturbance for the relative motion

$\boldsymbol{r} = \boldsymbol{r}_2 - \boldsymbol{r}_1 = [x, y, z]^T$ The vector from the hub to the telescope

$\boldsymbol{r}_{1i}$ The vector from the Sun to spacecraft i

$\boldsymbol{r}_1$ The vector from L_2 to spacecraft 1 (Hub in interferometry mission)

$\boldsymbol{r}_{2i}$ The vector from Earth-Moon barycentre to spacecraft i

$\boldsymbol{r}_2$ The vector from L_2 to spacecraft 2(Telescope

$\boldsymbol{r}_i = [X_{hi}, Y_{hi}, Z_{hi}]^T$ The vector from L_2 to spacecraft i

$\boldsymbol{u}_i$ The control vector of spacecraft i

$\boldsymbol{u}_{21} = [u_x, u_y, u_z]^T$ The relative control of the telescope with respect to the hub

$\hat{\boldsymbol{x}}$ The unit vector that parallels to Sun-Earth line, pointing from the Sun to the Earth

D_1 The distance from origin to the Sun

D_2 The distance from origin to the Earth-Moon barycentre

f The true anomaly of the Earth with respect to the Sun

$K_a(s), K_u(s), K_c(s), K_i(s)$ Controller gains

L_2	Libration point 2
n	The angular velocity of spacecraft body frame **ROF** with respect to the inertial frame **IHE**, $n = \dot{f}$
$P(s)$	The associated controllability space of eigenvector space
x_e	The distance from origin to L_2 point
$Z(s)$	The eigenvector space

Greek Symbols

ω_e	The error angular velocity
ω_i	The angular velocity vector of spacecraft i
τ_i	The control torque vector of spacecraft i
λ_i	The eigenvalue i of system state matrix
μ_1	The solar Keplerian constant
μ_2	The terrestrial Keplerian constant
μ_3	The lunar Keplerian constant
σ	A constant related to the Sun-Earth system

Abbreviations

IHE	Inertial Heliocentric Ecliptic Frame
RBF	Rotating Body Frame
REF	Rotating Reference Frame
ROF	Rotating Orbital Frame
AAS	Alcatel Alenia Space
BCS	Beam-Combining Spacecraft

CRTBP	Circular Restricted Three Body Problem
CS	Collector Spacecraft
DARWIN	Detection of Alien Remote Worlds by Interferometric Nulling
EA	Eigenstructure Assignment
EAS	EADS Astrium Space
ES	Extended Stability
ESA	European Space Agency
FEEP	Field Emission Electric Propulsion
FIT	Finite Inclusion Theorem
FRAS	Fine Relative Attitude Sensor
FS	Fringe Sensor
LMI	Linear Matrix Inequality
LPV	Linear Parameter-Varying
LQG	Linear Quadratic Gaussian
LQR	Linear Quadratic Regulator
LTI	Linear Time-Invariant
MAXIM	MicroArcsecond X-ray Imaging Mission
MIMO	Multiple Input Multiple Output
NASA	National Aeronautics and Space Administration
NP	Non-deterministic Polynomial-time
NRS	New Robust Stability
ODL	Optical Delay Line
OLS	Optical Laser Sensor

PEA	Polynomial Eigenstructure Assignment
QLPV	Quasi-Linear Parameter-Varying
QLTV	Quasi-Linear Time-Varying
QS	Quadratic Stability
RF	Radio Frequency
RS	Robust Stability
RTBP	Restricted Three Body Problem
SEM	Sun-Earth/Moon
SI	The Stellar Imager
SISO	Single Input Single Output
STR	Star-Tracker
T/T	Tip/Tilt
TPF	Terrestrial Planet Finder
TPF-I	Terrestrial Planet Finder Interferometer
TTN	Three Telescope Nuller
XUES	The X-Ray Evolving Universe Spectroscopy Mission

Chapter 1

Introduction

Spacecraft formation flying has been identified as a key technology for future missions and has received significant attention in recent decades. As opposed to traditional monolithic spacecraft, formation flying has many advantages, including feasibility and flexibility benefits, cost and risk reduction, system reconfigurability and robustness enhancement, for both scientific and military applications. Particularly for high accuracy large space interferometry or for large synthetic aperture radar, traditional single spacecraft are unable to accomplish such missions, but it becomes feasible by using formation flying: several mission proposals have been presented, such as the Detection of Alien Remote Worlds by Interferometric Nulling (DARWIN)(ESA, 2011a), The X-Ray Evolving Universe Spectroscopy Mission (XUES) (ESA, 2011b), The Terrestrial Planet Finder (TPF) (NASA, 2011), MicroArcsecond X-ray Imaging Mission (MAXIM) (Gendreau, 2011) and The Stellar Imager (SI) (Carpenter, 2011) to detect and characterize other Earth-like planets by using a large number of spacecraft in formation around the Sun-Earth libration points. To achieve the objective of such missions, high precision control performance is the major requirement for the entire formation to satisfy the conditions for interferometry. In this thesis, we apply a new control approach to formation flying to fulfil the requirements of one of these missions, the DARWIN mission.

1.1 DARWIN Mission Overview

The DARWIN mission proposed in 1993 (Leger et al., 1996; Penny et al., 1998; Fridlund & Capaccioni, 2002) is one of the most challenging space projects ever considered by the European Space Agency (ESA) since its objectives are to detect and characterize Earth-like planets as the primary focus, and to perform high resolution imaging of celestial targets using the aperture synthesis technique as secondary focus (ESA-SciA, 2007; Cockell et al., 2009).

In order to detect an Earth-like planet from the overwhelming flux of its host star, a telescope up to 100 m in diameter operating at mid-infrared wavelengths

is required since the angular size of the habitable zones around DARWIN target stars ranges between 10 and 100 *micro arc seconds* (*mas*). Due to the size limitation of a monolithic telescope, interferometry based on spacecraft formation flying has been identified as the best technique to realize these objectives.

As a result, the DARWIN mission has been conceived to be implemented on several Collector Spacecraft (CS) and one Beam-Combining Spacecraft (BCS), where the CS are located at equal distances from the BCS. During observation, the BCS will control the relative phase and intensity of the light collected by the CS. Once the light is combined in the BCS, the on-axis stellar light will be cancelled out (due to a π phase shift between the light collected by two CS) while allowing the signal from an off-axis planet to pass through. This technique, to suppress light by destructive interference, is called nulling interferometry (also named Bracewell interferometry (Cockell et al., 2009)). The principle of nulling using two-telescopes is illustrated in Fig. 1.1), which is the basis for the DARWIN mission and exoplanet detection and characterization.

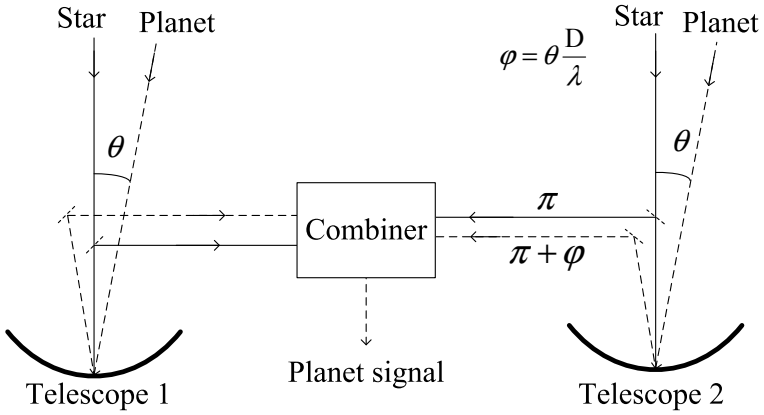

Figure 1.1: Principle of a Two-Telescope Bracewell Nulling Interferometry

To implement the DARWIN mission, there are several challenges particularly in the areas of 1) high precision static and dynamical optical systems as required by nulling interferometry, 2) thermal control of the cryogenic payload, and 3) operation of a multi-spacecraft formation (ESA-SciA, 2007). To address these problems, major top-level requirements of the DARWIN studies include (ESA-SciA, 2007; Cockell et al., 2009):

- Two observation modes: nulling for extrasolar planet detection and spectroscopy, and constructive imaging for general astrophysics;

- Placement at the second Lagrangia libration point L_2 for passive cooling and low ambient forces;
- Launch with a single Ariane 5 rocket or two Soyuz-ST/Fregat vehicles;
- The ability to search at least 225 candidate stars with an exozodiacal background of one zodi, 1 or 150 stars with an exozodiacal background of 10 zodis;
- Detection and measurement of terrestrial atmosphere biosignatures for at least 25 stars (with one zodi) or 15 stars (with 10 zodis; 2 m collectors);
- Time allocation of search as follows: G stars 50%, K stars 30%, F and M stars 10% each.

In order to provide a thermally and gravitationally stable environment for nulling interferometry, all spacecraft of the DARWIN mission will operate as a formation at the second Lagrangian libration point L_2 (described in detail in Fig. 1.12) of the Sun-Earth system, which is at a distance of one and half million kilometers from the Earth in the opposite direction from the Sun as depicted in Fig. 1.2).

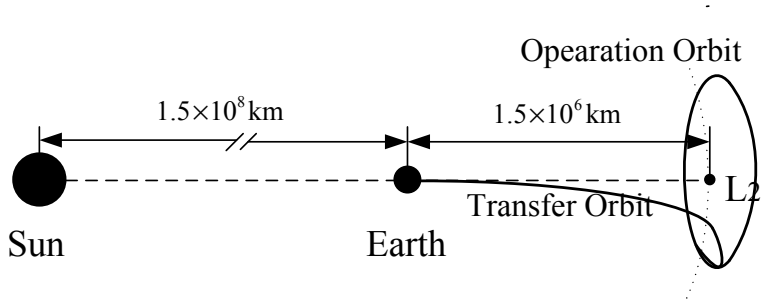

Figure 1.2: Schematic of the Transfer and Operational Orbits at L_2 Point of the Sun-Earth System (Wallner, 2007)

For the DARWIN formation flying architecture, the original configuration consists of five-telescopes developed by Leger et al. (1996) for nulling interferometry (see Fig. 1.3), and then in order to be beneficial for both the nulling and imaging objectives, it evolved into six free-flying 1.5 m telescopes, flying in a hexagonal configuration (see Fig. 1.4) (Fridlund & Capaccioni, 2002; Lagadec et al., 2002; Beugnon et al., 2004).

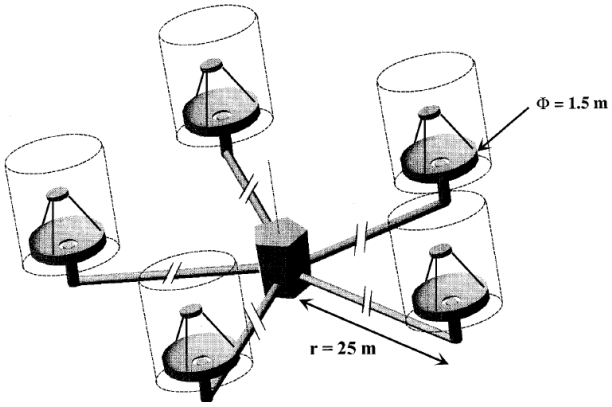

Figure 1.3: Scheme of DARWIN in a Five-Telescope Design (Leger et al., 1996)

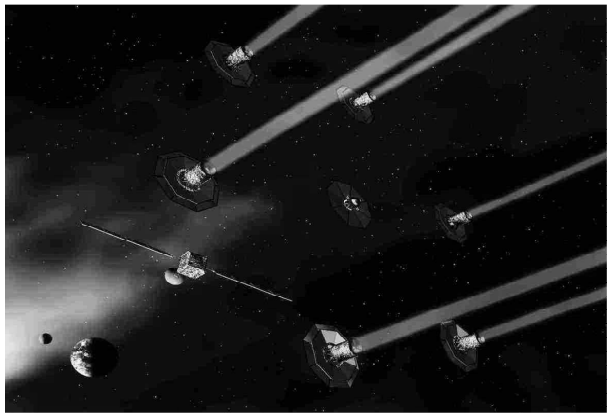

Figure 1.4: Scheme of DARWIN in a Six-Telescope Design (Beugnon et al., 2004)

Furthermore in 2005, two parallel studies of the DARWIN mission were established by considering serval constraints, including the requirements of the payload, the spacecraft and the ground segment which must satisfy the science mission requirements. Two possible formation concepts have been thoroughly developed in 2006 (ESA-SciA, 2007; Cockell et al., 2009): the Three Telescope Nuller (TTN) concept with a BCS above the plane of the CS (the so called Emma concept, proposed by Alcatel Alenia Space, AAS) and the X-array configuration with a co-planar BCS (EADS Astrium Space, EAS).

Figure 1.5 shows the Emma (TNN) concept. As illustrated in the figure, it consists of three free-flying CS, each carrying a 3.15 m diameter mirror, and a BCS located above the plane of the CS. The BCS is located 1200 m above the CS plane, allowing baselines of up to 168 m for nulling operation and 500 m for interferometric imaging. In this concept, the minimum number of telescopes is

used to obtain a θ^2 null for two simultaneous conjugate modulation states which will allow a maximum modulation efficiency for the planetary signal of 93.3% while maintaining a relatively simple optical design (ESA-SciA, 2007).

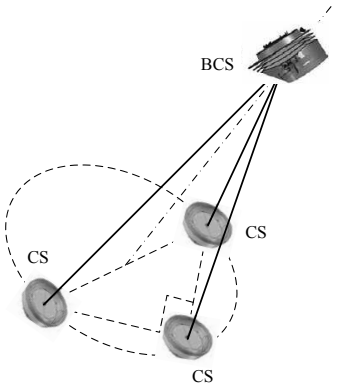

Figure 1.5: The DARWIN Emma Configuration (ESA-SciA, 2007)

Figure 1.6 shows the X-array concept, where all four CS and a BCS are located in a same plane to form an X-array configuration. The X-array concept consists of two single θ^2 nullers along the short baseline, which are combined with a $\pm\pi/2$ phase shift to provide two simultaneous modulation states. The long baseline provides a fine spaced modulation in the bright fringes to attain a high angular resolution for planet detection. Thus, the resolving power and nulling performance of the configuration are completely decoupled, which is a characteristic feature of the X-array configuration (ESA-SciA, 2007). The range of distance from the CS to the BCS is from 15 to 300 m.

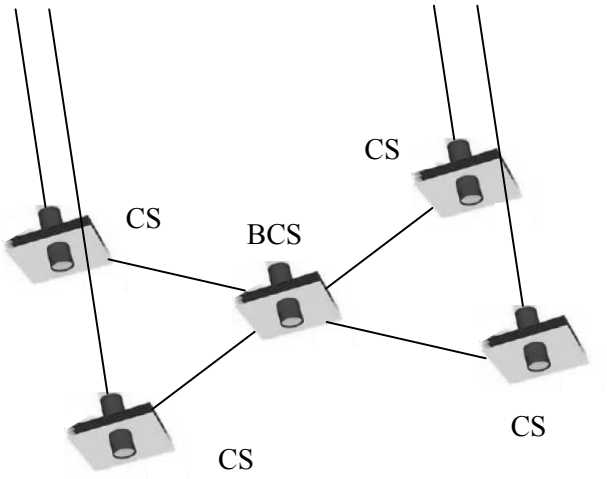

Figure 1.6: The DARWIN X-Array Configuration (ESA-SciA, 2007)

The previous research results and the assessment studies by AAS and EAS have verified that there is no technology barrier to this ambitious mission. However, two key areas require more attention and support in the future (Cockell et al., 2009):

- Formation flying of several spacecrafts with relative position control accuracy of a few centimetres.
- The feasibility of nulling interferometry in the $6 - 20\ \mu m$ range.

For these two key areas, the first one will be summarized in Section 1.1.2 since it is the research focus of the thesis, while for the second one, please refer to ESA-SciA (2007) and Cockell et al. (2009) for more information.

1.1.1 Terrestrial Planet Finder Mission

The Terrestrial Planet Finder Interferometer (TPF-I) mission was proposed by National Aeronautics and Space Administration (NASA) in 2002 to search for Earth-like planets orbiting other stars and probe their atmosphere for indications of life (Scharf et al., 2004; Lawson et al., 2007). The technology of nulling interferometry will be also implemented by using a system of formation flying telescopes, which is similar to that of the DARWIN mission. Due to similar goals and studies, both ESA and NASA have agreed on common figures of merit to evaluate their performance in 2004 (Lawson et al., 2007; Cockell et al., 2009).

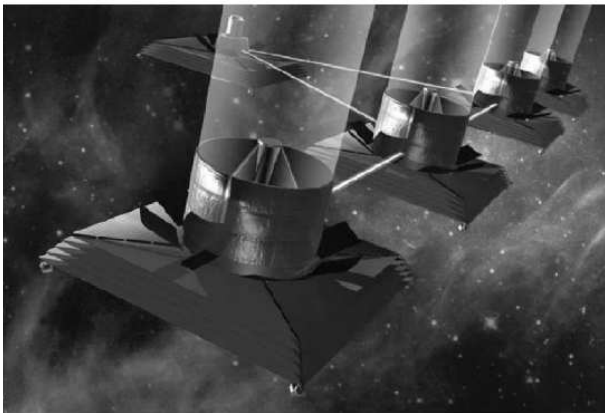

Figure 1.7: The TPF-I Linear Dual Chopped Bracewell Configuration (Lawson et al., 2007)

To fulfil the requirement of nulling interferometry, the early formation flying architecture of the TPF-I was the Linear Dual Chopped Bracewell configuration (see Fig. 1.7) because it is more efficient at converting planet photons into a modulated output signal (Scharf et al., 2004; Lawson et al., 2007).

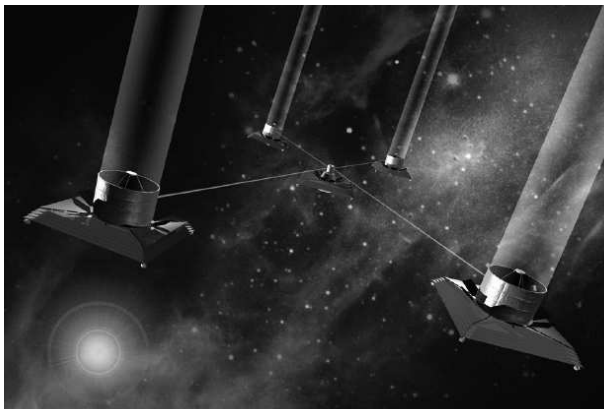

Figure 1.8: The TPF-I Stretched X-Array Configuration (Lawson et al., 2007)

In order to improve the imaging properties of the architecture, a new configuration known as the stretched X-array was developed in 2004 and is shown in Fig. 1.8. Using such an architecture, the nulling baseline lies along the short side of the rectangle and the imaging baseline along the long dimension (Lawson et al., 2007).

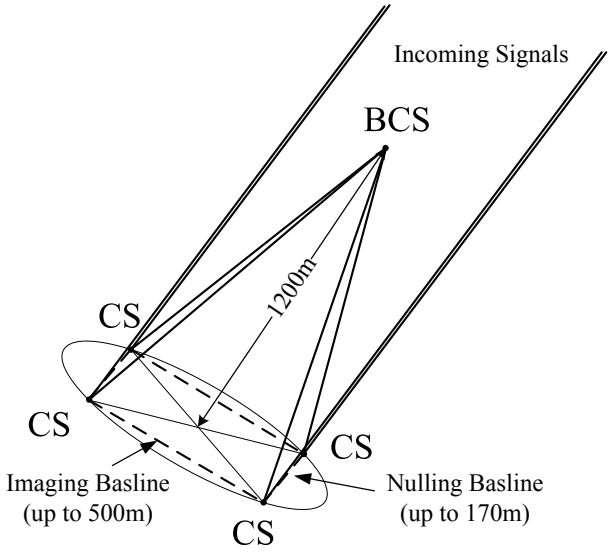

Figure 1.9: The TPF-I Emma Configuration

Later in 2006, in response to a new proposal from ESA, the Emma architecture

was evolved as the latest architecture of the TPF-I, as shown in Fig. 1.9. For this Emma concept, a stretched X-Array is used for all four CS, and a BCS is located above the plane of the CS. The advantage of this configuration is that it can simplify the telescope optics, eliminate the need for any deployments, and reduce the risk of catastrophic failure in the design of the sunshields (Lawson et al., 2007). A performance comparison between the Emma and the X-array architecture has been analysed at the Jet Propulsion Laboratory and shows the advantages of the former architecture in cost, mass, structure and launch (Martin et al., 2007).

Currently, both the DARWIN and the TPF-I have being studied independently by ESA and NASA, and an excellent working relationship is maintained between the science and technology teams of the TPF-I and the Darwin mission (Lawson et al., 2007; Cockell et al., 2009).

1.1.2 Formation Flying for the DARWIN Mission

To fulfil the requirements of nulling interferometry in the DARWIN mission, the formation flying system should be designed based on two factors: the first is that the interferometric baseline should vary between 50 and 500 m in order to provide the required angular resolution; and the second is that the differences in optical pathlength between the light from the CS must be kept below a thousandth of the science wavelength for perfect nulling (Beugnon et al., 2004). Thus, considering the science wavelength ($6 - 20\ \mu m$) in the mission, the control system has to guarantee a 5 nm stability over a distance of 500 m (Beugnon et al., 2004).

To satisfy such stringent requirements, the control system must be partitioned into the external control and the internal control. The external control has been decomposed into three levels (Ruilier et al., 2007; Beugnon et al., 2004):

- The first external control stage (the coarse level in Beugnon et al. (2004)): This aims to reach a centermetre control accuracy level. During the operation, the BCS keeps free-flying in its orbit in the vicinity of L_2 point and only performs orbit control manoeuvres if necessary. The nominal formation flying is done by the CS position keeping with respect to the BCS. The control will been realised in a decentralised structure since Radio Frequency (RF) sensors are directly available on each CS. The actuator are milli-Newton Field Emission

Electric Propulsion (FEEP) thrusters (see Fig. 1.10) and the measurement is fulfilled by RF sensors (see Fig. 1.11) and Autonomous Star Trackers (STR).

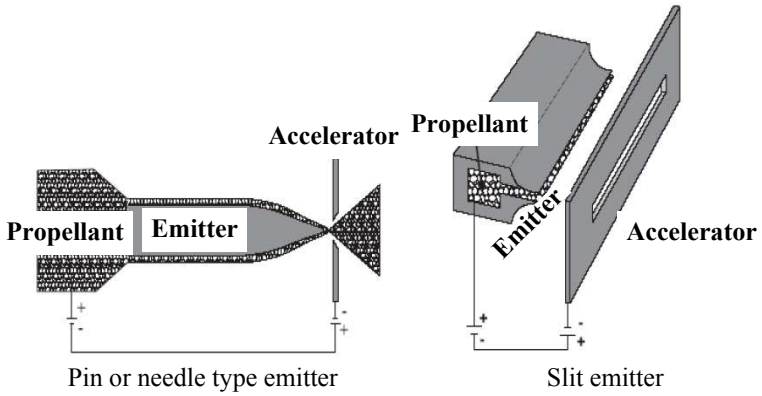

Figure 1.10: The Principle of FEEP Thruster (Luquette, 2006)

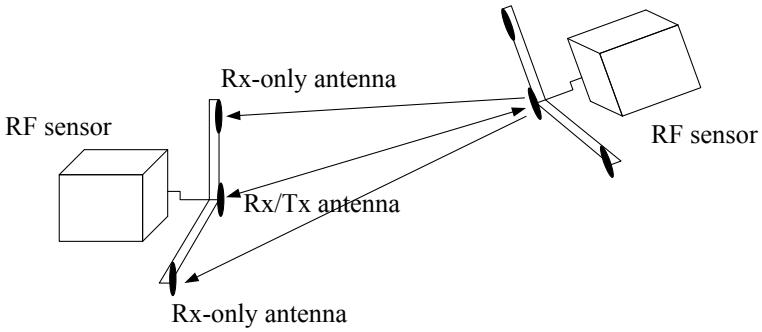

Figure 1.11: The Schematic of Radio Frequency Metrology (Ruilier et al., 2007)

- The second external control stage (the optical level in Beugnon et al. (2004)): This aims to attain a sub-millimetric control accuracy level. The stage is used to improve the control accuracy of the formation in order to meet the requirement for no loss of intensity in the transmission of the scientific beam from the CS to the BCS, the acquisition conditions of the Fringe Sensor (FS), and the strokes of the Optical Delay Line (ODL) and Tip/Tilt (T/T) mirror. The sensors and actuators are an Optical Laser Sensor (OLS) and a Fine Relative Attitude Sensor (FRAS) with micro-Newton FEEP thrusters.

- The third external control stage (the interferometric level in Beugnon et al. (2004)): This aims to realize a nanometre control accuracy level. The third external control stage, only implemented on the BCS, is the ultimate control

stage before recombination. Its measurements are provided by an FS and the actuators are ODL and T/T mirrors.

Due to unavoidable environmental perturbations (such as thermal effects and microvibrations), internal control is also required to compensate for drifts and instabilities within the very stringent requirement (5 nm) (Ruilier et al., 2007).

From the control level definitions above, we find that the first and second external control levels are related to formation flying control, which includes formation architecture deployment, baseline varyation (translation), position keeping and formation slewing and attitude rotation. From Ruilier et al. (2007); Pirson & Christy (2006) and Beugnon et al. (2004), the requirements of the formation control system are depicted in Table 1.1, which will be used during the controller designs and simulations in the thesis.

Table 1.1: The Formation Control Requirements of the DARWIN Mission

Control stage	Performance (3σ)	Actuator	Sensor (3σ)
First	<1 *cm*	FEEP thrusters	RF(<1.2 *mm*, <0.21 *deg*)
(Coarse)	<6 *as*	(10μN - 1.2 *mN*)	STR(<10 *as*)
Second	<1mm	FEEP thrusters	CLS(<1 *mm*)
(Optical)	<70 *mas*	(0.1 μN - 150 μN)	FSAS(<10mas)
Third	<1 *nm*	ODL	FS(<0.075 *nm*)
(Interferometric)	<3 *mas*	T/T mirrors	Corrective T/T (<3 *mas*)

1.1.3 Metrology and Actuators in the DARWIN Mission

In this section, the sensors and actuators used for the formation control system in the DARWIN mission are introduced briefly and are used in the simulations in later chapters of the thesis.

1.1.3.1 DARWIN Mission Metrology

In the DARWIN mission, the measurement of relative position for formation flying can be realised with two different sensors (Pirson & Christy, 2006):

- the RF system is used for coarse positioning. It delivers range, elevation and azimuth measurements to derive coarse relative longitudinal and lateral information: the longitudinal accuracy is 1.2 *mm* (3σ) and line of sight accuracy is ±0.21 *deg* (3σ),
- the OLS system is used for fine positioning. Absolute lateral and longitudinal measurement functions are embedded in the same unit. Its accuracy is better than 1 *mm* for longitudinal and better than 100 μm for lateral (3σ) measurements.

Two sensors are used to obtain relative attitude information (Pirson & Christy, 2006):

- an STR is implemented on each spacecraft with accuracy of 10 *arc seconds* (*as*) (3σ),
- an FRAS, which is used as a fine inertial attitude sensor, working as a very accurate STR, by directly using the telescope as a sensor, and a relative attitude sensor using a laser spot located on the hub and sent to both FRAS detectors. Its accuracy is 10 *mas* (3σ).

1.1.3.2 Actuators for the DARWIN Mission

The actuators used are FEEP thrusters. Two sets of 12 thrusters are used (Pirson & Christy, 2006):

- one is a milli-Newton FEEP with a thrust range of 10 μN to 1.2 mN; these thrusters have a resolution of 1 μN and thrust noise of 0.1% of the applied thrust,
- the other is a micro-Newton FEEP with a thrust range of 0.1μN to 150 μN, with a resolution of 0.1 μN between minimum thrust and 49.9 μN, and 0.3 μN between 50 μN and maximum thrust.

Both sets of actuators are able to create pure forces and pure torques to control the six-degrees of freedom of manoeuvre of the spacecraft. If the direction and location of the thrusters are positioned accurately as shown in table 1.2 (Luquette, 2006), the errors in direction and location are predicted to be ± 1 ° (3σ) and ± 1 cm (3σ), respectively.

*Table 1.2: Thruster Firing Direction and Location in Frame **RBF** of each Spacecraft (Luquette, 2006)*

Thruster Number	Firing Direction	Thruster location (m)		
		X	Y	Z
1	-Y	0	+0.5	-0.5
2	-Y	0	+0.5	+0.5
3	+Y	0	-0.5	-0.5
4	+Y	0	-0.5	+0.5
5	-X	+0.5	-0.5	0
6	-X	+0.5	+0.5	0
7	+X	-0.5	-0.5	0
8	+X	-0.5	+0.5	0
9	-Z	-0.5	0	+0.5
10	-Z	+0.5	0	+0.5
11	+Z	-0.5	0	-0.5
12	+Z	+0.5	0	-0.5

1.2 Libration Point Formation Flying Control Overview

In this section, a review of the modeling and control strategy for the relative motion in the vicinity of libration points is presented. The recent literature for the control of formation flying is also summarized.

1.2.1 Modeling for Libration Point Relative Motion

In the same manner as the Two-Body problem is applied to describe Earth orbit spacecraft motion, the Restricted Three Body Problem (RTBP) is the most common and simplest model used for the relative motion near the Sun-Earth/Moon (SEM) libration point. It accounts for the gravitational forces from the major primary body, the Sun, and second body, the Earth and Moon combination. This system, while simple, has no simple analytical solution to use to analyse the dynamic motion of spacecraft.

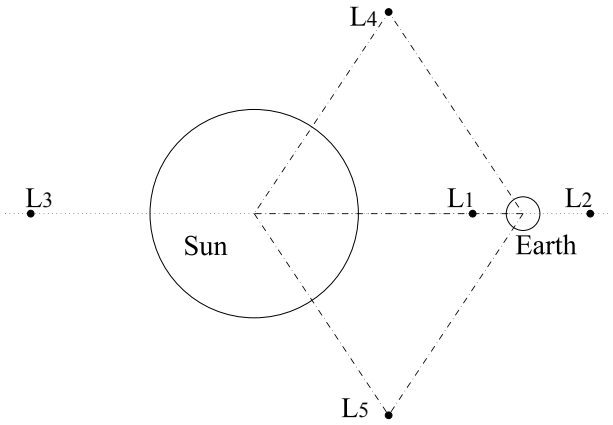

Figure 1.12: Lagrange Libration Points of the Sun-Earth System

To obtain a closed-form analytical solution of relative motion to the RTBP, there are three critical assumptions currently used to simplify the model. First, the mass of the third body (spacecraft) is assumed to be infinitesimally small relative to those of the other two bodies. Second, the Sun and the Earth-Moon combination are each considered to be point masses for the purposes of modeling the gravitational forces. In addition, the motion of one primary to the other is an elliptical orbit around the barycentre of the system. With these assumptions, the formulation of the RTBP can be investigated effectively. However, the elliptical motion is still complex. If the eccentricity of an elliptical orbit is near zero, the RTBP will reduce to the Circular Restricted Three Body Problem (CRTBP), whose solution can be expressed simply as three second-order scalar differential equations. Setting the first and second derivatives to zero in these equations leads to five solutions, called the Lagrange libration points (five points in the space) as shown in Fig. 1.12. All of these points are in the plane as the Sun-Earth motion. Three of them are collinear with the line that connects the Sun and the Earth, and the other two are located at the vertices of two different equilateral triangles whose other vertices are the centre of the Sun and the Earth-Moon. Substituting these points into the differential equations, the stability property of each Lagrange point can be determined: the former three collinear points are unstable, while the other two points are stable (Luquette, 2006).

Although there is no general analytical solution to the CRTBP, several researchers have attempted to develop approximate analytical solutions. Using a linearization method, it has been shown that there are periodic or quasi-periodic

trajectories in the vicinity of the collinear libration points (Richardson, 1980). The most general motion is the set of Lissajous trajectories which belong to three-dimensional quasi-periodic solutions.

In the 1980s, Richardson (1980) developed the analytical approximation for periodic motion near the collinear libration points in the SEM system. In his paper, the CRTBP differential equations were developed with respect to a collinear libration point. Using Taylor series expansion of the nonlinear terms, a hill-like linearized motion equation with its relevant analytical solution was obtained by truncating the higher order terms. Selecting suitable initial conditions, the solution gives rise to HALO orbit motion, which is a periodic orbit. Furthermore, in order to obtain a more accurate approximation for a HALO orbit over long periods of time, a third-order analytical solution was also presented in his paper by using the classical Lindstede-Poincare method. With this solution, an amplitude constraint relationship was derived between the out-of-plane and in-plane motions, and using this approach spacecraft can be initialized at any position on a HALO orbit. For the same problem, Howell & Barden (1999) employed manifold theory of dynamical systems to obtain periodic or quasi-periodic solutions to the CRTBP. In their paper, the motion around collinear libration points was considered in the context of centre manifolds.

Considering the formation flying of two spacecraft for the CRTBP, several authors have developed relative motion models in the vicinity of the stable libration points based on these quasi-periodic or periodic libration orbits, which has also been done for spacecraft formation flying motion in Earth orbit using a similar approach.

Following the approach of Richardson, Segerman & Zedd (2003) used a modified Lindstedt-Poincare method to develop a third order solution of the relative motion in a HALO-type reference orbit. Using Richardson's analytical solution as a reference orbit, Roberts (2005) obtained an expression for the gravity gradient and derived linearized relative motion equations. This motion model was then compared to the Satellite Tool Kit numerical orbit propagator and Segerman's higher order model. The author concluded that this linear gravity gradient model was sufficiently accurate for controller design rather than using other higher order models. Some researchers have selected unstable orbits as the reference orbit for dynamic modeling. Without considering disturbances, Collange & Leitner (2004)

designed Lissajous trajectories of relative motion using analogous methodologies. The dynamics of the relative motion in unstable orbits is also studied in Scheeres & Vinh (2000).

In order to apply linear control methods, Luquette & Sanner (2004) developed the linearized dynamics of relative motion for the CRTBP and further extended them to the RTBP. The dynamics equations are formulated in both the inertial frame and the rotating frame. The relative motion equations were used directly to produce an adaptive Lyapunov control law. The controller could then compensate for modeling errors of linearization and other disturbances and improve the performance of the relative motion.

Generating the dynamic equations for formation flying for the CRTBP will provide a good model to use for the design of control and navigation systems. However, models which only include the nonlinear gravitational forces in the model is inadequate for high precision interferometry missions. To improve the model accuracy, the perturbations from the Sun the Earth and the Moon should be included in the model. Therefore, the RTBP is transformed into the more complex n-body ephemeris problem, where the time invariance properties of the CRTBP are lost and precise periodic orbits will not exist in the vicinity of libration points. Furthermore, any formation flying control algorithms must be tested and validated using the n-body ephemeris model.

After reviewing the natural dynamics observed on the envelope of HALO orbits in the CRTBP, Barden & Howell (1999) investigated the relative motion of more complex dynamical models, including the perturbations from the Sun and the Moon. Further, Marchand & Howell (2003) extended these results into an n-body ephemeris model by considering other gravitational perturbations as well as solar radiation pressure. Later a summary of collinear libration point formation flying was presented in Howell & Marchand (2005), in which the natural and non-natural spacecraft formations near the SEM L_1 and L_2 libation points were discussed. Hamilton et al. (2002) developed a high fidelity dynamics model called Generator, which included the effects of eccentricity, an independent moon, the other planets and solar radiation pressure.

Reviewing the above papers and models, all of them are only concerned with the translational motion while assuming the spacecraft as a point mass. For the modeling of rotational motion, the effect of translational motion is neglected,

hence the translational motion and rotational motion are usually modeled separately as uncoupled systems. However, such an assumption is not possible for precision formation missions and the coupling effect caused by the displacement and misalignment of actuators needs to be modeled. In Pan & Kapila (2001) a coupled translation and rotation dynamic model was developed using a vector formalism approach, which is used for the Earth orbit formation flying but can also be applied to the relative motion in the vicinity of libration points. The modeling of relative translational and rotational dynamics was also considered in Gaulocher (2005) which was based on an interest in high precision measurement for the interferometry mission (Pegase). They linearized the coupled dynamics model with respect to the nominal configuration and used a linear fractional transformation to model varying parameters and their tolerances. However, this paper assumed that the formation state was very close to a nominal state and didn't concentrate on the influences of gravitational forces and other disturbances. Focusing on the coupling effect between translational and rotational control, Luquette (2006) modeled a coupled dynamics successfully by using a coupled matrix of thrusters with the misalignment and misplacement.

1.2.2 Control Algorithms for Libration Point Formation Flying

Recently, many approaches dealing with formation flying control around the Sun-Earth L_2 point have been presented in the literature. The most common control strategies focus on the design of position keeping and reconfiguration for spacecraft running on unstable but controllable orbits, including the HALO orbit and the Lissajous orbit. Due to the simplicity of the Linear Time-Invariant (LTI) model in the CTRBP, several Linear Quadratic Regulator (LQR) controllers for formation flying have been presented based on this model. Folta et al. (2000) presented a standard control technique using an LQR controller using linearization about a reference libration orbit. With the same LTI model, Hamilton et al. (2002) also developed an LQR controller for station keeping and formation manoeuvres of the SI mission around the L_2 point. Based on Floquet theory and a linear model, Howell & Marchand (2003) developed an LQR and a linear feedback controller to maintain a constant separation and relative orientation between two spacecraft

in the vicinity of the Sun-Earth libration points. Roberts (2005) designed similar LQR controllers for the relative motion as well. All these authors consider the use of the LQR controller for LTI models. Furthermore, to minimize the noise of transmission and propulsion, Beugnon et al. (2004) used the Linear Quadratic Gaussian (LQG) method to develop a controller for formation keeping and manoeuvring of the DARWIN mission. Using a CW-like model, Scheeres & Vinh (2000) presented a nontraditional control law to maintain the motion on a HALO orbit which was described by a set of time-varying linearized equations, but its accuracy was limited to application in the interferometry mission. Furthermore in Hsiao & Scheeres (2002), the feedback control gain was adjusted to induce large winding numbers which satisfied the mission requirements and reduced the tight relative position control constraints that were used before. However, the LTI models in these research programmes include only the second order term of the gravitational force for the L_2 point formation flying.

To improve the control accuracy and save fuel consumption, a more precise model such as a Linear Parameter-Varying (LPV) model or ephemeris model which will reduce the modeling error should be taken into account. Therefore, several authors have attempted to design gain-varying controllers by using an LPV system directly. A highly accurate LPV model for the relative motion around the L_2 point was developed in Segerman & Zedd (2003) by considering several disturbances using series expansion. With a similar LPV model, Chabot (2005) compared the fuel-cost and control performance among several simple controllers to conclude that a sophisticated model is effective in improving the closed-loop control performance. With a Hamiltonian formulation of the equations of motion in the CRTBP, Luquette & Sanner (2001) developed a nonlinear satellite trajectory control strategy using adaptive control algorithms.

Furthermore, to meet the future mission's stringent millimeter relative position accuracy, several authors have designed nonlinear controllers by using an ephemeris model directly. Marchand & Howell (2003) translated the continuous control of a LTI model into an n-body ephemeris successfully, and a discrete control system required for flight formation was designed for target approaching and station keeping to enforce this non-natural formation. These algorithms were also applied to the formation configurations in their later papers (Marchand & Howell, 2004; Howell & Marchand, 2005). Considering the baseline requirements in the

vicinity of libration points, they employed a decentralised control strategy based on existing linear and nonlinear control techniques, which can be applied to the CRTBP and the ephemeris model. In the same paper, they also discussed the potential constraints that may affect the formation control strategies, the conceptual design and the cost of the mission.

By using differential correction methods, Pernicka et al. (2005) developed discrete manoeuvring techniques for a formation maintained within required error tolerances. Infeld et al. (2007) cast the spacecraft formation flying control as a multi-agent, nonlinear, constrained optimal control problem and obtained the numerical solution to this problem by using a Legendre pseudospectral method implemented in DIDO (a Matlab optimization toolbox), which improved the precision of the optimal solution without any linearization. Xin et al. (2007) used a new sub-optimal control technique to carry out formation control based on nonlinear dynamics equations in deep space about the L_2 point. Input feedback linearization is another way to provide a unified frame for designing control laws for formation maintenance and reconfiguration (Vadali et al., 2004; Howell & Marchand, 2003). Using a novel nonlinear adaptive neural control methodology, Gurfil et al. (2003) developed a controller to keep the formation in high precision via a nonlinear model of the CRTBP which includes the disturbances of solar radiation pressure and lunar gravity. These nonlinear controller algorithms achieve good control performance for the formation system. However, the heavy computation burden of the on-board computer for these controllers should be considered before implementation.

Other factors have also been taken into account during the controller design to improve robustness. For example in order to reduce the communication bandwidth and enhance the robustness of faulty communication links, Gaulocher & Chretien (2006) designed decentralised H_2-suboptimal controllers to minimize the optical path difference of three-spacecraft formation flying interferometry mission (Pegase).

1.2.3 Control Architecture for Formation Flying

In the literature, many authors have proposed various strategies and approaches for formation flying control, which can be categorized into three types: the leader-

follower approach (Tanner et al., 2004; Shao et al., 2005), the behavioral approach (Balch & Arkin, 1998) and the virtual structure approach (Beard et al., 2001; Young et al., 2001; Ren & Beard, 2002, 2004).

Leader-Follower: In the leader-follower approach, one member is named as the leader and the others are called the followers following the leader's motion but offset by a set distance. The leader performs the high-level control tasks and monitors the status of all the follower spacecraft. It receives the commands from the earth and performs the decision-making for the fleet, such as formation reconfiguration, formation manoeuvre, formation slewing and so on. The briefness of the inter-spacecraft communication and the formation realization is the major advantage of this approach. In Shao et al. (2005), this approach was applied to achieve predetermined formations for autonomous mobile robots. In Tanner et al. (2004), the stability properties of mobile agent formations based on the leader-follower approach also was investigated. However this approach is a centralised implementation, which results in a single point failure mode of the leader. Another disadvantage of the leader-follower approach is that there is no formation information from the followers that will feed back to the leader. Thus the overall formation shape is difficult to maintain once one follower spacecraft malfunctions. The advanced function and high performance of the leader should be presented in the followers, otherwise the performance of the whole formation system can easily degrade.

Behavioral: The behavioral approach, which defines the weighting of certain actions for every spacecraft and from which the group dynamics emerge, is a decentralised implementation and only requires low bandwidth communication. This approach includes formation feedback among members to preserve the overall formation shape which reduces the risk of formation degradation due to member malfunction. The behavioral approach of a multi-robot formation control was described in Balch & Arkin (1998). However, the emergent group dynamics of this approach are hard to analyse mathematically and cannot prescribe and maintain the formation very well during manoeuvres (Ren & Beard, 2002, 2004).

Virtual Structure: Considering the advantages and disadvantages of the leader-follower and behavioral approaches, the third one, the virtual structure approach has been presented in Beard et al. (2001); Young et al. (2001); Ren & Beard (2002) and Ren & Beard (2004). In this approach, the entire formation is

treated as a single structure with supervisors that calculate the desired states for every spacecraft in one virtual structure frame. As the formation frame moves, the spacecraft track the desired positions and attitudes and the entire formation behaves as a rigid body. A virtual structure approach for spacecraft interferometry was proposed in Beard et al. (2001) that could prescribe and direct the group manoeuvres, but which didn't consider the formation information feedback among spacecraft. Young et al. (2001) developed a scheme that prescribes the formation manoeuvres, guarantees the system stability and includes formation feedback. Also formation feedback was included in the formation control via a virtual structure in Ren & Beard (2002). However, these virtual structure approaches are difficult to applied to a large-scale spacecraft formation due to the disadvantage of their centralised implementations.

Unlike the centralised control where every decision is determined by the leader, decentralised control requires that each satellite has the information of other spacecrafts in the fleet, and makes decisions by itself for its own manoeuvring and slewing. This architecture improves the system redundancy. For example, if a formation member malfunctions, a collective decision-making process would be required to, for example, pause the current action until the recovery of the fault or reconfigure the remaining spacecrafts and discard the faulty one. A new virtual structure approach based on decentralised architecture was presented in Ren & Beard (2004). Every spacecraft instantiated a local copy of the coordination vector synchronized among its neighbors by using bi-directional ring communication. With this strategy, the design was able to achieve the benefits of the virtual structure approach (Beard et al., 2001; Young et al., 2001; Ren & Beard, 2002) to overcome their limitations. Although it can be applied in a large-scale spacecraft formation, the disadvantages such as the heavy extra computation required to calculate the coordination vector in every spacecraft, fault detection for the other spacecraft and the time delay and the coordination vector error among every spacecraft still exist and will become worse if the number of spacecraft become larger.

1.3 Uncertain System Robust Stability Analysis Overview

Due to the variation of system properties, the performance of most systems are subject to model uncertainties. Two main classes of uncertainties called unstructured and structured uncertainties are distinguished for the system robust analysis (Bhattacharyya et al., 1995; Bruyere, 2004). Unstructured uncertainties, which represent the effects of nonlinearity, high frequency unmodeled dynamics and linearization truncations, are specified as a ball of norm-bounded operators in the analysis of the stability of systems (Tsourdos et al., 2001). Structured uncertainties, also called parametric uncertainties, represent the lack of precise knowledge of the actual system parameters.

The robust stability and performance analysis of linear systems with parametric uncertainties has been studied for many years in the robust control field. Although it is known to be an Non-deterministic Polynomial-time (NP) hard problem for the general case, many approaches are developed in the literature. In Gahinet et al. (1996), the authors categorized these approaches as Kharitonov's theorem and related results based on polynomials (Barmish, 1994; Bhattacharyya et al., 1995; Djaferis, 1995; Herion et al., 2001; Oliveira et al., 2002; Herion et al., 2001; Leite & Peres, 2003), quadratic stability methods based on Lyapunov functions (Geromel et al., 1998; Peaucelle et al., 2000; Ramos & Peres, 2001, 2002; Oliveira et al., 2002; Chesi et al., 2003; Oliveira & Peres, 2005; Oliveira & Geromel, 2006), and the μ or K_m stability theory (Barmish, 1994). A review of the first two categories is summarized in the following part as they are both used as a basis of the research described in this thesis.

1.3.1 Robustness Analysis via Polynomial Family and Polynomial Matrix Polytope

The approach based on polynomials and related extensions is one of the most important methods used to check the stability of uncertain systems as the characteristic equation of a Single-Input and Single-Output (SISO) uncertain system can be described by polynomials and polynomial families.

Especially after Kharitonov's theorem and its corresponding polynomials (Barmish, 1994; Bhattacharyya et al., 1995) were established in the literature, robust stability analysis of uncertain systems has received a lot of attention. Further results for affine polynomial families, multi-affine polynomial families and the more general polynomial family of polytopic parameter spaces have been extended successfully for the robust analysis. However, in practice these approaches are very computationally intensive due to the comprehensive frequency sweeping needed to satisfy the Zero Exclusion Theorem (Bruyere, 2004; Djaferis, 1995).

A more efficient approach, that of the Finite Inclusion Theorem (FIT), was introduced in order to analyse $\mathcal{D}$-stability performance of closed-loop systems in Bruye're et al. (2005). Using this FIT approach, the comprehensive frequency sweep can be reduced to a finite and small number of frequencies needed to check and determine the $\mathcal{D}$-stability of a polynomial family combined with the well-known Mapping Theorem (Djaferis, 1995).

However, those approaches are only suitable to assess the robust performance of SISO systems because all of the analysis is applied to polynomial families. Therefore, as a compromise to assess the robust performance of Multiple-Input and Multiple-Output (MIMO) system, the analysis methods for SISO system are usually used to analyse the performance of each single control channel of MIMO system separately. Combining the results for each channel, the MIMO system can be analysed Bruye're et al. (2005). During the analysis, all the coupling terms of the MIMO system are regarded as unstructured uncertainties or as negligible. Such assumptions induce conservativeness or even render the analysis results invalid. To address these problems, the best choice is to analyse the robust performance by using the MIMO model directly. Unfortunately, as mentioned in Herion et al. (2001), there is no satisfactory extension of these scalar approaches for the matrix case and it is difficult to check the stability of polynomial matrices and matrix polytopes without computing the zeros of matrix family determinant, which is a significant computational burden.

Polynomial matrices and polynomial matrix fraction descriptions can be used to represent the dynamics of MIMO systems, and further it is easy to obtain the denominator polynomial matrix of a matrix fraction description that determines the essential information for system stability Herion et al. (2001). Therefore, to solve the problem of checking the robust stability of uncertain systems, one needs

to check the robust stability of uncertain polynomial matrices. To analyse the robust stability of polynomial matrix polytopes with parametric uncertainties, Herion et al. (2001) present a sufficient Linear Matrix Inequality (LMI) condition which is expressed as a standard convex LMI feasibility problem. This approach will mean that assessing the stability of polynomial matrices becomes possible since the LMI feasibility problem can be solved efficiently and thus avoid the computational burden of evaluating matrix polynomial determinants directly. The LMI problems can also be solved using the LMI Control Toolbox in Matlab (Gahinet et al., 1995), hence it is an attractive approach to use in this research. Moreover, new LMI conditions which are less conservative have been developed for checking the robust stability of uncertain systems (Herion et al., 2001; Oliveira et al., 2002; Leite & Peres, 2003) and will form the basis for the robust analysis developed in the thesis.

1.3.2 Robustness Analysis via Lyapunov Function

Another important approach used to analyse robustness of uncertain systems is that of Lyapunov theory, which has been extensively reported in the recent two decades. In particular, the use of one common form of Lyapunov function, the quadratic Lyapunov function, known as Quadratic Stability (QS), has provided wide application for the robustness analysis of uncertain systems through the use of the convex optimization method used in LMIs, which can be solved efficiently in polynomial time (Boyd et al., 1994; Gahinet et al., 1995). The QS approach can even handle time-varying uncertain systems. However, it may lead to very conservative solutions when the uncertainties are time-invariant, since only one single function is used for the analysis of the entire uncertain system set.

To reduce the conservatism one new function, called the parameter-dependent Lyapunov function, has been extended from the QS approach as the function depends on the uncertain parameters directly. The affine parameter-dependent Lyapunov function is the simplest case of this extension, which has been applied successfully to achieve several different sufficient LMI conditions for robustness analysis, including Robust Stability (RS) in Ramos & Peres (2002) and Extended Stability (ES)in Peaucelle et al. (2000) for continuous system (Hurwitz stability) and RS in Ramos & Peres (2001) and ES in Peaucelle et al. (2000) for discrete sys-

tem (Schur stability) respectively. The performance of these approaches and the QS approach were compared in Oliveira et al. (2002) systematically through numerical examples, and the results indicate that both the RS and the ES approaches have less conservativness than the QS, but it is difficult to compare the RS and ES, because there are cases that can be solved by the RS but not by the ES and vice-versa. Using a relaxation procedure, a sequence of LMI conditions based on affine parameter-dependent Lyapunov functions were constructed in Oliveira & Peres (2005). As the number of LMIs increase, these sufficient conditions can become necessary as well.

A more complex function, the homogeneous parameter-dependent Lyapunov function, which depends polynomially on uncertain parameters is introduced to obtain less conservative LMI conditions. Using this function, Chesi et al. (2003) presented one LMI condition whose conservatism can be reduced as the degree of the polynomials increases. Using a similar structure of homogeneous function, Oliveira & Peres (2005) but not Chesi et al. (2003), Oliveira & Geromel (2006) proposed a less computationally intensive LMI condition. This LMI condition provides a complete characterization of robust stability as the degree of the polynomial Lyapunov matrices increases. However, as the number of LMIs or the degree of polynomials increases, the complexity of theses conditions will increase dramatically and testing of them will require much more computation than those in Oliveira et al. (2002) which are more conservative in certain cases. Therefore, a compromise between the complexity and the conservatism should be taken into account when applied to uncertain systems.

Unlike methods which are based on polynomial family and polynomial matrix polytope, the approach based on parameter-dependent Lyapunov function can be extended to cope with the time-varying uncertain systems. To analyse the robust stability of time-varying linear systems with slowly varying rate uncertain parameters, Gahinet et al. (1996) performed an LMI-based test with some conservatism derived from the construction of an affine parameter-dependent Lyapunov function. Using the same parameter-dependent Lyapunov function, P. & Geromel (2005) obtained a global asymptotic stability LMI condition for continuous-time varying polytopic systems. Considering a linear time-varying uncertain system with bounded rates of change of parameters, a sufficient LMI condition which is derived via a suitable homogeneous parameter-dependent Lyapunov function is

developed in Chesi et al. (2004) and Chesi et al. (2007) to analyse robust stability. For the same uncertain system, Oliveira et al. (2007) presented robust stability conditions by using integer powers of the dynamic uncertain matrix to reduce conservatism.

The LMI conditions mentioned so far are only suitable to assess the robust stability using either Hurwitz stability or Schur stability, but they are not able to analyse the $\mathcal{D}$-stability of matrix polytopes, that is the multi-parametric performance of uncertain systems, which is usually required for controller design. Noting the relation between Hurwitz stability and a positive realness condition, Geromel et al. (1998) proposed an LMI method to test a given matrix for $\mathcal{D}$-stability based on a parameter-dependent Lyapunov function. Based on the key idea of this paper, Peaucelle et al. (2000) developed robust $\mathcal{D}$-stability LMI conditions for uncertain systems. Using this approach, the performance of system can be assessed easily by solving the LMI conditions for the matrix polytope. This approach is the starting point for robust analysis in this thesis.

1.4 Objectives of the Thesis and its Structure

1.4.1 Thesis Objectives

This thesis has been driven by the following two objectives:

1. To design a high performance controller for the Sun-Earth L_2 point formation flying system. The control system should attain an invariant stringent performance over a wide range of conditions, and should be robust in the presence of parametric uncertainties.

2. To develop suitable robustness analysis approaches for the uncertain formation flying control system. These approaches should handle the robust stability of uncertain MIMO systems in an efficient way, and should obtain less conservative results than those in the literature. This would require the use of advanced optimization methods to determine the maximum variation range of the uncertain parameters.

1.4.2 Thesis Structure

The structure of the thesis outlined in five stages, as shown in Fig. 1.13:

Stage 1 is described in Chapter 2, which details the modeling for formation flying around the L_2 point of the Sun-Earth system. Taking into account the effects of solar radiation pressure and lunar gravity, the exact nonlinear model is developed as the base for linearization and simulation. Using serial expansion, LTI and LPV models are developed by retaining different order terms in the gravitational force, which are fundamental for the controller design in stage 2 and stage 3. To improve the modeling precision of the high precision formation control system, a Quasi-Linear Parameter-Varying (QLPV) model transformed from the exact nonlinear model without approximation is developed by using the Barbashin method. In order to check the effect of spacecraft flexibility, a QLPV model of flexible spacecraft formation flying is also developed.

Stage 2 is described in Chapter 3, which deals with the linear control design of the Sun-Earth L_2 point formation flying system. Using the LTI models developed in stage 1, LQR controllers are developed for the relative translational and rotational motion, respectively. In order to analyse the accuracy of metrology in the DARWIN mission, a Kalman Filter is used to estimate the system states. A formation scenario is simulated to assess the performance of the LQR closed-loop system, and the resulting controller is selected as a benchmark to evaluate the nonlinear control performance presented in Stage 3.

Stage 3 is described in Chapter 4, which focuses on the Polynomial Eigenstructure Assignment (PEA) controller design for LPV and QLPV systems. Due to the effect of modeling error, the performance of the LQR controller cannot be improved and other approaches are required. Fortunately a more precise model can be used for the PEA controller design to achieve invariant highly precision performance over a wide range of conditions. Hence, the PEA approach used for the LTI and the LPV models is extended to a QLPV model. Based on the LPV and the QLPV models, different PEA controllers for the Sun-Earth L_2 point formation flying are developed in this chapter. Furthermore, a combination method is used to consider the coupling effect between translation and rotation control systems. To limit the maximum maneuver rates and actuator inputs, a cascade-saturation control logic is applied to modify the controller. Formation flying scenarios are

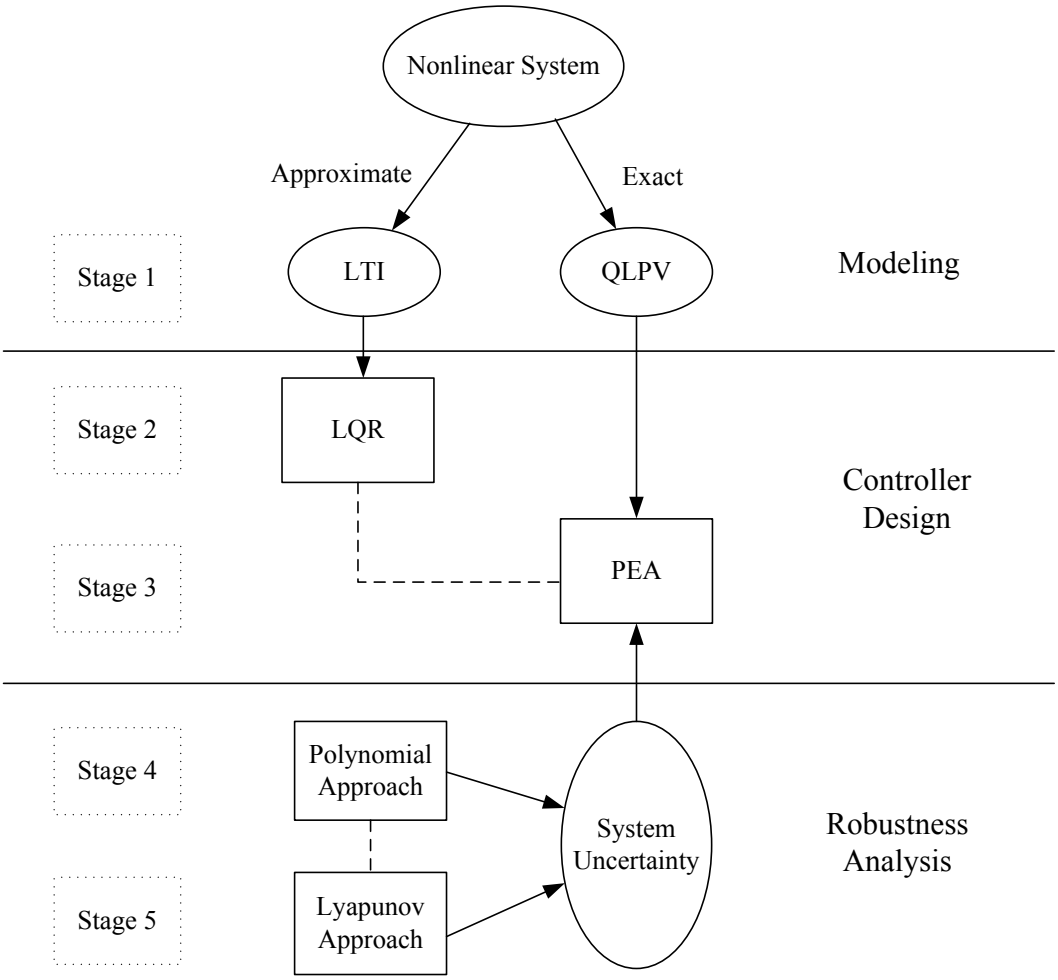

Figure 1.13: Thesis Structure

carried out to validate the performance of these controllers, and the results are compared with the benchmark results obtained in Stage 2. To investigate the effect of spacecraft flexibility on the system performance, the PEA controller is enhanced by adding a compensation term to suppress the vibration.

Stage 4 is described in Chapter 5, which uses polynomial methods to analyse the robust stability of LTI systems in the presence of parametric uncertainties. Since the formation flying system is subject to uncertainties due to variation in system parameters, it is necessary to check the robust performance and stability of the uncertain PEA control system. To assess the Hurwitz robust stability of the SISO uncertain PEA control system, Kharitonov's theorem and the Mapping Theorem are applied by considering two sources of parametric uncertainty, controller parameter uncertainty and dynamic derivative uncertainty, and then the

FIT is applied to analyse the robust $\mathcal{D}$-stability of the SISO closed-loop system. To consider the effect of the coupling terms for robust stability of the MIMO system, a new necessary and necessary LMI condition for polynomial matrices and a new sufficient LMI condition for polynomial matrix polytopes are developed, which are used in the $\mathcal{D}$-stability anlysis of the MIMO formation flying control system developed in Stage 3. Its simulation results are compared to those produced by the approach of the SISO system.

Stage 5 is described in Chapter 6, which handles the robust stability analysis of uncertain QLPV systems by using Lyapunov theory. The polynomial methods developed in Stage 4 cannot cope with time-varying systems, which require the use of new theory to address this robust stability analysis problem. To analyse the stability of QLPV systems, a quadratic Lyapunov functions is developed, and it is then extended to analyse the robust stability of uncertain a QLPV system with bounded uncertainties. To analyse the $\mathcal{D}$-stability of uncertain systems, an LMI approach via affine parameter-dependent Lyapunov function is developed by using the property of a multi-convex scalar quadratic function, and moreover, two improved methods are presented to reduce the conservatism of the new LMI approach. This allows the designer to use a less conservatism approach. These methods are implemented to analyse the $\mathcal{D}$-stability of the QLPV PEA MIMO formation control system developed in Stage 3, and their analysis results are compared to those attained in Stage 4.

1.5 Contributions

1.5.1 Main Contributions

- To improve the modeling accuracy for the high precision formation control of the interferometry mission, Chapter 2 develops a QLPV model transformed from the exact nonlinear model without approximation using the Barbashin method. With this QLPV form, the model can preserve the transparency of linear controller design while reflecting the nonlinearity of the system dynamics.
- In Chapter 4, the PEA approach used for LTI and LPV models is extended to

a QLPV model, in which the formulation allows polynomial eigenstructure to be used to compute the algebraic structure of the controller and naturally leads to a nonlinear controller without interpolation. The resulting controller renders the closed-loop system almost independent of the operating point, and thus performs a type of dynamic inversion while encompassing a broader class of LPV and QLPV systems to ensure that specific system performance can be achieved.

- In Chapter 4, the PEA approach is applied to the Sun-Earth L_2 point formation design to produce a closed-loop system with invariant performance over a wide range of conditions, in which a combination method is developed by taking the coupling effect between position and attitude control systems into account. Moreover, the controller is modified by a cascade-saturation control logic to limit the maximum maneuver rates and actuator inputs.

- To analyse the robust stability of MIMO systems in an intersecting region $\mathcal{D}$, a new necessary and sufficient LMI condition for polynomial matrices and a new sufficient LMI condition for polynomial matrix polytopes are developed in Chapter 5.

- To analyse the $\mathcal{D}$-stability of uncertain systems, an LMI approach using an affine parameter-dependent Lyapunov function is developed successfully by using the property of a multi-convex scalar quadratic function, and moreover, two improved methods are presented to reduce its conservatism.

1.5.2 Joint Contributions

- A LQR controller including an integrator is developed based on the LTI model in Chapter 2, which improves the system performance by a small increase in fuel cost.

- To investigate the effect of spacecraft flexibility in Chapter 4, the PEA controller is enhanced by adding a compensation term to suppress vibration .

- In Chapter 5, the robustness analysis of the SISO uncertain formation flying system is accomplished by using Kharitonov's theorem and the Mapping Theorem, in which two sources of parametric uncertainty, controller parameter uncertainty and dynamic derivative uncertainty are taken into account, and then to avoid the frequency sweeping, the FIT is used to analyse its robust $\mathcal{D}$-stability.

- The $\mathcal{D}$-stability performance of the MIMO formation flying in the presence of controller parameter uncertainty and dynamic derivative uncertainty are assessed by solving an LMI feasibility problem for a polynomial matrix polytope in Chapter 5

- In Chapter 6, a quadratic Lyapunov function is developed to analyse the robust stability of uncertain QLPV systems.

- The $\mathcal{D}$-stability analysis of the QLPV PEA MIMO formation control system is performed using the new LMI approach via an affine parameter-dependent Lyapunov function in Chapter 6.

1.6 Publications

The publications related to this study are listed as:

1. Feng Wang, Antonios Tsourdos, Rafał Żbikowski, Brian A. White, Finn Ankersen, and Adrian Stanley, Quasi-LTV Polynomial Eigenstructure Assignment Control for Formation Flying Around Sun-Earth L2 Point, 18th IFAC Symposium on Automatic Control in Aerospace ACA'2010, 6-10 September 2010, Nara, Japan.

2. Feng Wang, Antonios Tsourdos, Rafał Żbikowski, and Brian A. White, Robust Polynomial Eigenstructure Assignment Control of a Class of Nonlinear Systems, The 15th International Conference on Methods and Models in Automation and Robotics, 23-26 August 2010, Miedzyzdroje, Poland, pp:13-18.

3. Feng Wang, Antonios Tsourdos, Rafał Żbikowski, Brian A. White, Finn Ankersen, and Adrian Stanley, Relative Position and Attitude Coupling

Control of Sun-Earth L2 Point Formation Flying by QLTV Polynomial Eigenstructure Assignment, AIAA Guidance, Navigation, and Control Conference, 2-5 August, 2010, Toronto, Ontario, Canada, AIAA 2010-7716, The extension also is in the Proceedings of the IMechE, Part G: Journal of Aerospace Engineering (Accepted)

4. Feng Wang, Antonios Tsourdos, Rafał Żbikowski, and Brian A. White, Robust Control for a Quasi-Linear Parameter Varying Sun-Earth L2 Formation Flying, The 15th International Conference on Methods and Models in Automation and Robotics, 23-26 August 2010, Miedzyzdroje, Poland, pp:126-131.

5. Feng Wang, Nabil Aouf, Antonios Tsourdos, Centralized Decentralized Control for Spacecraft Formation Flying Near Sun-Earth L2 Point, The 4th IEEE Conference on Industrial Electronics and Application, 25-27 May, 2009, Xi'an, China.

6. Feng Wang, Antonios Tsourdos, Brian A. White, LPV Polynomial Eigenstructure Assignment for Formation Flying Control Around Sun-Earth L2 Point, AIAA Guidance, Navigation, and Control Conference, 11-13 August, 2009, Chicago, US, AIAA 2009-2688.

7. Feng Wang, XueQin Chen, Antonios Tsourdos, Brian A. White, and YunHua Wu, Nonlinear Relative Position Control of Precise Formation Flying Using Polynomial Eigenstructure Assignment, Acta Astronautica (2011), 68, pp: 1830-1838, doi:10.10.16/j.actaastro.2011.01.008.

8. Feng Wang, Antonios Tsourdos, Rafał Żbikowski, Brian A. White, Finn Ankersen, and Adrian Stanley, Formation Flying Control around Sun-Earth L2 Point Using Polynomial Eigenstructure Assignment, Aerospace Science and Technology (Accepted).

9. Feng Wang, Antonios Tsourdos, Rafał Żbikowski, Brian A. White, Finn Ankersen and Adrian Stanley, Using LMI Approach to Assess D-Stability Performance of Sun-Earth L2 Formation Flying Control System,International Journal of control (Under review).

10. Feng Wang, Antonios Tsourdos, Rafał Żbikowski, Brian A. White, Finn Ankersen and Adrian Stanley, The Design of a Quasi-Linear Parameter

Varying Controller and Its Robust Analysis for Sun-Earth L2 Formation, Aerospace Science and Technology (Under review).

11. Feng Wang, Antonios Tsourdos, Rafał Żbikowski, and Brian A. White, D-region Stability Analysis of Polynomial Matrices and Polynomial Matrix Polytopes by Using LMI Approach, International Journal of control (Under review).

12. Feng Wang, Antonios Tsourdos, Brian A. White, Finn Ankersen and Adrian Stanley, The Design of Polynomial Eigenstructure Assignment Controller and Its Robust Analysis for Flexible Spacecraft Precise Control System, AIAA Guidance, Navigation, and Control Conference. 2011, US. (Accept) Also submit to Journal of Guidance, Navigation, and Control (Under review)

13. Feng Wang, XueQin Chen, YunHua Wu, Antonios Tsourdos, and Brian A. White, New robust D-stability LMI conditions of matrix polytopes via affine parameter dependent Lyapunov functions, System and Control Letter (Under review).

Chapter 2

Modeling of DARWIN Formation Flying

In this chapter the dynamic equations, including nonlinear, linearised and Quasi-LPV models, of rigid spacecraft for formation flying around the L_2 point of the Sun-Earth system are developed in detail, in which the nonlinear model is used as the base for the simulation, and the other two are the nominal models for control algorithm design. Finally, a simple QLPV model of a flexible spacecraft formation is developed in order to consider the effects induced by the flexibility of the spacecraft .

2.1 Nonlinear Model of the L_2 Formation

The exact nonlinear dynamic equation for formation flying around the L_2 point of the Sun-Earth system is first presented as a foundation for the linearization, transformation, design, analysis and simulation of the formation problem in this thesis. With the assumption of ideal alignment and placement of thrusters, translational control and rotational control systems are described as decoupled systems in this chapter. Thereby dividing the dynamics into translational dynamics and rotational dynamics, respectively. The coupling effect caused by the misalignment and displacement of thrusters away from the nominal are described in Chapter 4.

2.1.1 Translational Dynamics

2.1.1.1 Single Spacecraft Translational Motion

For the Sun-Earth L_2 point formation, the RTBP is the most common nonlinear model to describe its relative motion. As shown in Fig. 2.1, the frame origin of the rotating orbital frame **ROF** is located at the barycentre of the Sun-Earth system, with its X-axis passing through the centre of the two masses and pointing from

the Sun to the barycentre of the Earth-Moon; its Z-axis is in the direction of the angular velocity of the two primary masses about the barycentre, and its Y-axis completes a right-handed triad. The dynamic equation of motion for a single spacecraft near the Sun-Earth L2 point is given by:

$$\ddot{\boldsymbol{r}}_i = -\left(\frac{\mu_1}{\|\boldsymbol{r}_{1i}\|^3} + \frac{\mu_2}{\|\boldsymbol{r}_{2i}\|^3}\right)\boldsymbol{r}_i - \left(\frac{\mu_1(x_e + D_1)}{\|\boldsymbol{r}_{1i}\|^3} + \frac{\mu_2(x_e - D_2)}{\|\boldsymbol{r}_{2i}\|^3}\right)\hat{\boldsymbol{x}} + n^2 x_e \hat{\boldsymbol{x}} \tag{2.1}$$

where $\boldsymbol{r}_i = [X_{hi}, Y_{hi}, Z_{hi}]^T$ is the vector from the L_2 point to spacecraft i; $\ddot{\boldsymbol{r}}_i$ is the second derivative of $\boldsymbol{r}_i$ with respect to the inertial frame **IHE**; μ_1 is the solar Keplerian constant; μ_2 is the terrestrial Keplerian constant (Earth+Moon); $\boldsymbol{r}_{1i}$ is the vector from the Sun to spacecraft i; $\boldsymbol{r}_{2i}$ is the vector from Earth-Moon barycentre to spacecraft i; x_e is the distance from origin to L_2 point; D_1 is the distance from origin to the Sun; D_2 is the distance from origin to Earth-Moon barycentre; $\hat{\boldsymbol{x}}$ is the unit vector that parallels to Sun-Earth line, pointing from the Sun to the Earth; n is the angular velocity of rotating orbital frame **ROF** with respect to the inertial frame **IHE**; $\boldsymbol{u}_i$ is the control vector of spacecraft i. The inertial frame **IHE** and all other undefined frames in this thesis are described in Appendix A.

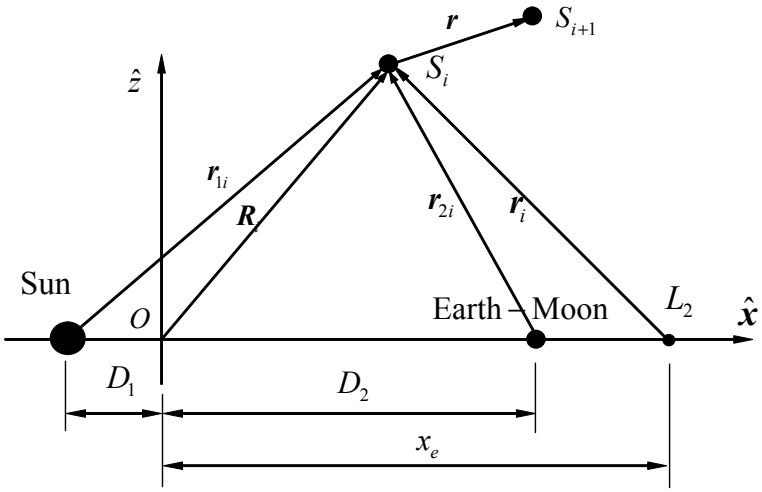

Figure 2.1: Restricted Three Body Problem

Denoting f as the true anomaly of Earth with respect to the Sun, the left side of Eq. (2.1) can be expanded in the **ROF** frame as:

$$\ddot{\boldsymbol{r}} = \begin{bmatrix} \ddot{X}_h - \dot{f}\ddot{Y}_h - 2\dot{f}\dot{Y}_h - \dot{f}^2 X_h \\ \ddot{Y}_h + \dot{f}\ddot{X}_h + 2\dot{f}\dot{X}_h - \dot{f}^2 Y_h \\ \ddot{Z}_h \end{bmatrix} \tag{2.2}$$

In the CRTBP, $\dot{f} = n$ is constant. Therefore, Eq. (2.2) can be rewritten as:

$$\ddot{\boldsymbol{r}} = \begin{bmatrix} \ddot{X}_h - 2n\dot{Y}_h - n^2 X_h \\ \ddot{Y}_h + 2n\dot{X}_h - n^2 Y_h \\ \ddot{Z}_h \end{bmatrix} \tag{2.3}$$

By using Eq. (2.3), the dynamic equation can be linearised as:

$$\begin{bmatrix} \ddot{X}_h - 2n\dot{Y}_h - (n^2 + 2\sigma)X_h \\ \ddot{Y}_h + 2n\dot{X}_h - (n^2 - \sigma)Y_h \\ \ddot{Z}_h + \sigma Z_h \end{bmatrix} = 0 \tag{2.4}$$

where $\sigma = \frac{\mu_1}{(x_e+D_1)^3} + \frac{\mu_2}{(x_e-D_2)^3}$. Its analytical solution is:

$$\begin{aligned} X_h &= A_1 e^{\varepsilon t} + A_2 e^{-\varepsilon t} + A_3 \cos\lambda t + A_4 \sin\lambda t \\ Y_h &= -k_1 A_1 e^{\varepsilon t} + k_1 A_2 e^{-\varepsilon t} - k_2 A_3 \sin\lambda t + k_2 A_4 \cos\lambda t \\ Z_h &= B_1 \cos\nu t + B_2 \sin\nu t \end{aligned} \tag{2.5}$$

where $\pm\varepsilon$ are the real roots and λ is the modulus of the imaginary roots of Eq. (2.4); $\nu^2 = \sigma$; k_1 and k_2 are positive proportionality constants; A_1, A_2, A_3, A_4, B_1 and B_2 are integration constants. This solution may indicate an unbounded motion due to its exponential terms, except when choosing the following suitable initial conditions:

$$\begin{aligned} X_h(0) &= A_3 \qquad \dot{X}_h(0) = \lambda A_4 \\ Y_h(0) &= k_2 A_4 \qquad \dot{Y}_h(0) = -k_2 \lambda A_3 \end{aligned} \tag{2.6}$$

Thus, A_1 and A_2 are set to zero, and the solution can be rewritten as:

$$\begin{aligned} X_h &= A_3 \cos\lambda t + A_4 \sin\lambda t \\ Y_h &= -k_2 A_3 \sin\lambda t + k_2 A_4 \cos\lambda t \\ Z_h &= B_1 \cos\nu t + B_2 \sin\nu t \end{aligned} \quad , \tag{2.7}$$

which can be represented more concisely as:

$$\begin{aligned} X_h &= -A_x \cos(\lambda t + \phi) \\ Y_h &= k A_x \sin(\lambda t + \phi) \\ Z_h &= A_z \sin(\nu t + \psi) \end{aligned} \quad , \tag{2.8}$$

where A_x and A_z characterize the amplitude of the in-plane and out-of plane motion, respectively and where k is equal to the k_2 in Eq. (2.7), which can be calculated as:

$$k = \frac{n^2+2\sigma+\lambda^2}{2\lambda n}. \tag{2.9}$$

The phase angles ϕ and ψ are determined by the initial conditions. The frequencies in Eq. (2.8) should be commensurate with the requirement of periodic motion, for instance the HALO orbit. (This requirement will be also taken into account in higher order approximations used in the thesis.) For this case the periodic motion orbit can be characterized by one parameter. Specifically, if ϕ and ψ satisfy:

$$\psi = \phi + \tfrac{N\pi}{2} \ , \tag{2.10}$$

then the solution is a HALO orbit. N is an integer in this equation, and setting $N = 1$ will result to a northern HALO orbit (the maximum out-of-plane component is above the X-Y plane ($Z > 0$)), while a southern HALO orbit (the maximum out-of-plane component is below the X-Y plane ($Z < 0$)) requires $N = 3$.

The analytic solution as Eq. (2.7) uses a second order truncation of Eq. (2.4) which is usually used for analysis and design. However, a higher order solution is required for the high precision required for more stringent missions, such as interferometry. In Richardson (1980), a third order analytical solution to the full three-dimensional dynamics of periodic motion about the L_2 point in the CRTBP frame is developed successfully, and which is given by:

$$\begin{aligned}
X_h &= a_{21}A_x^2 + a_{22}A_z^2 - A_x\cos\tau_1 + (a_{23}A_x^2 - a_{24}A_z^2)\cos 2\tau_1 + (a_{31}A_x^3 - a_{32}A_xA_z^2)\cos 3\tau_1 \\
Y_h &= kA_x\sin\tau_1 + (b_{21}A_z^2 - b_{22}A_2^2)\sin 2\tau_1 + (b_{31}A_x^2 - b_{32}A_xA_z^2)\sin 3\tau_1 \\
Z_h &= \delta_n A_z\cos\tau_1 + \delta_n d_{21}A_xA_z(\cos 2\tau_1 - 3) + \delta_n(d_{32}A_zA_x^2 - d_{31}A_z^3)\cos 3\tau_1
\end{aligned} \tag{2.11}$$

where A_x, A_y and A_z are the amplitudes of the linearised HALO solution in X_h, Y_h and Z_h direction, respectively; τ_1 is the independent variable relating frequency correction and orbital rate; and other parameters are displayed in Appendix B.

With a constrained relationship between A_x and A_z, it is easy to obtain the initial conditions of spacecraft for any point on a HALO orbit. Due to the higher order term, this solution is significantly more accurate than the second order solution in Eq. (2.7). For further details of the terms and parameters, please refer to Richardson (1980).

2.1.1.2 Relative Translational Motion

Using the single spacecraft translation dynamic equation, it is straightforward to obtain the relative dynamics of formation flying between two near-distance

spacecraft. We denote $\boldsymbol{r}_h$ and $\boldsymbol{r}_t$ as the vectors from the L_2 point to spacecraft 1 (the hub in interferometry mission) and spacecraft 2 (the telescope), respectively. The relative motion equation in the rotating orbital frame **ROF** can then be expressed as:

$$\begin{aligned}&\ddot{\boldsymbol{r}} = \ddot{\boldsymbol{r}}_t - \ddot{\boldsymbol{r}}_h = -\mu_1\left(\frac{\boldsymbol{r}_t}{\|\boldsymbol{r}_{1t}\|^3} - \frac{\boldsymbol{r}_h}{\|\boldsymbol{r}_{1h}\|^3}\right) - \\ &\mu_2\left(\frac{\boldsymbol{r}_t}{\|\boldsymbol{r}_{2t}\|^3} - \frac{\boldsymbol{r}_h}{\|\boldsymbol{r}_{2h}\|^3}\right) - \mu_1(x_e + D_1)\left(\frac{1}{\|\boldsymbol{r}_{1t}\|^3} - \frac{1}{\|\boldsymbol{r}_{1h}\|^3}\right)\hat{x} - \\ &\mu_2(x_e - D_2)\left(\frac{1}{\|\boldsymbol{r}_{2t}\|^3} - \frac{1}{\|\boldsymbol{r}_{2h}\|^3}\right)\hat{x} + \boldsymbol{u}_{th} + \boldsymbol{f}_d\end{aligned} \tag{2.12}$$

where $\boldsymbol{r}$ is the vector from the hub to the telescope, $\boldsymbol{r} = \boldsymbol{r}_t - \boldsymbol{r}_h = [x, y, z]^T$; $\boldsymbol{u}_{th} = [u_x, u_y, u_z]^T$ is the relative control force of the telescope with respect to the hub; and $\boldsymbol{f}_d$ is the disturbance for the relative motion.

In the RTBP, the Earth-Moon system is regarded as a combined mass located at its barycentre. To improve the precision of dynamic model, it is necessary to model them separately. Therefore, the lunar gravitational force should be computed individually as shown in Fig. 2.2, in which $\boldsymbol{\rho}_{3i}$ denotes the vector from the Moon to the spacecraft i (either the hub or the telescope), and μ_3 is the lunar Keplerian constant. The lunar force per unit mass on spacecraft i is given by:

$$-\mu_3\frac{\boldsymbol{\rho}_{3i}}{\|\boldsymbol{\rho}_{3i}\|^3} \tag{2.13}$$

Therefore, its contribution to the relative motion equation of the telescope with respect to the hub is:

$$\boldsymbol{f}_m = -\mu_3\left(\frac{\boldsymbol{\rho}_{3t}}{\|\boldsymbol{\rho}_{3t}\|^3} - \frac{\boldsymbol{\rho}_{3h}}{\|\boldsymbol{\rho}_{3h}\|^3}\right) \tag{2.14}$$

Using Eq. (2.14), Eq. (2.12) can be rewritten as:

$$\begin{aligned}&\ddot{\boldsymbol{r}} = \ddot{\boldsymbol{r}}_t - \ddot{\boldsymbol{r}}_h = -\mu_1\left(\frac{\boldsymbol{r}_t}{\|\boldsymbol{r}_{1t}\|^3} - \frac{\boldsymbol{r}_h}{\|\boldsymbol{r}_{1h}\|^3}\right) - \\ &\mu_2\left(\frac{\boldsymbol{r}_t}{\|\boldsymbol{r}_{2t}\|^3} - \frac{\boldsymbol{r}_h}{\|\boldsymbol{r}_{2h}\|^3}\right) - \mu_1(x_e + D_1)\left(\frac{1}{\|\boldsymbol{r}_{1t}\|^3} - \frac{1}{\|\boldsymbol{r}_{1h}\|^3}\right)\hat{x} - \\ &\mu_2(x_e - D_2)\left(\frac{1}{\|\boldsymbol{r}_{2t}\|^3} - \frac{1}{\|\boldsymbol{r}_{2h}\|^3}\right)\hat{x} + \boldsymbol{u}_{th} - \mu_3\left(\frac{\boldsymbol{\rho}_{3t}}{\|\boldsymbol{\rho}_{3t}\|^3} - \frac{\boldsymbol{\rho}_{3h}}{\|\boldsymbol{\rho}_{3h}\|^3}\right)\end{aligned} \tag{2.15}$$

Apart from the effect of lunar gravitational force, the solar radiation pressure should also be taken into account as well in our model. The solar radiation pressure force per unit mass on spacecraft i can be expressed as (Segerman & Zedd, 2003):

$$\frac{1.0198\times10^{17}C_R A_i \sigma_{sf}}{m_i\|\boldsymbol{\rho}_{1i}\|^2}\boldsymbol{\rho}_{1i} \tag{2.16}$$

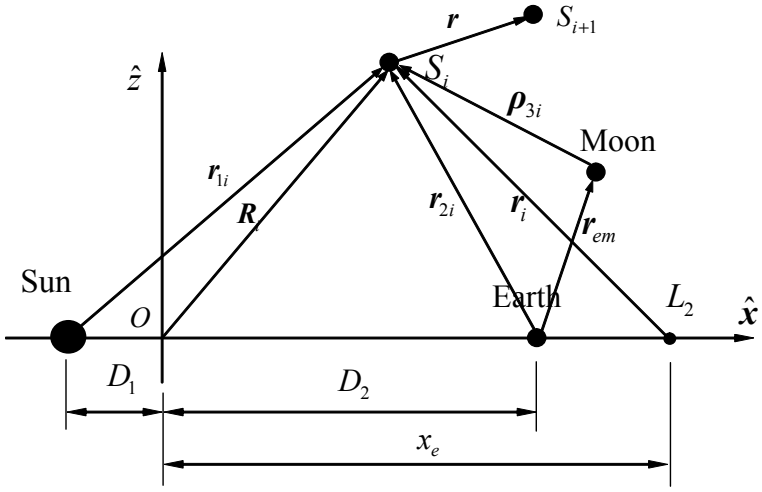

Figure 2.2: Sun-Earth-Moon L_2 Dynamics

where C_R is the characteristic parameter of reflectivity of the spacecraft surface facing the Sun: where $C_R = 0$ translucent, $C_R = 1$ perfectly absorbent, $C_R = 2$ perfectly reflective; A_i is the cross-sectional area of the spacecraft of mass m_i normally projected onto the spacecraft-Sun line; and σ_{sf} is luminosity reduction factor which ranges from zero (total eclipse) to unity (full sunlight). Therefore, the contribution of solar radiation pressure to the relative motion equation of the telescope with respect to the hub is described as:

$$\boldsymbol{f}_s = \frac{1.0198\times10^{17} C_R A_t \sigma_{sf}}{m_t \|\boldsymbol{\rho}_{1t}\|^2}\boldsymbol{\rho}_{1t} - \frac{1.0198\times10^{17} C_R A_h \sigma_{sf}}{m_h \|\boldsymbol{\rho}_{1h}\|^2}\boldsymbol{\rho}_{1h} \tag{2.17}$$

These two forces are the major disturbances for the relative motion of the L_2 point formation. If the hub motion orbit about the L_2 point is around $900,000$ km and the relative distance is around 500 m, the magnitude of lunar gravity force $\boldsymbol{f}_m$ in Eq. (2.14) is of the order of 10^{-15} m/s^2. For the same condition, the magnitude of solar radiation pressure $\boldsymbol{f}_s$ in Eq. (2.17) is of the order of 10^{-12} m/s^2 if the sunlight is perfect and the difference of the Area/Mass ratio A/m between two spacecraft is around 3%. From these data, it would seem that the effect of solar radiation pressure on the dynamic motion is much greater than that of lunar gravity. However, it is not usually true in practice. The reason is that the solar radiation pressure varies very slowly due to the unchanged sunlight direction in the **ROF** frame and the Area/Mass ratio difference rates are very small (assume the spacecraft are stabilized in the **ROF** frame) while the variation of lunar gravity is relatively fast due to the motion of the moon (its period is 29 *days*, which is

relatively short since the hub motion period is 180 *days*). The real values are illustrated in Fig. 3.27 and 3.28 in Section 3.4, where the minmum/maximum are $2.44\times10^{-12}/2.45\times10^{-12}\ m/s^2$ (solar radiation pressure) and $1\times10^{-15}/12\times10^{-15}\ m/s^2$ (lunar gravity). For control system design a slow varying one is relatively easy to be compensated by a controller in contrast to a fast varying disturbance. This will be verified in the simulation in the following chapters.

Considering these two major disturbances, the relative motion equation in Eq. (2.15) can then be rewritten as:

$$\begin{aligned}
&\ddot{\boldsymbol{r}} = \ddot{\boldsymbol{r}}_t - \ddot{\boldsymbol{r}}_h = -\mu_1\left(\frac{\boldsymbol{r}_t}{\|\boldsymbol{r}_{1t}\|^3} - \frac{\boldsymbol{r}_h}{\|\boldsymbol{r}_{1h}\|^3}\right) - \\
&\mu_2\left(\frac{\boldsymbol{r}_t}{\|\boldsymbol{r}_{2t}\|^3} - \frac{\boldsymbol{r}_h}{\|\boldsymbol{r}_{2h}\|^3}\right) - \mu_1(x_e + D_1)\left(\frac{1}{\|\boldsymbol{r}_{1t}\|^3} - \frac{1}{\|\boldsymbol{r}_{1h}\|^3}\right)\hat{x} - \\
&\mu_2(x_e - D_2)\left(\frac{1}{\|\boldsymbol{r}_{2t}\|^3} - \frac{1}{\|\boldsymbol{r}_{2h}\|^3}\right)\hat{x} - \mu_3\left(\frac{\boldsymbol{\rho}_{3t}}{\|\boldsymbol{\rho}_{3t}\|^3} - \frac{\boldsymbol{\rho}_{3h}}{\|\boldsymbol{\rho}_{3h}\|^3}\right) \\
&+\frac{1.0198\times10^{17}C_R A_t\sigma_{sf}}{m_t\|\boldsymbol{\rho}_{1t}\|^2}\boldsymbol{\rho}_{1t} - \frac{1.0198\times10^{17}C_R A_h\sigma_{sf}}{m_h\|\boldsymbol{\rho}_{1h}\|^2}\boldsymbol{\rho}_{1h} + \boldsymbol{u}_{th}
\end{aligned} \tag{2.18}$$

Equation (2.18) is the nonlinear relative dynamic equation in the vicinity of L_2 point with lunar gravitation and solar radiation pressure disturbances. Here, the relative translational and rotational coupling is not considered, however it will be assessed for its influence on system performance in Section 4.5.

2.1.2 Rotational Dynamics

Spacecraft rotational dynamics, also known as attitude dynamics, is the main topic in many books and research publications. In this section, a general review of rigid body rotational dynamics is summarized for the Sun-Earth L_2 point formation flying control problem.

2.1.2.1 Single Spacecraft Rotational Motion

Disregarding disturbance torques, the description of the rotational dynamics of a rigid spacecraft i without reaction wheels in the rotating body frame **RBF** is given by:

$$\boldsymbol{J}_i\dot{\boldsymbol{\omega}}_i + \boldsymbol{\omega}_i \times (\boldsymbol{J}_i\boldsymbol{\omega}_i) = \boldsymbol{\tau}_i \tag{2.19}$$

where $\boldsymbol{J}_i$ is the inertia matrix, $\boldsymbol{\omega}_i$ is the angular velocity vector, and $\boldsymbol{\tau}_i$ is the control torque vector.

2.1.2.2 Relative Rotational Motion

We denote $\boldsymbol{\omega}_h$ and $\boldsymbol{q}_h$ as the angular velocity and attitude quaternion of spacecraft 1 (the hub) with respect to the inertial frame **IHE** which are expressed in its body frame **RBF1**, and denote $\boldsymbol{\omega}_t$ and $\boldsymbol{q}_t$ as the angular velocity and attitude quaternion of spacecraft 2 (the telescope) with respect to the inertial frame **IHE** which are expressed in its body frame **RBF2**. The error angular velocity $\boldsymbol{\omega}_e$ and attitude quaternion $\boldsymbol{q}_e$ of frame **RBF2** with respect to frame **RBF1** are then given by:

$$\begin{aligned} \boldsymbol{\omega}_e &= \boldsymbol{\omega}_t - \boldsymbol{C}_{th}\boldsymbol{\omega}_h \\ \dot{\boldsymbol{q}}_e &= \tfrac{1}{2}\boldsymbol{q}_e \otimes \boldsymbol{\omega}_{eaug} \end{aligned} \tag{2.20}$$

where $\boldsymbol{C}_{th}$ is the rotation matrix relating frame **RBF1** to frame **RBF2**; $\otimes$ is quaternion multiplication; and $\boldsymbol{\omega}_{eaug}$ is $\boldsymbol{\omega}_e$ in quaternion form, $\boldsymbol{\omega}_{eaug} = [0 \;\; \boldsymbol{\omega}_e^T]^T$.

Substituting Eq. (2.20) into Eq. (2.19), the error dynamic equation of relative rotational motion is given as:

$$\boldsymbol{J}_t\dot{\boldsymbol{\omega}}_e = -(\boldsymbol{\omega}_e + \boldsymbol{C}_{th}\boldsymbol{\omega}_h) \times (J_t(\boldsymbol{\omega}_e + \boldsymbol{C}_{th}\boldsymbol{\omega}_t)) - \boldsymbol{J}_h(\boldsymbol{C}_{th}\dot{\boldsymbol{\omega}}_h - \boldsymbol{\omega}_e \times (\boldsymbol{C}_{th}\boldsymbol{\omega}_h)) + \boldsymbol{\tau} \tag{2.21}$$

Furthermore if the hub is three-axis stabilized in the **IHE** frame, that is $\boldsymbol{\omega}_1 = \boldsymbol{0}$, then $\boldsymbol{\omega}_e = \boldsymbol{\omega}_t$. Therefore Eq. (2.20) and Eq. (2.21) can be simplified to give:

$$\dot{\boldsymbol{q}}_e = \tfrac{1}{2}\boldsymbol{q}_e \otimes \boldsymbol{\omega}_{taug} \tag{2.22}$$

$$\boldsymbol{J}_t\dot{\boldsymbol{\omega}}_t = -\boldsymbol{\omega}_t \times (\boldsymbol{J}_t\boldsymbol{\omega}_t) + \boldsymbol{\tau} \tag{2.23}$$

which has the same as the dynamic model of a single spacecraft given by Eq. (2.19).

Thus, the dynamic equations and relative dynamic equations of spacecraft are expressed by Eq. (2.1), Eq. (2.18), Eq. (2.19) and Eq. (2.21), respectively.

2.2 Linear Model of the Sun-Earth L_2 Point Formation

This section developes the linearised models of translational and rotational motion, which are the topics of many articles (Segerman & Zedd, 2003; Roberts, 2005; Luquette, 2006).

2.2.1 Linear Model of Translational Motion

Since linear model is the major focus for control system design for the Sun-Earth L_2 point formation problem, the nonlinear model of translation dynamics must be linearised to obtain different linear models for system control design. The main linearised models used in the literature are described in this section.

2.2.1.1 Series Expansion of Nonlinear Model

For a nonlinear system in Eq. (2.18), using approximated models (LTI model and LPV model) rather than the nonlinear model is the normal strategy used to design the formation control system. To obtain these linear models, Series Expansion is used to linearize the nonlinear terms of Eq. (2.18).

For the vector $\boldsymbol{r}_{1h}$ from the Sun to the hub, one has:

$$\boldsymbol{r}_{1h} = (x_e + D_1)\hat{\boldsymbol{x}} + \boldsymbol{r}_h \tag{2.24}$$

where $\boldsymbol{r}_h$ is the vector from the L_2 point to the mass centre of hub which is given by Eq. (2.11). Let scalar a denote the norm of vector $\boldsymbol{a}$. The square of the magnitude of $\boldsymbol{r}_{1h}$ is:

$$\begin{aligned} r_{1h}^2 &= \boldsymbol{r}_{1h} \cdot \boldsymbol{r}_{1h} = (x_e + D_1)^2 + r_h^2 + 2(x_e + D_1)x_h \\ &= (x_e + D_1)^2 \left[1 + \left(\tfrac{r_h}{x_e + D_1}\right)^2 + \tfrac{2x_h}{x_e + D_1}\right] \end{aligned} \tag{2.25}$$

where x_h is the x-component of $\boldsymbol{r}_h$. Then, one has:

$$\frac{1}{\|\boldsymbol{r}_{1h}\|^3} = \frac{1}{(x_e + D_1)^3}\left[1 + \left(\tfrac{r_h}{x_e + D_1}\right)^2 + \tfrac{2x_h}{x_e + D_1}\right]^{-3/2} = (x_e + D_1)^{-3}(1 + \varepsilon_{1h})^{-3/2} \tag{2.26}$$

where $\varepsilon_{1h} = \left(\tfrac{r_h}{x_e + D_1}\right)^2 + \tfrac{2x_h}{x_e + D_1}$. Using a binomial expansion, Eq. (2.26) yields:

$$\frac{1}{\|\boldsymbol{r}_{1h}\|^3} = (x_e + D_1)^{-3}(1 + \varepsilon_{1h})^{-3/2} = (x_e + D_1)^{-3}\left[1 + \textstyle\sum_{k=1}^{\infty} C_k^{-3/2}\varepsilon_{1h}^k\right] \tag{2.27}$$

In the same way, for the telescope, we get:

$$\frac{1}{\|\boldsymbol{r}_{1t}\|^3} = (x_e + D_1)^{-3}(1 + \varepsilon_{1t})^{-3/2} = (x_e + D_1)^{-3}\left[1 + \textstyle\sum_{k=1}^{\infty} C_k^{-3/2}\varepsilon_{1t}^k\right], \tag{2.28}$$

where $\varepsilon_{1t} = \left(\tfrac{r_t}{x_e + D_1}\right)^2 + \tfrac{2x_t}{x_e + D_1}$.

Noting $\boldsymbol{r}_t = \boldsymbol{r}_h + \boldsymbol{r}$, then $r_t^2 = (\boldsymbol{r}_h + \boldsymbol{r}) \cdot (\boldsymbol{r}_h + \boldsymbol{r}) = r_h^2 + r^2 + 2\boldsymbol{r} \cdot \boldsymbol{r}_h$. Therefore:

$$\begin{aligned} \varepsilon_{1t} &= \left(\frac{r_t}{x_e+D_1}\right)^2 + \frac{2x_t}{x_e+D_1} = \frac{r_h^2+r^2+2\boldsymbol{r}\cdot\boldsymbol{r}_h}{(x_e+D_1)^2} + \frac{2(x_h+x)}{x_e+D_1} \\ &= \frac{r_h^2}{(x_e+D_1)^2} + \frac{2x_h}{x_e+D_1} + \frac{r^2+2\boldsymbol{r}\cdot\boldsymbol{r}_h}{(x_e+D_1)^2} + \frac{2x}{x_e+D_1} = \varepsilon_{1h} + \delta_1 \end{aligned} , \tag{2.29}$$

where $\delta_1 = \frac{r^2+2\boldsymbol{r}\cdot\boldsymbol{r}_h}{(x_e+D_1)^2} + \frac{2x}{x_e+D_1}$.

Using Eq. (2.29), Eq. (2.28) can be written as:

$$\begin{aligned} \frac{1}{\|\boldsymbol{r}_{1t}\|^3} &= (x_e + D_1)^{-3}(1 + \varepsilon_{1t})^{-3/2} \\ &= (x_e + D_1)^{-3}\left[1 + \sum_{k=1}^{\infty} C_k^{-3/2}\left(\varepsilon_{1h}^k + \sum_{j=1}^{k} C_j^k \delta_1^j \varepsilon_{1h}^{k-j}\right)\right] . \\ &= \frac{1}{\|\boldsymbol{r}_{1h}\|^3} + (x_e + D_1)^{-3} \sum_{k=1}^{\infty} C_k^{-3/2} \sum_{j=1}^{k} C_j^k \delta_1^j \varepsilon_{1h}^{k-j} \end{aligned} \tag{2.30}$$

Substituting this into Eq. (2.18), gives:

$$\frac{1}{\|\boldsymbol{r}_{1t}\|^3} - \frac{1}{\|\boldsymbol{r}_{1h}\|^3} = (x_e + D_1)^{-3} \sum_{k=1}^{\infty} C_k^{-3/2} \sum_{j=1}^{k} C_j^k \delta_1^j \varepsilon_{1h}^{k-j} . \tag{2.31}$$

Additionally,

$$\begin{aligned} \frac{\boldsymbol{r}_t}{\|\boldsymbol{r}_{1t}\|^3} - \frac{\boldsymbol{r}_h}{\|\boldsymbol{r}_{1h}\|^3} &= \frac{\boldsymbol{r}_h+\boldsymbol{r}}{\|\boldsymbol{r}_{1t}\|^3} - \frac{\boldsymbol{r}_h}{\|\boldsymbol{r}_{1h}\|^3} = \frac{\boldsymbol{r}_h}{\|\boldsymbol{r}_{1t}\|^3} - \frac{\boldsymbol{r}_h}{\|\boldsymbol{r}_{1h}\|^3} + \frac{\boldsymbol{r}}{\|\boldsymbol{r}_{1t}\|^3} \\ &= \frac{\boldsymbol{r}_h+\boldsymbol{r}}{(x_e+D_1)^3} \sum_{k=1}^{\infty} C_k^{-3/2} \sum_{j=1}^{k} C_j^k \delta_1^j \varepsilon_{1h}^{k-j} + \frac{\boldsymbol{r}}{(x_e+D_1)^3}\left[1 + \sum_{k=1}^{\infty} C_k^{-3/2} \varepsilon_{1h}^k\right] . \end{aligned} \tag{2.32}$$

A similar expansion may be used to form the following relationship for distances involving the Earth:

$$\frac{1}{\|\boldsymbol{r}_{2t}\|^3} - \frac{1}{\|\boldsymbol{r}_{2h}\|^3} = (x_e - D_2)^{-3} \sum_{k=1}^{\infty} C_k^{-3/2} \sum_{j=1}^{k} C_j^k \delta_2^j \varepsilon_{2h}^{k-j} , \tag{2.33}$$

$$\frac{\boldsymbol{r}_t}{\|\boldsymbol{r}_{2t}\|^3} - \frac{\boldsymbol{r}_h}{\|\boldsymbol{r}_{2h}\|^3} = \frac{\boldsymbol{r}_h+\boldsymbol{r}}{(x_e-D_2)^3} \sum_{k=1}^{\infty} C_k^{-3/2} \sum_{j=1}^{k} C_j^k \delta_2^j \varepsilon_{2h}^{k-j} + \frac{\boldsymbol{r}}{(x_e-D_2)^3}\left[1 + \sum_{k=1}^{\infty} C_k^{-3/2} \varepsilon_{2h}^k\right] , \tag{2.34}$$

where $\varepsilon_{2h} = \left(\frac{r_h}{x_e-D_2}\right)^2 + \frac{2x_h}{x_e-D_2}$,$\delta_2 = \frac{r^2+2\boldsymbol{r}\cdot\boldsymbol{r}_h}{(x_e-D_2)^2} + \frac{2x}{x_e-D_2}$

Using an identical development, the term of lunar gravitation is given by:

$$\frac{\boldsymbol{\rho}_{3t}}{\|\boldsymbol{\rho}_{3t}\|^3} - \frac{\boldsymbol{\rho}_{3h}}{\|\boldsymbol{\rho}_{3h}\|^3} = \frac{\boldsymbol{\rho}_{3h}}{\|\boldsymbol{\rho}_{3h}\|^3} \sum_{k=1}^{\infty} C_k^{-3/2} \delta_3^k + \frac{\boldsymbol{r}}{\|\boldsymbol{\rho}_{3h}\|^3}\left[1 + \sum_{k=1}^{\infty} C_k^{-3/2} \delta_3^k\right] , \tag{2.35}$$

where $\delta_3 = \frac{r^2+2\boldsymbol{r}\cdot\boldsymbol{\rho}_{3h}}{\|\boldsymbol{\rho}_{3h}\|^2}$. Substituting Eq. (2.31) ~ Eq. (2.35) into Eq. (2.18), the nonlinear relative motion equation described by the series expansion is thus:

$$\begin{aligned} &\ddot{\boldsymbol{r}} = \mu_1\left(\frac{\boldsymbol{r}_h+r}{(x_e+D_1)^3} \sum_{k=1}^{\infty} C_k^{-3/2} \sum_{j=1}^{k} C_j^k \delta_1^j \varepsilon_{1h}^{k-j} + \frac{\boldsymbol{r}}{(x_e+D_1)^3}\left[1 + \sum_{k=1}^{\infty} C_k^{-3/2} \varepsilon_{1h}^k\right]\right) \\ &-\mu_2\left(\frac{\boldsymbol{r}_h+\boldsymbol{r}}{(x_e-D_2)^3} \sum_{k=1}^{\infty} C_k^{-3/2} \sum_{j=1}^{k} C_j^k \delta_2^j \varepsilon_{2h}^{k-j} + \frac{\boldsymbol{r}}{(x_e-D_2)^3}\left[1 + \sum_{k=1}^{\infty} C_k^{-3/2} \varepsilon_{2h}^k\right]\right) \\ &-\frac{\mu_1\hat{\boldsymbol{x}}}{(x_e+D_1)^2}\left(\sum_{k=1}^{\infty} C_k^{-3/2} \sum_{j=1}^{k} C_j^k \delta_1^j \varepsilon_{1h}^{k-j}\right) - \frac{\mu_2\hat{\boldsymbol{x}}}{(x_e-D_2)^2}\left(\sum_{k=1}^{\infty} C_k^{-3/2} \sum_{j=1}^{k} C_j^k \delta_2^j \varepsilon_{2h}^{k-j}\right) . \\ &-\mu_3\left(\frac{\boldsymbol{\rho}_{3h}}{\|\boldsymbol{\rho}_{3h}\|^3} \sum_{k=1}^{\infty} C_k^{-3/2} \delta_3^k + \frac{\boldsymbol{r}}{\left\|\rho_{3h}\right\|^3}\left[1 + \sum_{k=1}^{\infty} C_k^{-3/2} \delta_3^k\right]\right) \\ &+\frac{1.0198\times10^{17} C_R A_t \sigma_{sf}}{m_t \|\boldsymbol{\rho}_{1t}\|^2}\boldsymbol{\rho}_{1t} - \frac{1.0198\times10^{17} C_R A_h \sigma_{sf}}{m_h \|\boldsymbol{\rho}_{1h}\|^2}\boldsymbol{\rho}_{1h} \end{aligned} \tag{2.36}$$

By selecting different truncation orders of series expansion in Eq. (2.36), different LTI and LPV models can easily be developed. In order to decide how many terms in Eq. (2.36) should be kept for the desired precision, the magnitude ordering of all the terms in Eq. (2.36) can be carried out by substituting typical numerical values which are shown in Table 2.1.

Table 2.1: Basic Constants of the Sun-Earth System

μ_1	$1.3271244 \times 10^{11}\ km^3/s^2$
μ_2	$3.9860044 \times 10^{5}\ km^3/s^2$
μ_3	$4.9027779 \times 10^{3}\ km^3/s^2$
D_1	$4.5484085 \times 10^{2}\ km$
D_2	$1.4959742 \times 10^{8}\ km$
e	0.01670862
n	$1.9909837 \times 10^{-7}\ rad/s$
x_e	$1.5110515 \times 10^{8}\ km$
$r_e m$	$38,000\ km$
$c_2\ (\sigma)$	$1.5619125 \times 10^{-13}\ 1/s^2$

Using the orbit information of spacecraft in Section 2.1.1.2 and the basic parameters of the Sun-Earth system in Table 2.1, the magnitude of each acceleration term in Eq. (2.36) is calculated and presented in Table 2.2. The effects of these accelerations over 90 days are presented as well. In this table, one can notice that $c_2 r$ has the largest value which means it is the most significant linear term in Eq. (2.36). Therefore, if only this term is retained in the right side of Eq. (2.36), one can obtain the simplest linear model, which is an LTI model as c_2 is constant. Furthermore, by retaining more terms, different LTI and LPV models can be produced. These are developed in the next section.

2.2.1.2 Linear Time-Invariant Model

A dynamic equations of an LTI model can be expressed as:

$$\dot{\boldsymbol{x}} = \boldsymbol{A}\boldsymbol{x} + \boldsymbol{B}\boldsymbol{u}, \quad \boldsymbol{y} = \boldsymbol{C}\boldsymbol{x}, \tag{2.37}$$

Table 2.2: The Magnitude of Acceleration in Relative Dynamic Equation over 90 days

Acceleration term	Magnitude (s/m^2)	Effect (km)
c_2re	1.3049×10^{-15}	0.0395
n^2re	3.3117×10^{-16}	0.0100
c_2r	7.8096×10^{-14}	2.3611
c_3rr_h	3.5119×10^{-14}	1.0618
$c_4rr_h^2$	2.0818×10^{-14}	0.6294
$c_5rr_h^3$	1.2380×10^{-14}	0.3743
$c_6rr_h^4$	7.3622×10^{-15}	0.2226
$c_7rr_h^5$	4.3782×10^{-15}	0.1324
$c_8rr_h^6$	2.6037×10^{-15}	0.0787
$c_9rr_h^7$	1.5484×10^{-15}	0.0468
$c_{10}rr_h^8$	9.2081×10^{-16}	0.0278
$c_{11}rr_h^9$	5.4760×10^{-16}	0.0166
$\mu_3rr_{em}/(\gamma D)^4$	1.8018×10^{-16}	0.0054
$\mu_3rr_{em}r_h/(\gamma D)^5$	1.0714×10^{-16}	0.0032

where $\boldsymbol{x}$ is the state vector, $\boldsymbol{u}$ is the input vector, $\boldsymbol{y}$ is the output vector and $\boldsymbol{A}$, $\boldsymbol{B}$, and $\boldsymbol{C}$ are constant matrices. The section below describes how to obtain such an LTI model from Eq. (2.36).

With the true anomaly of Earth's orbit, $\ddot{\boldsymbol{r}}$ in Eq. (2.36) can be expanded in the rotating **ROF** frame as:

$$\ddot{\boldsymbol{r}} = \begin{bmatrix} \ddot{x} - \ddot{f}y - 2\dot{f}\dot{y} - \dot{f}^2x \\ \ddot{y} + \ddot{f}x + 2\dot{f}\dot{x} - \dot{f}^2y \\ \ddot{z} \end{bmatrix}, \tag{2.38}$$

which has the same form as Eq. (2.2).

As $\dot{f} = n$ is constant in the CRTBP, Eq. (2.38) can be rewritten as:

$$\ddot{\boldsymbol{r}} = \begin{bmatrix} \ddot{x} - 2n\dot{y} - n^2x \\ \ddot{y} + 2n\dot{x} - n^2y \\ \ddot{z} \end{bmatrix}, \tag{2.39}$$

and that for all the terms in Eq. (2.36), only the second order term of gravitational force c_2r has time-invariant coefficient. Hence, retaining this term, the LTI model

of Eq. (2.39) can be written as:

$$\begin{bmatrix} \ddot{x} - 2n\dot{y} - (n^2 + 2\sigma)x \\ \ddot{y} + 2n\dot{x} - (n^2 - \sigma)y \\ \ddot{z} + \sigma z \end{bmatrix} = 0, \tag{2.40}$$

where $\sigma = \frac{\mu_1}{(x_e+D_1)^3} + \frac{\mu_2}{(x_e-D_2)^3}$.

This LTI model, which is derived from the linearization about a single equilibrium of the nonlinear model to enable linear controller design, can also be obtained by linearizing Eq. (2.12) directly. It has been utilized commonly in LQR controller design in the literature, but has limited applicability for the entire system control envelope. As a solution in order to satisfy the requirement across the control envelope, a strategy of gain scheduling is introduced to yield a global controller. The gain schedule is a collection of LTI controllers designed for the corresponding LTI model obtained from the nonlinear model at different equilibrium points which, during operation, is switched on when the current operating point of the control envelope is close to the relevant linearised equilibrium condition. In this strategy, an external scheduling variable is required to decide this switching schedule.

2.2.1.3 Linear Parameter-Varying Model

The LPV model is a more precise mathematical description of the dynamic system, expressed as:

$$\dot{\boldsymbol{x}} = \boldsymbol{A}(\boldsymbol{\theta}(t))\boldsymbol{x} + \boldsymbol{B}(\boldsymbol{\theta}(t))\boldsymbol{u}, \quad \boldsymbol{y} = \boldsymbol{C}(\boldsymbol{\theta}(t))\boldsymbol{x}, \tag{2.41}$$

where the entries of $\boldsymbol{A}$, $\boldsymbol{B}$, and $\boldsymbol{C}$ are time-varying; and parameter $\boldsymbol{\theta}$ varies over time and represents a set of scheduling variables. With the resulting form in Eq.(2.41), the LPV model can preserve the utility of the linear equations while capturing the rapidly varying system dynamics.

To obtain an LPV model for a formation flying system, the higher order terms in Eq. (2.12) should be retained. Using this strategy in Eq. (2.12), the simplest LPV model (LPV1), can be obtained by keeping the first two largest terms in Table 2.2.

Thus, the LPV1 model can be expressed as:

$$\begin{bmatrix} \ddot{x} - 2n\dot{y} - (n^2 + 2\sigma)x \\ \ddot{y} + 2n\dot{x} - (n^2 - \sigma)y \\ \ddot{z} + \sigma z \end{bmatrix} = -\begin{bmatrix} c_3(6xX_h + (3\boldsymbol{r}_h \cdot \boldsymbol{r} - 15xX_h)) \\ c_3(3xY_h + 3yX_h)) \\ c_3(3xZ_h + 3zX_h) \end{bmatrix}, \tag{2.42}$$

Retaining more terms in Eq. (2.12), a more complex LPV Model (LPV2), can be obtained and is given by:

$$\begin{aligned} &\ddot{\boldsymbol{r}} = c_2(-\boldsymbol{r} + 3x\hat{\boldsymbol{x}}) + c_3(3x\boldsymbol{r}_h + 3X_h\boldsymbol{r} + (3\boldsymbol{r}_h \cdot \boldsymbol{r} - 15xX_h)\hat{\boldsymbol{x}}) + \\ &c_4((3\boldsymbol{r}_h \cdot \boldsymbol{r} - 15xX_h)\boldsymbol{r}_h + \tfrac{3}{2}(r_h^2 - 5X_h^2)\boldsymbol{r} - \tfrac{15}{2}(2X_h\boldsymbol{r}_h \cdot \boldsymbol{r} - 7xX_h^2 + xr_h^2)\hat{\boldsymbol{x}}) + \\ &c_5(\tfrac{15}{2}\boldsymbol{r}_h(-xr_h^2 - 2X_h\boldsymbol{r}_h \cdot \boldsymbol{r} + 7xX_h^2) + \tfrac{5}{2}r(7X_h^3 - 3X_hr_h^2) + \\ &\quad \tfrac{15}{2}(-r_h^2\boldsymbol{r}_h \cdot \boldsymbol{r} + 7X_h^2\boldsymbol{r}_h \cdot \boldsymbol{r} + 7xX_hr_h^2 - 21xX_h^3)\hat{\boldsymbol{x}}) + \\ &c_6(\tfrac{15}{8}\boldsymbol{r}(14r_h^2X_h^2 - 21X_h^4 - r_h^4) + \tfrac{15}{2}\boldsymbol{r}_h(-21xX_h^3 - r_h \cdot rr_h^2 + 7\boldsymbol{r}_h \cdot \boldsymbol{r}X_h^2 + 7xr_h^2X_h) + \\ &\quad \tfrac{21}{128}(-1440xr_h^2X_h^2 + 320\boldsymbol{r}_h \cdot \boldsymbol{r}r_h^2X_h + 80xr_h^4 - 33xX_h^4 - 960\boldsymbol{r}_h \cdot \boldsymbol{r}r_h^3)\hat{\boldsymbol{x}}) \end{aligned}, \tag{2.43}$$

where $c_n = \frac{\mu_1}{(x_e + D_1)^{n+1}} + \frac{\mu_2}{(x_e - D_2)^{n+1}}$.

Noting $\boldsymbol{\rho}_{3h} = \boldsymbol{r}_{2h} - \boldsymbol{r}_{em}$, the contribution of lunar gravitation in Eq. (2.36) is given by:

$$\begin{aligned} &\boldsymbol{f}_m \approx -3\mu_3[(-2xx_{em} + yy_{em} + zz_{em})\hat{\boldsymbol{x}} + (yx_{em} + xy_{em})\hat{\boldsymbol{y}} + (zx_{em} + xz_{em})\hat{\boldsymbol{z}}]/(\gamma D)^4 - \\ &\mu_3[-15x_{em}x\boldsymbol{r} + 3\boldsymbol{r}_h \cdot \boldsymbol{r}_{em}\boldsymbol{r} - 15xx_h\boldsymbol{r}_{em} + 3\boldsymbol{r}_h \cdot \boldsymbol{r}\boldsymbol{r}_{em} + 3\boldsymbol{r}_h \cdot \boldsymbol{r}_{em}(-5x_h\hat{\boldsymbol{x}} + \boldsymbol{r}_h) + \\ &105xx_{em}x_h\hat{\boldsymbol{x}} - 15xx_{em}\boldsymbol{r}_h - 15x\boldsymbol{r}_h \cdot \boldsymbol{r}_{em}\hat{\boldsymbol{x}} - 15x_{em}\boldsymbol{r} \cdot \boldsymbol{r}_h\hat{\boldsymbol{x}}]/(\gamma D)^5 \end{aligned}. \tag{2.44}$$

Therefore, Eq. (2.36) becomes:

$$\begin{aligned} &\ddot{\boldsymbol{r}} = c_2(-\boldsymbol{r} + 3x\hat{\boldsymbol{x}}) + c_3(3x\boldsymbol{r}_h + 3X_h\boldsymbol{r} + (3\boldsymbol{r}_h \cdot \boldsymbol{r} - 15xX_h)\hat{\boldsymbol{x}}) + \\ &c_4((3\boldsymbol{r}_h \cdot \boldsymbol{r} - 15xX_h)\boldsymbol{r}_h + \tfrac{3}{2}(r_h^2 - 5X_h^2)\boldsymbol{r} - \tfrac{15}{2}(2X_h\boldsymbol{r}_h \cdot \boldsymbol{r} - 7xX_h^2 + xr_h^2)\hat{\boldsymbol{x}}) + \\ &c_5(\tfrac{15}{2}\boldsymbol{r}_h(-xr_h^2 - 2X_h\boldsymbol{r}_h \cdot \boldsymbol{r} + 7xX_h^2) + \tfrac{5}{2}r(7X_h^3 - 3X_hr_h^2) + \\ &\quad \tfrac{15}{2}(-r_h^2\boldsymbol{r}_h \cdot \boldsymbol{r} + 7X_h^2\boldsymbol{r}_h \cdot \boldsymbol{r} + 7xX_hr_h^2 - 21xX_h^3)\hat{\boldsymbol{x}}) + \\ &c_6(\tfrac{15}{8}\boldsymbol{r}(14r_h^2X_h^2 - 21X_h^4 - r_h^4) + \tfrac{15}{2}\boldsymbol{r}_h(-21xX_h^3 - r_h \cdot rr_h^2 + 7\boldsymbol{r}_h \cdot \boldsymbol{r}X_h^2 + 7xr_h^2X_h) + \\ &\quad \tfrac{21}{128}(-1440xr_h^2X_h^2 + 320\boldsymbol{r}_h \cdot \boldsymbol{r}r_h^2X_h + 80xr_h^4 - 33xX_h^4 - 960\boldsymbol{r}_h \cdot \boldsymbol{r}r_h^3)\hat{\boldsymbol{x}}) \\ &-3\mu_3[(-2xx_{em} + yy_{em} + zz_{em})\hat{\boldsymbol{x}} + (yx_{em} + xy_{em})\hat{\boldsymbol{y}} + (zx_{em} + xz_{em})\hat{\boldsymbol{z}}]/(\gamma D)^4 - \\ &\mu_3[-15x_{em}x\boldsymbol{r} + 3\boldsymbol{r}_h \cdot \boldsymbol{r}_{em}\boldsymbol{r} - 15xx_h\boldsymbol{r}_{em} + 3\boldsymbol{r}_h \cdot \boldsymbol{r}\boldsymbol{r}_{em} + 3\boldsymbol{r}_h \cdot \boldsymbol{r}_{em}(-5x_h\hat{\boldsymbol{x}} + \boldsymbol{r}_h) + \\ &105xx_{em}x_h\hat{\boldsymbol{x}} - 15xx_{em}\boldsymbol{r}_h - 15x\boldsymbol{r}_h \cdot \boldsymbol{r}_{em}\hat{\boldsymbol{x}} - 15x_{em}\boldsymbol{r} \cdot \boldsymbol{r}_h\hat{\boldsymbol{x}}]/(\gamma D)^5 \\ &+\frac{1.0198\times10^{17}C_RA\sigma_{sf}}{m\left\|(\gamma+1)D\hat{\boldsymbol{x}} + \boldsymbol{r}_h + \boldsymbol{r}\right\|^2}[(\gamma+1)D\hat{\boldsymbol{x}} + \boldsymbol{r}_h + \boldsymbol{r}] - \frac{1.0198\times10^{17}C_RA\sigma_{sf}}{m\left\|(\gamma+1)D\hat{\boldsymbol{x}} + \boldsymbol{r}_h\right\|^2}[(\gamma+1)D\hat{\boldsymbol{x}} + \boldsymbol{r}_h] \end{aligned}. \tag{2.45}$$

This LPV model is an extention of Segerman & Zedd (2003) as it retains terms up to sixth order. The effects of lunar and solar radiation pressure have also been taken into account in this model.

2.2.2 Linear Model of Rotational Motion

The dynamics of the rotational motion can be expressed in a linear form with the assumption of low body rates and small attitude errors.

For low body rates of the telescope ($\boldsymbol{\omega}_t \approx \mathbf{0}$), the nonlinear term $\boldsymbol{\omega}_t \times (\boldsymbol{J}_t\boldsymbol{\omega}_t)$ is negligible. Therefore, Eq. (2.23) becomes:

$$\boldsymbol{J}_t\dot{\boldsymbol{\omega}}_t = -\boldsymbol{\omega}_t \times (\boldsymbol{J}_t\boldsymbol{\omega}_t) + \boldsymbol{\tau}_t \approx \boldsymbol{\tau}_t. \tag{2.46}$$

For small attitude errors of the telescope with respect to the hub, ($\boldsymbol{q}_e \approx [1 \;\; 0 \;\; 0 \;\; 0]^T$), Eq. (2.22) becomes:

$$\dot{\boldsymbol{q}}_e = \tfrac{1}{2}\boldsymbol{\omega}_t \ . \tag{2.47}$$

Using the low rate and small error assumptions, the linear model of rotational motion is thus given by Eq. (2.46) and (2.47), and is written in matrix form as:

$$\begin{bmatrix} \dot{\tilde{\boldsymbol{q}}}_e & \dot{\boldsymbol{\omega}}_t \end{bmatrix} = \begin{bmatrix} 0 & \frac{1}{2}\boldsymbol{I}_3 \\ 0 & 0 \end{bmatrix} \begin{bmatrix} \tilde{\boldsymbol{q}}_e & \boldsymbol{\omega}_t \end{bmatrix} + \begin{bmatrix} 0 & \boldsymbol{J}_t^{-1} \end{bmatrix} \boldsymbol{\tau}_t. \tag{2.48}$$

2.3 Quasi-Linear Parameter-Varying Model

Equation (2.36) shows that the retaining the higher order terms in the gravitational force can improve the precision of the nominal model. However, the resulting LPV model can be difficult to be utilized in control algorithm design due to the complex expressions for the varying parameters. Furthermore it is impossible to distinguish between real disturbances and normal manifestations of nonlinearity (Tsourdos et al., 2001). Hence, it is necessary to use the nonlinear dynamics directly rather than treat it as in a linear model in order to improve the control system performance and robustness. The QLPV model is a mathematical description which incorporates the nonlinear dynamics explicitly, but without undue complexity.

The form of a canonical QLPV dynamic model is given by:

$$\dot{\boldsymbol{x}} = \boldsymbol{A}(\boldsymbol{x}, \boldsymbol{p}(\boldsymbol{t}))\boldsymbol{x} + \boldsymbol{B}(\boldsymbol{x}, \boldsymbol{p}(\boldsymbol{t}))\boldsymbol{u}, \quad \boldsymbol{y} = \boldsymbol{C}(\boldsymbol{x}, \boldsymbol{p}(\boldsymbol{t}))\boldsymbol{x}, \tag{2.49}$$

where the entries of $\boldsymbol{A}$, $\boldsymbol{B}$, and $\boldsymbol{C}$ depend on the states $\boldsymbol{x}$ and the time-varying parameter $\boldsymbol{p}$. This mathematical description is the focus of this thesis, because the nonlinear model in Eq. (2.12) can be expressed in the form of Eq. (2.49) by using the Barbashin method (Barbashin, 1970). With this QLPV form, the transparency of the linear controller design is preserved while retaining the nonlinearity of the full system dynamics and disturbances.

2.3.1 Barbashin Method

Consider the nonlinear control system described by equation:

$$\dot{\boldsymbol{x}} = \boldsymbol{f}(\boldsymbol{x}, \boldsymbol{u}), \tag{2.50}$$

where $\boldsymbol{x} \in R^n$ is the state vector, $\boldsymbol{u} \in R^m$ is the control input vector, and $\boldsymbol{f} : R^n \to R^n$ is a vector function, for which:

$$\boldsymbol{f}(\boldsymbol{0}, \boldsymbol{0}) = \boldsymbol{0}, \quad \partial f_i(\boldsymbol{x}, \boldsymbol{u})/\partial u_j = f_{u,ij}(\boldsymbol{x}) \tag{2.51}$$

for all $\boldsymbol{x} \in R^n$, $\|\boldsymbol{x}\| < \infty$, $i = 1, \cdots, n$, $j = 1, \cdots, m$. Under these conditions, Eq. (2.50) can be rewritten as the following Quasi-LPV form without any approximation:

$$\dot{\boldsymbol{x}} = \boldsymbol{A}(\boldsymbol{x}, \boldsymbol{p})\boldsymbol{x} + \boldsymbol{B}(\boldsymbol{x}, \boldsymbol{p})\boldsymbol{u}, \tag{2.52}$$

in which $\boldsymbol{p}$ is the time-varying parameter; $\boldsymbol{A}(\boldsymbol{x}, \boldsymbol{p}) \in R^{n \times n}$ and $\boldsymbol{B}(\boldsymbol{x}, \boldsymbol{p}) \in R^{n \times m}$ are the state matrix and the input matrix respectively, and their entries are given by:

$$a_{ij}(\boldsymbol{x}, \boldsymbol{p}) = \int_0^1 \frac{\partial f_i}{\partial x_j}(x_1, x_2, \cdots, \theta x_j, 0, \cdots, 0) d\theta, \tag{2.53}$$

$$b_{ij}(\boldsymbol{x}, \boldsymbol{p}) = \int_0^1 \frac{\partial f_i}{\partial u_j}(u_1, u_2, ..., \theta u_j, 0, ..., 0) d\theta. \tag{2.54}$$

Using this method on Eq. (2.53) and (2.54), the Quasi-LPV model of the nonlinear system can be calculated. However, there is a precondition, Eq. (2.51), required to be satisfied for this nonlinear model transform. For the case where

$\boldsymbol{f}(\boldsymbol{0},\boldsymbol{0}) \neq \boldsymbol{0}$, denote $\boldsymbol{g}(x,t) = \boldsymbol{f}(\boldsymbol{x},\boldsymbol{p}) - \boldsymbol{f}(\boldsymbol{0},\boldsymbol{p})$, then $\boldsymbol{g}(\boldsymbol{0},\boldsymbol{0}) = \boldsymbol{0}$. Therefore, $g(x,t)$ can be transformed as:

$$\boldsymbol{g}(\boldsymbol{x},\boldsymbol{p}) = \boldsymbol{A}_g(\boldsymbol{x},\boldsymbol{p})x + \boldsymbol{B}_g(\boldsymbol{x},\boldsymbol{p})\boldsymbol{u}, \tag{2.55}$$

where $\boldsymbol{A}_g(\boldsymbol{x})$ is the state matrix calculated by Eq. (2.53) and (2.54). With Eq. (2.55), $\boldsymbol{g}(\boldsymbol{x},\boldsymbol{p}) = \boldsymbol{f}(\boldsymbol{x},\boldsymbol{p}) - \boldsymbol{f}(\boldsymbol{0},\boldsymbol{p})$ can be expressed as:

$$\boldsymbol{f}(\boldsymbol{x},\boldsymbol{p}) = \boldsymbol{g}(\boldsymbol{x},\boldsymbol{p}) + \boldsymbol{f}(\boldsymbol{0},\boldsymbol{p}) = \boldsymbol{A}_g(\boldsymbol{x},\boldsymbol{p})\boldsymbol{x} + \boldsymbol{f}(\boldsymbol{0},\boldsymbol{p}) = (\boldsymbol{A}_g(\boldsymbol{x},\boldsymbol{p}) + \boldsymbol{C}_0(\boldsymbol{p}))\boldsymbol{x}, \tag{2.56}$$

where $\boldsymbol{C}_0(\boldsymbol{p})$ is any matrix which holds $\boldsymbol{C}_0\boldsymbol{x} = \boldsymbol{f}(0,\boldsymbol{p})$.

2.3.2 Quasi-Linear Parameter-Varying Model of Translational Motion

Define $\boldsymbol{r}$ and $\boldsymbol{r_d}$ as the real and desired position of the telescope with respect to the hub. Denoting $\delta\boldsymbol{r} = \boldsymbol{r} - \boldsymbol{r}_d = [\delta x, \delta y, \delta z]^T$ and noting the nonlinear model of the L_2 point formation in Eq. (2.12), the error dynamic equation of the formation can be obtained as:

$$\begin{aligned}
\delta\ddot{\boldsymbol{r}} = &-\mu_1\left(\tfrac{\boldsymbol{r}_h+\boldsymbol{r}_d+\delta\boldsymbol{r}}{\|\boldsymbol{r}_{1t}\|^3} - \tfrac{\boldsymbol{r}_h}{\|\boldsymbol{r}_{1h}\|^3}\right) - \\
&\mu_2\left(\tfrac{\boldsymbol{r}_h+\boldsymbol{r}_d+\delta\boldsymbol{r}}{\|\boldsymbol{r}_{2t}\|^3} - \tfrac{\boldsymbol{r}_h}{\|\boldsymbol{r}_{2h}\|^3}\right) - \mu_1(x_e + D_1)\left(\tfrac{1}{\|\boldsymbol{r}_{1t}\|^3} - \tfrac{1}{\|\boldsymbol{r}_{1h}\|^3}\right)\hat{x} - \\
&\mu_2(x_e - D_2)\left(\tfrac{1}{\|\boldsymbol{r}_{2t}\|^3} - \tfrac{1}{\|\boldsymbol{r}_{2h}\|^3}\right)\hat{x} + \boldsymbol{u}_{th} + \boldsymbol{f}_d
\end{aligned} \tag{2.57}$$

Defining the states and varying parameters in Eq. (2.49) as: $\boldsymbol{x} = [\delta\boldsymbol{r}^T, \delta\dot{\boldsymbol{r}}^T]^T$, $\boldsymbol{p} = [\boldsymbol{x}^T, \boldsymbol{r}_1^T]^T$, and using the Barbashin method, the error dynamic equation in Eq. (2.57) leads to the following QLPV form:

$$\dot{\boldsymbol{x}} = \boldsymbol{A}(\boldsymbol{p})\boldsymbol{x} + \boldsymbol{u}, \tag{2.58}$$

where the entries of matrix $\boldsymbol{A}(\boldsymbol{p})$ vary with the parameter $\boldsymbol{p}$. In this thesis, define the desired formation shape as fixed, therefore, $\dot{\boldsymbol{r}}_d = 0$, and thus $\boldsymbol{A}(\boldsymbol{p})$ can be evaluated as:

$$\boldsymbol{A}(\boldsymbol{p}) = \begin{bmatrix} & 0_{3\times3} & & & \mathrm{I}_{3\times3} & \\ a_{41} & a_{42} & a_{43} & a_{44} & a_{45} & a_{46} \\ a_{51} & a_{52} & a_{53} & a_{54} & a_{55} & a_{56} \\ a_{61} & a_{62} & a_{63} & a_{64} & a_{65} & a_{66} \end{bmatrix}, \tag{2.59}$$

where a_{ij} denotes $a_{ij}(\boldsymbol{p})$ and:

$$a_{41} = n^2 - \mu_1\left(\frac{h_1+\delta x}{\|\boldsymbol{r}_{1t1}\|^3} - \frac{h_1}{\|\boldsymbol{r}_{1tr}\|^3}\right)\frac{1}{\delta x} - \mu_2\left(\frac{h_2+\delta x}{\|\boldsymbol{r}_{2t1}\|^3} - \frac{h_2}{\|\boldsymbol{r}_{2tr}\|^3}\right)\frac{1}{\delta x}, \tag{2.60}$$

$$a_{42} = \ddot{f} - \mu_1\left(\frac{h_1+\delta x}{\|\boldsymbol{r}_{1t2}\|^3} - \frac{h_1+\delta x}{\|\boldsymbol{r}_{1t1}\|^3}\right)\frac{1}{\delta y} - \mu_2\left(\frac{h_2+\delta x}{\|\boldsymbol{r}_{2t2}\|^3} - \frac{h_2+\delta x}{\|\boldsymbol{r}_{2t1}\|^3}\right)\frac{1}{\delta y}, \tag{2.61}$$

$$a_{43} = -\mu_1\left(\frac{h_1+\delta x}{\|\boldsymbol{r}_{1t3}\|^3} - \frac{h_1+\delta x}{\|\boldsymbol{r}_{1t2}\|^3}\right)\frac{1}{\delta z} - \mu_2\left(\frac{h_2+\delta x}{\|\boldsymbol{r}_{2t3}\|^3} - \frac{h_2+\delta x}{\|\boldsymbol{r}_{2t2}\|^3}\right)\frac{1}{\delta z}, \tag{2.62}$$

$$a_{44} = -\mu_1\left(\frac{h_1}{\|\boldsymbol{r}_{1tr}\|^3} - \frac{h_1-x_d}{\|\boldsymbol{r}_{1h}\|^3}\right)\frac{1}{\delta \dot{x}} - \mu_2\left(\frac{h_2+x_d}{\|\boldsymbol{r}_{2tr}\|^3} - \frac{h_2}{\|\boldsymbol{r}_{2h}\|^3}\right)\frac{1}{\delta \dot{x}}, \tag{2.63}$$

$$a_{45} = 2n, a_{46} = 0, \tag{2.64}$$

$$a_{51} = -\ddot{f} - \mu_1\left(\frac{y_h+y_d}{\|\boldsymbol{r}_{1t1}\|^3} - \frac{y_h+y_d}{\|\boldsymbol{r}_{1tr}\|^3}\right)\frac{1}{\delta x} - \mu_2\left(\frac{y_h+y_d}{\|\boldsymbol{r}_{2t1}\|^3} - \frac{y_h+y_d}{\|\boldsymbol{r}_{2tr}\|^3}\right)\frac{1}{\delta x}, \tag{2.65}$$

$$a_{52} = n^2 - \mu_1\left(\frac{y_h+y_d+\delta y}{\|\boldsymbol{r}_{1t2}\|^3} - \frac{y_h+y_d}{\|\boldsymbol{r}_{1t1}\|^3}\right)\frac{1}{\delta y} - \mu_2\left(\frac{y_h+y_d+\delta y}{\|\boldsymbol{r}_{2t2}\|^3} - \frac{y_h+y_d}{\|\boldsymbol{r}_{2t1}\|^3}\right)\frac{1}{\delta y}, \tag{2.66}$$

$$a_{53} = -\mu_1\left(\frac{y_h+y_d+\delta y}{\|\boldsymbol{r}_{1t3}\|^3} - \frac{y_h+y_d+\delta y}{\|\boldsymbol{r}_{1t2}\|^3}\right)\frac{1}{\delta z} - \mu_2\left(\frac{y_h+y_d+\delta y}{\|\boldsymbol{r}_{2t3}\|^3} - \frac{y_h+y_d+\delta y}{\|\boldsymbol{r}_{2t2}\|^3}\right)\frac{1}{\delta z}, \tag{2.67}$$

$$a_{54} = -2n, a_{56} = 0, \tag{2.68}$$

$$a_{55} = -\mu_1\left(\frac{y_h+y_d}{\|\boldsymbol{r}_{1tr}\|^3} - \frac{y_h}{\|\boldsymbol{r}_{1h}\|^3}\right)\frac{1}{\delta \dot{y}} - \mu_2\left(\frac{y_h+y_d}{\|\boldsymbol{r}_{2tr}\|^3} - \frac{y_h}{\|\boldsymbol{r}_{2h}\|^3}\right)\frac{1}{\delta \dot{y}}, \tag{2.69}$$

$$a_{61} = -\mu_1\left(\frac{z_h+z_d}{\|\boldsymbol{r}_{1t1}\|^3} - \frac{z_h+z_d}{\|\boldsymbol{r}_{1tr}\|^3}\right)\frac{1}{\delta x} - \mu_2\left(\frac{z_h+z_d}{\|\boldsymbol{r}_{2t1}\|^3} - \frac{z_h+z_d}{\|\boldsymbol{r}_{2tr}\|^3}\right)\frac{1}{\delta x}, \tag{2.70}$$

$$a_{62} = -\mu_1\left(\frac{z_h+z_d}{\|\boldsymbol{r}_{1t2}\|^3} - \frac{z_h+z_d}{\|\boldsymbol{r}_{1t1}\|^3}\right)\frac{1}{\delta y} - \mu_2\left(\frac{z_h+z_d}{\|\boldsymbol{r}_{2t2}\|^3} - \frac{z_h+z_d}{\|\boldsymbol{r}_{2t1}\|^3}\right)\frac{1}{\delta y}, \tag{2.71}$$

$$a_{63} = -\mu_1\left(\frac{z_h+z_d+\delta z}{\|\boldsymbol{r}_{1t3}\|^3} - \frac{z_h+z_d}{\|\boldsymbol{r}_{1t2}\|^3}\right)\frac{1}{\delta z} - \mu_2\left(\frac{z_h+z_d+\delta z}{\|\boldsymbol{r}_{2t3}\|^3} - \frac{z_h+z_d}{\|\boldsymbol{r}_{2t2}\|^3}\right)\frac{1}{\delta z}, \tag{2.72}$$

$$a_{64} = 0, a_{65} = 0, \tag{2.73}$$

$$a_{66} = -\mu_1\left(\frac{z_h+z_d}{\|\boldsymbol{r}_{1tr}\|^3} - \frac{z_h}{\|\boldsymbol{r}_{1h}\|^3}\right)\frac{1}{\delta \dot{z}} - \mu_2\left(\frac{z_h+z_d}{\|\boldsymbol{r}_{2tr}\|^3} - \frac{z_h}{\|\boldsymbol{r}_{2h}\|^3}\right)\frac{1}{\delta \dot{z}}, \tag{2.74}$$

where $h_1 = x_e + D_1 + x_h + x_d$, $h_2 = x_e - D_2 + x_h + x_d$,

$$\|\boldsymbol{r}_{1t1}\| = \sqrt{(h_1+\delta x)^2 + (y_h+y_d)^2 + (z_h+z_d)^2}\,,$$

$$\|\boldsymbol{r}_{1tr}\| = \sqrt{(h_1)^2 + (y_h+y_d)^2 + (z_h+z_d)^2},$$

$$\|\boldsymbol{r}_{2t1}\| = \sqrt{(h_2+\delta x)^2 + (y_h+y_d)^2 + (z_h+z_d)^2},$$

$$\|\boldsymbol{r}_{2tr}\| = \sqrt{(h_2)^2 + (y_h+y_d)^2 + (z_h+z_d)^2},$$

$$\|\boldsymbol{r}_{1t2}\| = \sqrt{(h_1+\delta x)^2 + (y_h+y_d+\delta y)^2 + (z_h+z_d)^2},$$

$$\|\boldsymbol{r}_{1t3}\| = \|\boldsymbol{r}_{1t}\| = \sqrt{(h_1+\delta x)^2 + (y_h+y_d+\delta y)^2 + (z_h+z_d+\delta z)^2},$$

$$\|\boldsymbol{r}_{2t2}\| = \sqrt{(h_2+\delta x)^2+(y_h+y_d+\delta y)^2+(z_h+z_d)^2},$$
$$\|\boldsymbol{r}_{2t3}\| = \|\boldsymbol{r}_{2t}\| = \sqrt{(h_2+\delta x)^2+(y_h+y_d+\delta y)^2+(z_h+z_d+\delta z)^2},$$
$$\|\boldsymbol{r}_{1h}\| = \sqrt{(h_1)^2+(y_h)^2+(z_h)^2}\,, \|\boldsymbol{r}_{2h}\| = \sqrt{(h_2)^2+(y_h)^2+(z_h)^2}.$$

To verify that the QLPV form in Eq. (2.59) is equivalent to the nonlinear error dynamic equation Eq. (2.57), a simple calculation can be performed. From Eq. (2.59), we have:

$$\begin{aligned} &a_{41}\delta x + a_{42}\delta y + a_{43}\delta z + a_{44}\delta\dot{x} + a_{45}\delta\dot{y} + a_{46}\delta\dot{z} = \\ &n^2\delta x + \ddot{f}\delta y + 2n\delta\dot{y} - \mu_1\left(\frac{h_1+\delta x}{\|\boldsymbol{r}_{1t}\|^3} - \frac{h_1-x_d}{\|\boldsymbol{r}_{1h}\|^3}\right) - \mu_2\left(\frac{h_2+\delta x}{\|\boldsymbol{r}_{2t}\|^3} - \frac{h_2}{\|\boldsymbol{r}_{2h}\|^3}\right), \end{aligned} \tag{2.75}$$

$$\begin{aligned} &a_{51}\delta x + a_{52}\delta y + a_{53}\delta z + a_{54}\delta\dot{x} + a_{55}\delta\dot{y} + a_{56}\delta\dot{z} = \\ &n^2\delta y - \ddot{f}\delta x - 2n\delta\dot{x} - \mu_1\left(\frac{y_h+y_d+\delta y}{\|\boldsymbol{r}_{1t}\|^3} - \frac{y_h}{\|\boldsymbol{r}_{1h}\|^3}\right) - \mu_2\left(\frac{y_h+y_d+\delta y}{\|\boldsymbol{r}_{2t}\|^3} - \frac{y_h}{\|\boldsymbol{r}_{2h}\|^3}\right), \end{aligned} \tag{2.76}$$

$$\begin{aligned} &a_{61}\delta x + a_{62}\delta y + a_{63}\delta z + a_{64}\delta\dot{x} + a_{65}\delta\dot{y} + a_{66}\delta\dot{z} = \\ &-\mu_1\left(\frac{z_h+z_d+\delta y}{\|\boldsymbol{r}_{1t}\|^3} - \frac{z_h}{\|\boldsymbol{r}_{1h}\|^3}\right) - \mu_2\left(\frac{z_h+z_d+\delta y}{\|\boldsymbol{r}_{2t}\|^3} - \frac{z_h}{\|\boldsymbol{r}_{2h}\|^3}\right). \end{aligned} \tag{2.77}$$

From the above equation, one can find that Eq. (2.75) ~ Eq. (2.77) are the scalar forms of the nonlinear error dynamic equation in Eq. (2.57), which indicates that the expressions in Eq. (2.59) are correct.

2.3.3 Quasi-Linear Parameter-Varying Model of Rotational Motion

Using the same approach, the relative attitude nonlinear dynamics in Eq. (2.21) can be expressed in the following QLPV form:

$$\dot{\boldsymbol{x}}_e = \boldsymbol{A}(\boldsymbol{x}_e)\boldsymbol{x}_e + \boldsymbol{\tau}_t, \tag{2.78}$$

where $\boldsymbol{x}_e$ is the state vector including relative attitude quaternion and angular velocities; $\boldsymbol{x}_e = [\ \tilde{\boldsymbol{q}}_e^{\mathrm{T}}\ \ \boldsymbol{\omega}_e^{\mathrm{T}}\ ]^{\mathrm{T}}$; $\tilde{\boldsymbol{q}}_e$ is the vector part of $\boldsymbol{q}_e$; $\boldsymbol{\tau}_t$ is the relative control torque of telescope. The the entries of $\boldsymbol{A}(\boldsymbol{x}_e)$ are given by:

$$\begin{array}{cccccc} a_{11} = \frac{1}{4}\frac{\omega_{e1}q_{e0}}{q_{e1}} & a_{12} = \frac{1}{4}\omega_{e3} & a_{13} = -\frac{1}{4}\omega_{e2} & a_{14} = \frac{1}{4}q_{e0} & a_{15} = -\frac{1}{4}q_{e3} & a_{16} = \frac{1}{4}q_{e2} \\ a_{21} = -\frac{1}{4}\omega_{e3} & a_{22} = \frac{1}{4}\frac{\omega_{e2}q_{e0}}{q_{e2}} & a_{23} = \frac{1}{4}\omega_{e1} & a_{24} = \frac{1}{4}q_{e3} & a_{25} = \frac{1}{4}q_{e0} & a_{26} = -\frac{1}{4}q_{e1} \\ a_{31} = \frac{1}{4}\omega_{e2} & a_{32} = -\frac{1}{4}\omega_{e1} & a_{33} = \frac{1}{4}\frac{\omega_3 q_0}{q_3} & a_{34} = -\frac{1}{4}q_{e2} & a_{35} = \frac{1}{4}q_{e1} & a_{36} = \frac{1}{4}q_{e0} \end{array},$$

(2.79)

$$\begin{bmatrix} a_{41} & a_{42} & a_{43} \\ a_{51} & a_{52} & a_{53} \\ a_{61} & a_{62} & a_{63} \end{bmatrix} = \mathbf{0}_{3\times3}, \begin{bmatrix} a_{44} & a_{45} & a_{46} \\ a_{54} & a_{55} & a_{56} \\ a_{64} & a_{65} & a_{66} \end{bmatrix} = \begin{bmatrix} n_{11}+m_1 & n_{12} & n_{13} \\ n_{21}+m_1 & n_{22} & n_{23} \\ n_{31}+m_1 & n_{32} & n_{33} \end{bmatrix}, \tag{2.80}$$

where $\begin{bmatrix} n_{11} & n_{12} & n_{13} \\ n_{21} & n_{22} & n_{23} \\ n_{31} & n_{32} & n_{33} \end{bmatrix} = -\boldsymbol{J}_t^{-1}(\boldsymbol{\omega}_e + \boldsymbol{C}_{21}\boldsymbol{\omega}_1)^{\times}\boldsymbol{J}_t - (\boldsymbol{C}_{21}\boldsymbol{\omega}_1)^{\times}$,

$\begin{bmatrix} m_1 \\ m_2 \\ m_3 \end{bmatrix} = \frac{-\boldsymbol{J}_t^{-1}(\boldsymbol{C}_{21}\boldsymbol{\omega}_1)^{\times}\boldsymbol{J}_t\boldsymbol{C}_{21}\boldsymbol{\omega}_1+(\boldsymbol{C}_{21}\dot{\boldsymbol{\omega}}_1)^{\times})}{\omega_{e1}}$, $q_0 = (1-q_1^2-q_2^2-q_3^2)^{1/2}$,

and where $\begin{bmatrix} a \\ b \\ c \end{bmatrix}^{\times} = \begin{bmatrix} 0 & -c & b \\ c & 0 & -a \\ -b & a & 0 \end{bmatrix}$.

Using the same method to check the equation accuracy as shown in Eq. (2.75) ~ Eq. (2.77), one can verify conveniently that the expressions of the rotational motion QLPV model in Eq. (2.78) are equivalent to the relative attitude nonlinear system in Eq. (2.21).

2.4 Quasi-Linear Parameter-Varying Model of Flexible Spacecraft

To analyse the effect of the vibration induced by the flexibility of the spacecraft, the dynamics of flexible spacecraft formation flying is considered in this section. To simplify the problem, the hub of formation flying is assumed to be three-axis stabilized in the **IHE** frame without any translation motion.

Using the approach of Alazard et al. (2008), the dynamics of a flexible telescope can be modeled as an idealized rigid spacecraft with perturbations resulting from the flexibility of its structures. The flexible structures are assumed to be simple straight bending beams, clamped to a rigid body at one end and free at the other, with a point mass attached to the free end.

Denote $\boldsymbol{L}$ as the modal participation matrix of the flexible beam and $[\boldsymbol{r}, \quad \boldsymbol{\theta}]^T$ as the relative coordinates (translation and rotation) of the rigid body of the telescope

with respect to the hub. Then, assuming small rates, it is possible to neglect the nonlinear terms and the relative dynamic equations can be given by:

$$\begin{aligned} \begin{bmatrix} \ddot{\boldsymbol{r}} \\ \ddot{\boldsymbol{\theta}} \end{bmatrix} = \boldsymbol{M}^{-1}\Big(\begin{bmatrix} \boldsymbol{F} \\ \boldsymbol{T} \end{bmatrix} - \sum \boldsymbol{L}_k^T \ddot{\eta}_k\Big) = \boldsymbol{M}^{-1}\Big(\begin{bmatrix} \boldsymbol{F} \\ \boldsymbol{T} \end{bmatrix} - \boldsymbol{L}^T \ddot{\boldsymbol{\eta}}\Big), \\ \ddot{\eta}_k + 2\xi_k \omega_k \dot{\eta}_k + \omega_k^2 \eta_k = -\boldsymbol{L}_k \begin{bmatrix} \ddot{\boldsymbol{x}} \\ \ddot{\boldsymbol{\theta}} \end{bmatrix}, \end{aligned} \tag{2.81}$$

where $\boldsymbol{M}$ is the mass and inertia matrix of the telescope; $\boldsymbol{F}$ and $\boldsymbol{T}$ are all external forces and torques applied to the rigid body of the telescope, respectively; $\boldsymbol{\eta}$ is the vector of the n modal coordinates of the telescope, $\boldsymbol{\eta} = [\eta_1, \cdots, \eta_n]$; and ξ_k and ω_k are the damping ratio and natural angular frequency of k^{th} modal of the telescope.

The $\boldsymbol{L}^T \ddot{\boldsymbol{\eta}}$ term can be regarded as the flexible perturbation forces and torques acting on the rigid body of the telescope. Defining $\boldsymbol{L}^T \ddot{\boldsymbol{\eta}} = -[\boldsymbol{F}_{flex}, \ \boldsymbol{T}_{flex}]^T$, one can rewrite the relative motion equation as:

$$\begin{bmatrix} \ddot{\boldsymbol{r}} \\ \ddot{\boldsymbol{\theta}} \end{bmatrix} = \boldsymbol{M}^{-1}\left(\begin{bmatrix} \boldsymbol{F} \\ \boldsymbol{T} \end{bmatrix} + \begin{bmatrix} \boldsymbol{F}_{flex} \\ \boldsymbol{T}_{flex} \end{bmatrix}\right). \tag{2.82}$$

We denote $\boldsymbol{X} = [\boldsymbol{r}, \ \boldsymbol{\theta}, \ \dot{\boldsymbol{r}}, \ \dot{\boldsymbol{\theta}}]^T$, $\boldsymbol{U} = [\boldsymbol{F}, \ \boldsymbol{T}]^T$ and $\boldsymbol{U}_f = [\boldsymbol{F}_{flex}, \ \boldsymbol{T}_{flex}]^T$ as the system states, system inputs and perturbations, respectively. Note also that matrix $\boldsymbol{M}$ is time-varying due to the consumption of fuel and other variation of properties during the mission, thus Eq. (2.82) can be rewritten in the following QLPV form:

$$\dot{\boldsymbol{X}} = \boldsymbol{A}(\boldsymbol{p})\boldsymbol{X} + \boldsymbol{B}(\boldsymbol{p})\boldsymbol{U} + \boldsymbol{B}(\boldsymbol{p})\boldsymbol{U}_f, \tag{2.83}$$

where $\boldsymbol{A}(\boldsymbol{p}) = \boldsymbol{M}(\boldsymbol{p})^{-1}[\boldsymbol{0}_{6\times6} \ \ \boldsymbol{I}_{6\times6}; \boldsymbol{0}_{6\times6} \ \ \boldsymbol{0}_{6\times6}]$, $\boldsymbol{B}(\boldsymbol{p}) = \boldsymbol{M}(\boldsymbol{p})^{-1}[\boldsymbol{0}_{6\times6} \ \ \boldsymbol{I}_{6\times6}]$ and $\boldsymbol{p}$ is the time-varying parameter containing the spacecraft variables. Furthermore, taking into account the nonlinear terms, $\boldsymbol{A}(\boldsymbol{p})$ becomes the state matrix obtained in Section 2.3, where $\boldsymbol{p}$ depends on the model of spacecraft and the state of system.

2.5 Conclusions

Taking into account the effects of solar radiation pressure and lunar gravity, the exact nonlinear model of formation flying around the the L_2 point of the Sun-Earth

system is modeled successfully in Section 2.1. By retaining different order terms in the gravitational force, the LTI and LPV models are developed in Section 2.2, which are the fundamental used for controller design of Chapter 3 and 4.

To improve the modeling precision for the high precision formation control system of the interferometry mission, Section 2.3 developed a QLPV model which is obtained from the exact nonlinear model without any approximation by using the Barbashin method. With this QLPV form, the model can preserve the utility of linear controller designs while retaining the nonlinearity of the system dynamics and also separating the disturbances from the system variables. The development of this important model in this section is the first major contribution of the thesis.

In Section 2.4, a simple QLPV model of flexible spacecraft formation flying is developed as the foundation stone for checking the effect of spacecraft flexibility for the system control performance in Chapter 4.

Chapter 3

Linear Control Theory and Design

Using the LTI model in Eq. (2.40) for the Sun-Earth L_2 point formation, a technique of classical linear control strategy, LQR control theory, is applied in this chapter. The goal is to design a linear control system, focusing on both translation and rotation control. Section 3.1 reviews the theoretical basis of LQR control for LTI systems. Section 3.2 addresses the control algorithm design of the Sun-Earth L_2 point formation (The control laws are developed separately for both translational and rotational dynamics). The robustness of the translational controller is analysed in this section. Using the linear model, a Kalman filter is designed in Section 3.3 to provide an estimate of the states required for the LQR control law. Finally, simulations for translation and rotation control are carried out to confirm the performance of the system.

3.1 Linear Control Theory (LQR)

In this section, the basic concepts of LQR control theory for an LTI system are briefly summarized.

For an LTI control system, the state equations can be expressed in the form:

$$\begin{aligned} \dot{\boldsymbol{x}} &= \boldsymbol{A}\boldsymbol{x} + \boldsymbol{B}\boldsymbol{u} \\ \boldsymbol{y} &= \boldsymbol{C}\boldsymbol{x} + \boldsymbol{D}\boldsymbol{u} \end{aligned}', \tag{3.1}$$

where $\boldsymbol{x}$ is the state vector, $\boldsymbol{u}$ is the input vector, , $\boldsymbol{y}$ is the output vector and $\boldsymbol{A}$, $\boldsymbol{B}$, $\boldsymbol{C}$, and $\boldsymbol{D}$ are matrices with constant entries. For this LTI system, there are numerous control design methods available, but in this thesis the LQR method is selected as a benchmark to evaluate the nonlinear control performance against in Chapter 4.

The LQR approach is an optimal control technique which minimizes a quadratic cost function that is specified by the designer, usually constructed from a quadratic matrix function of the control input and the system state. Hence, given a time

invariant system modeled by Eq. (3.1), the cost function is defined as:

$$J_{cost} = \int_0^t (\tilde{\boldsymbol{x}}^T \boldsymbol{Q} \tilde{\boldsymbol{x}} + \boldsymbol{u}^T \boldsymbol{R} \boldsymbol{u}) dt. \tag{3.2}$$

where $\tilde{\boldsymbol{x}}$ is the state error.

By minimizing this cost function, the control input $\boldsymbol{u}$, is determined as a function of the design matrices $\boldsymbol{Q}$ and $\boldsymbol{R}$, which serve as weighting factors of the control input and the state respectively, selected for desired system performance. $\boldsymbol{Q}$ and $\boldsymbol{R}$ both are symmetric and positive definite matrices. The optimal solution of control input $\boldsymbol{u}$, is then given by:

$$\boldsymbol{u} = -\boldsymbol{K}\tilde{\boldsymbol{x}}, \quad \boldsymbol{K} = \boldsymbol{R}^{-1}\boldsymbol{B}^T\boldsymbol{P}, \tag{3.3}$$

where $\boldsymbol{P}$ is a positive definite matrix solution of the following Riccati equation:

$$\boldsymbol{A}^T\boldsymbol{P} + \boldsymbol{P}\boldsymbol{A} - \boldsymbol{P}\boldsymbol{B}\boldsymbol{R}^{-1}\boldsymbol{B}^T\boldsymbol{P} + \boldsymbol{Q} = 0. \tag{3.4}$$

The existence of this optimal LQR solution depends on the characteristics of the control system. Specifically, the system must be stabilizable and detectable.

3.2 Linear Control Design of the Sun-Earth L_2 Point Formation

In this section, the LQR controller is developed based on the LTI model of the Sun-Earth L_2 point formation. The robust stability is discussed as well by considering the uncertainty of the realistic system.

3.2.1 Linear Translational Dynamics

The linearised dynamic model of the formation has been developed in Chapter 2. From Eq. (2.40), the LTI model of the translational motion can be expressed in matrix form as:

$$\dot{\boldsymbol{\xi}} = \boldsymbol{A}_t\boldsymbol{\xi} + \boldsymbol{B}\boldsymbol{u}, \tag{3.5}$$

where $\boldsymbol{\xi} = \begin{bmatrix} \boldsymbol{x} \\ \dot{\boldsymbol{x}} \end{bmatrix}$, $\boldsymbol{A}_t = \begin{bmatrix} 0 & \boldsymbol{I}_3 \\ \boldsymbol{A}_1 & \boldsymbol{A}_2 \end{bmatrix}$, $\boldsymbol{B} = \begin{bmatrix} 0 \\ \boldsymbol{I}_3 \end{bmatrix}$, in which the expressions for $\boldsymbol{A}_1$ and $\boldsymbol{A}_2$ are $\boldsymbol{A}_1 = \begin{bmatrix} n^2+2\sigma & 0 & 0 \\ 0 & n^2-\sigma & 0 \\ 0 & 0 & -\sigma \end{bmatrix}$, $\boldsymbol{A}_1 = \begin{bmatrix} 0 & 2n & 0 \\ -2n & 0 & 0 \\ 0 & 0 & 0 \end{bmatrix}$.

3.2.1.1 Linear Control Design

Using the LTI model in Eq. (3.5), the control law development follows the LQR design, as discussed in Section 3.1. The cost function for the translational control is defined as:

$$J_{cost} = \int_0^t (\tilde{\boldsymbol{\xi}}^T \boldsymbol{Q} \tilde{\boldsymbol{\xi}} + \boldsymbol{u}^T \boldsymbol{R} \boldsymbol{u}) dt, \tag{3.6}$$

where $\tilde{\boldsymbol{\xi}} = \boldsymbol{\xi} - \boldsymbol{\xi}_d$, and where $\boldsymbol{\xi}_d$ is the desired state. To minimize the cost function J_{cost}, the optimized controller $\boldsymbol{u}$ is obtained as:

$$\boldsymbol{u} = -\boldsymbol{K}\tilde{\boldsymbol{\xi}}, \quad \boldsymbol{K} = \boldsymbol{R}^{-1}\boldsymbol{B}^T\boldsymbol{P}, \tag{3.7}$$

where $\boldsymbol{P}$ is a positive definite matrix solution of:

$$\boldsymbol{A}_t^T\boldsymbol{P} + \boldsymbol{P}\boldsymbol{A}_t - \boldsymbol{P}\boldsymbol{B}\boldsymbol{R}^{-1}\boldsymbol{B}^T\boldsymbol{P} + \boldsymbol{Q} = 0. \tag{3.8}$$

Equation (3.7) is the LQR controller designed via the basic LTI model of translational dynamics. However, this LTI model is linearised from the nonlinear relative motion dynamics, therefore a robust controller must have the ability to compensate for the truncation involved in the linearization as well as for solar radiation pressure and lunar gravitational force disturbances. The truncated term in the linearization is the gravity gradient associated with a setpoint offset between the hub and the telescope positions. Together with the disturbances, these modeling linearization errors with respect to the nominal LTI model will degrade the control performance significantly. Therefore, adding an integrator to the control algorithm is necessary to provide effective compensation for the gravity gradient and the disturbances.

To include an integrator in the controller, the LTI model in Eq. (3.5) is augmented as:

$$\dot{\boldsymbol{\xi}}_{aug} = \boldsymbol{A}_{taug}\boldsymbol{\xi}_{aug} + \boldsymbol{B}_{aug}\boldsymbol{u}, \tag{3.9}$$

where $\boldsymbol{\xi}_{aug} = \begin{bmatrix} \int \boldsymbol{x} \\ \boldsymbol{x} \\ \dot{\boldsymbol{x}} \end{bmatrix}$, $\boldsymbol{A}_{taug} = \begin{bmatrix} 0 & \boldsymbol{I}_3 & 0 \\ 0 & 0 & \boldsymbol{I}_3 \\ 0 & \boldsymbol{A}_1 & \boldsymbol{A}_2 \end{bmatrix}$, $\boldsymbol{B}_{aug} = \begin{bmatrix} 0 \\ 0 \\ \boldsymbol{I}_3 \end{bmatrix}$.

The cost function for the augment model is defined as:

$$J_{cost} = \int_0^t (\tilde{\boldsymbol{\xi}}_{aug}^T \boldsymbol{Q} \tilde{\boldsymbol{\xi}}_{aug} + \boldsymbol{u}^T \boldsymbol{R} \boldsymbol{u}) dt. \tag{3.10}$$

To minimize the cost function J_{cost}, the optimized controller $\boldsymbol{u}$ is obtained as:

$$\boldsymbol{u} = -\boldsymbol{K} \tilde{\boldsymbol{\xi}}_{aug}, \quad \boldsymbol{K} = \boldsymbol{R}^{-1} \boldsymbol{B}_{aug}^T \boldsymbol{P}, \tag{3.11}$$

where $\boldsymbol{P}$ is a positive definite matrix solution of:

$$\boldsymbol{A}_{taug}^T \boldsymbol{P} + \boldsymbol{P} \boldsymbol{A}_{taug} - \boldsymbol{P} \boldsymbol{B}_{aug} \boldsymbol{R}^{-1} \boldsymbol{B}_{aug}^T \boldsymbol{P} + \boldsymbol{Q} = 0. \tag{3.12}$$

Using the normal convention of classical linear feedback control, the negative of state error $-\tilde{\boldsymbol{\xi}}$ and the controller $\boldsymbol{u}$ are considered as the input and the output of the controller dynamics respectively. Therefore, the transfer function of the controller in Eq. (3.11) is evaluated as:

$$\boldsymbol{G}_c(s) = \frac{\boldsymbol{u}(s)}{-\tilde{\boldsymbol{x}}} = \boldsymbol{K} [\ \tfrac{\boldsymbol{I}_3}{s} \quad \boldsymbol{I}_3 \quad s\boldsymbol{I}_3\ ]^T. \tag{3.13}$$

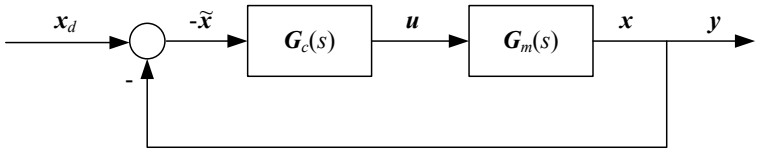

Figure 3.1: Closed-Loop Control Block Diagram

Defining $\boldsymbol{G}_m(s)$ as the plant model transfer function computed from Eq. (3.9) and using the block diagram shown in Fig. 3.1, the closed-loop transfer function $\boldsymbol{G}_{CL}(s)$ between the state $\boldsymbol{x}$ and the desired value $\boldsymbol{x}_d$ can be expressed as:

$$\boldsymbol{G}_{CL}(s) = \boldsymbol{G}_m(s) \boldsymbol{G}_c(s) (\boldsymbol{I} + \boldsymbol{G}_m(s) \boldsymbol{G}_c(s))^{-1}. \tag{3.14}$$

Using the specific design parameters set in Section 3.4 of this chapter, the bode diagram of the closed-loop system for all channels is plotted in Fig. 3.2 and 3.3. To compare the performance with nonlinear controller designed later in this thesis (PEA), the closed-loop gain of the LQR controller has a profile (dash line) similar to that of the PEA control system (solid line). The gain in all channels is almost identical for both designs at this set point because the magnitude of the natural frequency of the closed loop system is much larger than the entries of state matrix.

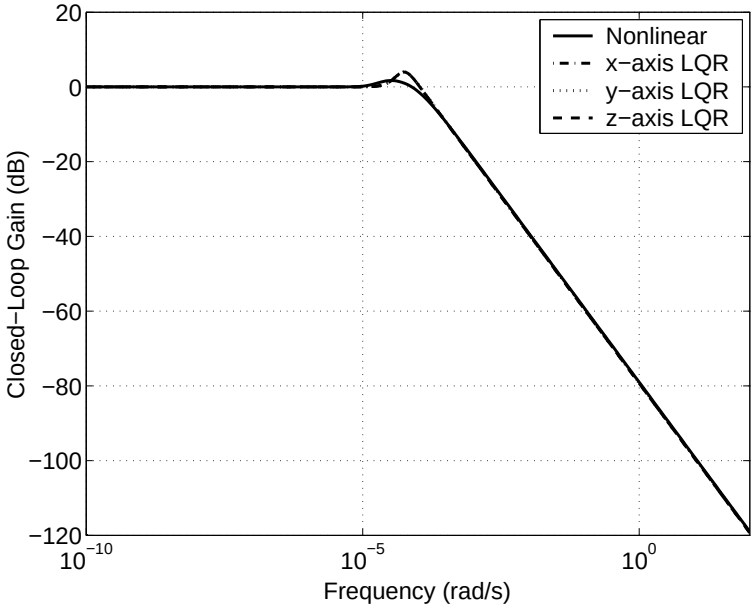

Figure 3.2: Closed-Loop Gain of All LQR Channels

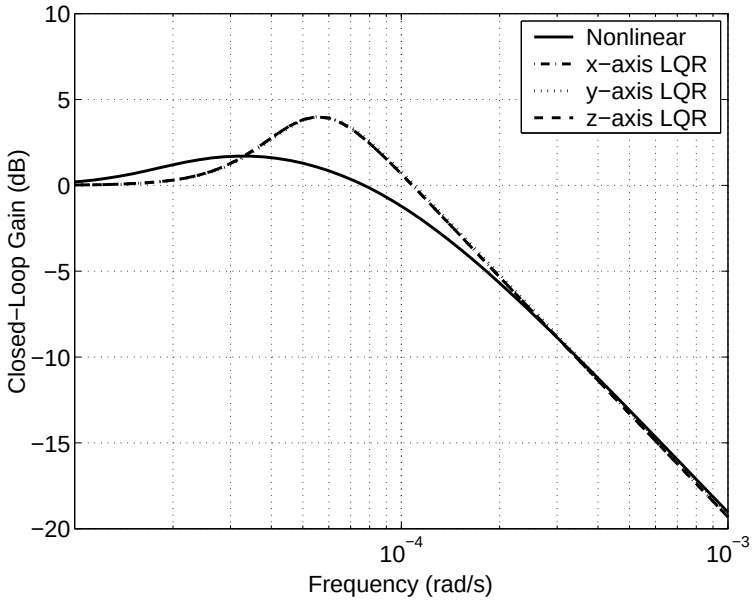

Figure 3.3: Part of Closed-Loop Gain

3.2.1.2 Robustness of Time-Invariant Model Design

Using the LTI model for design will introduce a modeling error $\boldsymbol{\Delta}(s,t)$, between the nominal linearised plant model $\boldsymbol{G}_m(s)$ and the actual nonlinear plant model which can be defined as a time dependant plant model $\boldsymbol{G}(s,t)$. Suppose the modeling error $\boldsymbol{\Delta}(s,t)$ is expressed as a multiplicative uncertainty in terms of the

nominal plant model $\boldsymbol{G}_m(s)$, then the actual plant model $\boldsymbol{G}(s,t)$ can be given as:

$$\boldsymbol{G}(s,t) = (\boldsymbol{I} + \boldsymbol{\Delta}(s,t))\boldsymbol{G}_m(s). \tag{3.15}$$

Without the time-invariant assumption, the Linear Time-Varying model of translational motion can be expressed in matrix form as:

$$\begin{aligned} \dot{\boldsymbol{\xi}} &= \boldsymbol{A}_t(t)\boldsymbol{\xi} + \boldsymbol{B}\boldsymbol{u} \\ \boldsymbol{y} &= \boldsymbol{C}\boldsymbol{\xi} \end{aligned}, \tag{3.16}$$

where $\boldsymbol{\xi} = \begin{bmatrix} \boldsymbol{x} \\ \dot{\boldsymbol{x}} \end{bmatrix}$, $\boldsymbol{A}_t(t) = \begin{bmatrix} 0 & \boldsymbol{I}_3 \\ \boldsymbol{A}_1(t) & \boldsymbol{A}_2 \end{bmatrix}$, $\boldsymbol{B} = \begin{bmatrix} 0 \\ \boldsymbol{I}_3 \end{bmatrix}$, $\boldsymbol{C} = \begin{bmatrix} \boldsymbol{I}_3 & 0 \end{bmatrix}$, and where $\boldsymbol{A}_2$ is the same as that in Eq. (3.9). In this analysis, $\boldsymbol{A}_1(t)$ can be obtained by using the numerical methods described in Chapter 2 to give LPV or QLPV models of the translational motion.

Based on Eq. (3.16), $\boldsymbol{G}(s,t)$ is evaluated as:

$$\begin{aligned} \boldsymbol{G}(s,t) &= \boldsymbol{C}(s\boldsymbol{I} - \boldsymbol{A}_t(t))^{-1}\boldsymbol{B} \\ &= \begin{bmatrix} \boldsymbol{I}_3 & 0 \end{bmatrix} \begin{bmatrix} 0 & \boldsymbol{I}_3 \\ \boldsymbol{A}_1(t) & \boldsymbol{A}_2 \end{bmatrix} \begin{bmatrix} 0 \\ \boldsymbol{I}_3 \end{bmatrix}. \\ &= (s^2\boldsymbol{I} - s\boldsymbol{A}_2 - \boldsymbol{A}_1(t))^{-1} \end{aligned} \tag{3.17}$$

Likewise, the nominal plant model is expressed as:

$$\boldsymbol{G}_m(s,t) = (s^2\boldsymbol{I} - s\boldsymbol{A}_2 - \boldsymbol{A}_1(t_0))^{-1}, \tag{3.18}$$

where $\boldsymbol{A}_1(t_0)$ is obtained either from the time varying matrix $\boldsymbol{A}_1(t)$ at initial time $t = t_0$ in Eq. (3.16) (LTI1 model), or from the constant matrix $\boldsymbol{A}_1$ in Eq. (3.9) (LTI2 model). Obviously, the former model is more precise than the latter. Different robustness results for the closed-loop system with uncertainty are analysed with these two nominal models.

Using $G(s,t)$ and $G_m(s,t)$, the modeling uncertainty is calculated as:

$$\begin{aligned} \boldsymbol{\Delta}(s,t) &= \boldsymbol{G}(s,t)\boldsymbol{G}_m(s)^{-1} - \boldsymbol{I} \\ &= (s^2\boldsymbol{I} - s\boldsymbol{A}_2 - \boldsymbol{A}_1(t))^{-1}(s^2\boldsymbol{I} - s\boldsymbol{A}_2 - \boldsymbol{A}_1(t_0)) - \boldsymbol{I} \end{aligned}. \tag{3.19}$$

To analyse the robustness of such uncertain system, one has the well-known *small gain theorem: Given a plant model in Eq.* (3.15) *with a stabilizing controller*

$\boldsymbol{G}_c(s)$, *the closed-loop system is well-posed and internally stable for all* $\boldsymbol{\Delta}(s,t)$ *with* $\bar{\sigma}(\boldsymbol{\Delta}(s,t))\bar{\sigma}(\boldsymbol{G}_{CL}) < 1$, *provided* $\boldsymbol{\Delta}(s,t)$ *is a rational transfer function such that* $\boldsymbol{G}(s,t)$ *and* $\boldsymbol{G}_m(s,t)$ *have the same number of poles in the closed-right-half plane.* $\boldsymbol{G}_{CL}$ is the nominal plant model for the controller design.

Using the specific design parameters described in Section 3.4, Fig. 3.4 and 3.5 depict the maximum singular vales of the inverse model uncertainty of the two different nominal LTI models associated with the closed-loop gains shown in Fig. 3.2, respectively.

As shown in Fig. 3.4 for the LTI1 model, the uncertainty $\boldsymbol{\Delta}(s,t)$ is computed after fixing the actual plant model $\boldsymbol{G}(s,t)$ at 1 day, 7 days, and 14 days individually. The figure indicates the condition $\bar{\sigma}(\boldsymbol{\Delta}(s,t))\bar{\sigma}(\boldsymbol{G}_{CL}) < 1$ is satisfied for all cases with frequencies larger than 10^{-6} *rad/sec*. However, it is violated in all cases around the frequency of 2.5×10^{-7} *rad/sec*, due to the natural harmonic motion of the formation (Luquette, 2006). The small gain condition cannot hold for all cases for frequencies less than 10^{-7} *rad/sec*. For the 1 day case the gain at these low frequencies is approximately 8, and for 7 days drops to 1.1, and further for 14 days it is below zero at -4.8. Therefore, the uncertain system is robust stable for up to 7 days if the controller is designed based on the LTI1 model.

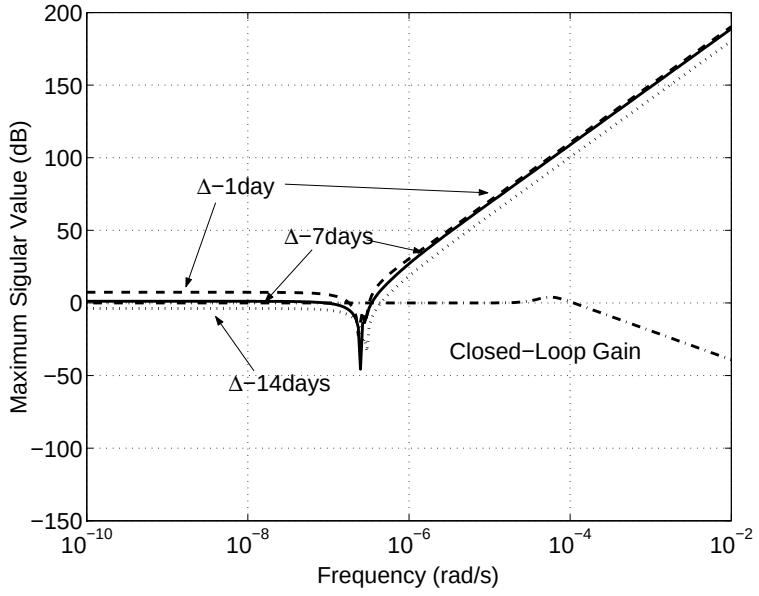

Figure 3.4: Maximum Singular Value of Inverse Model Uncertainty and the Closed-Loop Gain for the LTI1 Model

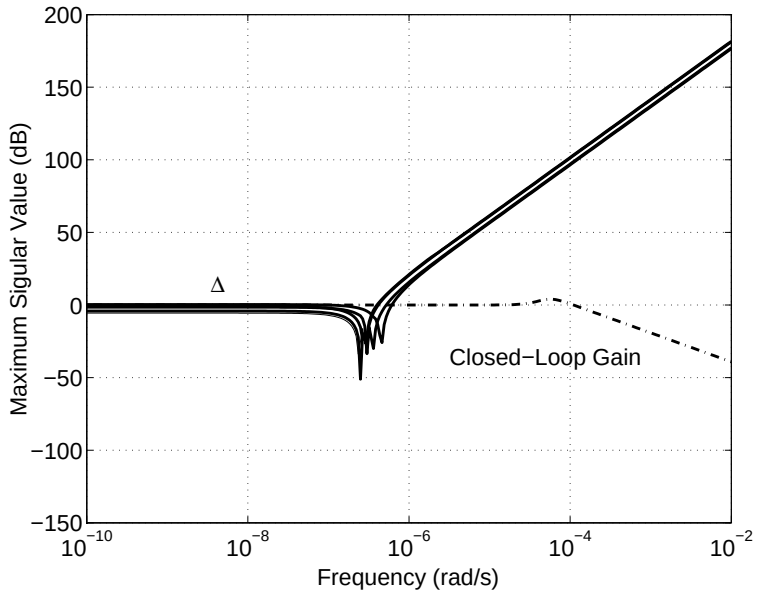

Figure 3.5: Maximum Singular Value of Inverse Model Uncertainty and the Closed-Loop Gain for the LTI2 Model

However, the situation is worse for the LTI2 model. As shown in Fig. 3.5, the condition $\bar{\sigma}(\boldsymbol{\Delta}(s,t))\bar{\sigma}(\boldsymbol{G}_{CL}) < 1$ is difficult to meet due to the initial modeling error of LTI2 model. In fact the condition is only satisfied for certain specific days. For these specific days, the modeling error is small enough to satisfy the small gain condition. Again, the violation happens around the frequency of 2.5×10^{-7} *rad*/*sec*.

With the above analysis, an improved closed-loop system robustness is achieved by using the more precise model (LTI1) as a nominal model to design the controller. However, even with the the LTI1 model, the results indicates the controller performance would benefit from the use of gain scheduling within an 8 day period.

3.2.1.3 Robustness Analysis of Double Integrator Dynamic Model

As reviewed in Chapter 1, several references (Beugnon et al., 2004; Smith & Hadaegh, 2005) employ a Double Integrator Dynamics (DID) model that assumes zero gravity for translation control design. Using the multiplicative model, the plant uncertainty is depicted in Fig. 3.6, evaluated at the end of day 1. The plant uncertainty profile is almost identical over the time interval 0.1 days through to 8 days. The condition $\bar{\sigma}(\boldsymbol{\Delta}(s,t))\bar{\sigma}(\boldsymbol{G}_{CL}) < 1$ is met only for frequencies above 10^{-6}

rad/*sec* and therefore the robust stability of system cannot be guaranteed.

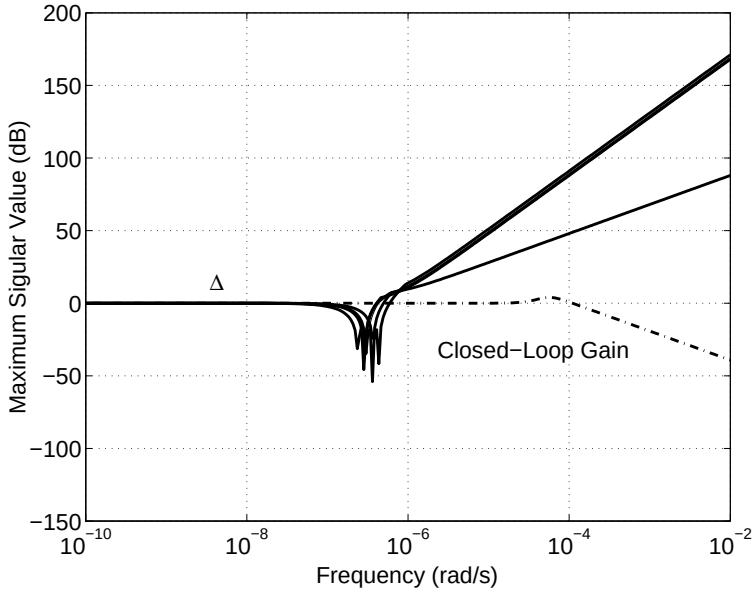

Figure 3.6: Maximum Singular Value of Inverse Model Uncertainty and the Closed-Loop Gain for the DID Model

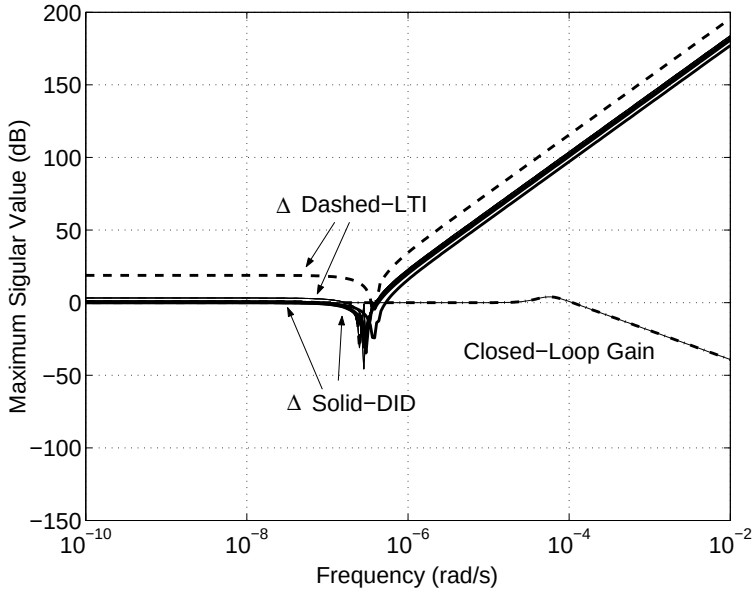

Figure 3.7: Maximum Singular Value of Inverse Model Uncertainty in Y-axis Channel between the DID Model and the LTI2 Model

In Fig. 3.7, the profiles between the DID model and the LTI2 model in the Y-axis control channel are compared. At low frequencies, the small gain condition is almost satisfied for the LTI2 model, however it fails for the DID model. This further

indicates that the model including the gravity could improve the robustness of the closed-loop system.

The robust stability analysis method in Subsection 3.2.1.2 and Subsection 3.2.1.3 is also described in Luquette (2006) , where a Lyapunov based method is developed for the robustness analysis.

3.2.2 Linear Rotational Dynamics

The robustness of the rotational dynamics follows a similar development. Eq. (2.48) is the linear equation of rotational motion obtained using the assumption of low body rates and small attitude errors. Assuming all states are measured, the matrices in canonical LTI form (3.1) can be expressed as:

$$\boldsymbol{A}_r = \begin{bmatrix} 0 & \frac{1}{2}\boldsymbol{I}_3 \\ 0 & 0 \end{bmatrix}, \quad \boldsymbol{B}_r = \begin{bmatrix} 0 & \boldsymbol{J}_t^{-1} \end{bmatrix}, \quad \boldsymbol{C}_r = \boldsymbol{I}_6, \quad \boldsymbol{D}_r = \boldsymbol{0}. \tag{3.20}$$

Similarly, to provide effective compensation for the modeling error and other disturbances, it is necessary to add an integrator into the controller. Therefore using an augmented state $\int \tilde{\boldsymbol{q}}_e$, the matrices in Eq. (3.20) are augmented to:

$$\boldsymbol{A}_{raug} = \begin{bmatrix} 0 & \boldsymbol{I}_3 & 0 \\ 0 & 0 & \frac{1}{2}\boldsymbol{I}_3 \\ 0 & 0 & 0 \end{bmatrix}, \quad \boldsymbol{B}_{raug} = \begin{bmatrix} 0 \\ 0 \\ \boldsymbol{J}_t^{-1} \end{bmatrix}, \quad \boldsymbol{C}_{raug} = \boldsymbol{I}_9, \quad \boldsymbol{D}_{raug} = \boldsymbol{0}. \tag{3.21}$$

Using these augmented matrices, the LQR approach is applied to design the controller for rotational control. The controller $\boldsymbol{\tau}_t$ can be expressed as:

$$\boldsymbol{\tau}_t = -\boldsymbol{K}_r \begin{bmatrix} \int \tilde{\boldsymbol{q}}_e \\ \tilde{\boldsymbol{q}}_e \\ \boldsymbol{\omega}_t \end{bmatrix}, \quad \boldsymbol{K}_r = \boldsymbol{R}^{-1}\boldsymbol{B}_{raug}^T\boldsymbol{P}, \tag{3.22}$$

where $\boldsymbol{P}$ is a positive definite matrix solution of:

$$\boldsymbol{A}_{raug}^T\boldsymbol{P} + \boldsymbol{P}\boldsymbol{A}_{raug} - \boldsymbol{P}\boldsymbol{B}_{raug}\boldsymbol{R}^{-1}\boldsymbol{B}_{raug}^T\boldsymbol{P} + \boldsymbol{Q} = 0. \tag{3.23}$$

3.3 Kalman Filter for Metrology

In Section 3.2, all the system states are required for feedback control. However in the DARWIN mission, the metrology sensors can only measure partial states of the system. Moreover, due to the properties of the sensors, the measured noise is inevitable, which will degrade the accuracy of closed-loop system performance. To address these problems, the state estimator should be included to reconstruct the full state.

Due to the large advances in digital computing, Kalman filters have become the subjects of extensive research and application, particularly in the area of navigation systems (Welch & Bishop, 2001). A typical Kalman filter application is shown in Fig. 3.8, and the fundamentals are introduced briefly in this section. For detailed information about the Kalman filter, please refer to Welch & Bishop (2001) and other related estimation references.

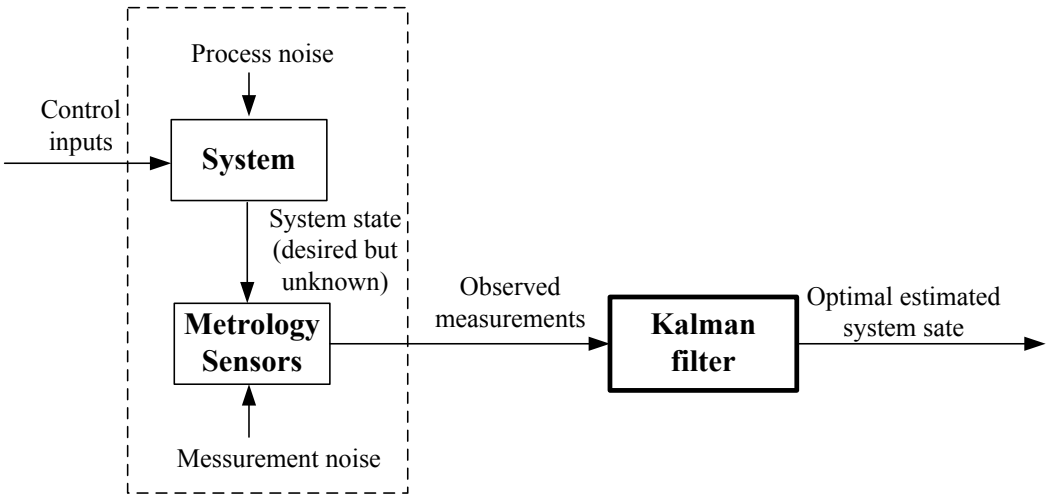

Figure 3.8: Typical Kalman Filter Application

3.3.1 Fundamentals of the Kalman Filter

The discrete Kalman filter addresses the problem of estimating the state $x \in \mathbb{R}^n$ of a dynamic system which is governed by a linear stochastic difference equation:

$$\boldsymbol{x}_k = \boldsymbol{A}\boldsymbol{x}_{k-1} + \boldsymbol{B}\boldsymbol{u}_k + \boldsymbol{w}_{k-1}, \tag{3.24}$$

with a measurement $\boldsymbol{z} \in \mathbb{R}^m$ that is:

$$\boldsymbol{z}_k = \boldsymbol{H}\boldsymbol{x}_k + \boldsymbol{v}_k. \tag{3.25}$$

The random variables $\boldsymbol{w}_k$ and $\boldsymbol{v}_k$ represent the process and measurement noise with the assumption of independent, white and normal probability distributions, that is $\boldsymbol{p}(\boldsymbol{w}) \sim \boldsymbol{N}(0, \boldsymbol{Q})$ and $\boldsymbol{p}(\boldsymbol{v}) \sim \boldsymbol{N}(0, \boldsymbol{R})$. $\boldsymbol{Q}$ and $\boldsymbol{R}$ are the process noise covariance and measurement noise covariance.

We define $\hat{\boldsymbol{x}}_k^- \in \mathbb{R}^n$ as an a priori state estimate at step k and $\hat{\boldsymbol{x}}_k \in \mathbb{R}^n$ as an a posteriori state estimate at step k given measurement $\boldsymbol{Z}_k$. Then a priori and a posteriori estimate errors can be defined as: $\boldsymbol{e}_k^- \triangleq \boldsymbol{x}_k - \hat{\boldsymbol{x}}_k^-$ and $\boldsymbol{e}_k \triangleq \boldsymbol{x}_k - \hat{\boldsymbol{x}}_k$ together with a priori and a posteriori estimate error covariances are $\boldsymbol{P}_k^- = E[\boldsymbol{e}_k^- \boldsymbol{e}_k^{-T}]$ and $\boldsymbol{P}_k = E[\boldsymbol{e}_k \boldsymbol{e}_k^T]$.

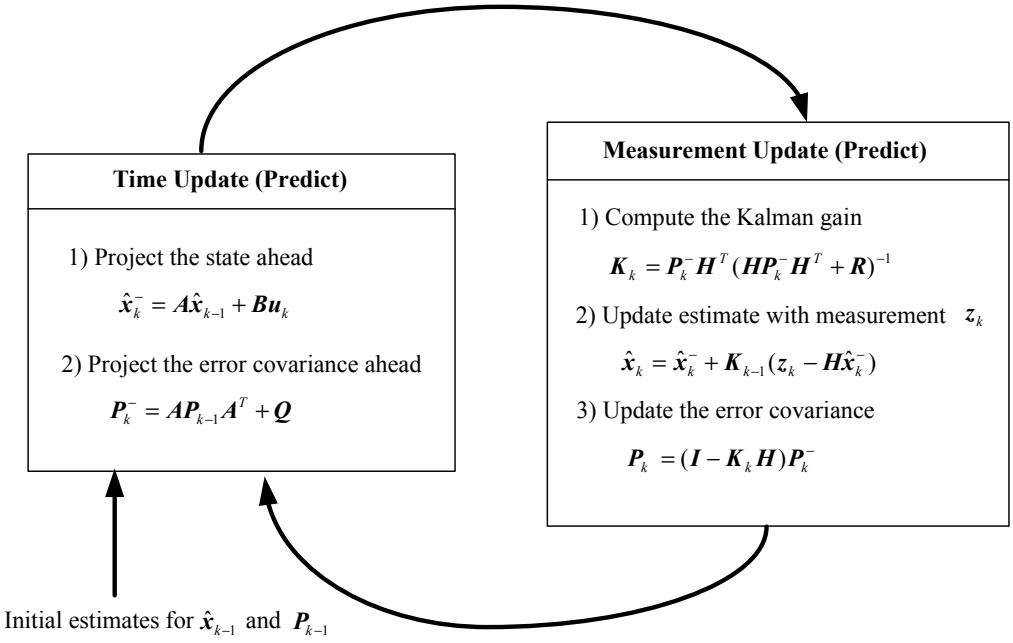

Figure 3.9: The Operation Diagram of a Kalman Filter (Welch & Bishop, 2001)

When using the Kalman filter, the a posteriori state estimate $\hat{\boldsymbol{x}}_k$ can be computed as a linear combination of the a priori estimate $\hat{\boldsymbol{x}}_k^-$ and the difference between the actual measurement $\boldsymbol{z}_k$ and the predicted measurement $\boldsymbol{H}\hat{\boldsymbol{x}}_k^-$, expressed as:

$$\hat{\boldsymbol{x}}_k = \hat{\boldsymbol{x}}_k^- + \boldsymbol{K}(\boldsymbol{z}_k - \boldsymbol{H}\hat{\boldsymbol{x}}\boldsymbol{k}^-), \tag{3.26}$$

where $\boldsymbol{K} \in n \times m$ is the filter gain that minimizes the a posteriori error covariance $\boldsymbol{P}_k$ which is obtained from:

$$\boldsymbol{K}_k = \boldsymbol{P}_k^- \boldsymbol{H}^T (\boldsymbol{H} \boldsymbol{P}_k^- \boldsymbol{H}^T + \boldsymbol{R})^{-1}. \tag{3.27}$$

To complete the filter algorithm, the a priori and a posteriori estimate error covariances are evaluated from:

$$\boldsymbol{P}_k^- = \boldsymbol{A} \boldsymbol{P}_{k-1} \boldsymbol{A}^T + \boldsymbol{Q}, \tag{3.28}$$

$$\boldsymbol{P}_k = (\boldsymbol{I} - \boldsymbol{K}_k \boldsymbol{H}) \boldsymbol{P}_k^-. \tag{3.29}$$

Figure 3.9 shows the Kalman filter operation diagram to estimate the system state. In the figure, the relationship between the *Time Update* and the *Measurement Update* of the Kalman filter is depicted.

Note that the focus of this thesis is to design and analysis control algorithms for the DARWIN formation system and therefore it will be assumed that the Kalman filter is used to estimate the required system states for the metrology DARWIN mission. The resulted system states estimates used for visualisation purposes will be implemented in the simulation of the following chapters.

3.3.2 State Estimation for the DARWIN Mission

Using the linear dynamic equations of relative translation and rotation in Eq. (3.9) and (2.48), the Kalman filters to reconstruct both system states are designed using the parameters of the sensors described in Section 1.1.3.1 of the DARWIN Mission. The state estimates are computed using MATLAB's **kalman(*SYS*, *Q*, *R*)** routine.

The initial relative position of the telescope with respect to the hub is $[-0.05\sqrt{2}\ \ 0.05\sqrt{2}\ \ 0]^{\mathrm{T}}\ km$. Therefore the initial distance between the hub and the telescope is 70.7 m. This is the same as that in Section 3.4 for the closed-loop simulation. The initial relative quaternion of the telescope with respect to the hub is $[0.9997\ \ 0.0100\ \ -0.0100\ \ 0.0200]^{\mathrm{T}}$. With these initial conditions, the filters are simulated over 200 days, but in order to illustrated the convergent times of filters, the state estimation results of the relative position and velocity are only illustrated over 1 day in Fig. 3.10 ~ Fig. 3.17, and the state estimation results of relative

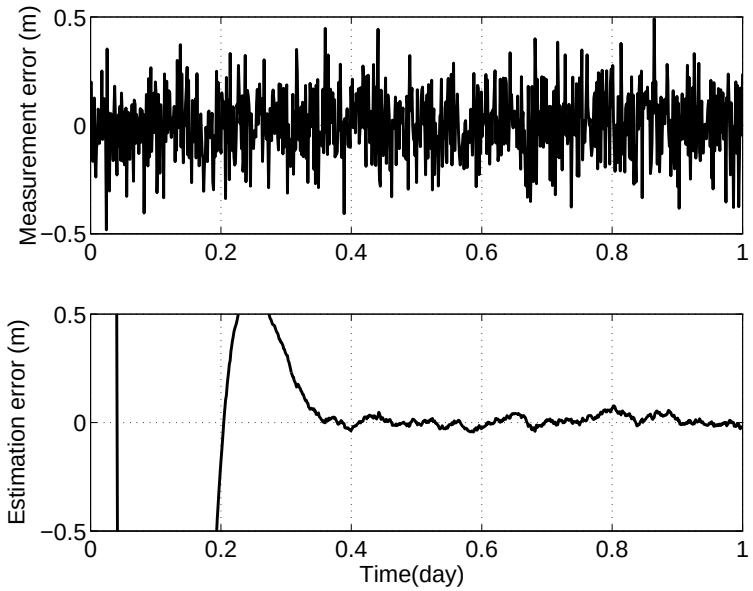

Figure 3.10: The Measurement and Estimation Errors of X-Axis Relative Position for the RF Measurements

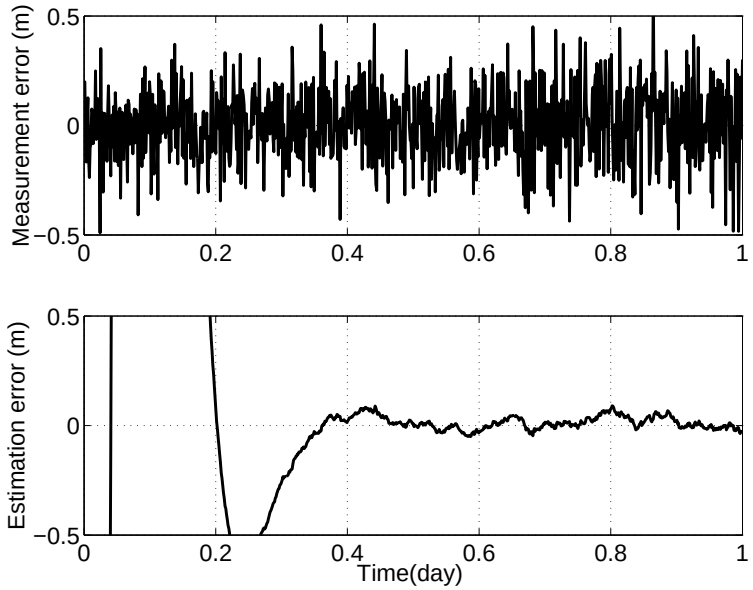

Figure 3.11: The Measurement and Estimation of Y-Axis Relative Position for the RF Measurements

quaternion and angular velocity are illustrated over 2000 seconds in Fig. 3.18 ~ Fig. 3.25.

For the RF measurements, the longitudinal accuracy is 1.2 mm (3σ) and the line

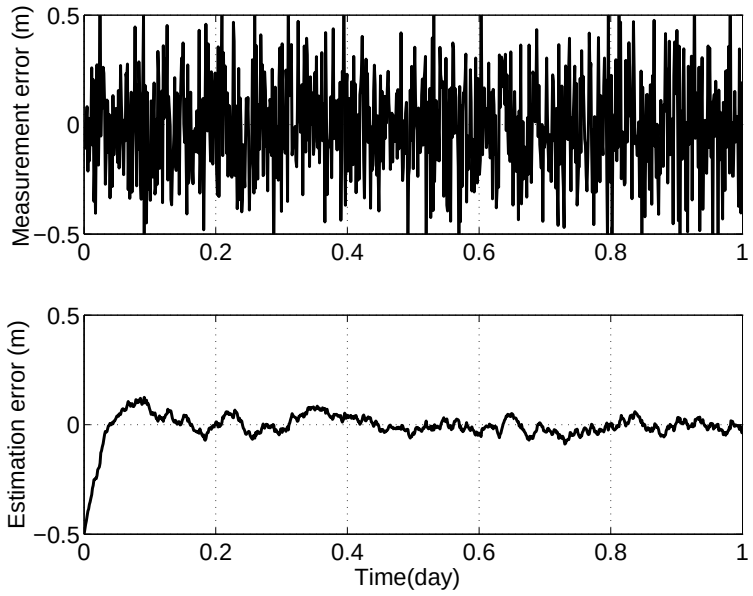

Figure 3.12: The Measurement and Estimation Errors of Z-Axis Relative Position for the RF Measurements

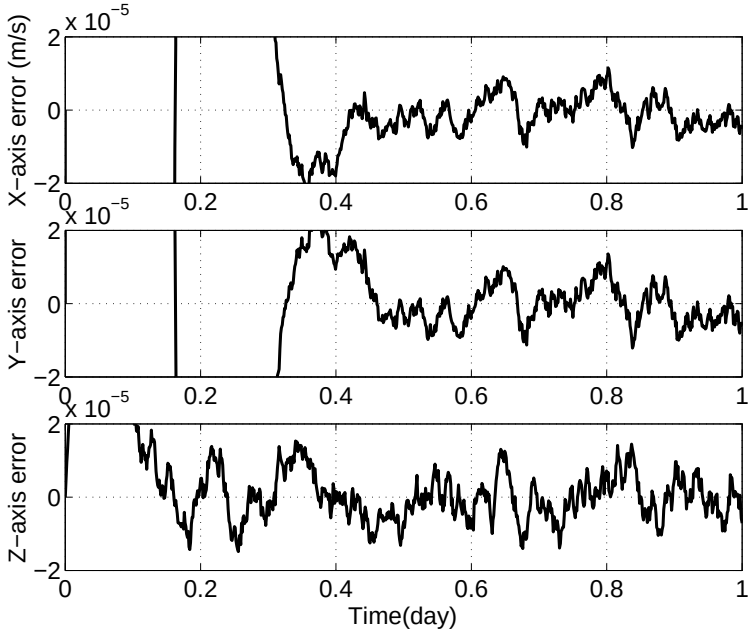

Figure 3.13: The Measurement and Estimation Errors of Relative Velocity for the RF Measurements

of sight accuracy is ±0.21° (3σ). The initial parameters of this filter are set as:

$$\begin{aligned} \boldsymbol{Q} &= \boldsymbol{I}_3 \times 10^{-14} \\ \boldsymbol{R} &= \boldsymbol{I}_3 \\ \hat{\boldsymbol{x}}_0 &= \mathbf{0}_{6\times 1} \end{aligned} \quad . \tag{3.30}$$

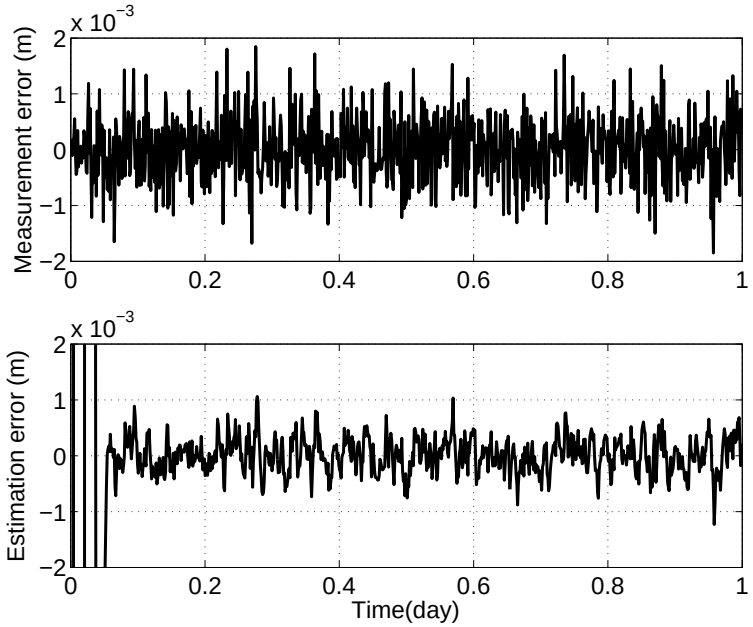

Figure 3.14: The Measurement and Estimation Errors of X-Axis Relative Position for the OLS Measurements

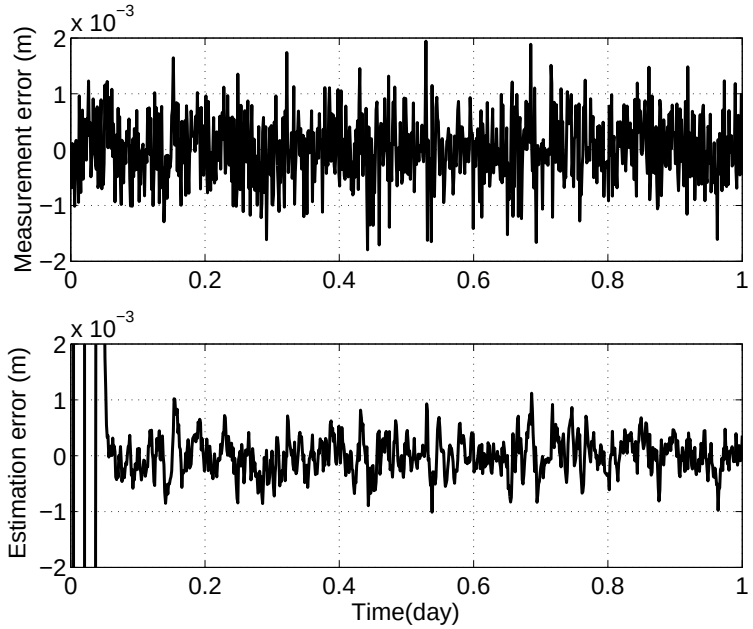

Figure 3.15: The Measurement and Estimation of Y-Axis Relative Position for the OLS Measurements

Figure 3.10 ~ Figure 3.13 show the measurement and estimation errors of the relative position and velocity with the RF measurements. The measurement error in each axis is 0.3 m, while the estimation errors reduce to 0.1 m. The relative

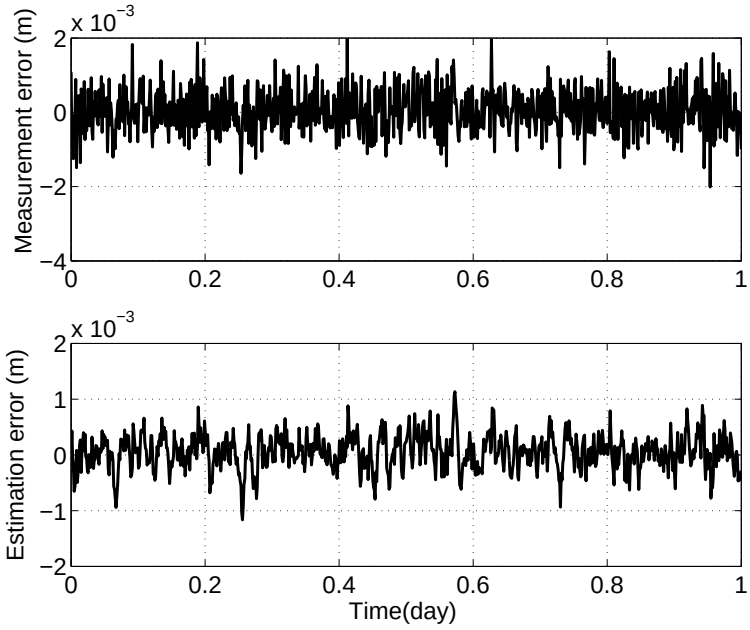

Figure 3.16: The Measurement and Estimation Errors of Z-Axis Relative Position for the OLS Measurements

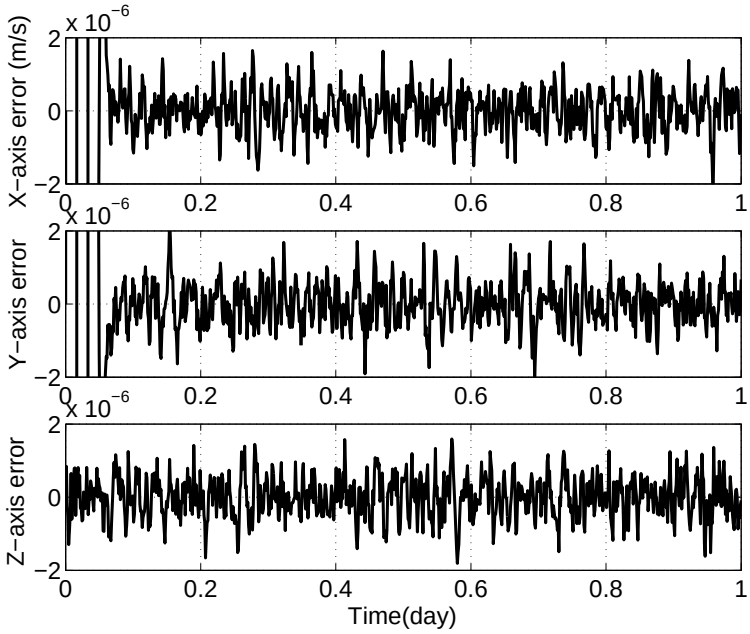

Figure 3.17: The Measurement and Estimation Errors of Relative Velocity for the OLS Measurements

velocity errors are shown to be less than 2 $\mu m/s$. The convergence times of the three channels of the filter are different, for the X-axis and Y-axis, both are approximately 0.4 day, whereas for the Z-axis the convergence is approximately

0.1 day.

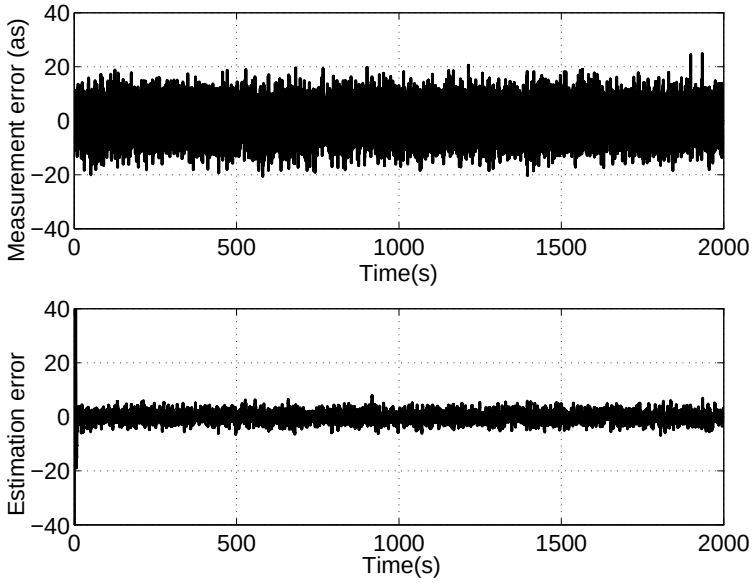

Figure 3.18: The Measurement and Estimation Errors of q_1 for the ST Measurements

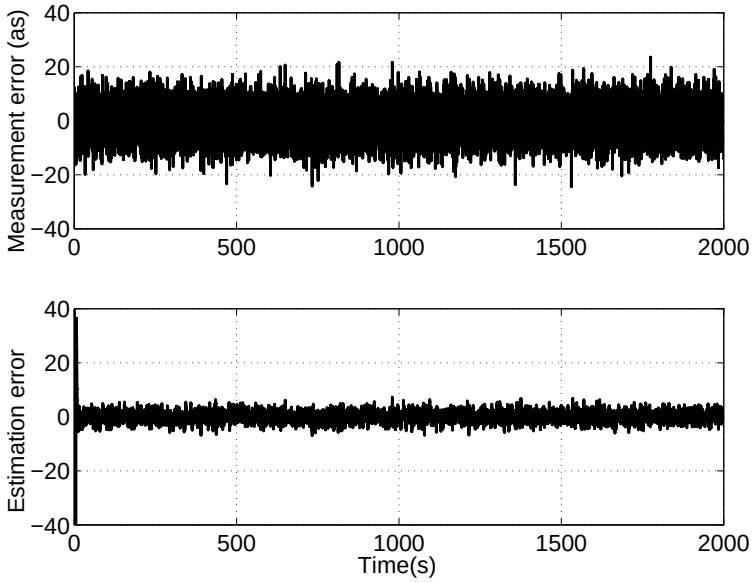

Figure 3.19: The Measurement and Estimation Errors of q_2 for the ST Measurements

For the OLS measurements, the accuracy of each axis is better than 1 mm (3σ). The initial parameters of this filter are set as:

$$\begin{aligned} \boldsymbol{Q} &= \boldsymbol{I}_3 \times 10^{-14} \\ \boldsymbol{R} &= \boldsymbol{I}_3 \times 10^{-4} \\ \hat{\boldsymbol{x}}_0 &= \boldsymbol{0}_{6\times 1} \end{aligned} \quad . \tag{3.31}$$

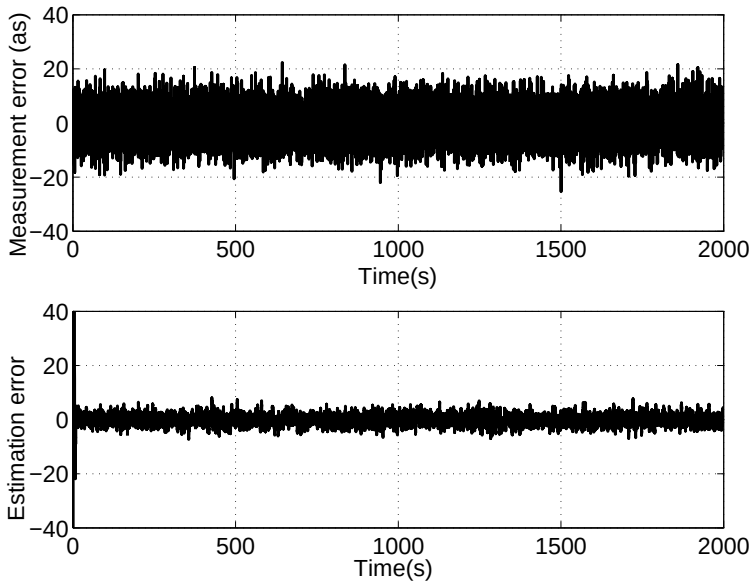

Figure 3.20: The Measurement and Estimation Errors of q_3 for the ST Measurements

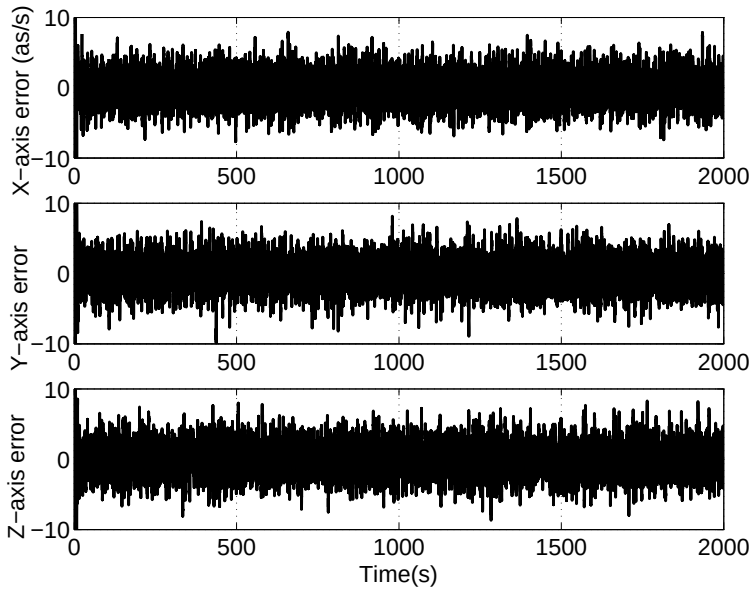

Figure 3.21: The Measurement and Estimation Errors of Relative Angular Velocity for the ST Measurements

Figure 3.14 ~ Figure 3.17 show the measurement and estimation errors of the relative position and velocity with the OLS measurements. The measurement error in each axis is 1 mm, while the estimation errors reduce to 0.5 mm. The relative velocity errors are shown to be less than 0.5 $\mu m/s$. The convergence times of the three channels are different. For the X-axis and Y-axis, both of them are

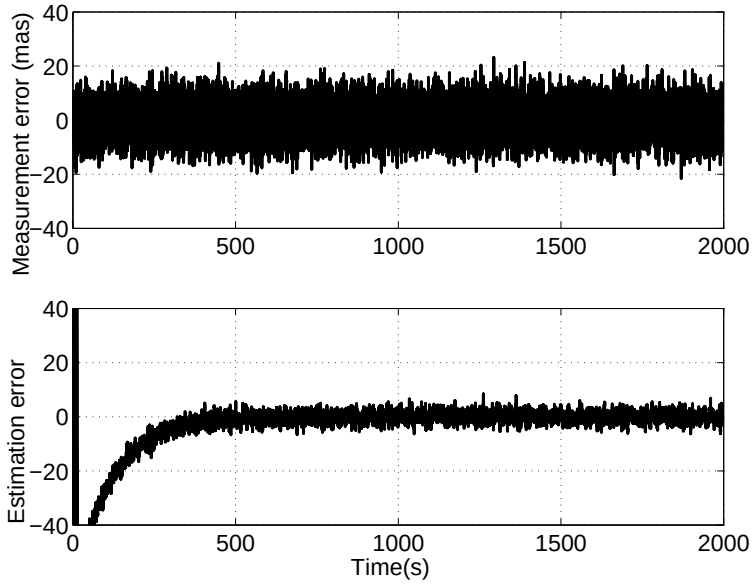

Figure 3.22: The Measurement and Estimation Errors of q_1 for the FRAS Measurements

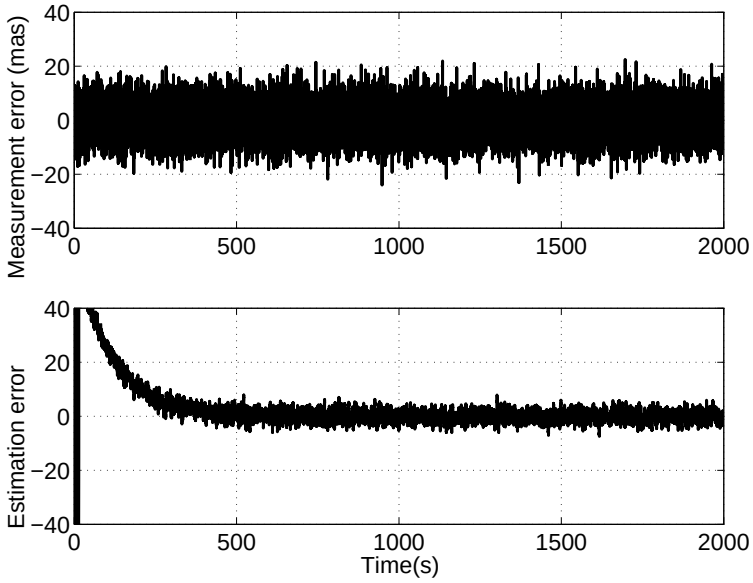

Figure 3.23: The Measurement and Estimation Errors of q_2 for the FRAS Measurements

less than 0.08 day. For the Z-axis, it converges in 0.01 day as the estimation error is very small. Due to the smaller measurement noise covariance $\boldsymbol{R}$ (comparing Eq. (3.30) and Eq. (3.31)), the convergence time of this filter is quicker than that of the RF measurements.

The measurement accuracy for the ST measurements is 10 *as* (3σ). The initial

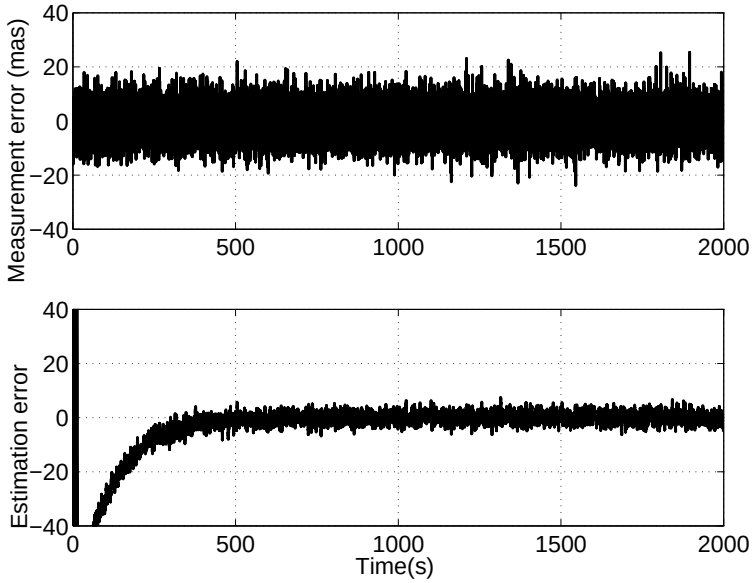

Figure 3.24: The Measurement and Estimation Errors of q_3 for the FRAS Measurements

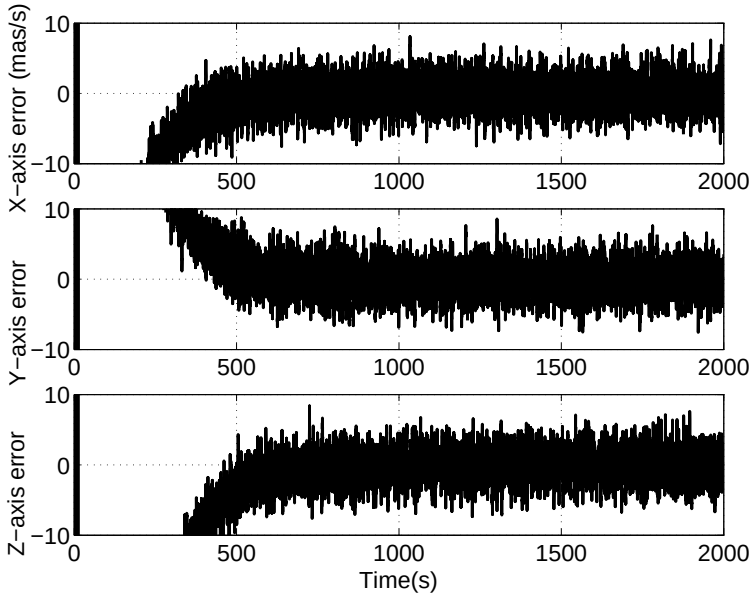

Figure 3.25: The Measurement and Estimation Errors of Relative Angular Velocity for the FRAS Measurements

parameters of this filter are set as:

$$\begin{aligned} \boldsymbol{Q} &= \boldsymbol{I}_3 \times 10^{-14} \\ \boldsymbol{R} &= 0.25 \times \boldsymbol{I}_3 \times 10^{-14} \\ \hat{\boldsymbol{x}}_0 &= \boldsymbol{0}_{6\times 1} \end{aligned} \quad . \tag{3.32}$$

Figure 3.18 ~ Figure 3.21 show the measurement and estimation errors of the

relative attitude and angular velocity using the ST measurements. The measurement error in each axis is 10 *as*, while the estimation errors reduce to 5 *as*. The relative velocity error are seen to be less than 4 as/s. The filter converges in 50 seconds.

The accuracy using the FRAS measurements is 10 *mas* (3σ). The initial parameters of this filter are set as the same as those of the ST measurement filter. Figure 3.22 ~ Figure 3.25 show the measurement and estimation errors of the relative attitude and angular velocity using the FRAS measurements. The measurement error in each axis is approximately 10 *mas*, while the estimation errors reduce to approximately 5 *mas*. The relative velocities are shown to have less than 4 mas/s error. The filter converges in 500 seconds for each axis.

3.4 Simulation Results and Analysis

In this section, a formation flying scenario which comprises four telescopes located at the vertexes of a square is considered (the X-array of DARWIN mission) and all of the spacecraft are controlled using the LQR controller designed in this chapter. The nonlinear model of the relative motion in Eq. (2.18) is used during the simulation rather than the linearised model. The effects of solar radiation pressure and lunar gravity in Eq. (2.17) and Eq. (2.14) are taken into account as well.

3.4.1 Translational Control Simulation

The formation flying scenario depicted in Fig. 3.26 is first presented in Xin et al. (2007), where the hub is located at the square centre and the telescopes are located at the four vertexes. During the simulation, the formation telescopes are always kept at the square vertices which are extended gradually from $0.1\sqrt{2} \times 0.1\sqrt{2}\ km$ (solid line in Fig. 3.26) to $\sqrt{2} \times \sqrt{2}\ km$ (dash line in Fig. 3.26).

The hub follows the nominal Lissajous trajectory (dash-dot line in Fig. 3.26) about the L_2 point, and its initial position (circle in Fig. 3.26) and velocity are given in Table 3.1. All of the telescopes follow the hub, and their initial relative positions (rectangles in Fig. 3.26) and desired relative positions (triangles in Fig. 3.26) are

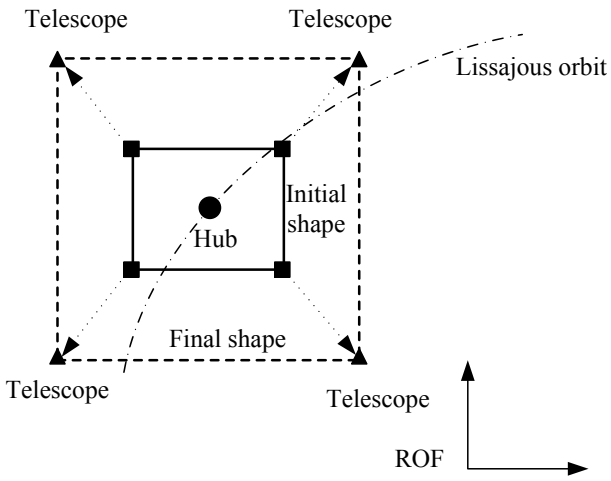

Figure 3.26: Formation Flying Simulation Scenario

*Table 3.1: The Initial Position and Velocity of the Hub with respect to L_2 Point in the **ROF** Frame (Xin et al., 2007)*

Axis	Position (km)	Velocity (m/s)
X-axis	87028.508409	-8.985878
Y-axis	-24739.512630	-121.605675
Z-axis	-229951.974656	9.457953

described in Table 3.2. Both the initial and the desired relative velocities with respect to the central hub of all telescopes are set to zero, which means that, before and after the manoeuvre, all of the telescopes are position-keeping with respect to the hub.

*Table 3.2: The Initial and Desired Relative Positions of all Telescopes with respect to the Hub in the **ROF** Frame (Xin et al., 2007)*

Telescope	Initial position (km)	Desired position (km)
Upper left	$[-0.05\sqrt{2} \;\; 0.05\sqrt{2} \;\; 0]^{\mathrm{T}}$	$[-0.5\sqrt{2} \;\; 0.5\sqrt{2} \;\; 0]^{\mathrm{T}}$
Upper right	$[0.05\sqrt{2} \;\; 0.05\sqrt{2} \;\; 0]^{\mathrm{T}}$	$[0.5\sqrt{2} \;\; 0.5\sqrt{2} \;\; 0]^{\mathrm{T}}$
Lower left	$[0.05\sqrt{2} \;\; -0.05\sqrt{2} \;\; 0]^{\mathrm{T}}$	$[0.5\sqrt{2} \;\; -0.5\sqrt{2} \;\; 0]^{\mathrm{T}}$
Lower right	$[-0.05\sqrt{2} \;\; -0.05\sqrt{2} \;\; 0]^{\mathrm{T}}$	$[-0.5\sqrt{2} \;\; -0.5\sqrt{2} \;\; 0]^{\mathrm{T}}$

The hub mass is set to 500 kg, and each telescope mass is set to 500 kg. The parameters of solar radiation pressure in Eq. (2.17) are set to: $C_R = 2$; $A_h = 5\ m^2$, $A_t = 4.965\ m^2$; $\sigma_{sf} = 1$. Figure 3.27 shows the effect of solar radiation pressure

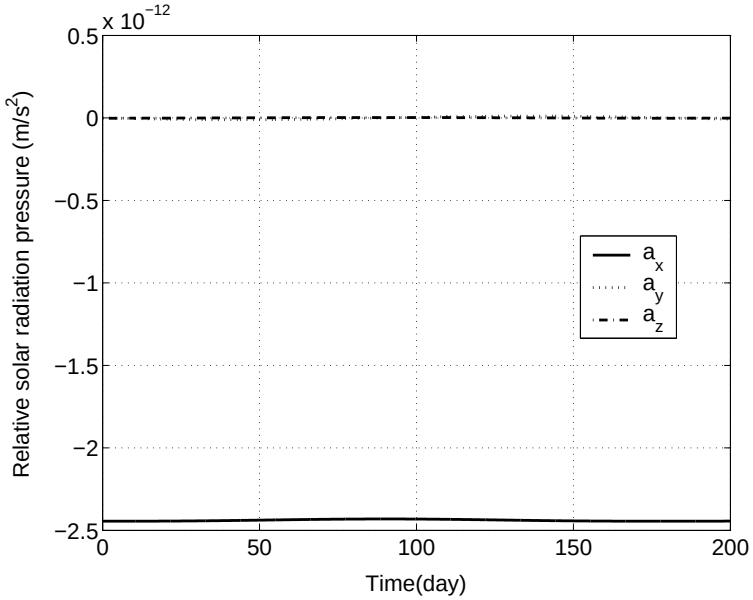

Figure 3.27: The Effect of Solar Radiation Pressure for the Relative Motion

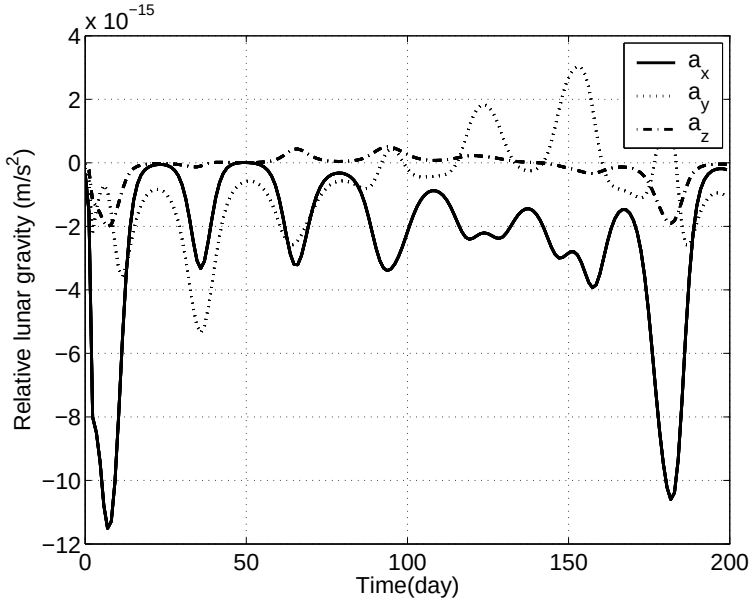

Figure 3.28: The Effect of Lunar Gravity for the Relative Motion

on the relative motion, and Fig. 3.28 shows the effect of lunar gravity on the relative motion. As discussed in Section 2.1, the solar radiation pressure is almost constant over 200 days, and the major effect is in X-axis channel, as the sunlight direction is along X-axis in the **ROF** frame. While the lunar gravity force varies over 200 days, and it has a peak each 29 days due to the periodic motion of the

Moon. Around 8 days and 182 days, the disturbance of the lunar gravity becomes maximum, which occurs when the distance between the Moon and spacecraft in at a minimum.

In order to compare the performance for different controllers, the LQR controller is benchmark to use in comparing performance and robustness for PEA controller designed in Chapter 4. The settling time for the LQR controller is 5 days. The values of $\boldsymbol{Q}$ and $\boldsymbol{R}$ are set to $\boldsymbol{Q} = diag\{5\times10^{-8},\ 5\times10^{-8},\ 5\times10^{-8},\ 4\times 10^{-4},\ 4\times10^{-4},\ 4\times10^{-4},\ ,10^{-4},\ 10^{-4},\ 10^{-4}\}\times10^{-13}$, $\boldsymbol{R} = 6.4\times10^{-7}\times\boldsymbol{I}_3$.

The simulation time in this thesis for all controllers is to 200 days, over one period of the reference orbit. However, the time scales of figures are also chosen as 5 days, 20 days, 100 days, and 200 days to provide illustration of various properties. For example, position manoeuvring could start at 1 day to examine convergence of the Kalman filter designs.

Figure 3.29 ~ Figure 3.36 depict the simulation results for the upper left telescope controlled by the LQR controller without an integrator.

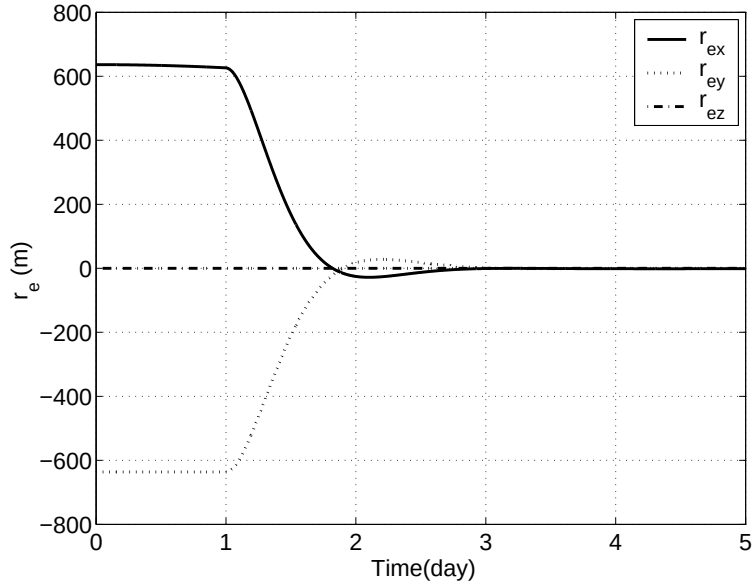

Figure 3.29: The Relative Position Errors for the Upper Left Telescope Controlled by the LQR without an Integrator over the First 5 days

Figure 3.29 ~ Figure 3.32 show the simulation results over the first 5 days. In these figures, the characteristics of the transient response of the error states are shown very clearly. As one can see in Fig. 3.29, the errors in position drops

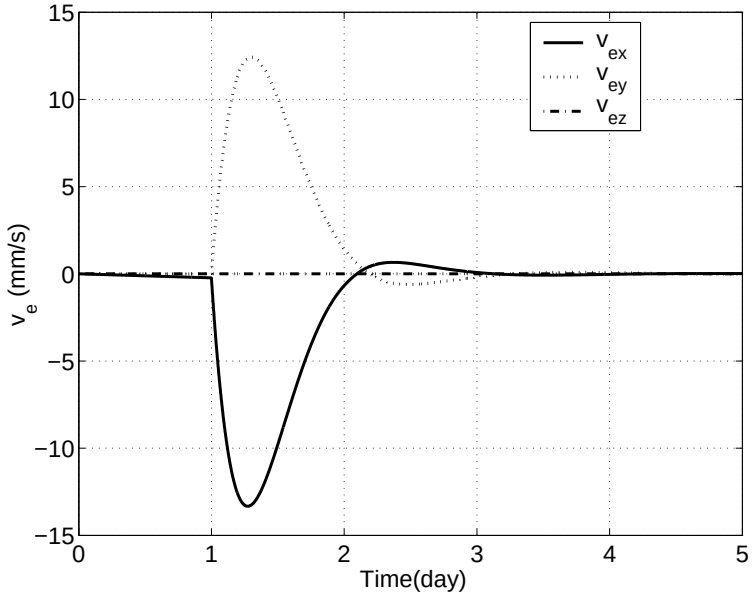

Figure 3.30: The Relative Velocity Errors for the Upper Left Telescope Controlled by the LQR without an Integrator over the First 5 days

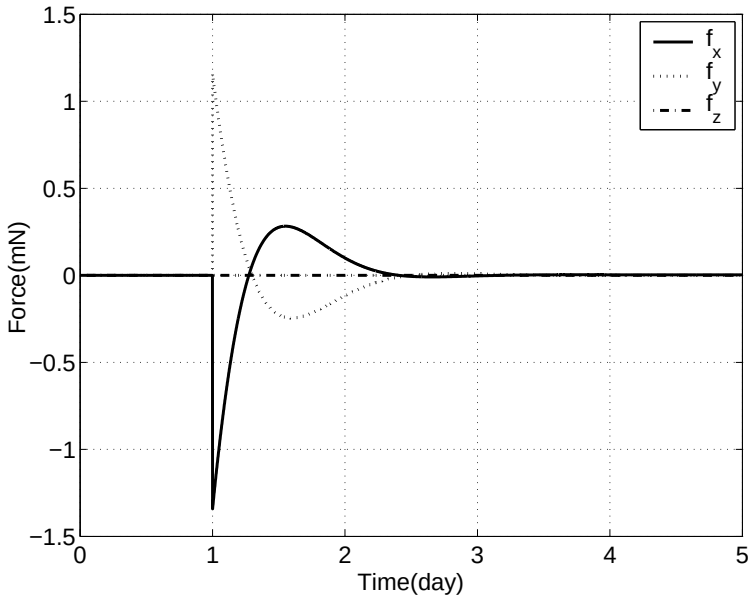

Figure 3.31: The Control Forces for the Upper Left Telescope Controlled by the LQR without an Integrator over the First 5 days

down very quickly to near zero in the first few days. Figure 3.30 depicts the maximum velocity peaking at 12.5 mm/s and 13.3 mm/s for the X-axis and the Y-axis channels. The maximum force is 1.2 mN at the beginning of manoeuvre is shown in Fig. 3.31. To overcome the initial position and velocity errors, the fuel

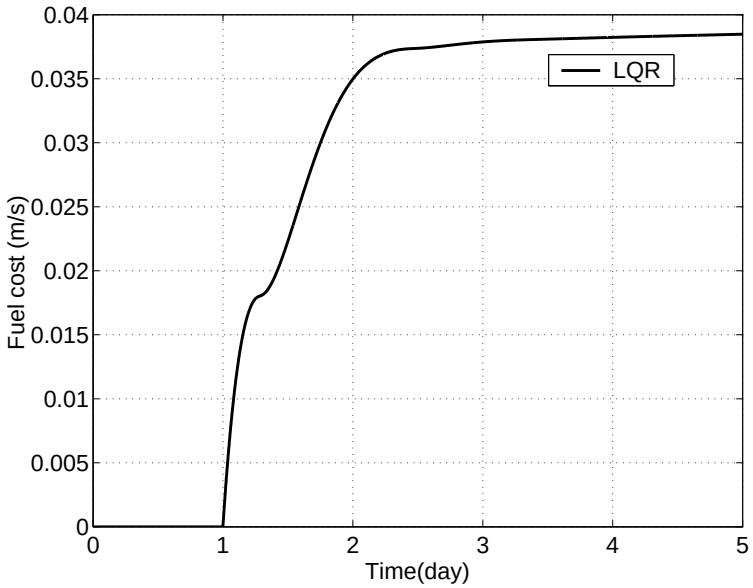

Figure 3.32: The Fuel Cost for the Upper Left Telescope Controlled by the LQR without an Integrator over the First 5 days (Position Keeping)

cost is 0.039 m/s as shown in Fig. 3.32.

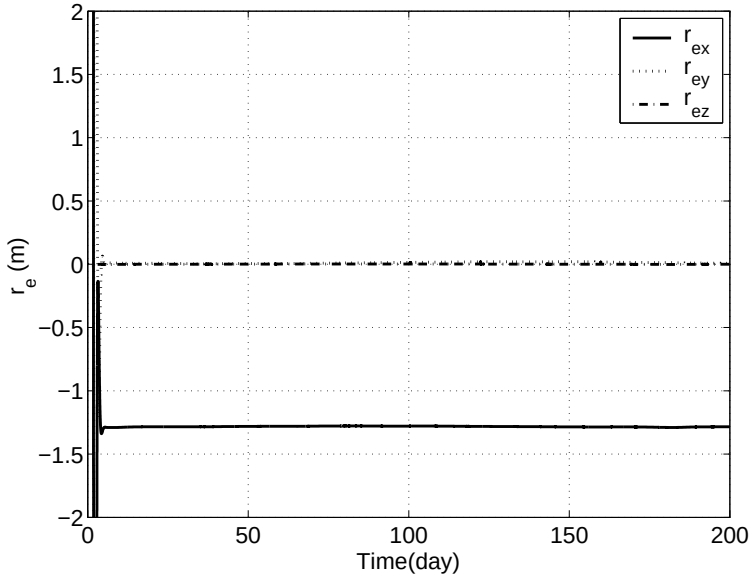

Figure 3.33: The Relative Position Errors for the Upper Left Telescope Controlled by the LQR without an Integrator over 200 days

Figure 3.33 ~ Figure 3.36 show the simulation results over all 200 days. From these figures, the control force and error states decline to meter levels once the initial state errors are eliminated. This represents the stabilized control for position

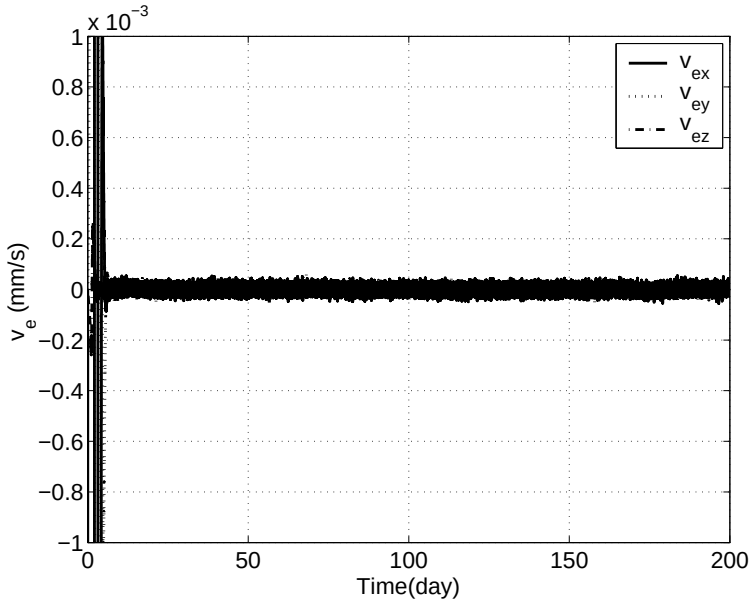

Figure 3.34: The Relative Velocity Errors for the Upper Left Telescope Controlled by the LQR without an Integrator over 200 days

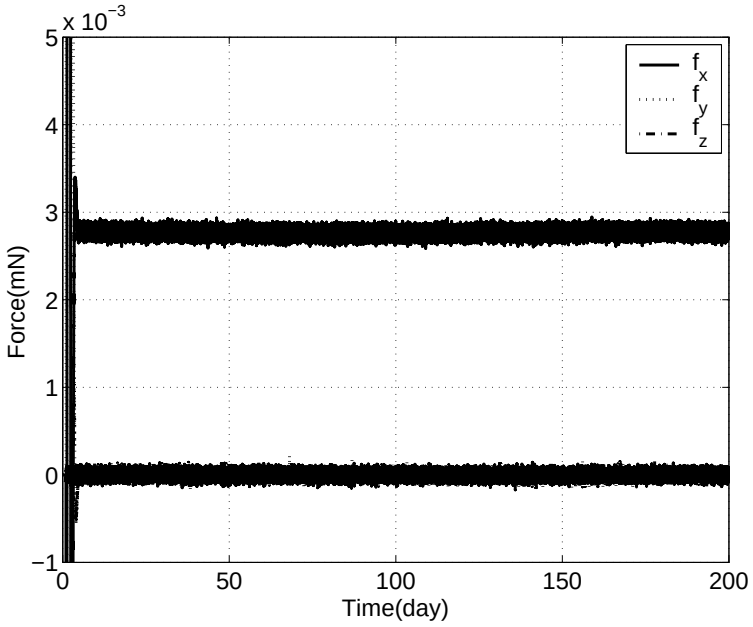

Figure 3.35: The Control Forces for the Upper Left Telescope Controlled by the LQR without an Integrator over 200 days

keeping which are overcoming the disturbances in the relative formation motion during the mission. However in Fig. 3.33, the position error in the X-axis remains at a large steady error value (1.5 m), due to the effect of solar radiation pressure.

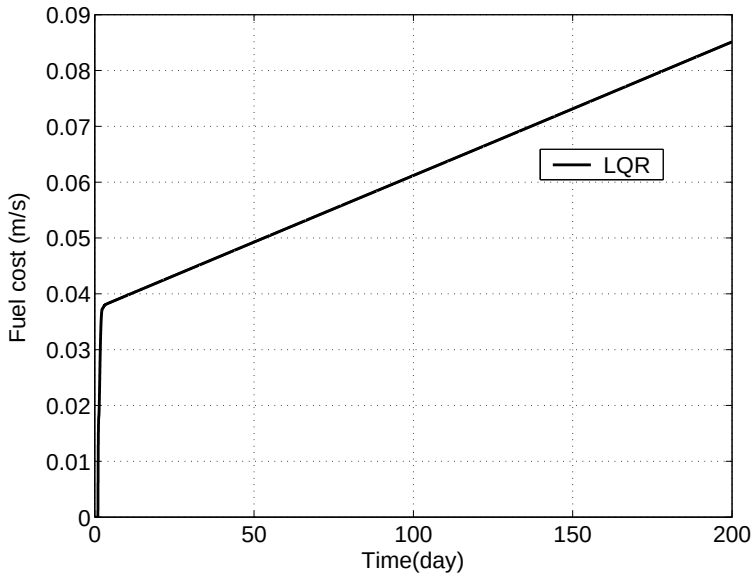

Figure 3.36: The Fuel Cost for the Upper Left Telescope Controlled by the LQR without an Integrator over 200 days (Position Keeping)

The velocity errors drop to less than 0.1 $\mu m/s$ for all three channels. The control force in the X-axis is 2.8 μN which leads to the fuel cost rising to 0.085 m/s at the end of 200 days (0.046 m/s for position keeping). The control forces for the other two axes are very small, in the range 0.1 μN. These results indicate that the LQR controller is unable to reduce the effect of system disturbance to acceptable levels.

Figure 3.37 ~ Figure 3.44 depict the simulation results for the upper left telescope controlled by the LQR controller with an integrator.

Figure 3.37 ~ Figure 3.40 show the simulation results over the first 5 days, which are very similar to those in Fig. 3.29 ~ Fig. 3.32. From Fig. 3.37, the position error also drops down very quickly to near zero in the first few days. In Fig. 3.38, the maximum velocity is 12.5 mm/s and 13.3 mm/s for the X-axis and the Y-axis channels, respectively. The maximum force is 1.2 mN at the beginning of manoeuvre (Fig. 3.39). The fuel cost is 0.040 m/s at the end of this manoeuvre.

However, the results of position keeping between Fig. 3.33 and Fig. 3.41 are quite different. The major difference is that the large steady error of the X-axis in Fig. 3.41 is reduced significantly and the position error of each axis is now kept less than 1 mm. While, the velocity (less than 0.1$\mu m/s$), force (2.8 μN in the X-axis) and fuel cost (0.086 m/s in total, 0.046 m/s for position keeping) in Fig. 3.42 ~ Fig. 3.44 are still maintained at similar levels to that in Fig. 3.34 ~ Fig. 3.36.

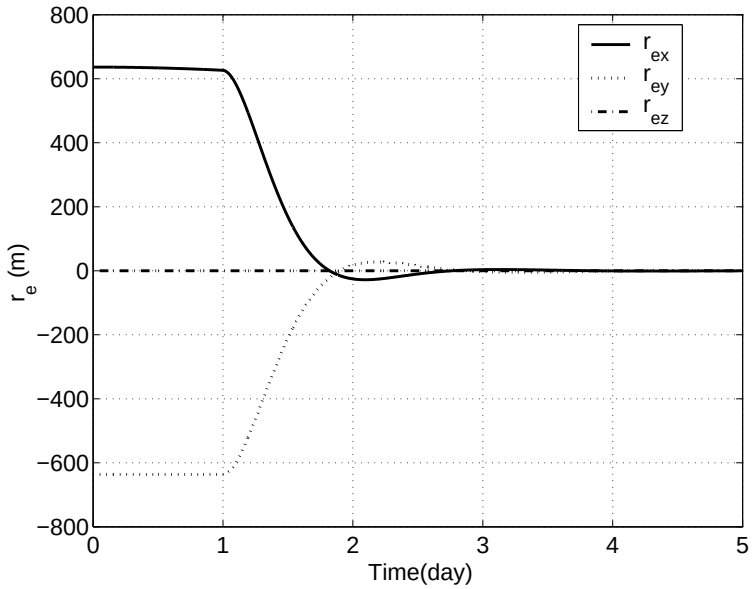

Figure 3.37: The Relative Position Errors for the Upper Left Telescope Controlled by the LQR with an Integrator over the First 5 days

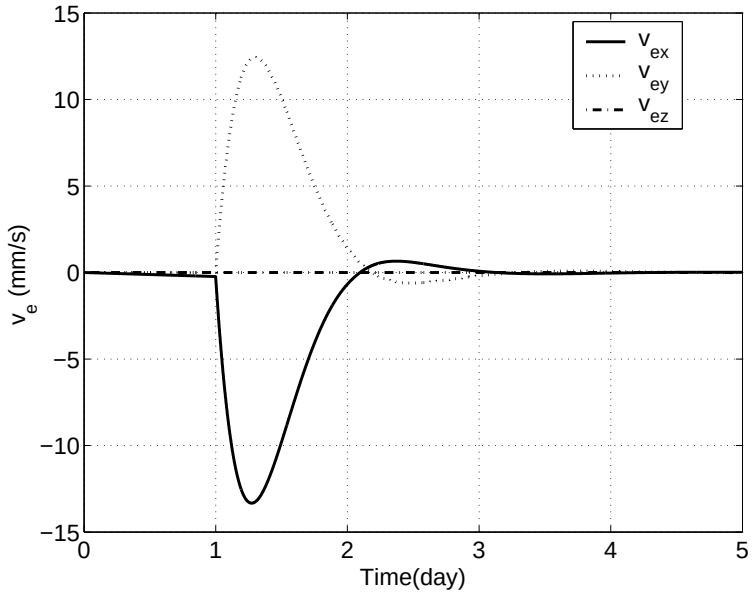

Figure 3.38: The Relative Velocity Errors for the Upper Left Telescope Controlled by the LQR with an Integrator over the First 5 days

These results indicate that the LQR controller including an integrator is able to reduce the effect of disturbance to improve the system performance with only a small increase in fuel cost. However, as one can see from Fig. 3.41, the remained steady error cannot be reduced further by this controller due to the effect of

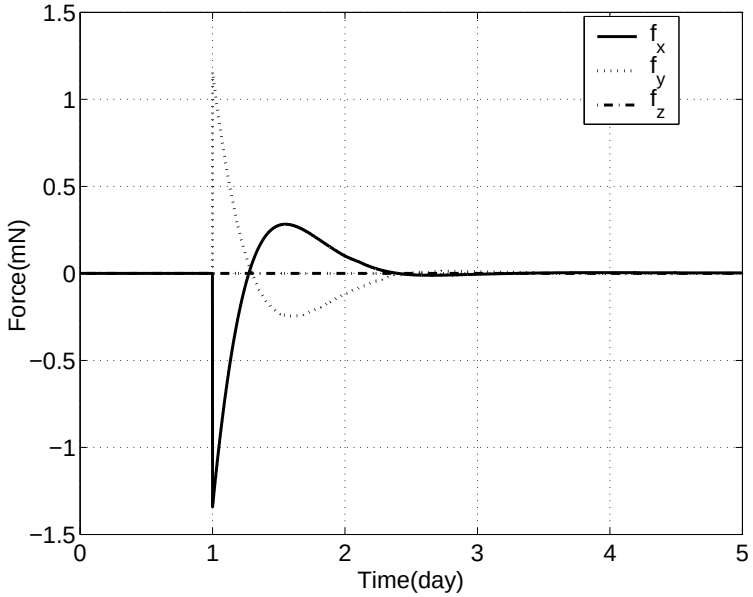

Figure 3.39: The Control Forces for the Upper Left Telescope Controlled by the LQR with an Integrator over the First 5 days

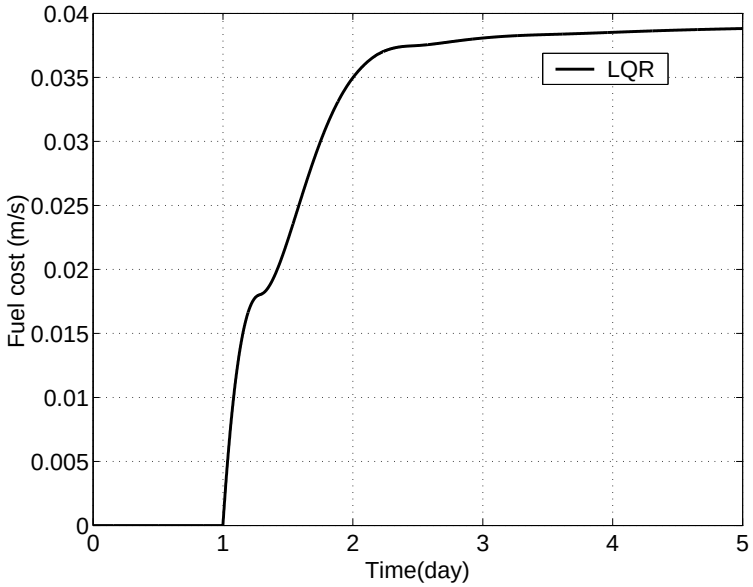

Figure 3.40: The Fuel Cost for the Upper Left Telescope Controlled by the LQR with an Integrator over the First 5 days (Position Keeping)

the system nonlinearity and the disturbances (solar radiation pressure and lunar gravity), which is depicted clearly over 200 days and rises to the maximum at 180 days. Therefore, in order to achieve higher precise control performance, it is necessary to use more precision models during the controller design, such as is

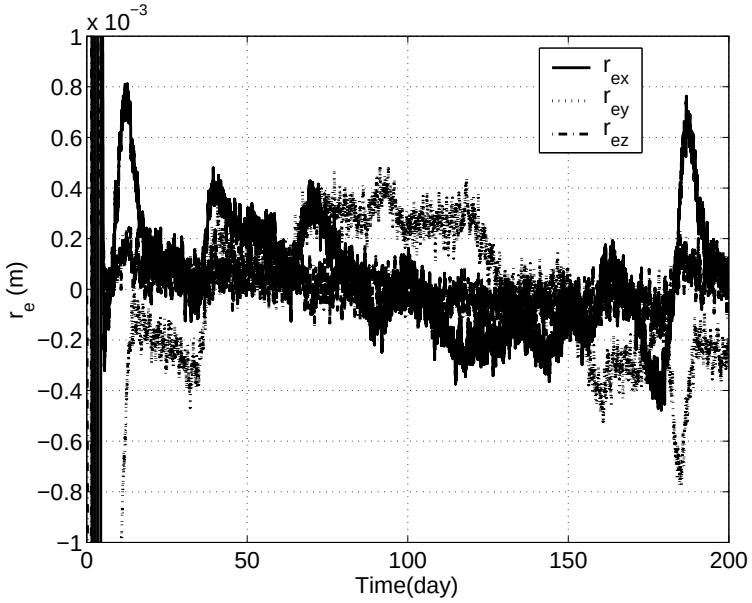

Figure 3.41: The Relative Position Errors for the Upper Left Telescope Controlled by the LQR with an Integrator over 200 days

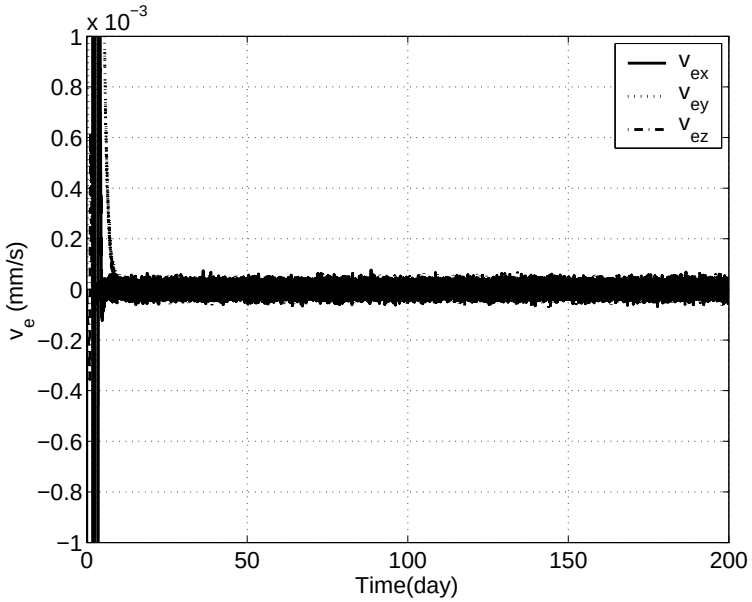

Figure 3.42: The Relative Velocity Errors for the Upper Left Telescope Controlled by the LQR with an Integrator over 200 days

the case for the LPV or QLPV model.

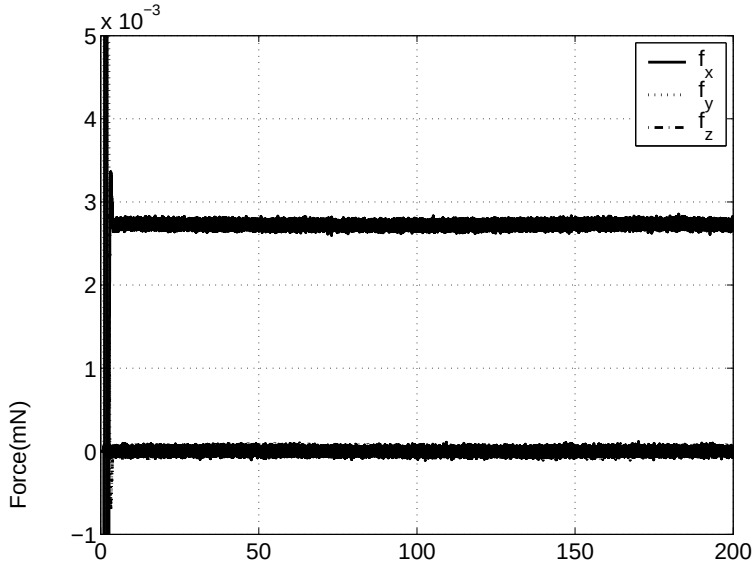

Figure 3.43: The Control Forces for the Upper Left Telescope Controlled by the LQR with an Integrator over 200 days

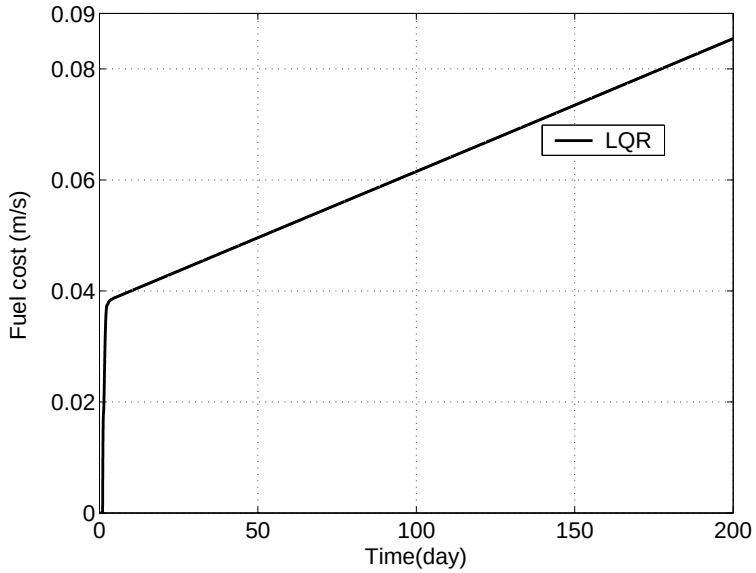

Figure 3.44: The Fuel Cost for the Upper Left Telescope Controlled by the LQR with an Integrator over 200 days (Position Keeping)

3.4.2 Rotational Control Simulation

The inertia matrix of the telescope is given by (Luquette, 2006):

$$\boldsymbol{J}_t = \begin{bmatrix} 200 & 10 & 5 \\ 10 & 300 & 15 \\ 5 & 15 & 200 \end{bmatrix} kgm^2. \tag{3.33}$$

The initial attitude of each corner telescope with respect to the hub is identical and set to $\boldsymbol{q}_e = [1 \quad 0 \quad 0 \quad 0]^{\mathrm{T}}$ and the desired attitude is set to $\boldsymbol{q}_e = [0.707 \quad 0 \quad 0 \quad 0.707]^{\mathrm{T}}$. The formation is then subject to a 90 *deg* slew manoeuvre about the inertial $\hat{\boldsymbol{z}}$ axis. During the simulation, rate and torque saturation limits are not considered.

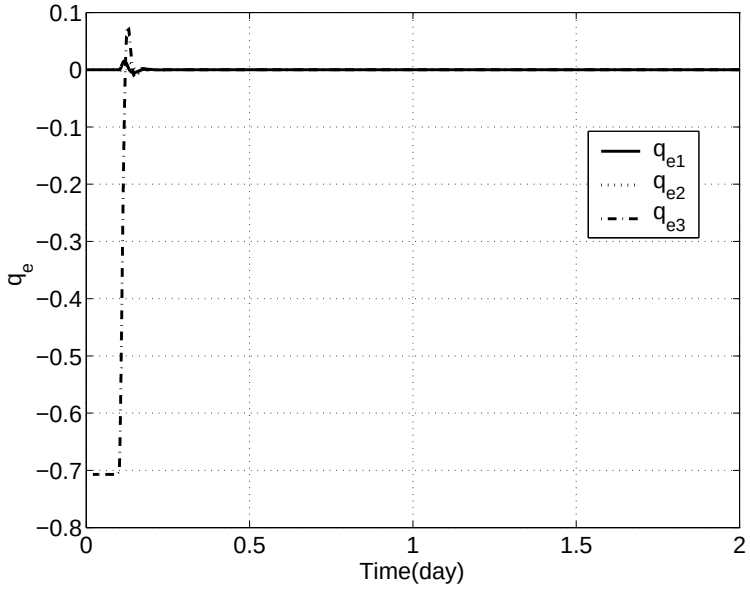

Figure 3.45: The Relative Quaternion Errors for the Upper Left Telescope Controlled by the LQR over 2 days

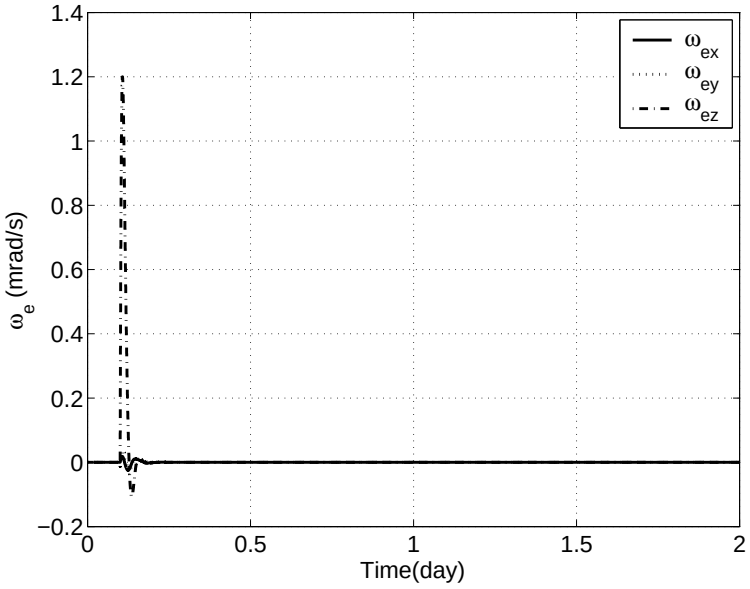

Figure 3.46: The Relative Angular Velocity Errors for the Upper Left Telescope Controlled by the LQR with an Integrator over 2 days

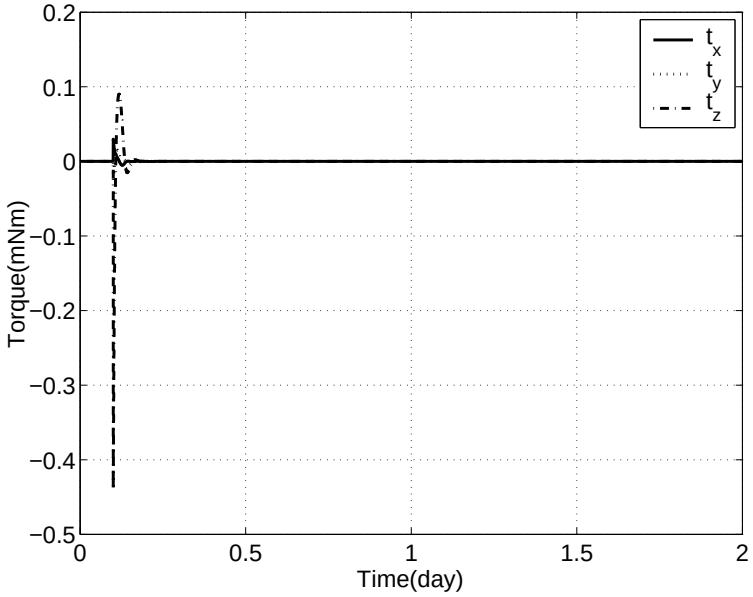

Figure 3.47: The Control Torques for the Upper Left Telescope Controlled by the LQR with an Integrator over 2 days

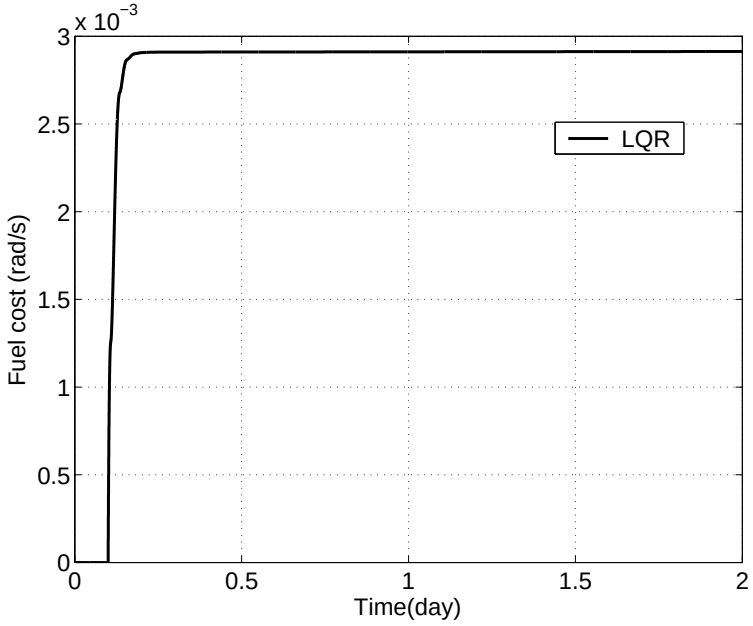

Figure 3.48: The Fuel Cost for the Upper Left Telescope Controlled by the LQR over 2 days (Attitude Manoeuvre)

For the comparison for the benchmark basic LQR controller, the values of $\boldsymbol{Q}$ and $\boldsymbol{R}$ are set as $\boldsymbol{Q} = 1.3 \times \boldsymbol{I}_6 \times 10^{-10}$, $\boldsymbol{R} = 3 \times \boldsymbol{I}_3$. The attitude manoeuvre starts at 0.1 day.

Figure 3.45 ~ Figure 3.48 depict the simulation results for the upper left telescope over 2 days, which indicates the transient response characteristic of error states clearly. From Fig. 3.45, the errors of the quaternion drop down very quickly to near zero in the first 2 hours (0.1 days). Figure 3.46 depicts the velocity which peaks at 1.2 $mrad/s$ in the Z-axis. The maximum torque is 0.44 mNm at the beginning of the manoeuvre (Fig. 3.47). To overcome the initial quaternion error, the fuel cost is 0.00291 rad/s (Fig. 3.48). The error in angle and angular velocity reaches 1 $mrad$ and 1.5 $mrad/s$ after 6 hours of manoeuvre.

3.5 Conclusions

In this chapter, the LQR control theory is applied to the translation and rotation control of the Sun-Earth L_2 point formation problem. In Section 3.2, several LQR controllers are developed based on the LTI model presented in Chapter 2. The robustness of the resulting LQR controller is analysed briefly in this section. In order to analyse the accuracy of metrology in the DARWIN Mission, a Kalman filter is used to estimate the system states in Section 3.3. Finally, a formation scenario is simulated out to assess the performance of each LQR closed-loop control system. The results indicate that in contrast to the traditional LQR controller, one including an integrator improves the system performance to approximately 1 mm with only a small increase in the cost of fuel.

The design of this controller is the main contribution in this chapter and its performance is selected as a benchmark to evaluate the nonlinear control performance presented in Chapter 4.

However, due to the effect of modeling error, the performance of this LQR controller cannot be improved further. In Chapter 4, more precise models (the LPV or the QLPV model) will be used for the controller design to achieve higher precision control performance.

Chapter 4

Polynomial Eigenstructure Assignment

LQR theory has been applied to the control of the Sun-Earth L_2 point formation in Chapter 3 based on an LTI model considering only the second order truncation of the gravitational force in the vicinity of a specific equilibrium. However due to the modeling error between the linearized and actual models, the LQR controller requires gain scheduling over the whole operating envelop (Tsourdos et al., 2001). Hence, the control system design will involve obtaining linearized models for the formation at finitely many equilibrium points, designing the LQR controller to satisfy local performance objectives for each equilibrium point, and then adjusting the controller gains in real time as the operating conditions vary. Furthermore, a crucial problem required to be solved is to determine the optimal scheduling routine for this strategy. An ad hoc approach, such as linear interpolation and curve fitting may be sufficient for simple static-gain controllers, but it is a complex and tedious process to do the same for multi-variable controllers (Bruye're et al., 2002).

To achieve control performance over the whole operational envelop and to avoid gain scheduling, more precise models such as LPV and QLPV models are used for the design of a gain-varying controller. In this chapter, a series of new control algorithms based on LPV and QLPV models are developed using PEA techniques for the Sun-Earth L_2 point formation.

Eigenstructure Assignment (EA) has been studied for many years, focusing on LTI systems for system controller design and performance analysis (Liu & Patton, 1998; Soylemez, 1999). It has been continuously improved and adapted to handle LPV systems with scheduled designs (White, 1995). However, the design and analysis criteria are usually associated with time responses and handling criteria, as well as deriving conditions for robustness, sensitivity, decoupling, actuator requirements, and transient responses properties(Bruye're et al., 2002), which can be difficult to be applied in controller design.

In this chapter, a PEA technique developed in recent research work (White,

1997; Bruye're et al., 2002; Bruyere, 2004; Bruye're et al., 2006; White et al., 2007) for LTI and LPV systems using polynomial matrices is extended to a QLPV system which is transformed from the nonlinear model using the Barbashin method (Barbashin, 1970; Solodovnik et al., 2004). This approach uses the key elements of EA, but no longer relies on the initial selection of an eigenstructure. In detail, the eigenspace is formulated as a set of polynomial matrices and the system open-loop transfer function is formed from a coprime factorization of these matrices. The formulation allows the polynomial eigenstructure to be used to compute the algebraic structure of the controller and naturally leads to a nonlinear controller without interpolation. The resulting controller renders the closed-loop system almost independent of the operating point, and thus performs a type of dynamic inversion while encompassing a broader class of LPV and QLPV systems to ensure that specific system performance can be achieved. Unlike nonlinear dynamic inversion techniques, this PEA technique deals with the poles in the closed-loop system design without requiring any cancelation of the zero-dynamics in order to produce a standard feedback form (Bruye're et al., 2006).

The outline of the chapter is as follows. In Section 4.1, a brief overview of PEA for LTI systems is presented, and then it is extended for LPV and QLPV formulations in Section 4.2. In Section 4.3 and 4.4, the control algorithm is applied to the design of translation control using LPV and QLPV models. Section 4.5 combines the translation and rotation controllers by using thrusters as actuators. In this section, the coupling effects due to the misalignment and misplacement of thrusters are also taken into account. Manoeuvre rate limits and the saturation of actuators are also considered using cascade-saturation control logic (Wie & Lu, 1995; Wang et al., 2006). In Section 4.6, the effect of spacecraft flexibility for PEA controller is investigated. The PEA controller is further enhanced by adding a compensation term to suppress the vibration of flexible spacecraft.

4.1 PEA for LTI Systems

In classical eigenstructure assignment research (White, 1995; Liu & Patton, 1998; Soylemez, 1999), the authors attempt to modify the modes of the open-loop system by a choice of closed-loop eigenvalues and their associated eigenvector spaces. For example, the i^{th} eigenvalue λ_i associated with the right eigenvector $\boldsymbol{z}_i$ and

corresponding control vector $\boldsymbol{p}_i$, can be achieved (Bruyere, 2004) by defining an output feedback controller K, given by the solution of:

$$\begin{aligned} \lambda_i \boldsymbol{z}_i &= \boldsymbol{A}\boldsymbol{z}_i + \boldsymbol{B}\boldsymbol{p}_i \\ \boldsymbol{p}_i &= \boldsymbol{K}(\boldsymbol{C}\boldsymbol{z}_i + \boldsymbol{D}\boldsymbol{p}_i) \end{aligned} \tag{4.1}$$

where $\boldsymbol{K}$ is the output feedback static controller, and $\boldsymbol{A}, \boldsymbol{B}, \boldsymbol{C}, \boldsymbol{D}$ are the matrices of LTI system given in Eq. (3.1). There are several methods used to solve this problem by selecting the eigenvalue and its associated eigenvector (White, 1995). However, these methods are very complex and cannot set the complete assignment of the eigenstructure (Bruyere, 2004). Using the framework of polynomial matrices, PEA can formulate the problem in Eq. (4.1) as the generalisation of the solution to:

$$\begin{bmatrix} \boldsymbol{A} - \lambda_i \boldsymbol{I} & \boldsymbol{B} \end{bmatrix} \begin{bmatrix} \boldsymbol{z}_i \\ \boldsymbol{p}_i \end{bmatrix} = 0 \tag{4.2}$$

So, taking into account all the eigenvalues in Eq. (4.2), one can combine them into a polynomial matrix form by using variable s instead of λ, to get:

$$\begin{bmatrix} \boldsymbol{A} - s\boldsymbol{I} & \boldsymbol{B} \end{bmatrix} \begin{bmatrix} \boldsymbol{Z}(s) \\ \boldsymbol{P}(s) \end{bmatrix} = 0 \tag{4.3}$$

where s represents the eigenvalues as well as the Laplace variable. $\boldsymbol{Z}(s)$ and $\boldsymbol{P}(s)$ represent the eigenvector space and its associated controllability space. Using these two spaces, the open-loop transfer function $\boldsymbol{G}(s)$ in Eq. (3.1) can be rewritten as:

$$\begin{aligned} \boldsymbol{G}(s) &= \boldsymbol{C}(\boldsymbol{I} - \boldsymbol{A})^{-1}\boldsymbol{B} + \boldsymbol{D} = \boldsymbol{C}\boldsymbol{Z}(s)\boldsymbol{P}(s)^{-1} + \boldsymbol{D} \\ &= (\boldsymbol{C}\boldsymbol{Z}(s) + \boldsymbol{D}\boldsymbol{P}(s))\boldsymbol{P}(s)^{-1} = \boldsymbol{Z}_0(s)\boldsymbol{P}(s)^{-1} \end{aligned} \tag{4.4}$$

In the sequel, the controller K can be written in polynomial form as $\boldsymbol{K}(s)$. Noting Eq. (4.1), one has:

$$\boldsymbol{P}(s) = \boldsymbol{K}(s)\boldsymbol{Z}_0(s) \tag{4.5}$$

where the space $\boldsymbol{Z}_0(s)$ contains the outputs of system. Therefore using this feedback, the closed-loop transfer function $\boldsymbol{G}_{CL}(s)$ in Eq. (3.1) is given as:

$$\boldsymbol{G}_{CL}(s) = \boldsymbol{G}(s)\boldsymbol{K}(s)\boldsymbol{Z}_0(s) = \boldsymbol{Z}_0(s)\boldsymbol{P}(s)^{-1}\boldsymbol{P}(s) = \boldsymbol{Z}_0 \tag{4.6}$$

where the dynamics of open-loop system are inverted but the zeros are unchanged, which is different from the normal dynamic inversion approach in that the zeros are not cancelled. In PEA, an effective controller structure is able to modify the dynamics of the open-loop system without making the zero dynamics unobservable (White, 1997; Bruye're et al., 2002).

Also, during the choice of the structure of the closed-loop system, constraints to improve stability, performance, tracking, sensitivity, and robustness should be considered. With this mind in White (1997) and Bruye're et al. (2002), we choose the controller structure shown in Fig. 4.1, which provides adequate flexibility for the requirements of most engineering applications. The controller $\boldsymbol{K}_a(s)$ shapes the tracking response of the closed-loop system which is usually chosen to contain an integrator, the controller $\boldsymbol{K}_u(s)$ shapes the inputs to the plant, $\boldsymbol{K}_i(s)$ feeds back the inner-loop measurable outputs $\boldsymbol{y}_i$ (see below), and $\boldsymbol{K}_c(s)$ feeds back the controlled outputs $\boldsymbol{y}_c$ to shape the transient response. To design the control system, the dynamic order of $\boldsymbol{K}_u(s)$ should meet or exceed the order of the other gains $\boldsymbol{K}_a(s)$, $\boldsymbol{K}_i(s)$ and $\boldsymbol{K}_c(s)$. These gains are unknown and are required to be calculated to meet the desired closed-loop performance of the system. To obtain the expressions of these gains, firstly, the transfer function from reference input r to output y_c needs be calculated as:

$$\boldsymbol{T}_{\boldsymbol{y}}^{\boldsymbol{r}} = \boldsymbol{G}_c(\boldsymbol{I} + \boldsymbol{K}_u^{-1}((\boldsymbol{K}_a + \boldsymbol{K}_c)\boldsymbol{G}_c + \boldsymbol{K}_i\boldsymbol{G}_i))^{-1}\boldsymbol{K}_u^{-1}\boldsymbol{K}_a \tag{4.7}$$

From Fig. 4.1, the output is partitioned into controlled outputs and other measured outputs to obtain the desired eigenstructure. Hence, the eigenvector matrix $\boldsymbol{Z}_0(s)$ can be partitioned into

$$\boldsymbol{Z}_0(s) = \begin{bmatrix} \boldsymbol{Z}_0^c(s) \\ \boldsymbol{Z}_0^i(s) \end{bmatrix} \tag{4.8}$$

Therefore, the closed-loop transfer function $\boldsymbol{T}_{\boldsymbol{y}}^{\boldsymbol{r}}$ can also be split into two parts relating to the controlled outputs and inner-loop outputs, namely $\boldsymbol{T}_{\boldsymbol{y}_c}^{\boldsymbol{r}}$, and $\boldsymbol{T}_{\boldsymbol{y}_i}^{\boldsymbol{r}}$. Together with Eq. (4.5) and Eq. (4.8), they can be expressed as

$$\boldsymbol{T}_{\boldsymbol{y}_c}^{\boldsymbol{r}} = \boldsymbol{Z}_0^c(\boldsymbol{K}_u\boldsymbol{P} + (\boldsymbol{K}_a + \boldsymbol{K}_c)\boldsymbol{Z}_0^c + \boldsymbol{K}_i\boldsymbol{Z}_0^i)^{-1}\boldsymbol{K}_a \tag{4.9}$$

$$\boldsymbol{T}_{\boldsymbol{y}_i}^{\boldsymbol{r}} = \boldsymbol{Z}_0^i(\boldsymbol{K}_u\boldsymbol{P} + (\boldsymbol{K}_a + \boldsymbol{K}_c)\boldsymbol{Z}_0^c + \boldsymbol{K}_i\boldsymbol{Z}_0^i)^{-1}\boldsymbol{K}_a \tag{4.10}$$

where $\boldsymbol{T}_{\boldsymbol{y}_c}^{\boldsymbol{r}}$ is used for controller gain determination, and $\boldsymbol{T}_{\boldsymbol{y}_i}^{\boldsymbol{r}}$ can be used to evaluate system performance.

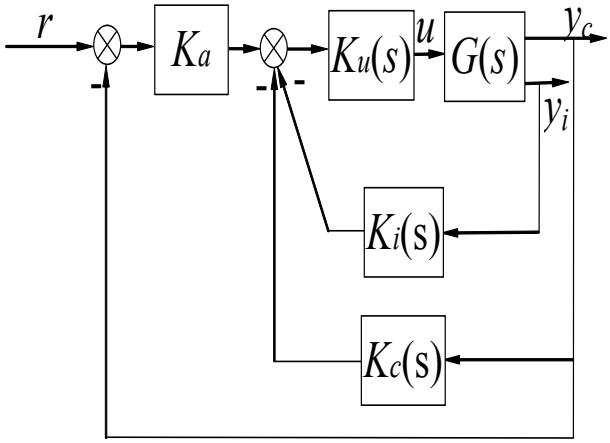

Figure 4.1: Controller Structure Chosen for LTI Systems

Once the number of inputs, states and outputs, n_i, n_s and n_o, meet the Kimura condition (Kimura, 1975), $n_s \leq n_i + n_o - 1$, pole placement for the whole closed-loop system can be performed. This condition is obviously met for our full state feedback control system. Hence, the full eigenstructure assignment is possible for the system in Eq. (3.1) by matching the closed-loop transfer function $\boldsymbol{T}_{\boldsymbol{y}_c}^{\boldsymbol{r}}$ to a desired transfer function $\boldsymbol{T}_{\boldsymbol{y}}^{\boldsymbol{d}}$, which can be written as a coprime factorization:

$$\boldsymbol{T}_{\boldsymbol{y}}^{\boldsymbol{d}}(s) = \boldsymbol{N}_d(s)\boldsymbol{D}_d^{-1}(s) \tag{4.11}$$

where $\boldsymbol{N}_d(s)$ is the numerator matrix of the desired transfer function, including the open loop zeros of the plant and $\boldsymbol{D}_d(s)$ is the desired denominator matrix, defining the poles required to be assigned to the closed-loop system. All the objectives for the closed-loop system are contained in the desired transfer function.

However, there are matching conditions which should be held to obtain the equations for the controller gains. Firstly, the PEA method doesn't attempt to cancel the open-loop zeros, but retains them in the closed-loop system by meeting condition Eq. (4.12). This avoids the problem of feedback linearization where the open loop zeros are cancelled by making them unobservable. Secondly, the closed-loop system has zero steady state error for constant inputs, as the controller has a free integrator, which is expressed in condition Eq. (4.13). Finally, the system has the same number of inputs and outputs, matching $\boldsymbol{T}_{\boldsymbol{y}_c}^{\boldsymbol{r}}$ to $\boldsymbol{T}_{\boldsymbol{y}}^{\boldsymbol{d}}$ leading to condition Eq. (4.14). So:

$$|\boldsymbol{N}_d(s)| = \left|\boldsymbol{Z}_0^c(s)\right|, \tag{4.12}$$

$$\boldsymbol{D}_d(0) = \boldsymbol{Z}_0^c(0), \tag{4.13}$$

$$\boldsymbol{D}_d(s)\boldsymbol{N}_d^{-1}(s) = (s\boldsymbol{K}_u(s)\boldsymbol{P}(s) + s\boldsymbol{K}_c(s)\boldsymbol{Z}_0(s) + s\boldsymbol{K}_i(s)\boldsymbol{Z}_0^i(s) + \boldsymbol{Z}_0^c(s))(\boldsymbol{Z}_0^c(s))^{-1} \tag{4.14}$$

Thus, the controller gains can be calculated from Eq. (4.14) by computing the left null space, which takes the form:

$$\begin{bmatrix} \boldsymbol{K}_u(s) & \boldsymbol{K}_c(s) & \boldsymbol{K}_i(s) & \boldsymbol{I} \end{bmatrix} \begin{bmatrix} \boldsymbol{P}(s)(\boldsymbol{Z}_0^c(s))^{-1}(s) \\ \boldsymbol{Z}_0(s)(\boldsymbol{Z}_0^c(s))^{-1} \\ \boldsymbol{Z}_0^i(s)(\boldsymbol{Z}_0^c(s))^{-1} \\ \frac{1}{s}(\boldsymbol{Z}_0(s)(\boldsymbol{Z}_0^c(s))^{-1} - \boldsymbol{D}_d(s)\boldsymbol{N}_d^{-1}(s)) \end{bmatrix} = 0 \tag{4.15}$$

This equation is used to select the controller that matches the desired closed-loop system. As each controller gain is a polynomial, it can be written as:

$$\boldsymbol{K}(s) = \boldsymbol{K}_0 + \boldsymbol{K}_1 s + \boldsymbol{K}_2 s^2 + \cdots + \boldsymbol{K}_q s^q \tag{4.16}$$

where q is the degree of the polynomial matrix. Substituting $\boldsymbol{P}(s)$ and $\boldsymbol{Z}_0(s)$ into Eq. (4.15) using the polynomial form given in Eq. (4.16), it is possible to obtain many solutions of varying order. Among these solutions, the one with minimum order is the base to construct the other high-order solutions whose parameters can be determined by other additional criteria for the closed-loop system. The multiple-solution condition for Eq. (4.15) is discussed in the next section when the controller is utilized in an application to the Sun-Earth L_2 point formation problem. Using these controller gains and setting the reference input r to zero, a state feedback controller can be achieved in the form:

$$\boldsymbol{u} = \boldsymbol{K}_u^{-1}(\boldsymbol{K}_a\boldsymbol{e} - \boldsymbol{K}_c\boldsymbol{y}_c - \boldsymbol{K}_i\boldsymbol{y}_i) \tag{4.17}$$

Thus, the controller design for LTI system is completed, and it is now possible to obtain the desired performance of the closed-loop system using the PEA method.

Although the LTI system is described in MIMO form, the procedure of PEA approach in this section is still only for SISO system as is that in White (1997) and Bruye're et al. (2002).

4.2 PEA for LPV and QLPV Systems

The PEA approach presented so far is only valid for LTI systems. Fortunately, it can be extended to LPV and QLPV systems by assigning the eigenstructure to

be (almost) independent of the operating point, which results in identical closed-loop dynamics over the operating envelope. Although to be strictly independent is not always possible due to the un-canceled open-loop zeros varying over the operating envelope, the closed-loop system is still very similar to that of an LTI system and has a desired characteristic polynomial which achieves the performance objectives for the system. In this section, the process of using the PEA approach for LPV and QLPV systems is described.

Considering the LPV form in Eq. (2.41) and the QLPV form in Eq. (2.49), both can be expressed in a canonical form as:

$$\dot{\boldsymbol{x}} = \boldsymbol{A}(\boldsymbol{p})\boldsymbol{x} + \boldsymbol{B}(\boldsymbol{p})\boldsymbol{u}, \quad \boldsymbol{y} = \boldsymbol{C}(\boldsymbol{p})\boldsymbol{x} + \boldsymbol{D}(\boldsymbol{p})\boldsymbol{u} \tag{4.18}$$

where the entries of $\boldsymbol{A}$, $\boldsymbol{B}$, $\boldsymbol{C}$ and $\boldsymbol{D}$ are dependent on parameter $\boldsymbol{p}$, which is the vector of varying parameter $\boldsymbol{\theta}$ for the LPV system and the state vector $\boldsymbol{x}$ and varying parameter $\boldsymbol{\theta}$ for the QLPV system respectively.

For the PEA approach to be used for LPV and QLPV systems, the main strategy attempts to modify the modes of open-loop system by choosing closed-loop eigenvalues and their associated eigenvector spaces in the same manner as for LTI systems. With the definition of eigenvalue and their associated eigenvector spaces for LPV systems described in Bruye're et al. (2006) and Wang et al. (2009), we get, for LPV and QLPV systems:

$$[\boldsymbol{A}(\boldsymbol{p}) - s\boldsymbol{I} \quad \boldsymbol{B}(\boldsymbol{p})]\,[\boldsymbol{Z}(s,\boldsymbol{p}) \quad \boldsymbol{P}(s,\boldsymbol{p})]^{\mathrm{T}} = 0 \tag{4.19}$$

where s represents the eigenvalues of the system as well as the Laplace variable. $\boldsymbol{Z}(s,\boldsymbol{p})$ and $\boldsymbol{P}(s,\boldsymbol{p})$ represent the eigenvector space and its associated eigenvector space. Thus, for a controllable and observable system, the open-loop transfer function $\boldsymbol{G}(s,\boldsymbol{p})$ can be defined as:

$$\boldsymbol{G}(s,\boldsymbol{p}) = \boldsymbol{Z}_0(s,\boldsymbol{p})\boldsymbol{P}(s,\boldsymbol{p})^{-1} \tag{4.20}$$

where: $\boldsymbol{Z}_0(s,\boldsymbol{p}) = \boldsymbol{C}\boldsymbol{Z}(s,\boldsymbol{p}) + \boldsymbol{D}\boldsymbol{P}(s,\boldsymbol{p})$ is the eigenvector matrix for LPV and QLPV systems.

In the PEA approach, the controller structure is able to modify the dynamics of the open-loop system without making the zero dynamics unobservable to improve the system stability and robustness, as discussed in previous sections.

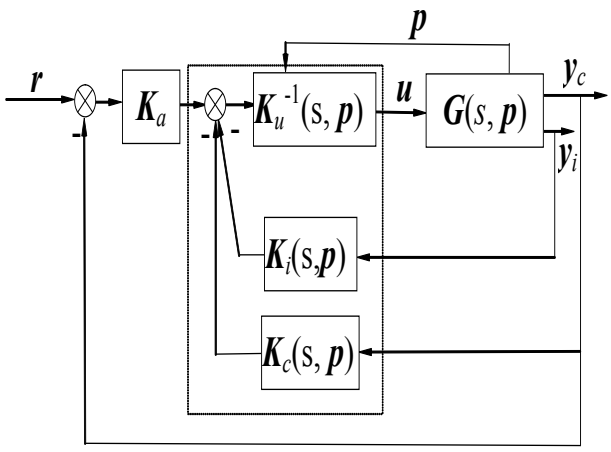

Figure 4.2: Controller Structure Chosen for LPV and QLPV systems

The structure shown in Fig. 4.2, has been used successfully in the controller design for LTI and LPV systems (Bruye're et al., 2006; Wang et al., 2009) and gives adequate flexibility to realize the stability and robustness of the closed-loop system, as the order of controller can be chosen freely. In this structure, the outputs are partitioned into controlled outputs $\boldsymbol{y}_c$ and the inner loop outputs $\boldsymbol{y}_i$, and the latter usually is the derivative of the former. All the gains have the similar definitions in Fig. 4.1 to the LTI system formulation, but they are now functions of parameter $\boldsymbol{p}$.

Likewise, the proposed controller for LPV and QLPV systems in Fig. 4.2 is given by:

$$\boldsymbol{u} = \boldsymbol{K}_u^{-1}(\boldsymbol{K}_a\boldsymbol{e} - \boldsymbol{K}_c\boldsymbol{y}_c - \boldsymbol{K}_i\boldsymbol{y}_i) \tag{4.21}$$

where the parameter $(s, \boldsymbol{p})$ is dropped for clarity. The gains $\boldsymbol{K}_u$, $\boldsymbol{K}_a$, $\boldsymbol{K}_i$ and $\boldsymbol{K}_c$ represented in polynomial form define the controller structure. Similarly, The proposed closed-loop transfer function T_y^r in this controller structure can be expressed as:

$$\boldsymbol{T}_{\boldsymbol{y}}^r = \boldsymbol{G}(\boldsymbol{I} + \boldsymbol{K}_u^{-1}((\boldsymbol{K}_a + \boldsymbol{K}_c)\boldsymbol{G}_c + \boldsymbol{K}_i\boldsymbol{G}_i))^{-1}\boldsymbol{K}_u^{-1}\boldsymbol{K}_a \tag{4.22}$$

where all the gains are unknown.

Similar to the LTI system, the output can be partitioned into controlled outputs and inner-loop outputs. Therefore, the eigenvector matrix $\boldsymbol{Z}_0(s, \boldsymbol{p})$ can also be

partitioned into

$$\boldsymbol{Z}_0(s,\boldsymbol{p}) = \begin{bmatrix} \boldsymbol{Z}_0^c(s,\boldsymbol{p}) \\ \boldsymbol{Z}_0^i(s,\boldsymbol{p}) \end{bmatrix} \tag{4.23}$$

Therefore, the transfer function $T_{y_c}^r$ can be expressed as

$$\boldsymbol{T}_{\boldsymbol{y}_c}^{\boldsymbol{r}} = \boldsymbol{Z}_0^c(\boldsymbol{K}_u\boldsymbol{P} + (\boldsymbol{K}_a + \boldsymbol{K}_c)\boldsymbol{Z}_0^c + \boldsymbol{K}_i\boldsymbol{Z}_0^i)^{-1}\boldsymbol{K}_a \tag{4.24}$$

For the LTI system, pole placement for the whole closed-loop system can be performed once the number of inputs, states and outputs, n_i, n_s and n_o, meet the Kimura condition (Kimura, 1975), $n_s \leq n_i + n_o - 1$. This method can also be applied to the nonlinear system using LPV and QLPV models shown in Eq. (4.18), while the parameters $\boldsymbol{p}$ should be considered as constant during controller design. The Kimura condition is obviously met for the full state feedback control in Eq. (4.21). Hence, the full eigenstructure assignment is possible for the system in Eq. (4.18) by matching the proposed transfer function $\boldsymbol{T}_{\boldsymbol{y}_c}^{\boldsymbol{r}}$ to a desired transfer function $\boldsymbol{T}_{\boldsymbol{y}}^{\boldsymbol{d}}$, given as a coprime factorization:

$$\boldsymbol{T}_{\boldsymbol{y}}^{\boldsymbol{d}} = \boldsymbol{N}_d\boldsymbol{D}_d^{-1} \tag{4.25}$$

where $\boldsymbol{N}_d$ is a polynomial matrix containing the open-loop zeros and $\boldsymbol{D}_d$ is the desired denominator matrix, defining the closed-loop poles. All the objectives for the closed-loop system are contained in the desired transfer function.

Likewise, the three conditions which are required to be solved for the unknown controller gains can be expressed in Eq. (4.26) to Eq. (4.28) as:

$$\boldsymbol{N}_d(s,\boldsymbol{p}) = \boldsymbol{k}\boldsymbol{Z}_0^c(s,\boldsymbol{p}), \tag{4.26}$$

$$\boldsymbol{D}_d(0,\boldsymbol{p}) = \boldsymbol{N}_d(0,\boldsymbol{p}), \tag{4.27}$$

$$\boldsymbol{D}_d\boldsymbol{N}_d^{-1} = (s\boldsymbol{K}_u\boldsymbol{P} + s\boldsymbol{K}_c\boldsymbol{Z}_0^c + s\boldsymbol{K}_i\boldsymbol{Z}_0^i + \boldsymbol{Z}_0^c)(\boldsymbol{Z}_0^c)^{-1}. \tag{4.28}$$

where $\boldsymbol{k}$ is an unknown diagonal constant matrix and $\boldsymbol{p}$ is the time-varying parameter vector.

Thus, the controller gains can be calculated from Eq. (4.28) if each gain is given in polynomial form as

$$\boldsymbol{K}(s,\boldsymbol{p}) = \boldsymbol{K}_0(\boldsymbol{p}) + \boldsymbol{K}_1(\boldsymbol{p})s + \boldsymbol{K}_2(\boldsymbol{p})s^2 + \cdots + \boldsymbol{K}_q(\boldsymbol{p})s^q \tag{4.29}$$

where q is the degree of the polynomial matrix. Substituting the solved $\boldsymbol{K}_u(s,\boldsymbol{p})$, $\boldsymbol{K}_i(s,\boldsymbol{p})$ and $\boldsymbol{K}_c(s,\boldsymbol{p})$ into Eq. (4.21), the required full state feedback controller is designed for LPV and QLPV systems.

Using the same approach, the corresponding controllers are designed via the LPV and the QLPV models for the Sun-Earth L_2 point formation control system, respectively in the following sections.

4.3 PEA for the Sun-Earth L_2 Point Formation Using the LPV Model

For the DARWIN mission (X-array), formation flying consists of four spacecraft forming a fixed square in the rotating frame **ROF**, where each telescope spacecraft is located at the vertex of the square and the centre of the square is the hub spacecraft, as shown in Fig. 3.26. The procedure to design a relative controller for each telescope spacecraft with respect to the hub is similar. Hence, only the controller design for one telescope is described here.

4.3.1 Controller Design

The system in Eq. (2.42) is already in LPV form, however theoretically, it has to be taken as a linearization of nonlinear system around its equilibrium point. For an equilibrium point $[x_0 \;\; y_0 \;\; z_0 \;\; \dot{x}_0 \;\; \dot{y}_0 \;\; \dot{z}_0]^{\mathrm{T}}$, which satisfies Eq. (2.42), the system error state can be defined as:

$$\begin{bmatrix} \delta x_0 \\ \delta y_0 \\ \delta z_0 \\ \delta \dot{x}_0 \\ \delta \dot{y}_0 \\ \delta \dot{z}_0 \end{bmatrix} = \begin{bmatrix} x - x_0 \\ y - y_0 \\ z - z_0 \\ \dot{x} - \dot{x}_0 \\ \dot{y} - \dot{y}_0 \\ \dot{z} - \dot{z}_0 \end{bmatrix} \tag{4.30}$$

where x, y, z, $\dot{x}$, $\dot{y}$, $\dot{z}$ are the states for relative motion. Noting the LPV model shown in Eq. (2.42) and adding control forces to each axis, the error state satisfies

the following LPV form:

$$\begin{bmatrix} \delta\dot{x} \\ \delta\dot{y} \\ \delta\dot{z} \\ \delta\ddot{x} \\ \delta\ddot{y} \\ \delta\ddot{z} \end{bmatrix} = \begin{bmatrix} 0 & 0 & 0 & 1 & 0 & 0 \\ 0 & 0 & 0 & 0 & 1 & 0 \\ 0 & 0 & 0 & 0 & 0 & 1 \\ a_{11} & a_{12} & a_{13} & 0 & a_{15} & 0 \\ a_{21} & a_{22} & 0 & a_{24} & 0 & 0 \\ a_{31} & 0 & a_{33} & 0 & 0 & 0 \end{bmatrix} \begin{bmatrix} \delta x \\ \delta y \\ \delta z \\ \delta\dot{x} \\ \delta\dot{y} \\ \delta\dot{z} \end{bmatrix} + \begin{bmatrix} 0 & 0 & 0 \\ 0 & 0 & 0 \\ 0 & 0 & 0 \\ 1 & 0 & 0 \\ 0 & 1 & 0 \\ 0 & 0 & 1 \end{bmatrix} \begin{bmatrix} u_x \\ u_y \\ u_z \end{bmatrix} \tag{4.31}$$

$$\begin{bmatrix} y_c \\ y_i \end{bmatrix} = \begin{bmatrix} \delta x \\ \delta y \\ \delta z \\ \delta\dot{x} \\ \delta\dot{y} \\ \delta\dot{z} \end{bmatrix} \tag{4.32}$$

where $a_{11} = \dot{f}^2 + \sigma + 6c_3X_h$, $a_{12} = -3c_3Y_h$, $a_{13} = -3c_3Z_h$, $a_{15} = 2\dot{f}$, $a_{21} = -3c_3Y_h$, $a_{22} = \dot{f}^2 - \sigma - 3c_3X_h$, $a_{24} = -2\dot{f}$, $a_{31} = -3c_3Z_h$, $a_{33} = -\sigma - 3c_3X_h$, where all the parameters are from Eq. (2.42); u_x, u_y and u_z are the controller inputs; and y_c and y_i are the controlled outputs and other measured outputs, respectively. For convenience in analysis, the state equations can be rewritten as:

$$\begin{aligned} \dot{\boldsymbol{x}} &= \begin{bmatrix} \boldsymbol{r} \\ \dot{\boldsymbol{r}} \end{bmatrix} = \boldsymbol{A}(\boldsymbol{r}_h)\boldsymbol{x} + \boldsymbol{B}\boldsymbol{u} \\ \boldsymbol{y} &= \begin{bmatrix} \boldsymbol{y}_c \\ \boldsymbol{y}_i \end{bmatrix} = \begin{bmatrix} \boldsymbol{r} \\ \dot{\boldsymbol{r}} \end{bmatrix} \end{aligned} \tag{4.33}$$

For this LPV system, the time-varying parameter $\boldsymbol{p}$ is the position vector $\boldsymbol{r}_h$ of the hub in the **ROF** frame. Therefore, the matching conditions in Eq. (4.26) ~ Eq. (4.28) for LPV and QLPV systems can be modified to give:

$$\boldsymbol{N}_d(s, \boldsymbol{r}_h) = \boldsymbol{Z}_0^c(s, \boldsymbol{r}_h) \tag{4.34}$$

$$\boldsymbol{D}_d(0, \boldsymbol{r}_h) = \boldsymbol{Z}_0^c(0, \boldsymbol{r}_h) \tag{4.35}$$

$$\boldsymbol{D}_d(s, \boldsymbol{r}_h) = s\boldsymbol{K}_u(s, \boldsymbol{r}_h)\boldsymbol{P}(s, \boldsymbol{r}_h) + s\boldsymbol{K}_c(s, \boldsymbol{r}_h)\boldsymbol{Z}_0(s, \boldsymbol{r}_h) + s\boldsymbol{K}_i(s, \boldsymbol{r}_h)\boldsymbol{Z}_0^i(s, \boldsymbol{r}_h) + \boldsymbol{Z}_0^c(s, \boldsymbol{r}_h) \tag{4.36}$$

where the polynomial matrixes $\boldsymbol{D}_d(s, \boldsymbol{r}_h)$ and $\boldsymbol{N}_d(s, \boldsymbol{r}_h)$ represent the desired closed-loop transfer function. Likewise, Eq. (4.36) can be rewritten as:

$$\left[\begin{array}{cccc} \boldsymbol{K}_u(s, \boldsymbol{r}_h) & \boldsymbol{K}_c(s, \boldsymbol{r}_h) & \boldsymbol{K}_i(s, \boldsymbol{r}_h) & \boldsymbol{I} \end{array} \right] \left[\begin{array}{c} \boldsymbol{P}(s, \boldsymbol{r}_h)(\boldsymbol{Z}_0^c(s, \boldsymbol{r}_h))^{-1} \\ \boldsymbol{Z}_0^c(s, \boldsymbol{r}_h)(\boldsymbol{Z}_0^c(s))^{-1} \\ \boldsymbol{Z}_0^i(s, \boldsymbol{r}_h)(\boldsymbol{Z}_{0,\boldsymbol{r}_h}^c(s))^{-1} \\ \frac{1}{s}(\boldsymbol{Z}_0^c(s, \boldsymbol{r}_h) - \boldsymbol{D}_d(s, \boldsymbol{r}_h)) \end{array} \right] = 0 \tag{4.37}$$

Using this equation, the controller gains can be calculated by computing the left null space. For SISO systems, the computation and expression of controller are relative simple, but for MIMO systems, they can become complex to solve, especially when the order of the system is larger than 4^{th} order. The equations for formation control in Eq. (4.33) is a three-axis coupled MIMO system. To produce a controller which can decouple the three axes control of the closed-loop system, the desired numerator matrix and desired denominator matrix in Eq. (4.25) can be chosen as:

$$\boldsymbol{N}_d(s, \boldsymbol{r}_h) = \left[\begin{array}{ccc} N_x^d(s, \boldsymbol{r}_h) & 0 & 0 \\ 0 & N_y^d(s, \boldsymbol{r}_h) & 0 \\ 0 & 0 & N_z^d(s, \boldsymbol{r}_h) \end{array} \right] \tag{4.38}$$

$$\boldsymbol{D}_d(s, \boldsymbol{r}_h) = \left[\begin{array}{ccc} D_x^d(s, \boldsymbol{r}_h) & 0 & 0 \\ 0 & D_y^d(s, \boldsymbol{r}_h) & 0 \\ 0 & 0 & D_z^d(s, \boldsymbol{r}_h) \end{array} \right] \tag{4.39}$$

where the control performance objective is set for each closed-loop channel. For a static controller gain solution for X-axis control in Eq. (4.33), the system is third-order (that is, a second-order plant and a first-order pure integrator). Hence, the desired closed-loop transfer function can be described by a third-order characteristic polynomial in the form:

$$T_x^d(s, \boldsymbol{r}_h) = N_x^d(s, \boldsymbol{r}_h)/D_x^d(s) = Z_{x0}^c(s, \boldsymbol{r}_h)/(d_{x0} + d_{x1}s + d_{x2}s^2 + s^3) \tag{4.40}$$

where the coefficients of the desired denominator d_{x0}, d_{x1} and d_{x2} are defined by the desired pole positions of the closed-loop system. Similarly, the desired closed-loop transfer function for the other two axes are given by:

$$T_y^d(s, \boldsymbol{r}_h) = N_y^d(s, \boldsymbol{r}_h)/D_y^d(s) = Z_{y0}^c(s, \boldsymbol{r}_h)/(d_{y0} + d_{y1}s + d_{y2}s^2 + s^3) \tag{4.41}$$

$$T_z^d(s, \boldsymbol{r}_h) = N_z^d(s, \boldsymbol{r}_h)/D_z^d(s) = Z_{z0}^c(s, \boldsymbol{r}_h)/(d_{z0} + d_{z1}s + d_{z2}s^2 + s^3) \tag{4.42}$$

Using the PEA method, the eigenvector space $\boldsymbol{Z}_0(s, \boldsymbol{r}_h)$ and its associated controllability space $\boldsymbol{P}(s, \boldsymbol{r}_h)$ are given by:

$$\left[\begin{array}{cc} \boldsymbol{A}(\boldsymbol{r}_h) - s\boldsymbol{I} & \boldsymbol{B} \end{array} \right] \left[\begin{array}{c} \boldsymbol{Z}_0(s, \boldsymbol{r}_h) \\ \boldsymbol{P}(s, \boldsymbol{r}_h) \end{array} \right] = 0 \tag{4.43}$$

Theoretically, more than one solution exists for Eq. (4.43). However, by considering the number of eigenvalues for the state matrix of each axis dynamics and by considering the PEA solution for the LTI system, $\boldsymbol{Z}_0(s)$ and $\boldsymbol{P}(s)$ can be chosen to be the minimum order-polynomial as:

$$\boldsymbol{Z}_0(s) = \left[\begin{array}{c} \boldsymbol{Z}_0^c(s, \boldsymbol{r}_h) \\ \boldsymbol{Z}_0^i(s, \boldsymbol{r}_h) \end{array} \right] = \left[\begin{array}{c} Z_{x0}^c(s, \boldsymbol{r}_h) \\ Z_{y0}^c(s, \boldsymbol{r}_h) \\ Z_{z0}^c(s, \boldsymbol{r}_h) \\ Z_{x0}^c(s, \boldsymbol{r}_h) \\ Z_{y0}^i(s, \boldsymbol{r}_h) \\ Z_{z0}^i(s, \boldsymbol{r}_h) \end{array} \right] = \left[\begin{array}{c} z_{x0}^c(\boldsymbol{r}_h) + z_{x1}^c(\boldsymbol{r}_h)s \\ z_{y0}^c(\boldsymbol{r}_h) + z_{y1}^c(\boldsymbol{r}_h)s \\ z_{z0}^c(\boldsymbol{r}_h) + z_{z1}^c(\boldsymbol{r}_h)s \\ z_{x0}^i(\boldsymbol{r}_h) + z_{x1}^i(\boldsymbol{r}_h)s \\ z_{y0}^i(\boldsymbol{r}_h) + z_{y1}^i(\boldsymbol{r}_h)s \\ z_{z0}^i(\boldsymbol{r}_h) + z_{z1}^i(\boldsymbol{r}_h)s \end{array} \right] \tag{4.44}$$

$$\boldsymbol{P}(s) = \left[\begin{array}{c} P_x(s, \boldsymbol{r}_h) \\ P_y(s, \boldsymbol{r}_h) \\ P_z(s, \boldsymbol{r}_h) \end{array} \right] = \left[\begin{array}{c} p_{x0}(r_h) + p_{x1}(\boldsymbol{r}_h)s + p_{x2}(\boldsymbol{r}_h)s^2 \\ p_{y0}(\boldsymbol{r}_h) + p_{y1}(\boldsymbol{r}_h)s + p_{y2}(\boldsymbol{r}_h)s^2 \\ p_{z0}(\boldsymbol{r}_h) + p_{z1}(\boldsymbol{r}_h)s + p_{z2}(\boldsymbol{r}_h)s^2 \end{array} \right] \tag{4.45}$$

which are the bases for the eigenvector space and its associated controllability space, respectively. Therefore, the other solutions in Eq. (4.43) can be constructed by a linear combination of the bases (in the sense of polynomial addition). Regarding the condition in Eq. (4.35), one has:

$$\begin{aligned} z_{x0}^c(\boldsymbol{r}_h) &= d_{x0} \\ z_{y0}^c(\boldsymbol{r}_h) &= d_{y0} \\ z_{z0}^c(\boldsymbol{r}_h) &= d_{z0} \end{aligned} \tag{4.46}$$

Substituting Eq. (4.44) into Eq. (4.43), $\boldsymbol{Z}_0(s)$ and $\boldsymbol{P}(s)$ can be evaluated as:

$$\boldsymbol{Z}_0(s) = \left[\begin{array}{c} \boldsymbol{Z}_0^c(s, \boldsymbol{r}_h) \\ \boldsymbol{Z}_0^i(s, \boldsymbol{r}_h) \end{array} \right] = \left[\begin{array}{c} d_{x0} \\ d_{y0} \\ d_{z0} \\ d_{x0}s \\ d_{y0}s \\ d_{z0}s \end{array} \right] \tag{4.47}$$

$$\boldsymbol{P}(s) = \begin{bmatrix} P_x(s, \boldsymbol{r}_h) \\ P_y(s, \boldsymbol{r}_h) \\ P_z(s, \boldsymbol{r}_h) \end{bmatrix} = \begin{bmatrix} -a_{11}d_{x0} - a_{12}d_{y0} - a_{13}d_{z0} - a_{15}d_{y0}s + d_{x0}s^2 \\ -a_{21}d_{x0} - a_{22}d_{y0} - a_{24}d_{x0}s + d_{y0}s^2 \\ -a_{31}d_{x0} - a_{33}d_{z0} + d_{z0}s^2 \end{bmatrix} \tag{4.48}$$

Hence, using $\boldsymbol{Z}_0(s)$ and $\boldsymbol{P}(s)$ in Eq. (4.47) and Eq. (4.48), the controller gains can be calculated using the condition in Eq. (4.37). In order to decouple the MIMO system, this condition can be partitioned into three parts:

$$\begin{bmatrix} K_{ux}(s, \boldsymbol{r}_h) & K_{ux}(s, \boldsymbol{r}_h) & K_{ux}(s, \boldsymbol{r}_h) & 1 \end{bmatrix} \begin{bmatrix} P_x(s, \boldsymbol{r}_h)(Z^c_{x0}(s))^{-1} \\ Z^c_{x0}(s, \boldsymbol{r}_h)(Z^c_{x0}(s))^{-1} \\ Z^i_{x0}(s, \boldsymbol{r}_h)(Z^c_{x0}(s))^{-1} \\ \frac{1}{s}(Z^c_{x0}(s, \boldsymbol{r}_h) - D^d_x(s, \boldsymbol{r}_h)) \end{bmatrix} = 0 \tag{4.49}$$

$$\begin{bmatrix} K_{uy}(s, \boldsymbol{r}_h) & K_{uy}(s, \boldsymbol{r}_h) & K_{uy}(s, \boldsymbol{r}_h) & 1 \end{bmatrix} \begin{bmatrix} P_y(s, \boldsymbol{r}_h)(Z^c_{y0}(s))^{-1} \\ Z^c_{y0}(s, \boldsymbol{r}_h)(Z^c_{y0}(s))^{-1} \\ Z^i_{y0}(s, \boldsymbol{r}_h)(Z^c_{y0}(s))^{-1} \\ \frac{1}{s}(Z^c_{y0}(s, \boldsymbol{r}_h) - D^d_y(s, \boldsymbol{r}_h)) \end{bmatrix} = 0 \tag{4.50}$$

$$\begin{bmatrix} K_{uz}(s, \boldsymbol{r}_h) & K_{uz}(s, \boldsymbol{r}_h) & K_{uz}(s, \boldsymbol{r}_h) & 1 \end{bmatrix} \begin{bmatrix} P_z(s, \boldsymbol{r}_h)(Z^c_{z0}(s))^{-1} \\ Z^c_{z0}(s, \boldsymbol{r}_h)(Z^c_{z0}(s))^{-1} \\ Z^i_{z0}(s, \boldsymbol{r}_h)(Z^c_{z0}(s))^{-1} \\ \frac{1}{s}(Z^c_{z0}(s, \boldsymbol{r}_h) - D^d_z(s, \boldsymbol{r}_h)) \end{bmatrix} = 0 \tag{4.51}$$

Substituting for $\boldsymbol{Z}_0(s)$ and $\boldsymbol{P}(s)$, the controller gains can be calculated as:

$$\boldsymbol{K}_u(s, \boldsymbol{r}_h) = \begin{bmatrix} K_{ux}(s, \boldsymbol{r}_h) \\ K_{uy}(s, \boldsymbol{r}_h) \\ K_{uz}(s, \boldsymbol{r}_h) \end{bmatrix} = \begin{bmatrix} 1/d_{x0} \\ 1/d_{y0} \\ 1/d_{z0} \end{bmatrix} \tag{4.52}$$

$$\boldsymbol{K}_c(s, \boldsymbol{r}_h) = \begin{bmatrix} K_{cx}(s, \boldsymbol{r}_h) \\ K_{cy}(s, \boldsymbol{r}_h) \\ K_{cz}(s, \boldsymbol{r}_h) \end{bmatrix} = \begin{bmatrix} (a_{13}d_{z0} + a_{11}d_{x0} + a_{12}d_{y0} + d_{x1}d_{x0})/d^2_{x0} \\ (a_{22}d_{y0} + a_{23}d_{z0} + a_{21}d_{x0} + d_{y1}d_{y0})/d^2_{y0} \\ (a_{31}d_{x0} + a_{33}d_{z0} + d_{z1}d_{z0})/d^2_{z0} \end{bmatrix} \tag{4.53}$$

$$\boldsymbol{K}_i(s, \boldsymbol{r}_h) = \begin{bmatrix} K_{ix}(s, \boldsymbol{r}_h) \\ K_{iy}(s, \boldsymbol{r}_h) \\ K_{iz}(s, \boldsymbol{r}_h) \end{bmatrix} = \begin{bmatrix} (a_{15}d_{y0} + d_{x2}d_{x0})/d^2_{x0} \\ (a_{24}d_{x0} + d_{y2}d_{y0})/d^2_{y0} \\ d_{z2}/d_{z0} \end{bmatrix} \tag{4.54}$$

Thus, the controller for an LPV system has been developed using the PEA approach. As shown in Eq. (4.52) ~ Eq. (4.54), the controller gains are functions

of the state matrix entries, which indicates that the PEA approach can realize the gain scheduling for any operating point and guarantee the closed-loop system performance.

However, these gains are only the minimum-order solution for Eq. (4.49) ~ Eq. (4.51). In fact, as mentioned before, it is possible to obtain multiple-solutions during the process using the condition in Eq. (4.37). Choosing the design of the X-axis as an example, it shows how to get multiple-solutions of the PEA controller. Noting the X-axis condition in Eq. (4.49), each gain ($\boldsymbol{K}_{ux}(s, \boldsymbol{r}_h)$, $\boldsymbol{K}_{cx}(s, \boldsymbol{r}_h)$, $\boldsymbol{K}_{ix}(s, \boldsymbol{r}_h)$) in the controller can be assumed any specific order polynomial, which satisfies the condition that the order of $\boldsymbol{K}_{ux}(s, \boldsymbol{r}_h)$ should not exceed the order of other polynomial gains $\boldsymbol{K}_{cx}(s, \boldsymbol{r}_h)$ and $\boldsymbol{K}_{ix}(s, \boldsymbol{r}_h)$ to ensure the dynamic controller is proper and thus can be realized. If $\boldsymbol{K}_{ux}(s, \boldsymbol{r}_h)$ is a first-order polynomial, then the characteristic polynomial of the closed-loop system should be a forth-order polynomial. Thus, the denominator of the desired transfer function should be set to forth-order. Noting the vector on the left of Eq. (4.49), the highest order of its components is three, which means there are four constraint equations if one expands and collects the terms in Eq. (4.49) obtained by substituting each gain with its corresponding coefficients. For the four constraint equations, only four unknown coefficients can be solved by these equations. If both $\boldsymbol{K}_{cx}(s, \boldsymbol{r}_h)$ and $\boldsymbol{K}_{ix}(s, \boldsymbol{r}_h)$ are first-order polynomial as well, then the condition of multiple-solution is obtained. Therefore, they can be assumed as constant if only a unique solution of the designed controller is required. This is a simple example to discuss the condition of multiple-solution during the process of solving Eq. (4.49). Furthermore, an optimal solution can be obtained among these solutions if more additional criteria for the closed-loop system, including the performance, decoupling and robustness measures, are taken into account for other transfer functions in Fig. 4.2.

In this section, the PEA approach is used to solve a MIMO system problem. However as an extension to the SISO system design, elements of SISO system design still remained since all the matrices used during the design are vectors, which implies the PEA approach described in this section cannot solve the MIMO system problem efficiently in general. A more generic PEA approach for MIMO system will be developed in the next section.

4.3.2 Simulation Results and Analysis

Using the same formation scenario described in Section 3.4, a simulation is carried out to validate the controller developed using the PEA approach. The initial conditions are the same as that for the LQR controller examined in Section 3.4.1.

The desired characteristic polynomial for the closed-loop system of each axis is selected as the combination of a second-order polynomial and an additional first-order polynomial, as:

$$D^d(s) = (s + p_t)(s^2 + 2\xi\omega_n s + \omega_n^2) \tag{4.55}$$

where ξ is the damping ratio, set at 0.8, ω_n is the natural frequency, for our system set at 2×10^{-5} rad/s, and p_t is the third pole, set at 8×10^{-5} rad/s. This controller has the same settling time as that of the LQR controller designed in Chapter 3.

The states for the controller are estimated by the Kalman Filter designed in Section 3.3. In order to validate the performance of the controller, the nonlinear relative motion model in Eq. (2.18) is used for the simulation.

Figure 4.3 ~ Figure 4.10 show the simulation results for the upper left telescope controlled by the LPV PEA controller.

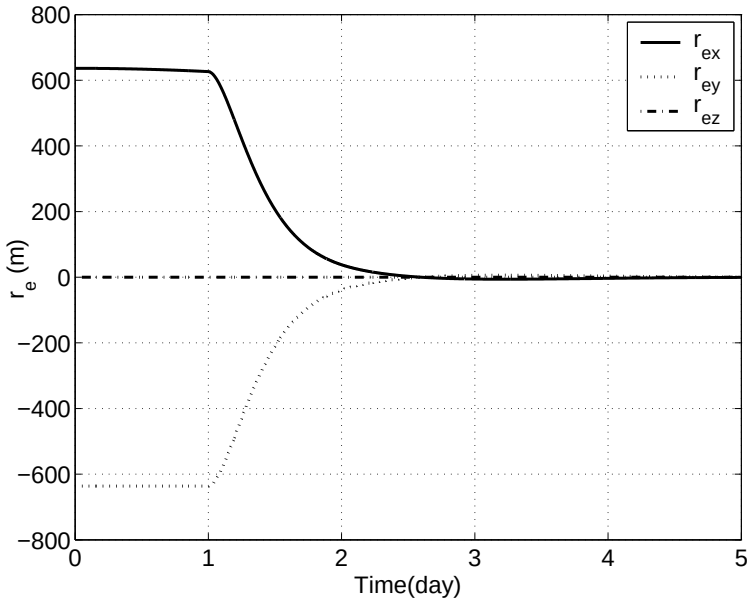

Figure 4.3: The Relative Position Errors for the Upper Left Telescope Controlled by the LPV PEA over the First 5 days

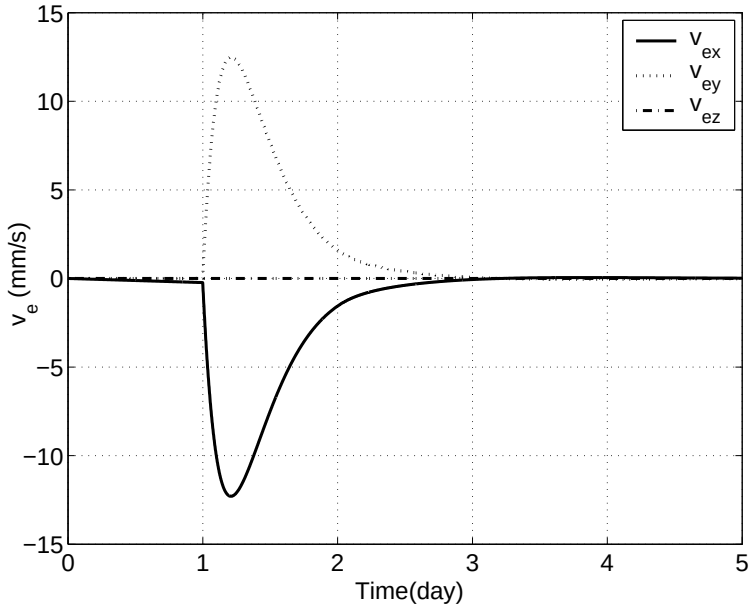

Figure 4.4: The Relative Velocity Errors for the Upper Left Telescope Controlled by the LPV PEA over the First 5 days

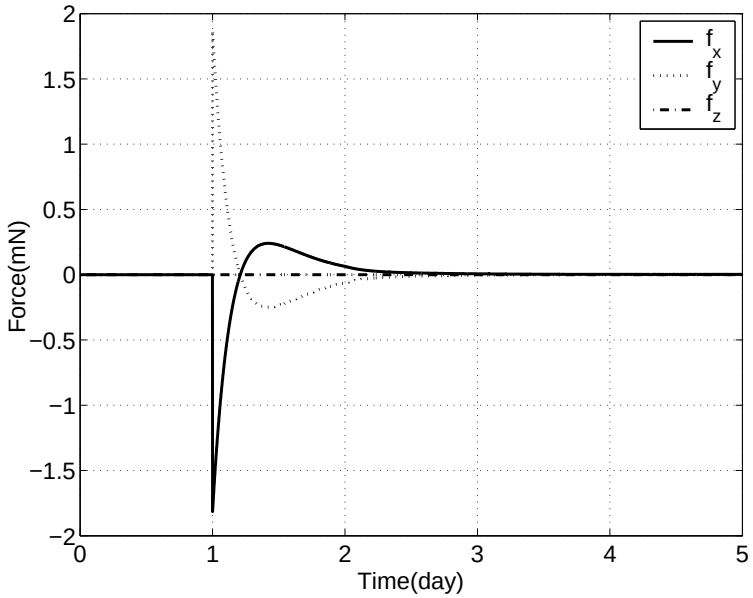

Figure 4.5: The Control Forces for the Upper Left Telescope Controlled by the LPV PEA over the First 5 days

Figure 4.3 ~ Figure 4.6 show the simulation results for the first 5 days, which are very similar to those in Fig. 3.29 ~ Fig. 3.32. From Fig. 4.3, the position errors drop down very quickly to near zero in first few days. The maximum velocity is

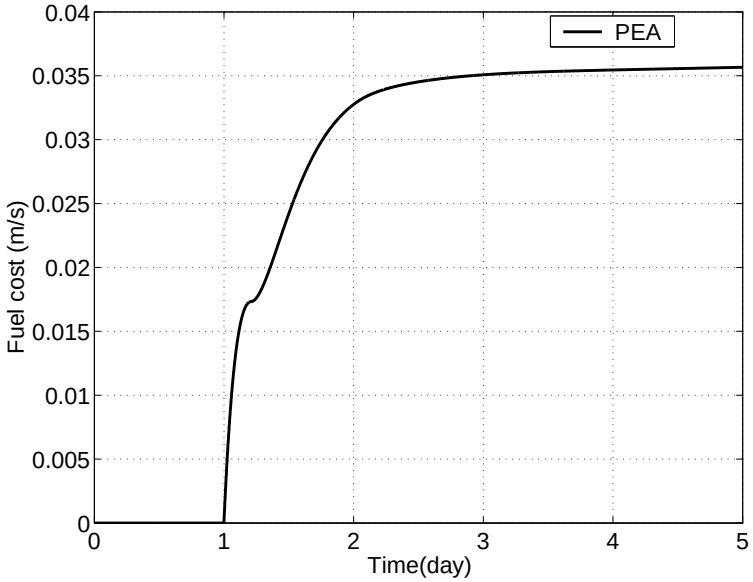

Figure 4.6: The Fuel Cost for the Upper Left Telescope Controlled by the LPV PEA over the First 5 days

12.5 mm/s and 12.3 mm/s for the Y-axis and the X-axis, respectively. The maximum force is 1.8 mN at the beginning of manoeuvre. The fuel cost is 0.036 m/s, which is less than that of the LQR design (0.040 m/s). The system controlled by the PEA controller has identical settling time as that of the the LQR controller over the first 5 days.

However, the position keeping performances of two controllers are different as we can see from Fig. 4.7 and Fig. 3.41. The steady state error of the LPV PEA system is 0.3 mm, which is better than that of the LQR controller (1 mm). This confirms the assumption that the more complex LPV model represents the real system more accurately. The velocity (less than 0.1 $\mu m/s$) and the force (2.8 μN in X-axis) and the fuel cost (0.082 m/s in total, 0.046 m/s for the position keeping) are similar to those in Fig. 3.42 ~ Fig. 3.44.

The above results indicate that the LPV PEA controller is able to improve the system performance since more precise nominal model for the controller design. The LPV model has less modeling error than the LTI model since the former includes effects of solar radiation pressure, lunar gravity and higher order terms. However, the position error increases around 180 days in Fig. 4.7 due to the remained modeling error between this LPV model and the real system equations used in the simulation. The major part of remained modeling error consists of

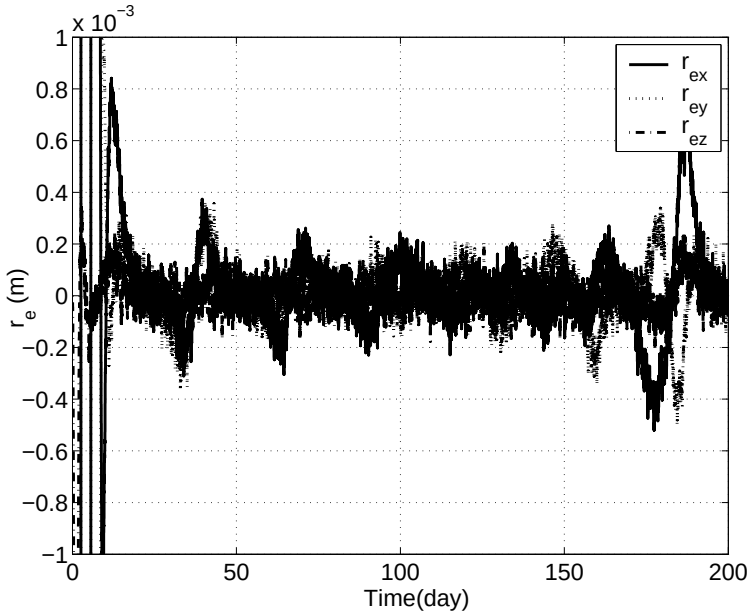

Figure 4.7: The Relative Position Errors for the Upper Left Telescope Controlled by the LPV PEA over 200 days

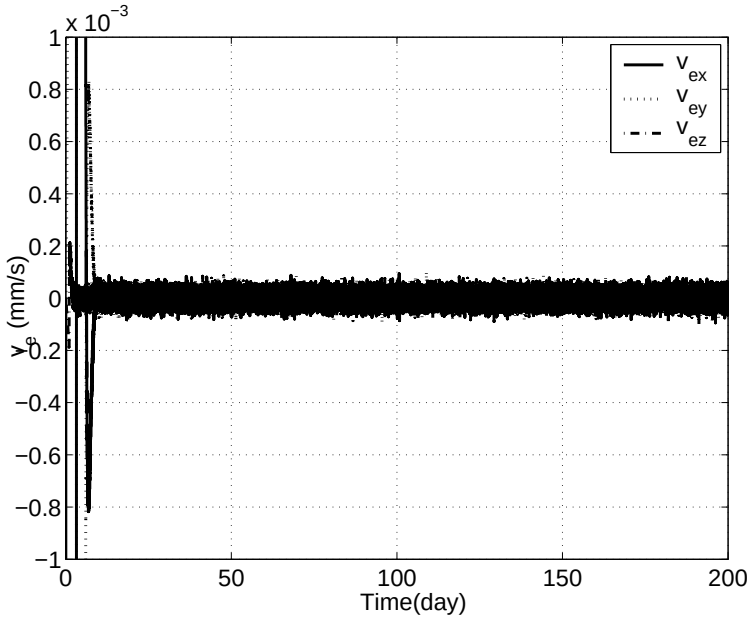

Figure 4.8: The Relative Velocity Errors for the Upper Left Telescope Controlled by the LPV PEA over 200 days

the rapid variation of lunar gravity in the space environment, which has been depicted and discussed in Fig. 3.28 (at a maximum around 180 days). Usually, this kind of modeling error is difficult to include in an LPV model because the

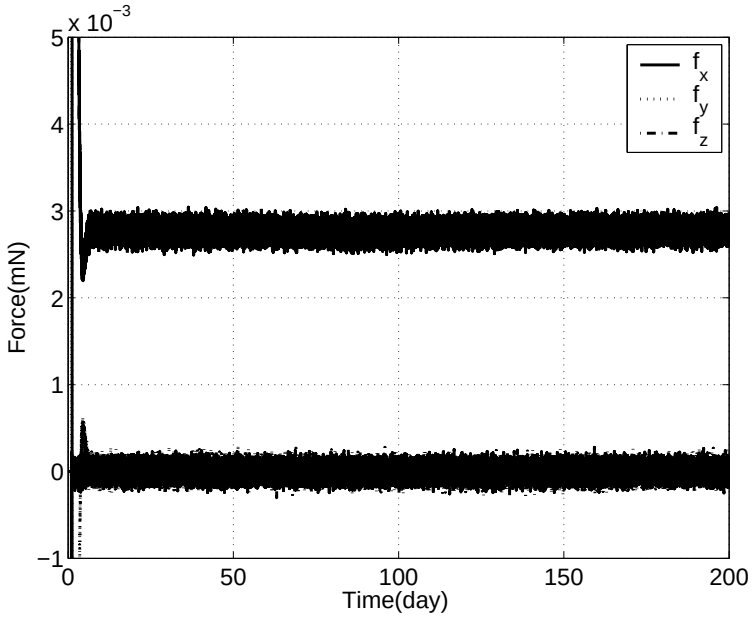

Figure 4.9: The Control Forces for the Upper Left Telescope Controlled by the LPV PEA over 200 days

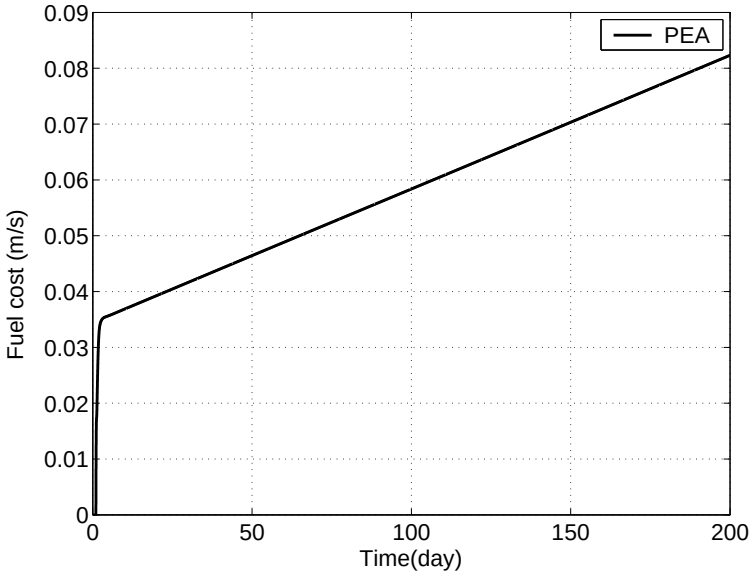

Figure 4.10: The Fuel Cost for the Upper Left Telescope Controlled by the LPV PEA over 200 days

large variation of the unmodelled parameter of the nonlinear system. To solve this problem, we consider using the nonlinear model directly as one efficient method to improve the performance, which is the main focus in the next section.

4.4 PEA for the Sun-Earth L_2 Point Formation Using a QLPV Model

The PEA method has been improved and adapted to use an LPV model for the control of the L_2 point formation. However, to meet the mission's stringent millimeter relative position accuracy requirement, a nonlinear controller is still required to be designed by using the ephemeris model directly, which can improve the control performance to satisfy the more stringent accuracy requirement. The ephemeris model of formation flying has been rewritten as a QLPV form without any approximation in Eq. (2.58) by utilising the Barbashin method, as described in Chapter 2. Based on this QLPV model, a continuous scheduling nonlinear controller is designed using the PEA approach in this section.

4.4.1 Controller Design

Using the same strategy as in the last section Eq. (2.58), which describes a MIMO system with three-axis control, is used to design three controllers for the telescope. The desired numerator matrix and desired denominator matrix in Eq. (4.25) is given by:

$$\boldsymbol{N}_d(s,\boldsymbol{p}) = \begin{bmatrix} N_x^d(s,\boldsymbol{p}) & 0 & 0 \\ 0 & N_y^d(s,\boldsymbol{p}) & 0 \\ 0 & 0 & N_z^d(s,\boldsymbol{p}) \end{bmatrix} \tag{4.56}$$

$$\boldsymbol{D}_d(s,\boldsymbol{p}) = \begin{bmatrix} D_x^d(s,\boldsymbol{p}) & 0 & 0 \\ 0 & D_y^d(s,\boldsymbol{p}) & 0 \\ 0 & 0 & D_z^d(s,\boldsymbol{p}) \end{bmatrix} \tag{4.57}$$

which decouples the MIMO system into three SISO systems and sets the control performance objective for each closed-loop system channel.

For a static controller gain solution for the x-axis control in Eq. (2.58), the system is third-order, that is a second-order plant and a first-order integrator. Hence, the desired closed-loop transfer function can be described with a third-order characteristic polynomial and written as:

$$T_x^d(s,\boldsymbol{p}) = N_x^d(s,\boldsymbol{p})/D_x^d(s) = Z_{x0}^c(s,\boldsymbol{p})/(d_{x0} + d_{x1}s + d_{x2}s^2 + s^3) \tag{4.58}$$

where the coefficients of the desired denominator coefficients d_{x0}, d_{x1} and d_{x2} are defined by the desired poles of the closed-loop system. Similarly, the desired closed-loop transfer functions for the other two axes can be expressed as:

$$T_y^d(s,\boldsymbol{p}) = Z_{y0}^c(s,\boldsymbol{p})/(d_{y0} + d_{y1}s + d_{y2}s^2 + s^3) \tag{4.59}$$

$$T_z^d(s,\boldsymbol{p}) = Z_{z0}^c(s,\boldsymbol{p})/(d_{z0} + d_{z1}s + d_{z2}s^2 + s^3) \tag{4.60}$$

with the coefficients in each equation. Using the PEA approach, the eigenvector space $\boldsymbol{Z}_0(s,\boldsymbol{p})$ and its associated controllability space $\boldsymbol{P}(s,\boldsymbol{p})$ is calculated by Eq. (4.19). By considering the number of eigenvalues for the state matrix of each axis dynamics, $\boldsymbol{Z}_0(s)$ and $\boldsymbol{P}(s)$ can be defined with the minimum order-polynomial solution as:

$$\boldsymbol{Z}_0^c(s) = \begin{bmatrix} z_{x10}^c + z_{x11}^c s & z_{x20}^c & z_{x30}^c \\ z_{y10}^c & z_{y20}^c + z_{y21}^c s & z_{y30}^c \\ z_{z10}^c & z_{z20}^c & z_{z30}^c + z_{z31}^c s \end{bmatrix} \tag{4.61}$$

$$\boldsymbol{Z}_0^i(s) = \begin{bmatrix} z_{x10}^i + z_{x11}^i s & z_{x20}^i & z_{x30}^i \\ z_{y10}^i & z_{y20}^i + z_{y21}^i s & z_{y30}^i \\ z_{z10}^i & z_{z20}^i & z_{z30}^i + z_{z31}^i s \end{bmatrix} \tag{4.62}$$

$$\boldsymbol{P}(s) = \begin{bmatrix} p_{x10} + p_{x11}s + p_{x12}s^2 & p_{x20} + p_{x21}s & p_{x30} + p_{x31}s \\ p_{y10} + p_{y11}s & p_{y20} + p_{y21}s + p_{y22}s^2 & p_{y20} + p_{y21}s \\ p_{z10} + p_{z11}s & p_{z20} + p_{z21}s & p_{z30} + p_{z31}s + p_{z32}s^2 \end{bmatrix} \tag{4.63}$$

which are the bases for the eigenvector space and its associated controllability space, respectively. Regarding the matching conditions in Eq. (4.26) and Eq. (4.27), one has:

$$z_{x10}^c = d_{x0}, \quad z_{y20}^c = d_{y0}, \quad z_{z30}^c = d_{z0} \tag{4.64}$$

Substituting Eq. (4.62) and Eq. (4.63) into Eq. (4.19), $\boldsymbol{Z}_0(s)$ and $\boldsymbol{P}(s)$ are defined as:

$$\boldsymbol{Z}_0^c(s) = \begin{bmatrix} d_{x0} & 0 & 0 \\ 0 & d_{y0} & 0 \\ 0 & 0 & d_{z0} \end{bmatrix} \tag{4.65}$$

$$\boldsymbol{Z}_0^i(s) = \begin{bmatrix} d_{x0}s & 0 & 0 \\ 0 & d_{y0}s & 0 \\ 0 & 0 & d_{z0}s \end{bmatrix} \tag{4.66}$$

$$\boldsymbol{P}(s) = \begin{bmatrix} -a_{41}d_{x0} - a_{44}d_{x0}s + d_{x0}s^2 & -a_{42}d_{y0} - a_{45}d_{y0}s & -a_{43}d_{z0} - a_{46}d_{z0}s \\ -a_{51}d_{x0} - a_{54}d_{x0}s & -a_{52}d_{y0} - a_{55}d_{y0}s + d_{y0}s^2 & -a_{53}d_{z0} - a_{56}d_{z0}s \\ -a_{61}d_{x0} - a_{64}d_{x0}s & -a_{62}d_{y0} - a_{65}d_{y0}s & -a_{63}d_{z0} - a_{66}d_{z0}s + d_{z0}s^2 \end{bmatrix} \tag{4.67}$$

Substituting $\boldsymbol{Z}_0(s)$ and $\boldsymbol{P}(s)$ into the matching condition Eq. (4.28), the gains for the controller can be calculated as:

$$\boldsymbol{K}_u(s) = \begin{bmatrix} 1/d_{x0} & 0 & 0 \\ 0 & 1/d_{y0} & 0 \\ 0 & 0 & 1/d_{z0} \end{bmatrix} \tag{4.68}$$

$$\boldsymbol{K}_c(s) = \begin{bmatrix} (a_{41} + d_{x1})/d_{x0} & a_{42}/d_{x0} & a_{43}/d_{x0} \\ a_{51}/d_{y0} & (a_{52} + d_{y1})/d_{y0} & a_{53}/d_{y0} \\ a_{61}/d_{z0} & a_{62}/d_{z0} & (a_{63} + d_{z1})/d_{z0} \end{bmatrix} \tag{4.69}$$

$$\boldsymbol{K}_i(s) = \begin{bmatrix} (a_{44} + d_{x2})/d_{x0} & a_{45}/d_{x0} & a_{46}/d_{x0} \\ a_{54}/d_{y0} & (a_{55} + d_{y2})/d_{y0} & a_{56}/d_{y0} \\ a_{64}/d_{z0} & a_{65}/d_{z0} & (a_{66} + d_{z2})/d_{z0} \end{bmatrix} \tag{4.70}$$

Thus, the relative position controller designed by the QLPV PEA approach for the MIMO formation system has been developed. Noting Eq. (4.69) and Eq. (4.70), the resulting PEA controller is a function of the system varying parameters and produces a closed-loop system with invariant performance over a wide range of operating conditions.

4.4.2 Simulation Results and Analysis

Using the same formation flying scenario as in Section 3.4, a simulation is carried out to validate the accuracy of the closed-loop system controlled using the QLPV PEA controller.

The desired characteristic polynomial for each axis closed-loop system is selected as the combination of a second-order polynomial and an additional first-order polynomial, given as:

$$D^d(s) = (s + p_t)(s^2 + 2\xi\omega_n s + \omega_n^2) \tag{4.71}$$

where ξ is the damping ratio, set at 0.8, ω_n is the natural frequency, for our system set at 2×10^{-5} rad/s and p_t is the third pole, set at 8×10^{-5} rad/s. These values are the same as those of the LPV PEA controller.

The states for the controller are estimated by the Kalman Filter designed in Section 3.3 and the nonlinear relative motion model in Eq. (2.18) is used for the simulation.

Figure 4.11 ~ Figure 4.18 show the simulation results for the upper left telescope controlled by the QLPV PEA controller.

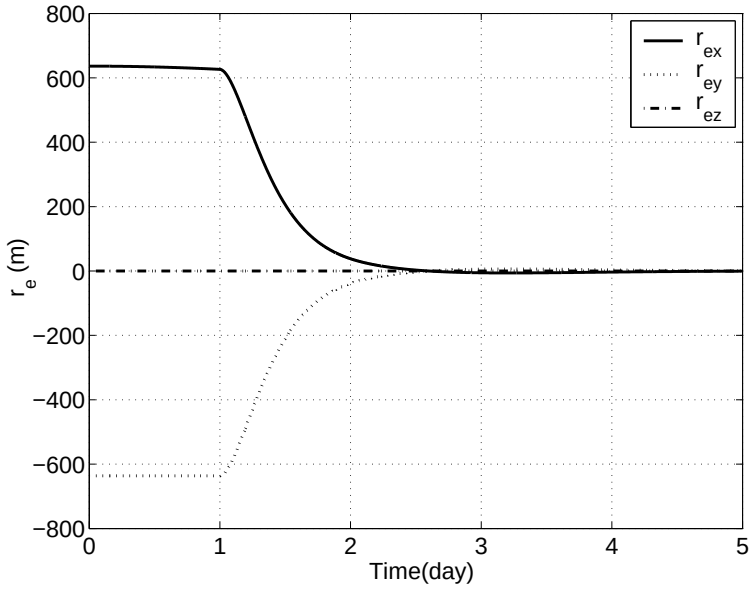

Figure 4.11: The Relative Position Errors for the Upper Left Telescope Controlled by the QLPV PEA over the First 5 days

Figure 4.11 ~ Figure 4.14 illustrates the formation control results for the upper left telescope over the first 5 days, which are almost the same as those in Fig. 4.3 ~ Fig. 4.6. As shown in Fig. 4.11 and 4.12, the relative position and relative velocity errors drop down very quickly to zero in the first 5 days. From Fig. 4.13, the control forces start at 1.8 mN and drive the relative position errors to zero, but quickly reduce to very small levels after 5 days to maintain the relative position requirement, which is the same as that of the LPV PEA and LQR designs. In Fig. 4.14, the fuel cost of the QLPV PEA for the first 5 days initial control is 0.036 m/s, which is identical to that of the LPV PEA controller, and less than that of LQR controller (0.040 m/s).

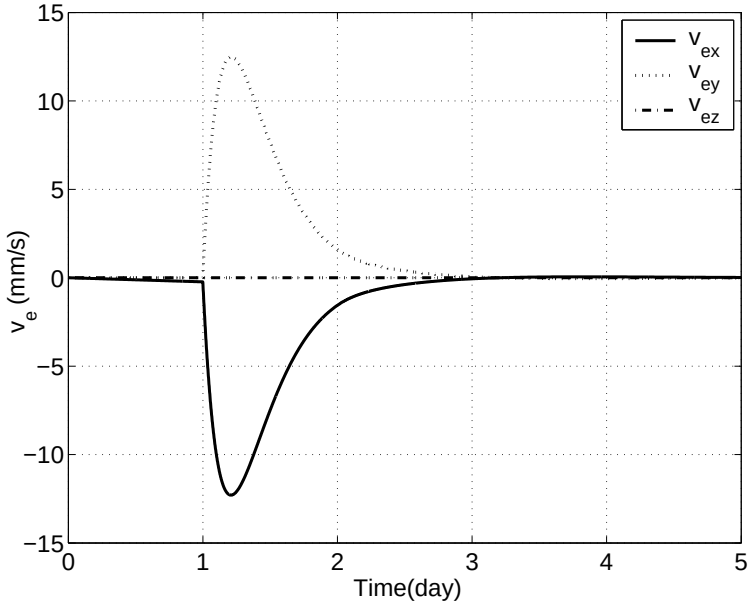

Figure 4.12: The Relative Velocity Errors for the Upper Left Telescope Controlled by the QLPV PEA over the First 5 days

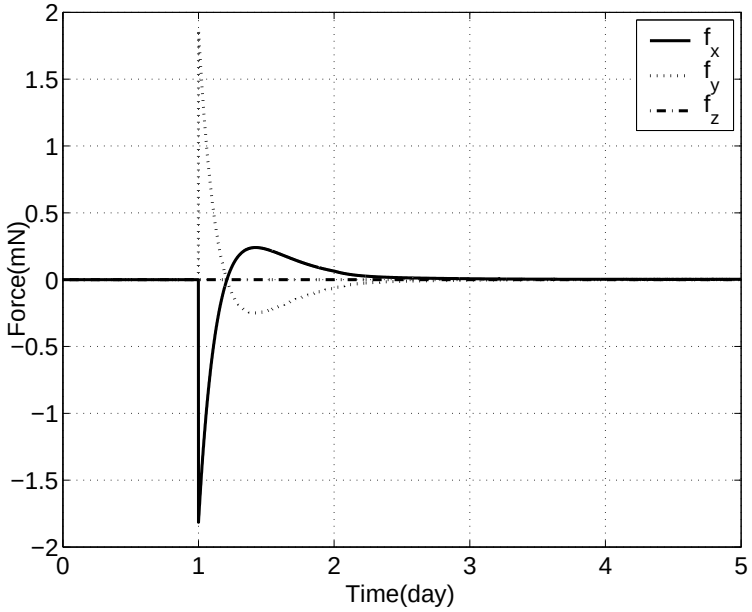

Figure 4.13: The Control Forces for the Upper Left Telescope Controlled by the QLPV PEA over the First 5 days

Figure 4.15~ Figure 4.18 show the formation control results for the upper left telescope over 200 days. From Fig. 4.15, the relative position errors are relatively stable, all around $0.1mm$ during the simulation period, which is better than that

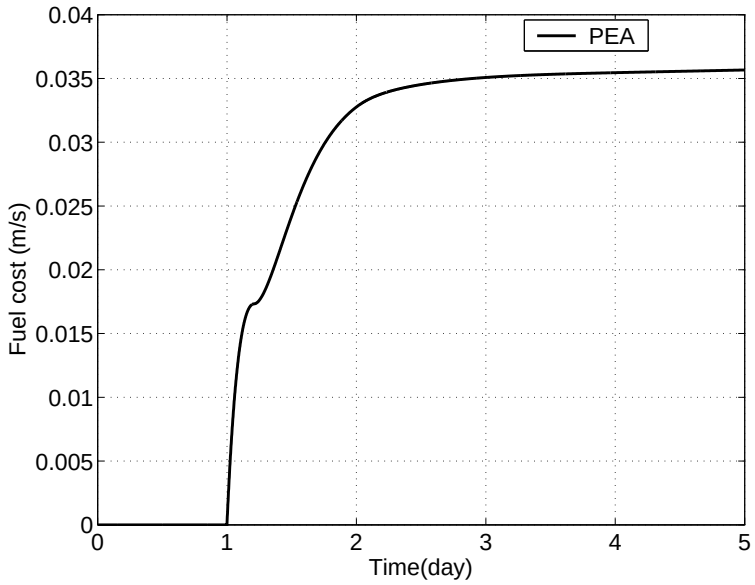

Figure 4.14: The Fuel Cost for the Upper Left Telescope Controlled by the QLPV PEA over the First 5 days

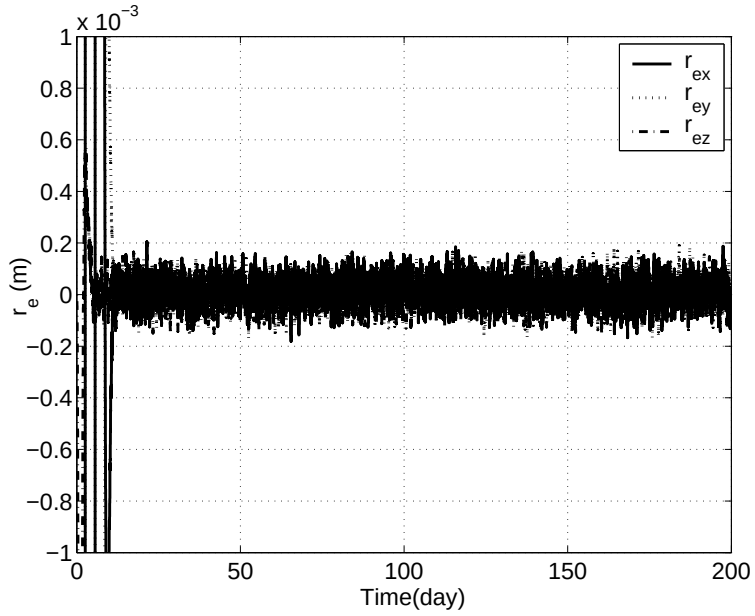

Figure 4.15: The Relative Position Errors for the Upper Left Telescope Controlled by the QLPV PEA over 200 days

of both the LPV PEA (0.3 *mm*) controller and the LQR controller (1 *mm*). The reason for the improvment is that the gains of the QLPV PEA controller vary in the same manner as the nonlinear system, while the gains for the LPV PEA follow the LPV model and the gains of the LQR controller are constant. The relative

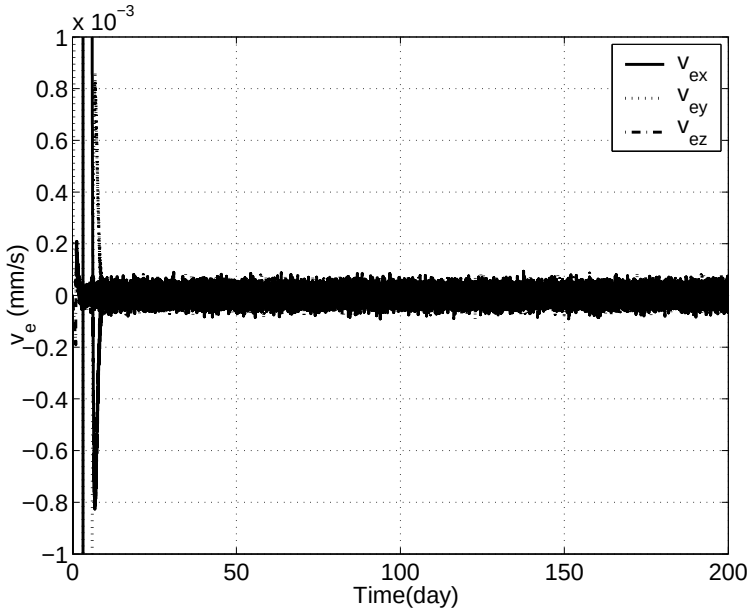

Figure 4.16: The Relative Velocity Errors for the Upper Left Telescope Controlled by the QLPV PEA over 200 days

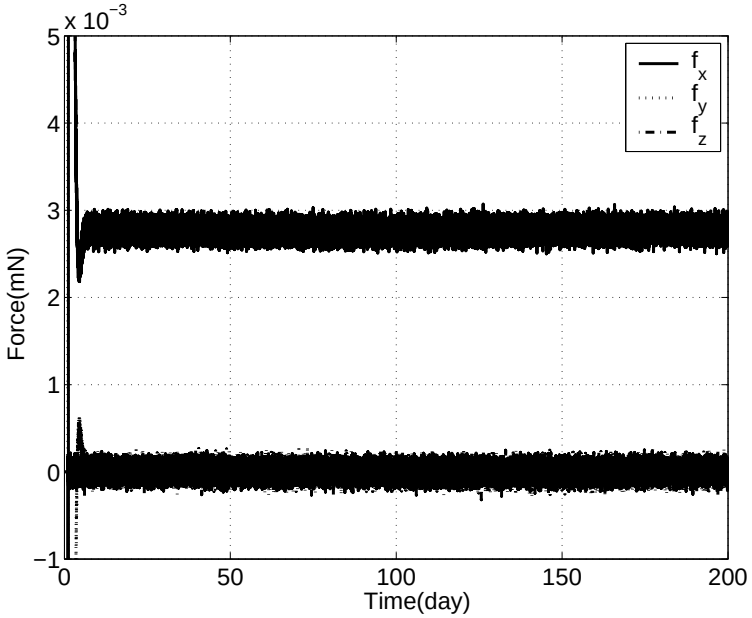

Figure 4.17: The Control Forces for the Upper Left Telescope Controlled by the QLPV PEA over 200 days

velocity errors and the control forces for the QLPV design are shown in Fig. 4.16 and Fig. 4.17 and are similar to those of the LPV PEA design. The fuel cost in Fig. 4.18 is similar, about 0.082 m/s and the fuel cost for position keeping is about

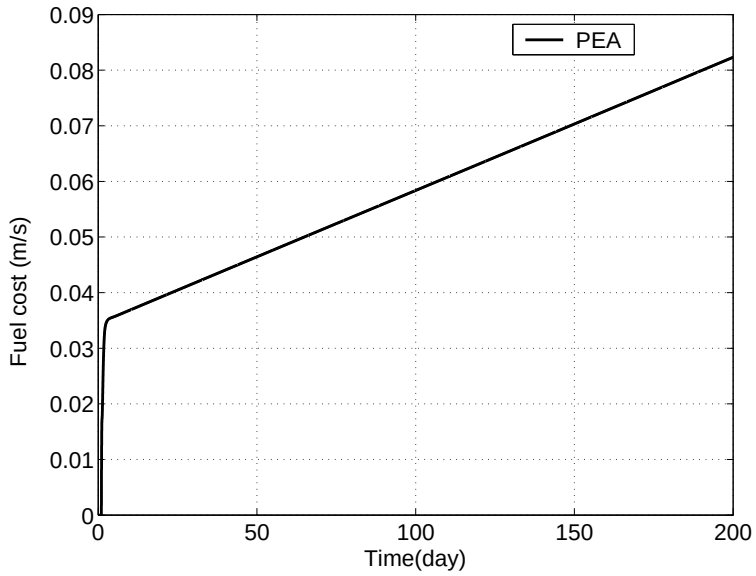

Figure 4.18: The Fuel Cost for the Upper Left Telescope Controlled by the QLPV PEA over 200 days

0.046 m/s (equal to 0.086 m/s per year for a long term mission).

From the analysis of the control results for the LQR , LPV PEA and QLPV PEA controllers, it has been shown that the QLPV PEA controller has the best performance as a result of the controller gains varying more accurately with the nonlinear equation of the system. The QLPV model has less modeling error than the LPV and LTI models since the former is derived directly from the nonlinear equation which includes all the effects of solar radiation pressure, lunar gravity and other nonlinear terms.

For all the simulations up to now in this thesis, the rate limits and actuator saturation of the spacecraft are not considered. However in the real application, both should be taken into account. Therefore, a new control logic will be applied to include these limitations in the next section.

4.5 PEA for Coupling Translational and Rotational Control with Thrusters

In this section, the controllers for relative position and attitude control are designed firstly via each nonlinear dynamic equation. Once the controller design is

accomplished, more realistic dynamic coupling effects are taken into account for the application. As the major actuator for high precision formation flying, continuous low thrust introduces the coupling effect between relative position control and attitude control. Thus, a combined method is presented to consider such coupling effect and obtains a combined controller which can improve the control performance. By considering the limitation of manoeuvre rates and the saturation of actuators, the controller is modified by using cascade-saturation control logic (Wie & Lu, 1995; Wang et al., 2006) to limit manoeuvre rates and actuator outputs.

4.5.1 Rotational Control

The translational controller has been designed in Section 4.4. The following details the design of rotational controller. The nonlinear model of relative rotation motion is described as a QLPV form in Eq. (2.78) using the Barbashin method. With this QLPV model, the relative attitude control model also is a MIMO system with three-axis coupling dynamics, which is similar to that of relative position control. Therefore, using the same strategy of PEA approach, the MIMO system can be decoupled into three SISO systems and the control performance for each closed-loop system can be set separately. As full states feedback control for the system, the desired numerator matrix and desired denominator matrix in Eq. (4.25) can be chosen as the same forms in Eq. (4.56) and Eq. (4.57), and the desired transfer function for each channel is expressed as

$$T^d_{ax}(s,\boldsymbol{p}) = Z^c_{ax0}(s,\boldsymbol{p})/(d_{ax0} + d_{ax1}s + d_{ax2}s^2 + s^3) \tag{4.72}$$

$$T^d_{ay}(s,\boldsymbol{p}) = Z^c_{ay0}(s,\boldsymbol{p})/(d_{ay0} + d_{ay1}s + d_{ay2}s^2 + s^3) \tag{4.73}$$

$$T^d_{az}(s,\boldsymbol{p}) = Z^c_{az0}(s,\boldsymbol{p})/(d_{az0} + d_{az1}s + d_{az2}s^2 + s^3) \tag{4.74}$$

where the coefficients of the desired denominator d_{axi}, d_{ayi} and d_{azi}, $(i = 0, 1, 2.)$, are determined by the desired performance of the closed-loop system. With the techniques of PEA, the relative PEA controller gains can be calculated as

$$\boldsymbol{K}_{au}(s) = \begin{bmatrix} a_{14}/d_{ax0} & a_{15}/d_{ax0} & a_{16}/d_{ax0} \\ a_{24}/d_{ay0} & a_{25}/d_{ay0} & a_{26}/d_{ay0} \\ a_{34}/d_{az0} & a_{35}/d_{az0} & a_{36}/d_{az0} \end{bmatrix} \tag{4.75}$$

$$\boldsymbol{K}_{ac}(s) = \begin{bmatrix} ac_{11} & ac_{12} & ac_{13} \\ ac_{21} & ac_{22} & ac_{23} \\ ac_{31} & ac_{32} & ac_{33} \end{bmatrix} \tag{4.76}$$

where $ac_{11} = (d_{ax1} + a_{11}d_{ax2} + a_{11}^2 + a_{31}a_{13} + a_{21}a_{12})/d_{ax0}$

$ac_{12} = (a_{12}d_{ax2} + a_{32}a_{13} + a_{12}a_{11} + a_{22}a_{12})/d_{ax0}$

$ac_{13} = (a_{13}d_{ax2} + a_{33}a_{13} + a_{13}a_{11} + a_{23}a_{12})/d_{ax0}$

$ac_{21} = (a_{21}d_{ay2} + a_{21}a_{22} + a_{11}a_{21} + a_{31}a_{23})/d_{ay0}$

$ac_{22} = (d_{ay1} + a_{22}d_{ay2} + a_{22}^2 + a_{12}a_{21} + a_{32}a_{23})/d_{ay0}$

$ac_{23} = (a_{23}d_{ay2} + a_{33}a_{23} + a_{23}a_{22} + a_{13}a_{21})/d_{ay0}$

$ac_{31} = (a_{31}d_{az2} + a_{11}a_{31} + a_{21}a_{32} + a_{31}a_{33})/d_{az0}$

$ac_{32} = (a_{32}d_{az2} + a_{32}a_{33} + a_{22}a_{32} + a_{12}a_{31})/d_{az0}$

$ac_{33} = (d_{az1} + a_{33}d_{az2} + a_{33}^2 + a_{23}a_{32} + a_{13}a_{31})/d_{az0}$.

$$\boldsymbol{K}_{ai}(s) = \begin{bmatrix} ai_{11} & ai_{12} & ai_{13} \\ ai_{21} & ai_{22} & ai_{23} \\ ai_{31} & ai_{32} & ai_{33} \end{bmatrix} \tag{4.77}$$

where $ai_{11} = (a_{12}a_{24} + a_{14}d_{ax2} + a_{34}a_{13} + a_{14}a_{11} + a_{64}a_{16} + a_{15}a_{54} + a_{14}a_{44})/d_{ax0}$

$ai_{12} = (a_{65}a_{16} + a_{15}d_{ax2} + a_{13}a_{35} + a_{15}a_{55} + a_{25}a_{12} + a_{15}a_{11} + a_{14}a_{45})/d_{ax0}$

$ai_{13} = (a_{36}a_{13} + a_{16}d_{ax2} + a_{15}a_{56} + a_{16}a_{66} + a_{26}a_{12} + a_{16}a_{11} + a_{46}a_{14})/d_{ax0}$

$ai_{21} = (a_{34}a_{23} + a_{24}d_{ay2} + a_{24}a_{22} + a_{64}a_{26} + a_{14}a_{21} + a_{24}a_{44} + a_{15}a_{54})/d_{ay0}$

$ai_{22} = (a_{45}a_{24} + a_{25}d_{ay2} + a_{23}a_{35} + a_{25}a_{55} + a_{25}a_{22} + a_{26}a_{65} + a_{15}a_{21})/d_{ay0}$

$ai_{23} = (a_{26}a_{22} + a_{26}d_{ay2} + a_{24}a_{46} + a_{26}a_{66} + a_{36}a_{23} + a_{21}a_{16} + a_{56}a_{25})/d_{ay0}$

$ai_{31} = (a_{32}a_{24} + a_{34}d_{az2} + a_{64}a_{36} + a_{35}a_{54} + a_{34}a_{33} + a_{14}a_{31} + a_{34}a_{44})/d_{az0}$

$ai_{32} = (a_{35}a_{33} + a_{35}d_{az2} + a_{35}a_{55} + a_{36}a_{65} + a_{32}a_{25} + a_{15}a_{31} + a_{34}a_{45})/d_{az0}$

$ai_{33} = (a_{26}a_{32} + a_{36}d_{az2} + a_{31}a_{16} + a_{34}a_{46} + a_{36}a_{33} + a_{56}a_{35} + a_{36}a_{66})/d_{az0}$.

Thus, the PEA controller for relative attitude control is designed for the formation flying.

The controller gains shown in Eq. (4.69) and Eq. (4.70) for relative position control and in Eq. (4.76) and Eq. (4.78) for relative attitude control are the functions

of the state matrix entries, which indicates that the PEA approach can realize the gain scheduling with the operating point and ensure the closed-loop system performance as well.

4.5.2 Combined Controller

Traditionally, the models for spacecraft control systems neglect the coupling effect between translational and rotational motion and design the relative position and attitude control separately. However, for high precision missions, particularly for interferometry formation flying, continuous low thrust is required to achieve millimeter, even sub-millimeter accuracy for translation control and arc-second accuracy for rotation control. For such missions, the coupling between position control and attitude control must be considered to attain the required precise performance. For systems without reaction wheels, the control force for relative position control and the control torque for relative attitude control are both realized by using thrusters. The relationship between the controller outputs (force and torque) and the thruster output are expressed as (Luquette, 2006):

$$\boldsymbol{U}_b = \begin{bmatrix} \boldsymbol{m}_t \boldsymbol{C}_{bI}(\boldsymbol{q}) \boldsymbol{u}_t \\ \boldsymbol{J}_t \boldsymbol{\tau}_t \end{bmatrix} = \boldsymbol{S}\boldsymbol{F}, \tag{4.78}$$

where $\boldsymbol{U}_b$ is the combined controller outputs in the telescope body frame **RBF**, $\boldsymbol{m}_t$ and $\boldsymbol{J}_t$ are the mass and inertia matrices of telescope respectively, $\boldsymbol{C}_{bI}(\boldsymbol{q})$ is the rotation matrix from the inertial frame **IHE** to the body frame **RBF**, $\boldsymbol{u}_t$ and $\boldsymbol{\tau}_t$ are the force and torque for translation and rotation control respectively, $\boldsymbol{S}$ is the control sensitivity matrix related to the position of the thruster and $\boldsymbol{F} = [\ f_1,\ \ f_2,\ \ \cdots,\ \ f_n\ ]^{\mathrm{T}}$, is the thruster output. With proper placement of the thrusters , the thruster commands can be computed by the pseudo inverse of control sensitively matrix $\boldsymbol{S}$ (Luquette, 2006), given by:

$$\boldsymbol{F} = \boldsymbol{S}^{\mathrm{T}}(\boldsymbol{S}\boldsymbol{S}^{\mathrm{T}})^{-1}\boldsymbol{U}_b. \tag{4.79}$$

In addition to this equation, a thruster biasing method (Luquette, 2006) can be applied to guarantee $\boldsymbol{F} \geq 0$ since the thruster can only produce positive thrust and not negative.

Using this approach, the thrusters can generate the desired force and torque for both positional and rotational control systems.

4.5.3 Rate and Actuator Limitation

For the controller design, the translation and rotation manoeuvre rates cannot exceed certain values in order to satisfy the mission requirements, and the actuator output will also be limited by physical constraints on the thrusters. Therefore, the controller should limit its outputs. In order to take these limits into account a multi-layer cascade-saturation control logic for the controller can be used (Wie & Lu, 1995; Wang et al., 2006). Using this control logic, the limitation of different states (velocity, acceleration, and so on) can be described clearly.

A two-layer cascade-saturation control logic to define the actuator limits can be expressed as:

$$\boldsymbol{U} = \boldsymbol{Q}_2 \underset{n}{sat}[\boldsymbol{P}_2\dot{\boldsymbol{X}} + \boldsymbol{Q}_1 sat(\boldsymbol{P}_1\boldsymbol{X})] \tag{4.80}$$

where $\boldsymbol{P}_i$ and $\boldsymbol{Q}_i$ are the controller gain matrices. $\underset{n}{sat}(\boldsymbol{x})$ is the normalized saturation function of an n-dimensional vector $\boldsymbol{x}$ and is defined as:

$$\underset{n}{sat}(\boldsymbol{x}) = \begin{cases} \boldsymbol{x} & \sigma(\boldsymbol{x}) < 1 \\ \boldsymbol{x}/\sigma(\boldsymbol{x}) & \sigma(\boldsymbol{x}) \geq 1 \end{cases} \tag{4.81}$$

where $\sigma(\boldsymbol{x})$ is a positive scalar function of $\boldsymbol{x}$ that characterizes the size of the vector $\boldsymbol{x}$. Usually a vector norm is used to characterize its size, that is $\sigma(\boldsymbol{x}) = \|\boldsymbol{x}\|_2 = \sqrt{\boldsymbol{x}^T\boldsymbol{x}}$ or $\sigma(\boldsymbol{x}) = \|\boldsymbol{x}\|_\infty = \max_i |x_i|$.

To ensure that the rate and actuator are within their constraint limits, the amplitude of the error states in the controller should be limited during the controller output construction. Using this strategy, the controller needs to feed back scaled error states once they become too large, which keeps the manoeuvre rates and the actuator inputs within limits. In detail, the saturated position error $sat(\delta\boldsymbol{x}_t)$ is defined as:

$$sat(\delta\boldsymbol{x}_t) = \begin{cases} \delta\boldsymbol{x}_t & \|\delta\boldsymbol{x}_t\|_\infty / \delta x_{t\max} < 1 \\ \delta\boldsymbol{x}_t \delta x_{t\max} / \|\delta\boldsymbol{x}_t\|_\infty & \|\delta\boldsymbol{x}_t\|_\infty / \delta x_{t\max} \geq 1 \end{cases} \tag{4.82}$$

where $\delta x_{t\max}$ is the maximum permitted translation error for the controller, determined by the limit properties of the thruster actuator. It is not necessary to apply the saturation algorithm to the velocity error as it will be limited by the position saturation signal. Similarly, the saturated attitude error quaternion $sat(\tilde{\boldsymbol{q}}_e)$ can be

defined as:

$$sat(\tilde{\boldsymbol{q}}_e) = \begin{cases} \tilde{\boldsymbol{q}}_e & \|\tilde{\boldsymbol{q}}_e\|_\infty / q_{e\max} < 1 \\ \tilde{\boldsymbol{q}}_e q_{e\max} / \|\tilde{\boldsymbol{q}}_e\|_\infty & \|\tilde{\boldsymbol{q}}_e\|_\infty / q_{e\max} \geq 1 \end{cases} \tag{4.83}$$

where $q_{e\max}$ is the maximum permitted error quaternion for the controller, again determined by properties of the thruster actuators.

These limits can be converted into force and torque limits. Define $sat(\boldsymbol{u})$ and $sat(\boldsymbol{\tau})$ as:

$$sat(\boldsymbol{u}) = \begin{cases} \boldsymbol{u} & \|\boldsymbol{u}\|_\infty / u_{\max} < 1 \\ \boldsymbol{u} u_{\max} / \|\boldsymbol{u}\|_\infty & \|\boldsymbol{u}\|_\infty / u_{\max} \geq 1 \end{cases} \tag{4.84}$$

$$sat(\boldsymbol{\tau}) = \begin{cases} \boldsymbol{\tau} & \|\boldsymbol{\tau}\|_\infty / \tau_{\max} < 1 \\ \boldsymbol{\tau} \tau_{\max} / \|\boldsymbol{\tau}\|_\infty & \|\boldsymbol{\tau}\|_\infty / \tau_{\max} \geq 1 \end{cases} \tag{4.85}$$

where $u_{\max}$ and $\tau_{\max}$ are the maximum permitted output for translation control and rotation control, determined by the thruster limits. Thus, the cascade-saturation controllers for formation flying relative position control and attitude control can be expressed as:

$$\begin{aligned} \boldsymbol{u}_t &= sat(-\boldsymbol{K}_{pu}^{-1}((\boldsymbol{K}_{pa} + \boldsymbol{K}_{pc}) sat(\delta \boldsymbol{x}_t) - \boldsymbol{K}_{pi} \delta \dot{\boldsymbol{x}}_t)) \\ \boldsymbol{\tau}_t &= sat(-\boldsymbol{K}_{au}^{-1}((\boldsymbol{K}_{aa} + \boldsymbol{K}_c) sat(\tilde{\boldsymbol{q}}_e) - \boldsymbol{K}_{ai} \omega_e)) \end{aligned} \tag{4.86}$$

where all the controller gains are defined in Eq. (4.68) ~ Eq. (4.70) and Eq. (4.75) ~ Eq. (4.78). With these controllers, the manoeuvre rates of the telescope will be limited to the required values.

Likewise, due to the misalignment and misplace of thrusters, the coupling effect between translation and rotation control systems can be taken into account for the system design. Using the method described in Section 4.5.2, the thruster command of control translation and rotation control for the thruster limits is obtained by using the controllers in Eq. (4.86) into Eq. (4.79).

4.5.4 Simulation Results and Analysis

In this section, a leader-follower formation flying scenario is investigated using the limit based controller to validate its accuracy.

As the leader in the mission, the hub follows a nominal Lissajous trajectory about the L_2 point, whose initial conditions are given in Table 3.1.

The thruster positions and orientations are described in Table 1.2, and the inertia matrix of telescope is given by Eq. (3.33).

The initial relative position of the telescope with respect to the hub in the **ROF** frame is $[40 \quad 0 \quad 0]^{\mathrm{T}}$ m, and the desired position is $[100 \quad 0 \quad 0]^{\mathrm{T}}$ m.

The initial relative attitude of the telescope with respect to the hub is set to zero, hence $\boldsymbol{q}_e = [1 \quad 0 \quad 0 \quad 0]^{\mathrm{T}}$ and the desired attitude is $\boldsymbol{q}_e = [0.707 \quad 0 \quad 0 \quad 0.707]^{\mathrm{T}}$, which represents a slew manoeuvre of 90 deg about the inertial $\hat{\boldsymbol{z}}$ axis. The start of the attitude manoeuvre is postponed by one day to reduce the maximum output of thruster.

The desired characteristic polynomial for each channel of the closed-loop system is selected as the combination of a second-order polynomial and an additional first-order pole. It can be written as

$$D^d(s) = (s + p_t)(s^2 + 2\xi\omega_n s + \omega_n^2) \tag{4.87}$$

where ξ is damping ratio, set to 0.6, ω_n is the natural frequency, for position control channels set to 0.0002 rad/s, for attitude channels setting 0.0001 rad/s, p_t is the third pole, set to 6×10^{-4}.

The maximum manoeuvre rates are set to 10 m/day and 20 deg/day for translation and rotation, respectively. The maximum thruster torque is 100 μN. The thruster position and direction errors are 1 cm and 1 deg, respectively. The position and velocity measurement noise are set to 2 mm and 0.002 mm/s, and set 0.02 as and 0.02 as/s for attitude and angular measurement.

Noting that the manoeuvre of the entire simulation scenario can complete in a relatively short time, the simulation time in all the figures is set to 20 days rather than 200 days as before. For the performance over the remaining 180 days, please refer to Section 4.4.2 as the control over the remaining 180 days is the same as that in Section 4.4.2.

With these initial conditions, the simulation results are shown in Fig. 4.19 ~ Fig. 4.34. The results without any limitation are also shown for comparison.

Figure 4.19 ~ Figure 4.26 show the simulation results for the system state errors.

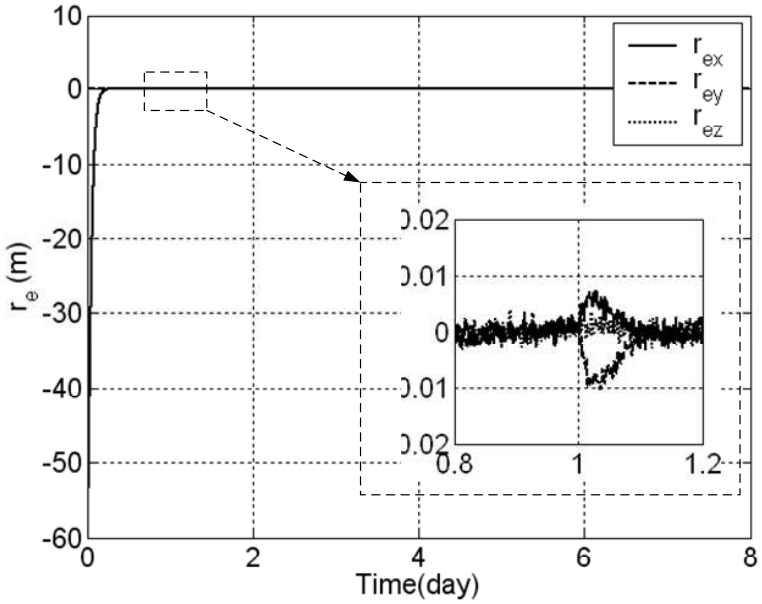

Figure 4.19: The Relative Position Errors of Translational Control System without Limitation

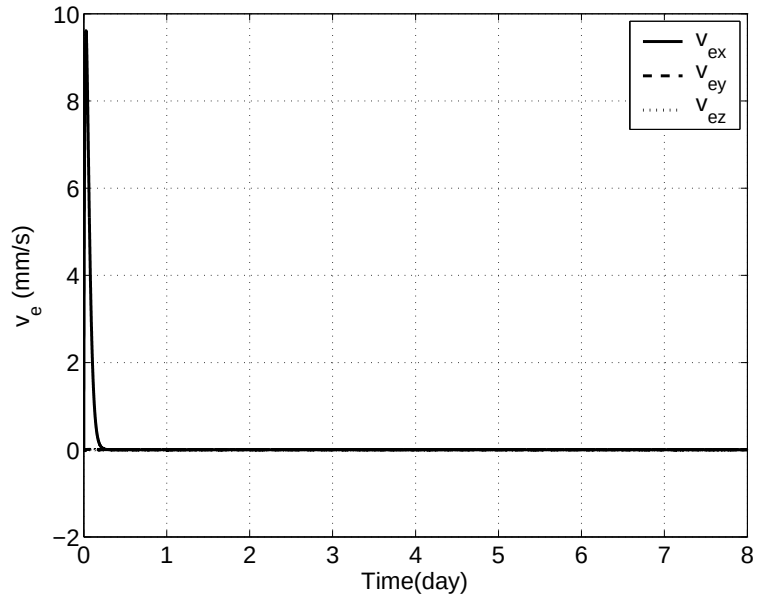

Figure 4.20: The Relative Velocity Errors of Translational Control System without Limitation

Figure 4.19 ~ Figure 4.22 show the results without limitation of manoeuvre rates, while Fig. 4.23 ~ Fig. 4.26 show the results including actuator limits.

In Fig. 4.19, the relative position errors are shown to reduce quickly in the first few hours and reach the required relative position easily, however the maximum

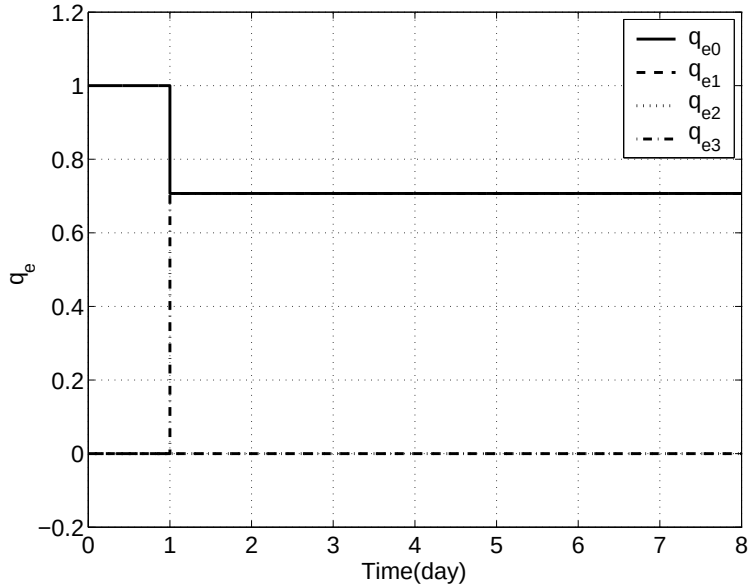

Figure 4.21: The Relative Quaternion Errors of Rotational Control System without Limitation

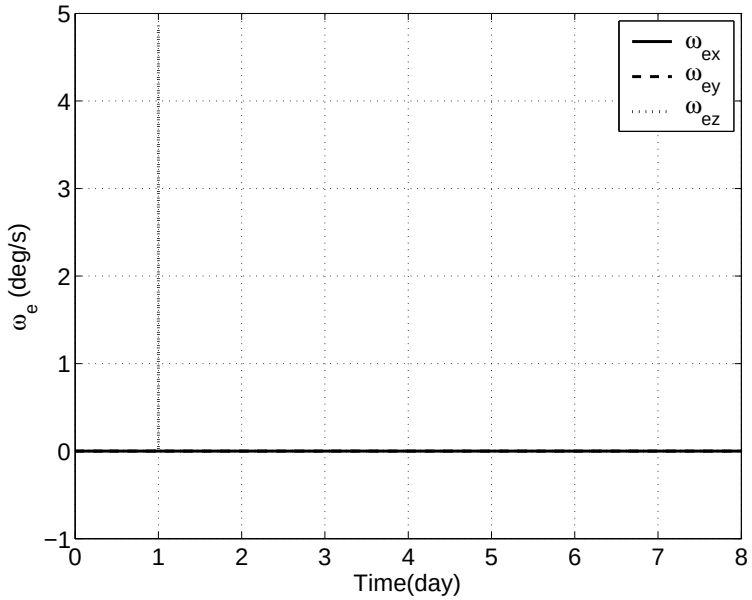

Figure 4.22: The Relative Angular Velocity Errors of Rotational Control System without Limitation

manoeuvre velocity in Fig. 4.20 peaks at approximately 10 mm/s, which exceeds the rate limit. The attitude control responses are shown in Fig. 4.21, and shows that the quaternion errors stabilize in 100 seconds with a maximum angular velocity of 5 deg/s, which exceeds the maximum rate.

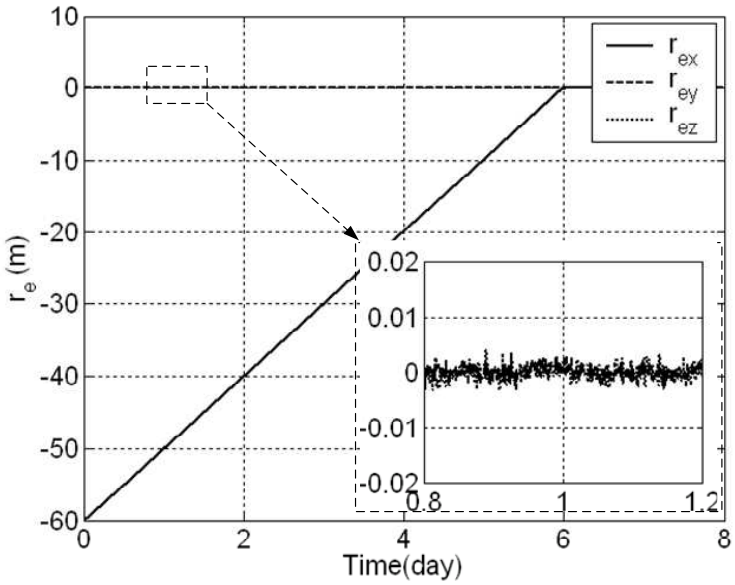

Figure 4.23: The Relative Position Errors of Translational Control System with Limitation

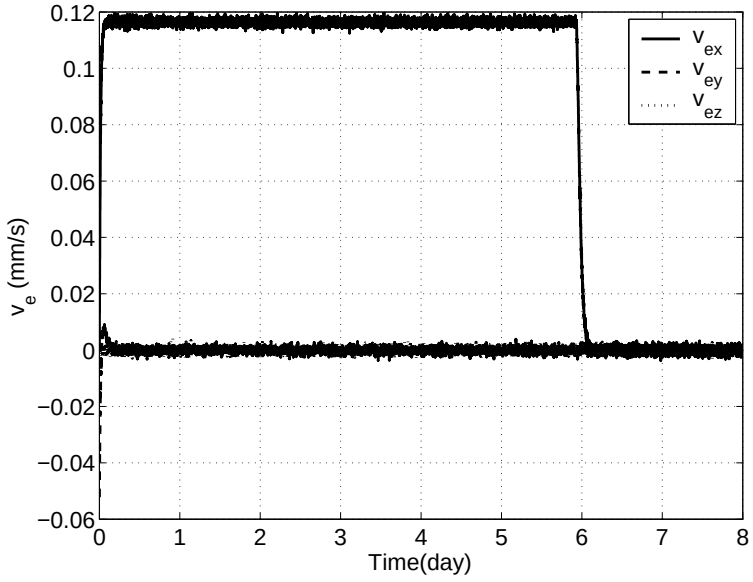

Figure 4.24: The Relative Velocity Errors of Translational Control System with Limitation

Using the cascade-saturation control logic, the control performance stays within the required limits, as shown in Fig. 4.23. This shows that the relative position errors decrease slowly and tend to zero in 6 days, whilst staying within the required manoeuvre rate limits of 10 m/day, which is shown very clearly in Fig. 4.24. The attitude control is very similar to that of the position control: the quaternion errors converge to the desired values in 4.5 days (Fig. 4.25), with a

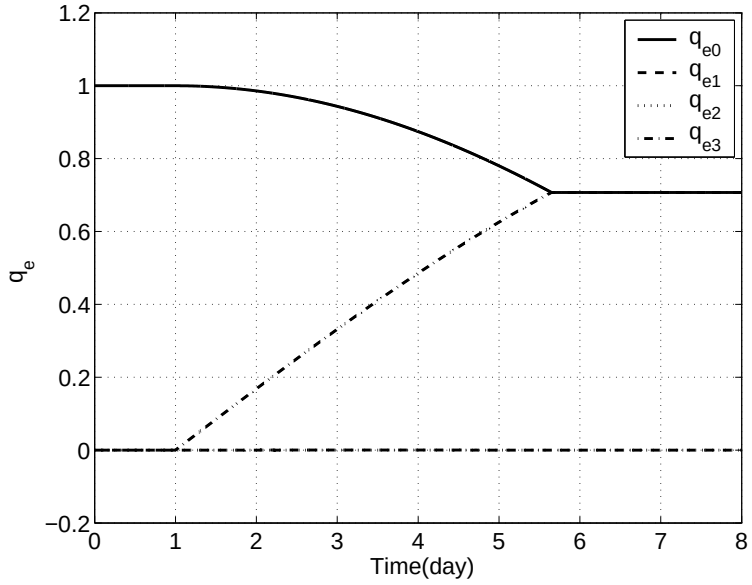

Figure 4.25: The Relative Quaternion Errors of Rotational Control System with Limitation

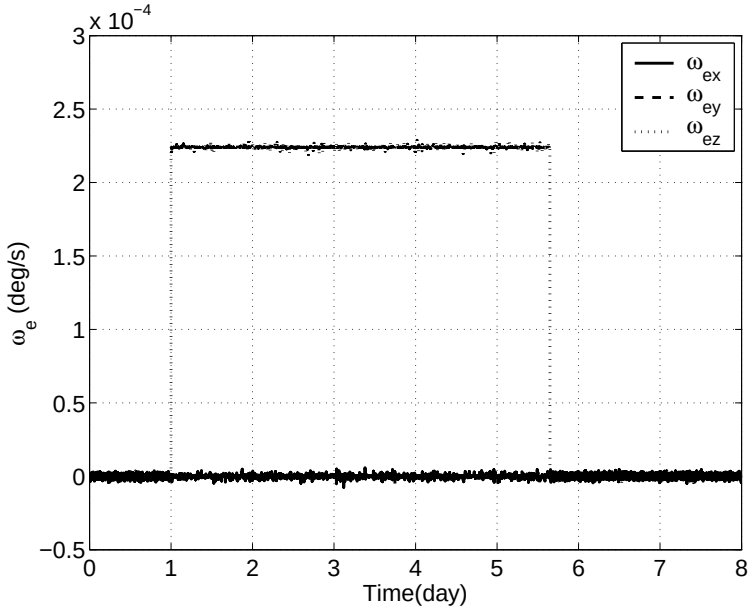

Figure 4.26: The Relative Angular Velocity Errors of Rotational Control System with Limitation

maximum manoeuvre angular velocity of $2.315\times10^{-4}\ deg/s$ ($20\ deg/day$, Fig. 4.26).

Figure 4.27 ~ Figure 4.34 show the outputs of the controllers and the thrusters for the control system. Figure 4.27 ~ Figure 4.30 show the actuator performance without the thruster saturation algorithm, while Fig. 4.31 ~ Fig. 4.34 figure the actuator performance with the saturation algorithm.

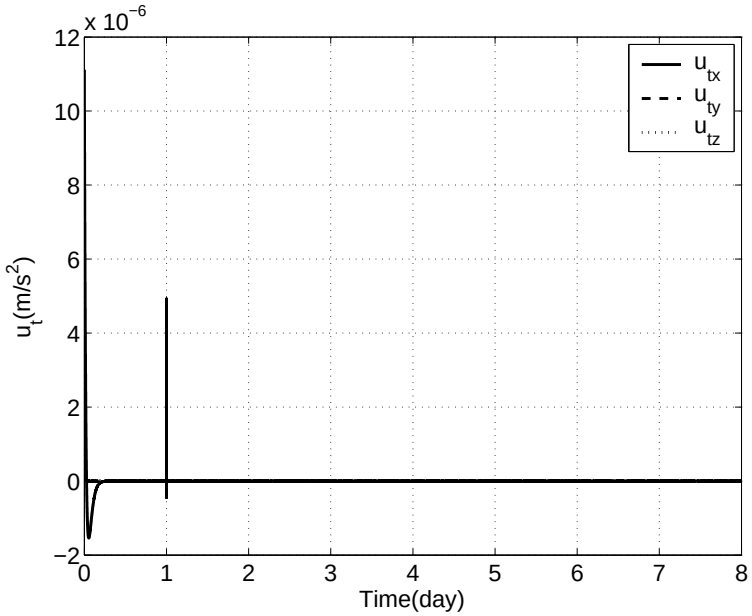

Figure 4.27: The Relative Position Controller Outputs without Saturation

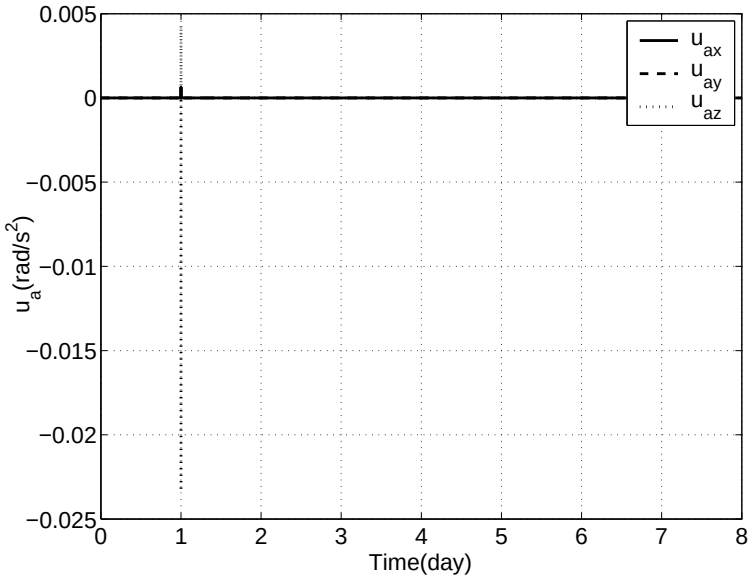

Figure 4.28: The Relative Attitude Controller Outputs without Saturation

In Fig. 4.27 and Fig. 4.28, the outputs of the position controller and the attitude controller are greater than 10^{-5} m/s^2 and 0.02 rad/s, and the thruster maximum output in Fig. 4.29 and Fig. 4.30 is greater than $1N$ which exceeds the limits for continuous operation of the thruster. For the saturation algorithm, the outputs of the position controller and the attitude controller are less than 10^{-7} m/s^2 and 10^{-6} rad/s^2 (Fig. 4.31 and Fig. 4.32), and the thruster maximum output is 60 μN

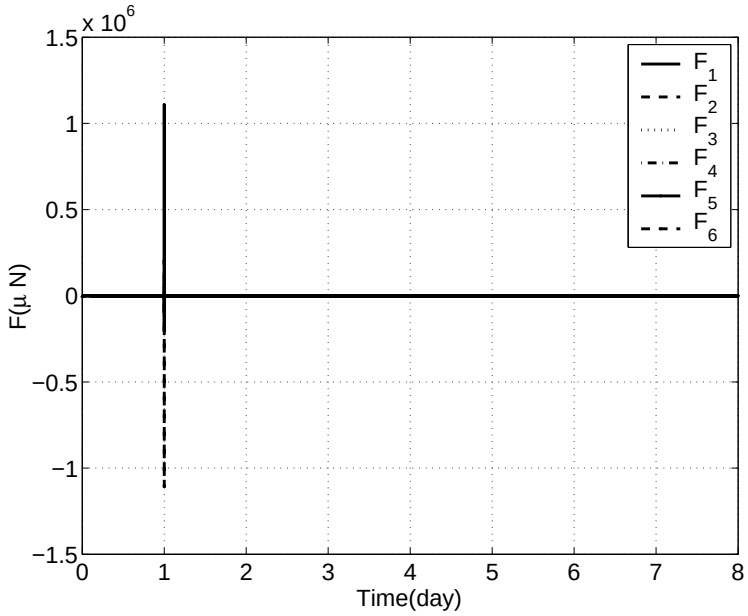

Figure 4.29: No.1-6 Thruster Outputs without Saturation

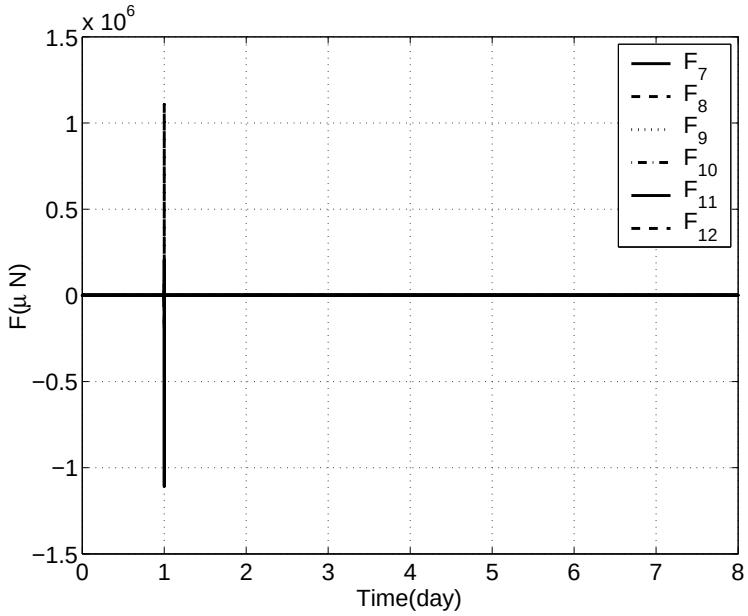

Figure 4.30: No.7-12 Thruster Outputs without Saturation

(Fig. 4.33 and Fig. 4.34), which is less than the maximum permitted value of 100 μN.

Due to the relative large magnitude of the controller outputs, the coupling effect is clearly seen in Fig. 4.27: the position controller is coupled into the attitude control and induces a rate of $5\times10^{-6}\ m/s^2$ during the first day, which in turn induces

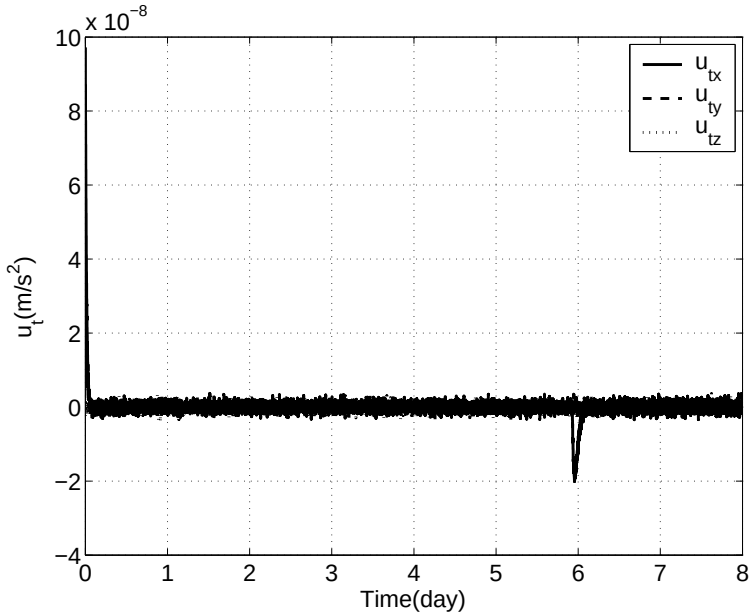

Figure 4.31: The Relative Position Controller Outputs with Saturation

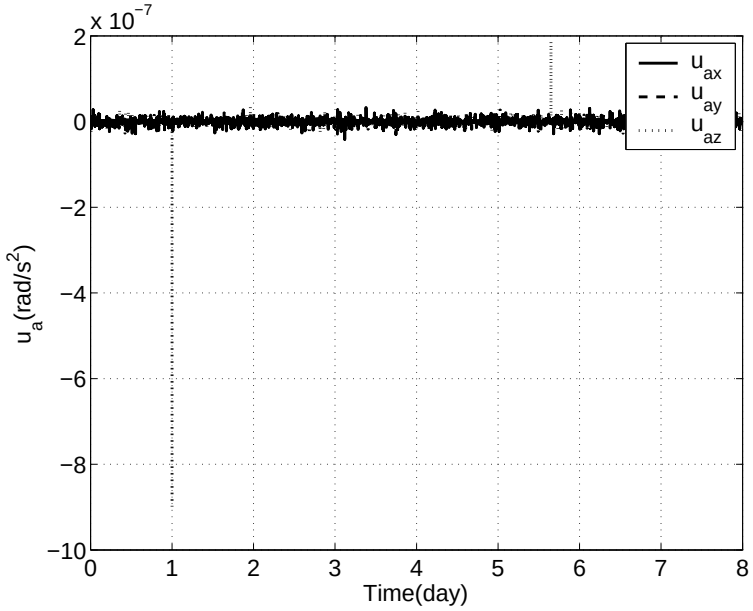

Figure 4.32: The Relative Attitude Controller Outputs with Saturation

a relative position error, increasing from 2.2 mm (Fig. 4.23) to 10.4 mm (Fig. 4.19). Whereas, with the limit algorithm in place, which limits the manoeuvre rates, there is very little coupling effect in the controller outputs in Fig. 4.31, which indicates that by reducing the thrust maximum output maintains the coupling effect at a negligible level. As one can see in Fig. 4.31, the position controller

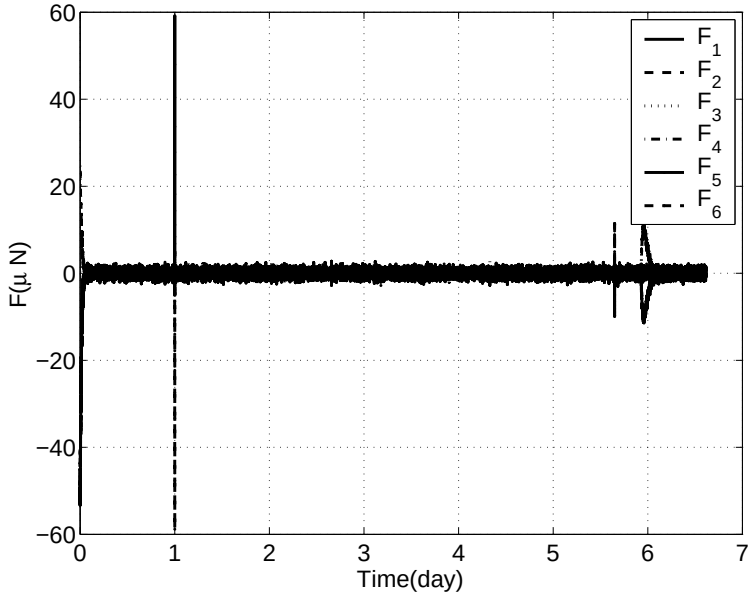

Figure 4.33: No.1-6 Thruster Outputs with Saturation

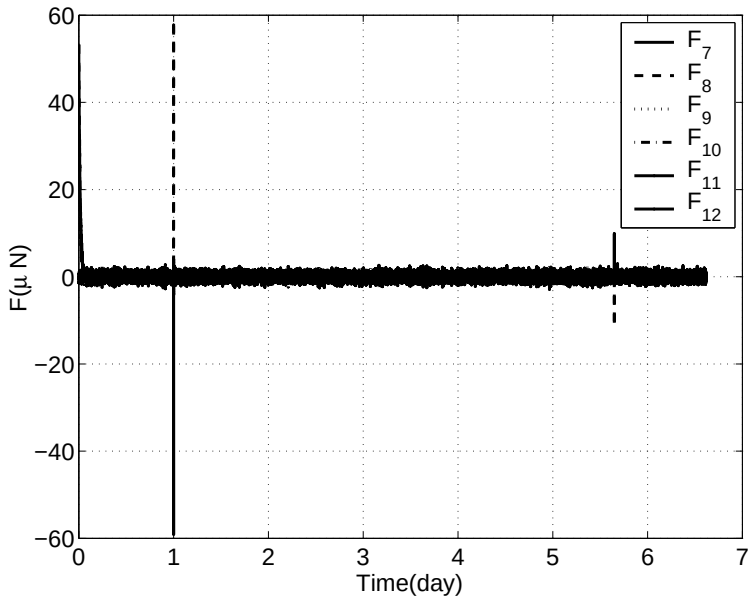

Figure 4.34: No.7-12 Thruster Outputs with Saturation

produces a small force around 6 days to complete the manoeuvre and in Fig. 4.31, a small torque is produced around 5.5 days by the attitude controller to complete the rotation manoeuvre.

4.6 The Effect of Spacecraft Flexibility on System Performance

Ignoring the perturbations caused by the spacecraft flexibility, the control system in Eq. (2.83) can be decoupled into two MIMO systems (position control and attitude control) with three axis controllers. The design process is the same as that in Section 4.5, and the controller for position control and attitude control can be expressed as:

$$\boldsymbol{U} = \begin{bmatrix} \boldsymbol{F} \\ \boldsymbol{T} \end{bmatrix} = \boldsymbol{K}_{up}^{-1}(\boldsymbol{p})((\boldsymbol{X}_p - \boldsymbol{X}_{pd})/s - \boldsymbol{K}_c(\boldsymbol{p})\boldsymbol{X}_p - \boldsymbol{K}_i(\boldsymbol{p})\dot{\boldsymbol{X}}_p) \tag{4.88}$$

where $\boldsymbol{X}_{pd}$ is the vector of the desired position and attitude, and the controller gains for position control and attitude control are the same expressions as those in Section 4.5, respectively.

4.6.1 Mode Compensation for the PEA Controller

During the previous PEA controller design, the perturbations induced by spacecraft flexibility, $\boldsymbol{U}_f$, are not taken into account to simplify the design. However, such a simplification could degrade the performance or result in the instability of the close-loop system. Therefore, it is necessary to modify the designed controller to compensate for the effect of the flexibility.

Noting the dynamics of flexible beam described in Eq. (2.81), the compensation term in the controller can be chosen as:

$$\boldsymbol{U}_c(s) = \begin{bmatrix} \boldsymbol{F}_c \\ \boldsymbol{T}_c \end{bmatrix} = \boldsymbol{L}^T\boldsymbol{L}\boldsymbol{X}(s)s^2\frac{s^2}{s^2 + 2\xi_k\omega_k s + \omega_k^2\eta_k} \tag{4.89}$$

which can suppress the perturbation of spacecraft flexibility exactly if the parameters of spacecraft flexible modes can be obtained precisely and there is no time delay for the operation of the sensors and actuators. However, uncertainty in the spacecraft flexible mode parameters and uncertainty in the delay of the sensors and actuators will degrade the system performance.

4.6.2 Simulation Results and Analysis

Using the PEA controller with the flexible mode compensation, simulation is carried out to check the effect of spacecraft flexibility on system performance.

All the parameters of spacecraft are the same as those in Section 3.4. The flexible beam length and mass are assumed to be 3 m and 10 Kg, and the bending mode frequency and damping ratio of the beam are 0.11 Hz and 0.1375, respectively.

The desired transfer function for each axis nominal closed-loop system is selected as the combination of a second-order plant and an integrator. To check the effect of spacecraft flexibility, the desired characteristic polynomial of each nominal SISO channel is set to: $d^d(s) = (s+p_t)(s^2+2\xi\omega_n s+\omega_n^2)$, where $\xi = 0.8$, $\omega_n = 0.02\times 2\pi\ rad/s, p_t = 2\xi\omega_n$. The gain margin and phase margin of this PEA controller are 15.2 dB and 66.2°, respectively. Using the flexible mode compensation defined in Eq. (4.89), the closed-loop system has pole-zero cancelation in the left hand plane which suppresses the effect of flexible modes on the system performance. Also, the third pole in the desired transfer function is relatively close to the main pole pair used in previous designs, which alleviates the mismatch in mode parameters caused by the uncertainty.

To assess the system performance clearly, the sensors and actuators have no noise injected during the simulation. The simulation results are shown in Fig. 4.35 ~ Fig. 4.56.

Figure 4.35 ~ Figure 4.42 show the control performance of the PEA controller with and without mode compensation and with no time delay on the sensors and the actuators and no mode parameter uncertainty. In each case, both the position system and attitude system converge in 70 seconds. However, the effect of the mode flexibility is very clear and lasts more than 200 seconds for the controller without compensation. At 80 seconds, the position error is 1×10^{-4} m and the attitude error is 1×10^{-4} deg. However, with mode compensation, the effect of the mode flexibility is eliminated.

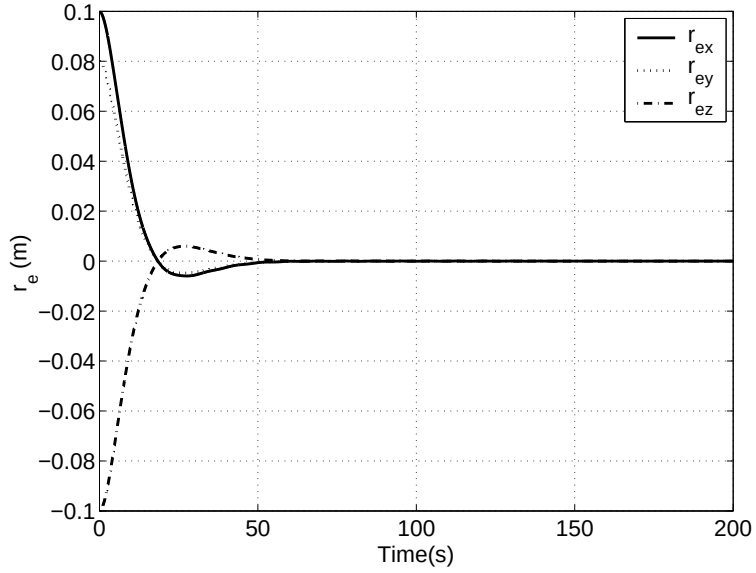

Figure 4.35: The Position Errors of Control System without Compensation (no delay)

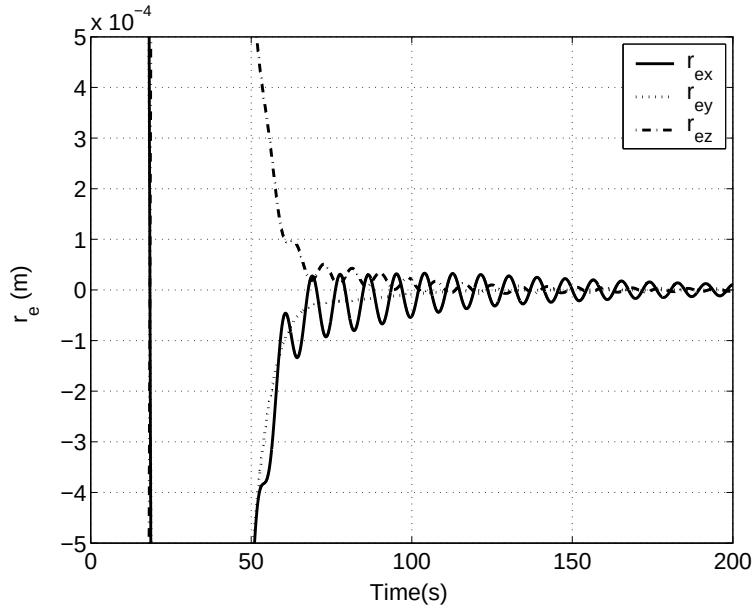

Figure 4.36: The Position Errors of Control System without Compensation (no delay, zoom in of the previous figure)

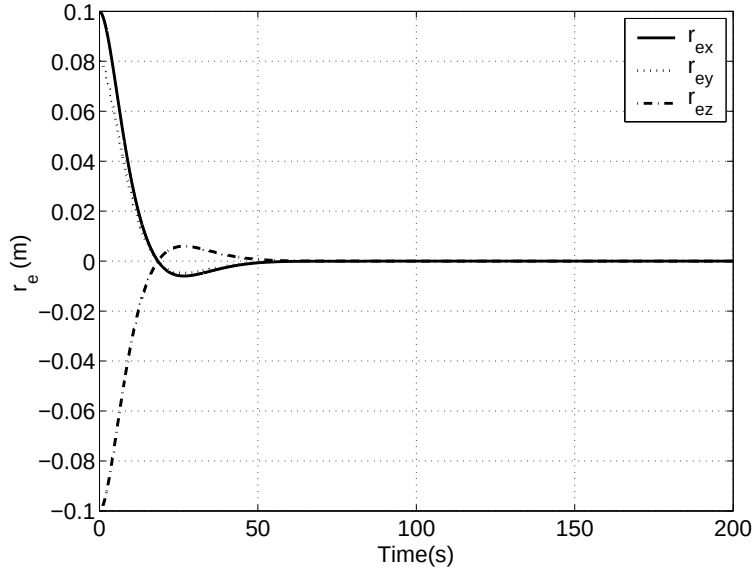

Figure 4.37: The Position Errors of Control System with Compensation (no delay)

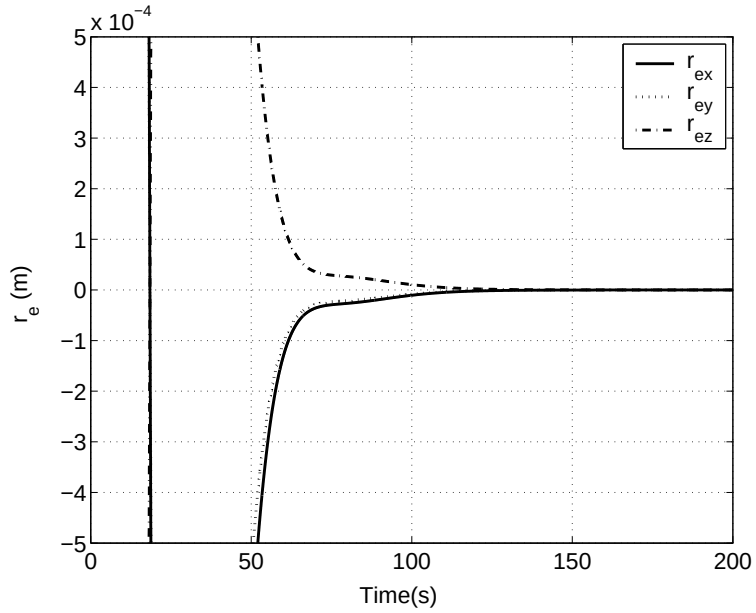

Figure 4.38: The Position Errors of Control System with Compensation (no delay, zoom in of the previous figure)

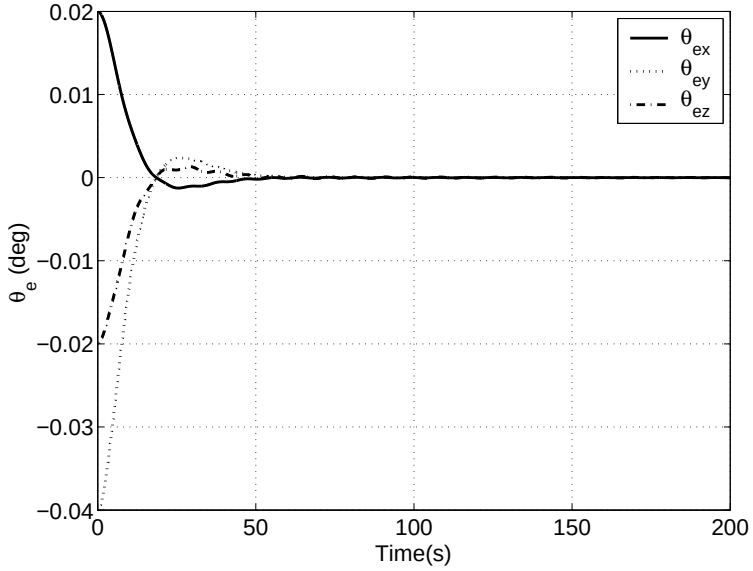

Figure 4.39: The Attitude Errors of Control System without Compensation (no delay)

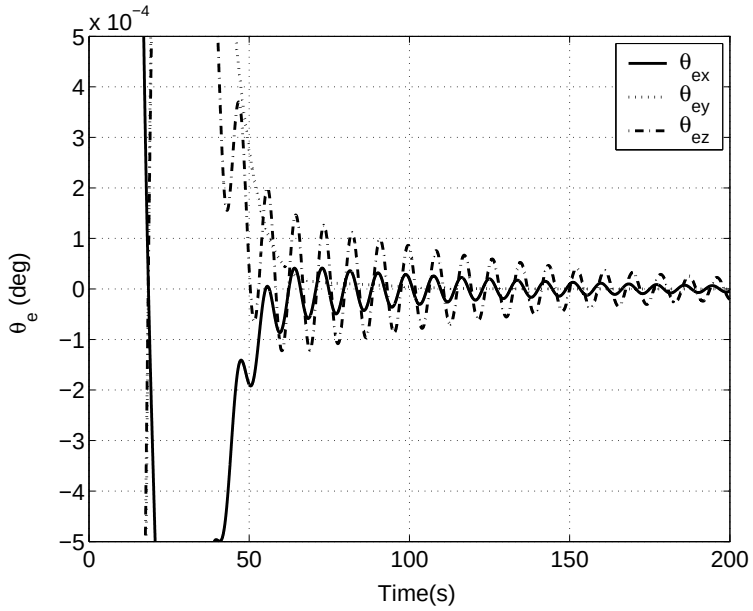

Figure 4.40: The Attitude Errors of Control System without Compensation (no delay, zoom in of the previous figure)

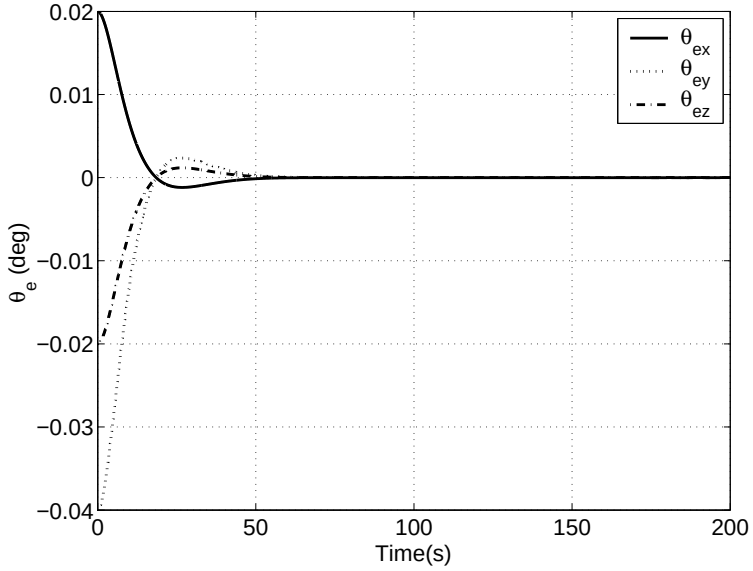

Figure 4.41: The Attitude Errors of Control System with Compensation (no delay)

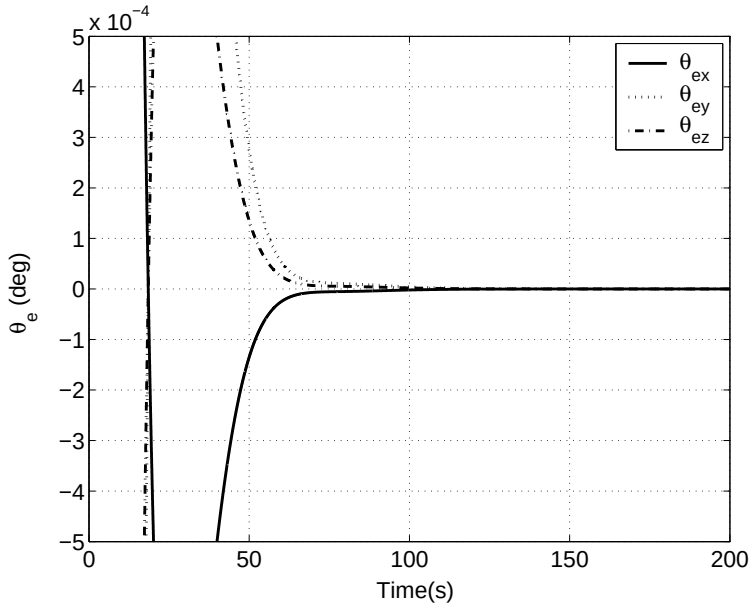

Figure 4.42: The Attitude Errors of Control System with Compensation (no delay, zoom in of the previous figure)

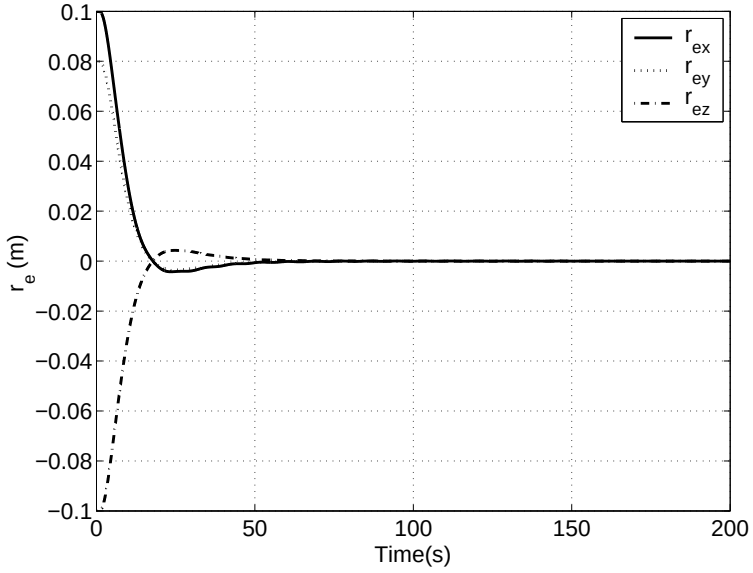

Figure 4.43: The Position Errors of Control System without Compensation (1s delay)

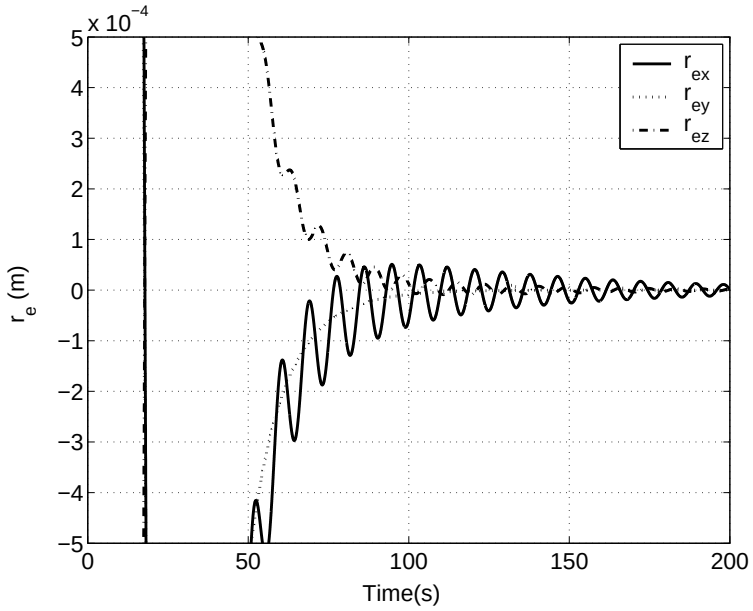

Figure 4.44: The Position Errors of Control System without Compensation (1s delay, zoom in of the previous figure)

Figure 4.43 ~ Figure 4.50 show the performance of the PEA controller with and without mode compensation for the case of 1 second time delay in the sensor and actuator operation. The position system and attitude system converge in 70 seconds for both cases. However, the effect of mode flexibility is much more obvious and lasts more than 200 seconds for the controller without mode compensation.

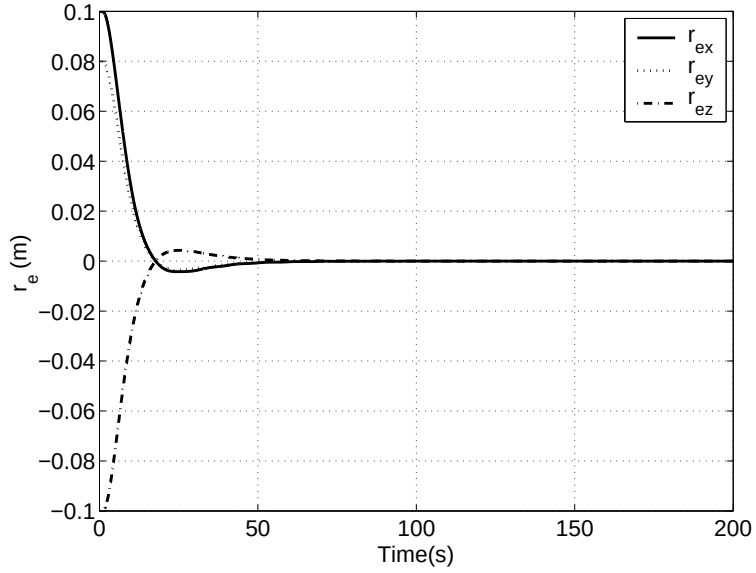

Figure 4.45: The Position Errors of Control System with Compensation (1s delay)

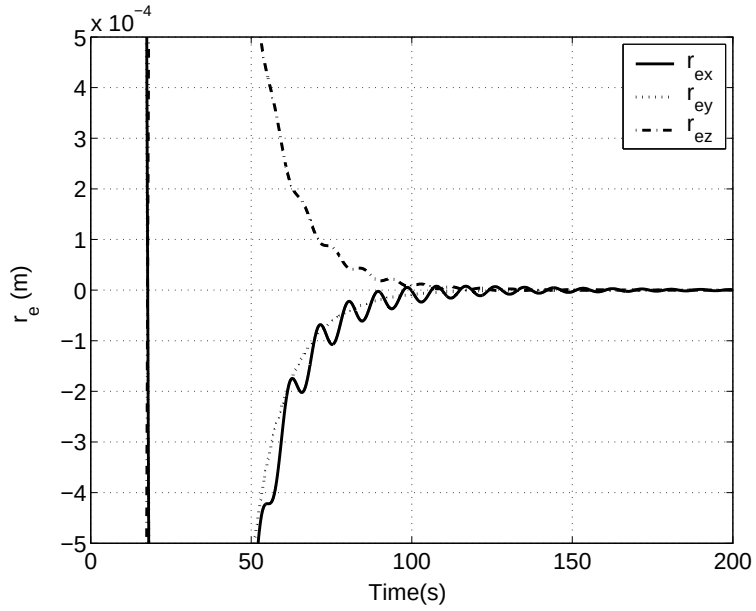

Figure 4.46: The Position Errors of Control System with Compensation (1s delay, zoom in of the previous figure)

At 80 seconds, the position error is 1.3×10^{-4} m and the attitude error is 1.8×10^{-4} deg. Due to the time delay, there is a small degradation of the system performance when using mode compensation. At 80 seconds, the position error is 0.5×10^{-4} m and the attitude error is 0.5×10^{-4} deg. They both converge and approach zero in 150 seconds.

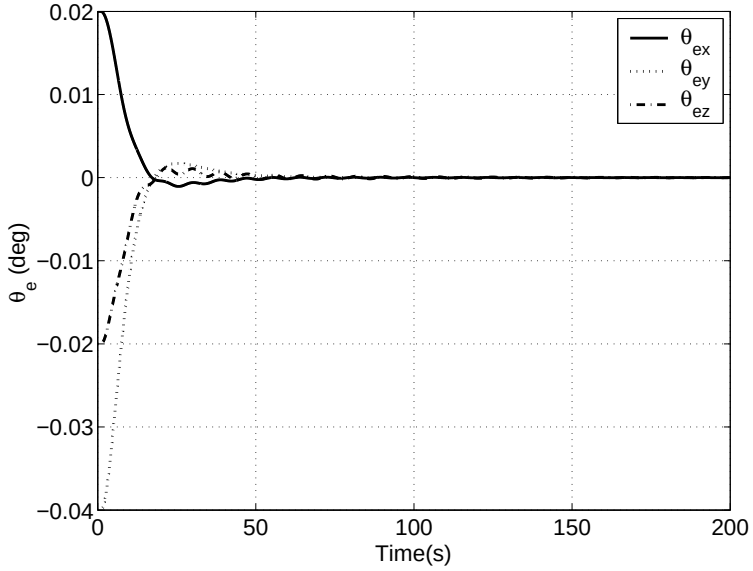

Figure 4.47: The Attitude Errors of Control System with Compensation (1s delay)

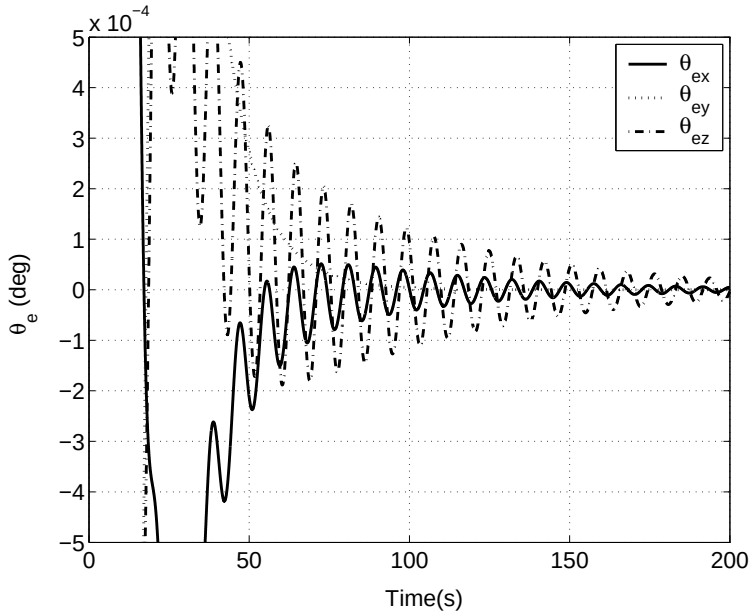

Figure 4.48: The Attitude Errors of Control System with Compensation (1s delay, zoom in of the previous figure)

Figure 4.51 ~ Figure 4.56 show the control performances of the PEA controller with and without mode compensation for the case of 2 seconds time delay in the operation of the sensors and actuators. The position system and attitude system become unstable without mode compensation. At 80 seconds, the position error is 4×10^{-3} *m* and attitude error is 8×10^{-3} *deg*, and both of them increase slowly

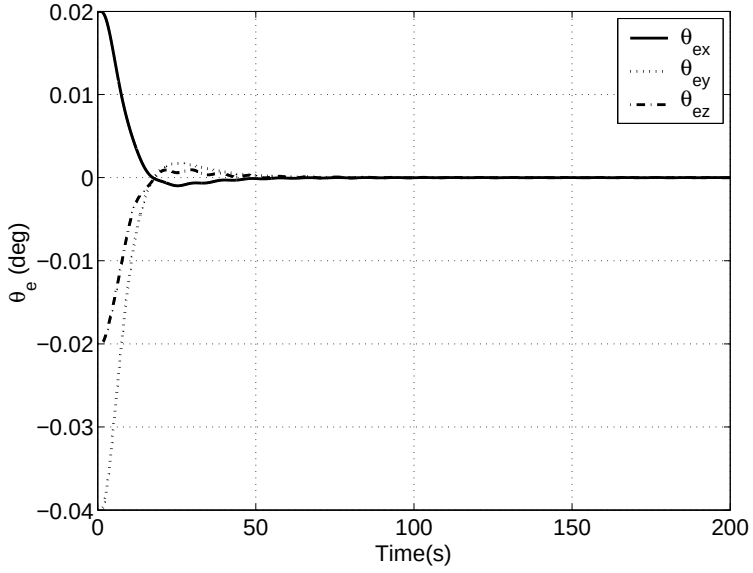

Figure 4.49: The Attitude Errors of Control System with Compensation (1s delay)

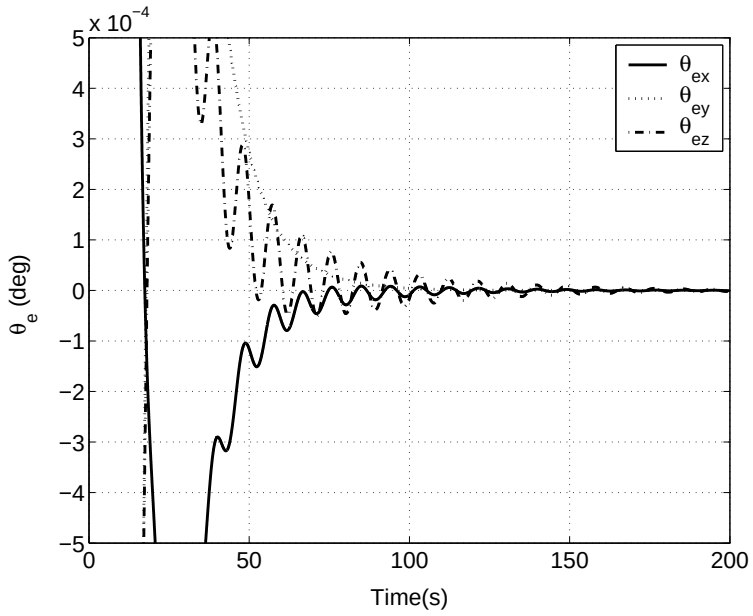

Figure 4.50: The Attitude Errors of Control System with Compensation (1s delay, zoom in of the previous figure)

due to the instability of the system. This indicates that the nominal stable closed-loop system without compensation strategy becomes unstable for flexibility in the telescope when there is significant delay in the sensor and actuator operation.

In contrast, the control system with mode compensation is still stable with a 2 seconds time delay and the effect of mode flexibility is relatively small. At 80

seconds, the position error is 1×10^{-3} m and attitude error is 1×10^{-4} deg. Both of them converge quickly and approach zero in 150 seconds.

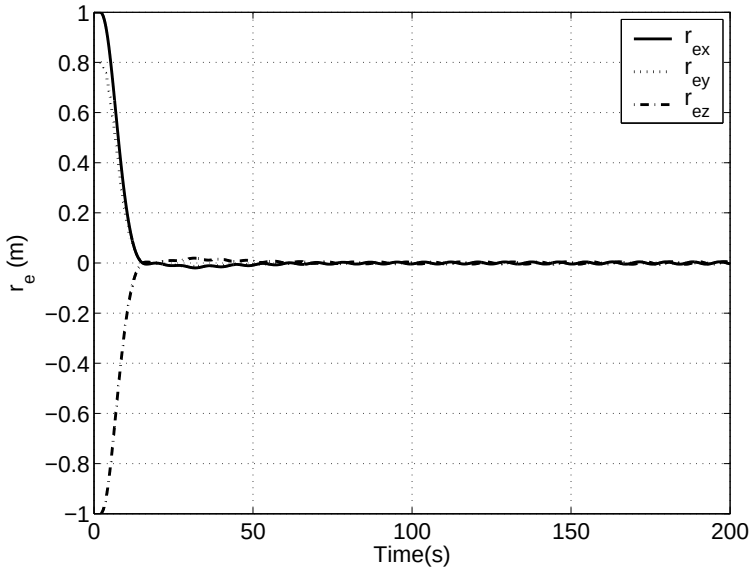

Figure 4.51: The Position Errors of Control System without Compensation (2s delay)

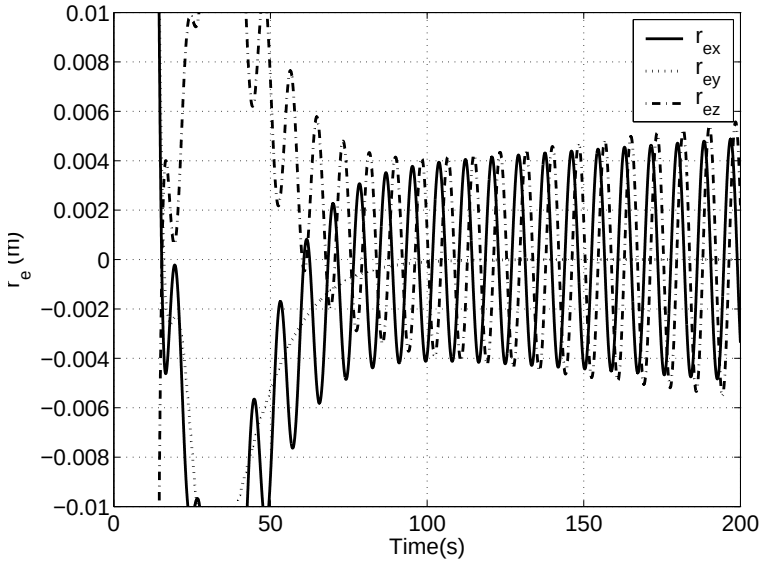

Figure 4.52: The Position Errors of Control System without Compensation (2s delay, zoom in of the previous figure)

The simulation results indicate that the effect of spacecraft flexibility can degrade the performance and even destroy the stability of the closed-loop PEA control system if the controller does not have any mode compensation, and the

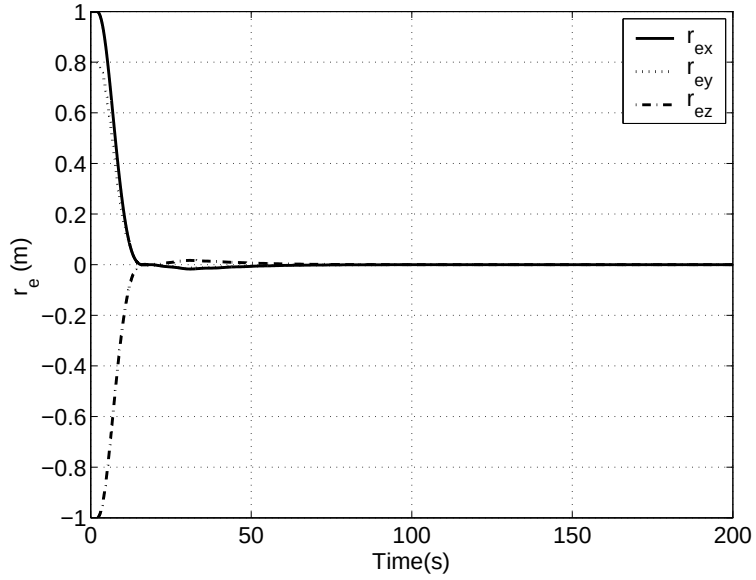

Figure 4.53: The Position Errors of Control System with Compensation (2s delay)

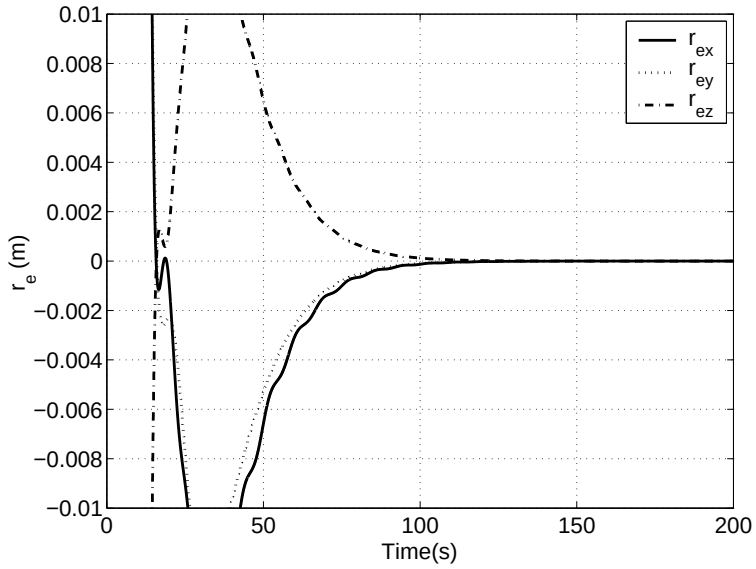

Figure 4.54: The Position Errors of Control System with Compensation (2s delay, zoom in of the previous figure)

mode compensated PEA controller suppresses the vibration of spacecraft flexibility effectively. Further, from the simulation results, one can observe that the effect of any vibration induced by flexibility is quite small and will be negligible in the presence of measurement and actuator noise since the noise disturbance is one magnitude larger than the flexible mode disturbance. This implies that spacecraft flexibility has a very small effect on the performance of formation control system

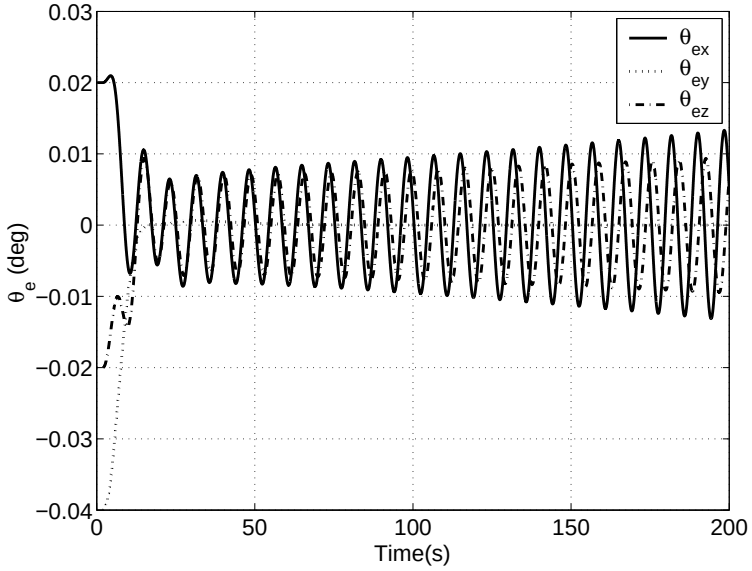

Figure 4.55: The Attitude Errors of Control System with Compensation (2s delay)

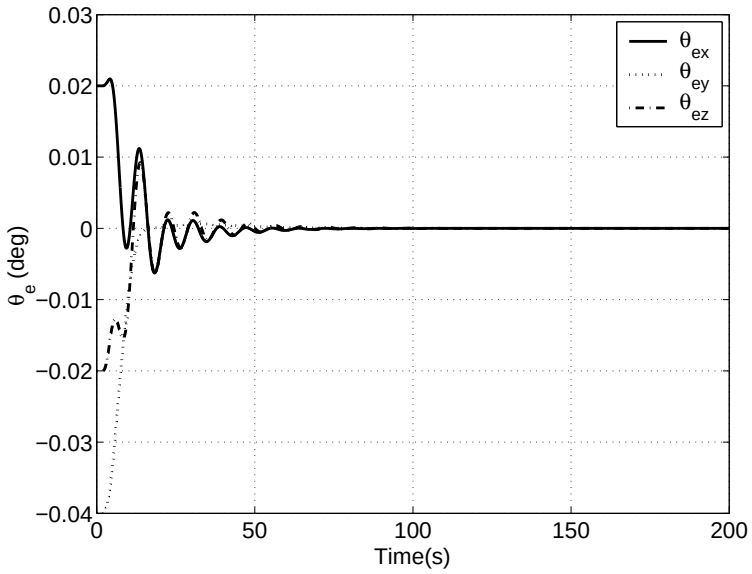

Figure 4.56: The Attitude Errors of Control System with Compensation (2s delay)

even with relatively significant time delay in the operation of the sensors and actuators.

4.7 Conclusions

In this chapter, the Polynomial Eigenstructure Assignment approach for LPV and QLPV systems is developed. In detail, the eigenspace of the open-loop system is formulated as a set of polynomial matrices and the system transfer function is formed from a coprime factorization of these matrices. This formulation allows the polynomial eigenstructure to be used to compute the algebraic structure of the controller and naturally leads to a nonlinear controller without any interpolation. The resulting controller renders the closed-loop system almost independent of the operating point, and thus performs a type of dynamic inversion while encompassing a broader class of LPV and QLPV systems which ensures that a specific system performance can be achieved. This is the first contribution in this chapter.

The second contribution is the design of different PEA controllers for the Sun-Earth L_2 point formation by using LPV and QLPV models. In detail, the PEA approach is applied to the relative position control (Section 4.3 and Section 4.4) and the attitude control (Section 4.5.1) to produce a closed-loop system with invariant performance over a wide range of operating conditions. Then a method to combine relative position and attitude controllers is developed to take account of the coupling effect between these two control systems in Section 4.5. In the same section, the controller is modified by the addition of cascade-saturation control logic to limit the maximum value of manoeuvre rates and actuator limits. From Section 4.3 to Section 4.5, simulations are carried out to validate the performance of these controllers. Comparing the results with that of the LQR controller in Chapter 3, the results indicate that both the LPV PEA and the QLPV PEA controllers improve the control performance significantly and also use less fuel. The QLPV PEA controller has the best performance because its controller gains vary by reference to the QLPV model, which has less modeling error than the LPV and LTI models, since it contains all the effects of solar radiation pressure, lunar gravity and other nonlinear terms.

The last contribution is to investigate the effect of spacecraft flexibility for the PEA controller in Section 4.6. In this Section, the controller is enhanced by adding a mode compensation term to suppress the telescope vibration mode, and the simulation results indicate that this modified PEA controller suppresses the vibration of spacecraft flexibility effectively.

All the controllers in Chapter 3 and Chapter 4 are designed based on the nominal models. But most systems are subject to uncertainties in system, sensor and actuator parameters. Such uncertainties will degrade the closed-loop system performance and in certain circumstances result in instability. The formation control system is complex and has uncertainties, and thus it is necessary to analyse the robust performance and stability of the uncertain PEA control system. In the following chapters, these robust analysis problems will be addressed by using both a polynomial method described in Chapter 5 and a Lyapunov method described in Chapter 6, respectively.

Chapter 5

Robust Stability Analysis via Polynomial Families and Polynomial Matrix Polytopes

The controllers designed in Chapter 3 and Chapter 4 are based on the nominal models, which means the control performance of the actual system may vary due to the uncertainties in the system parameters and other properties. Actually, most systems are subject to uncertainties due to errors in measurement or estimation of the system parameters. For the formation flying mission, the disturbances due to the space environment and the parameters of each spacecraft are also time-varying. Therefore these varying factors, together with the noise on the metrology sensors and actuators, will introduce uncertainties into the system nominal model. Such uncertainties will degrade the closed-loop system performance and even induce instability. Hence, it is necessary to analyse the robust performance and stability of the PEA control system in the face of these uncertainties. In this chapter, the polynomial method will be developed to address the robust stability of the PEA control system for formation flying. In order to check robust stability, two methods are used: the polynomial family (SISO) or polynomial matrix polytope (MIMO) as these techniques will link well with the PEA approach.

Hence, the first part of this chapter (Section 5.1 ~ Section 5.3) will give an overview of Kharitonov's and related theorems on polynomial uncertainty. These theorems are used to analyse the robustness of interval polynomial families, affine polynomial families, multi-affine polynomial families and a more general polynomial family based on polytopic parameter spaces. Once the overview of these approaches is complete, the Hurwitz robust stability analysis of systems with parametric uncertainties is carried out for the PEA controller designed in Chapter 4. In order to use Kharitonov's theorem and the Mapping theorem (Djaferis, 1995), the dynamics of the system are decoupled into three SISO systems by neglecting coupling effects. Two sources of parametric uncertainty, controller parameter uncertainty and dynamic derivative uncertainty are considered in order

to analyse the robustness of the closed-loop system. For unstructured uncertainties, the worst-case H_∞ stability margin is also considered by computing the maximum H_∞ norm of the Kharitonov polynomials each channel.

However, the application of these approaches is very computationally intensive due to the comprehensive frequency sweeping required to satisfy the Zero Exclusion Theorem (Djaferis, 1995; Bruyere, 2004). To avoid frequency sweeping a more efficient approach, the Finite Inclusion Theorem (FIT), is introduced to analyse the robustness of the PEA controller. With this FIT approach, the comprehensive frequency sweep can be reduced to a finite, small number of frequencies checks to determine the $\mathcal{D}$-stability of a polynomial family using the Mapping Theorem. The $\mathcal{D}$-stability analysis of the formation control system using the PEA controller is presented at the end of this section.

In the second part of the chapter (Section 5.4 and 5.5), a necessary and sufficient LMI condition for polynomial matrices and a sufficient LMI condition for polynomial matrix polytopes to analyse robust stability of MIMO systems for intersecting stability regions $\mathcal{D}$ are developed. The definition of the intersecting stability regions usually involves complex analysis but the LMI solver in Matlab can only solve real-valued LMI problems. The real-valued LMI conditions associated with complex-valued LMI conditions presented in Herion et al. (2001) and Herion et al. (2001) are assessed and developed. Finally, $\mathcal{D}$-stability for the formation flying MIMO control system using the PEA controller is assessed by the newly developed LMI method.

5.1 Hurwitz Stability of Polynomial Families

Different definitions and theorems are described in this section for the Hurwitz stability analysis of SISO systems. A polynomial is Hurwitz (stable) if all its roots are in the left-hand plane. A polynomial family is Hurwitz if all its polynomials are Hurwitz.

5.1.1 Interval Polynomial Family

For an interval polynomial family, the *Kharitonov's theorem* is an efficient analytical solution to analyse its robust stability. Here are some required definitions..

Definition 1 (Box parameter space) *A box parameter space has the form* $\Pi_b = \{\boldsymbol{q} | \boldsymbol{q} \in \mathbb{R}^{n+1}, \forall i \in \mathbb{N}_n^* \;\; q_i^- \leq q_i \leq q_i^+\}$, *where* $\boldsymbol{q} = [q_0, q_1, ..., q_n]^T$.

Definition 2 (Interval polynomial family) *An interval polynomial family,* $\Phi_i(s)$, *is a family of polynomial in the form*

$$p(s, \boldsymbol{q}) = q_0 + q_1 s + q_2 s^2 + q_3 s^3 + ... + q_n s^n \tag{5.1}$$

where the coefficient $\boldsymbol{q}$ *lies with the box parameter space* Π_b, *and* $q_n \neq 0$ *such that the degree n of p(s) is always preserved.*

Definition 3 (The four Kharitonov polynomials) *Assuming an interval polynomial* $\Phi_i(s)$ *defined in Eq. (5.1), its four Kharitonov polynomials are given by*

$$\begin{aligned}
K_1(s) &= q_0^- + q_1^- s + q_2^+ s^2 + q_3^+ s^3 + q_4^- s^4 + q_5^- s^5 + q_6^+ s^6 + ... \\
K_2(s) &= q_0^- + q_1^+ s + q_2^+ s^2 + q_3^- s^3 + q_4^- s^4 + q_5^+ s^5 + q_6^+ s^6 + ... \\
K_3(s) &= q_0^+ + q_1^- s + q_2^- s^2 + q_3^+ s^3 + q_4^+ s^4 + q_5^- s^5 + q_6^- s^6 + ... \\
K_4(s) &= q_0^+ + q_1^+ s + q_2^- s^2 + q_3^- s^3 + q_4^+ s^4 + q_5^+ s^5 + q_6^- s^6 + ...
\end{aligned} \tag{5.2}$$

Then Kharitonov's theorem, a very elegant characterization of robust stability for an interval polynomial family is given by:

Theorem 1 (Kharitonov's Theorem) *The interval polynomial family in 5.1 is Hurwitz if and only if its four Kharitonov polynomials are Hurwitz.*

As an example, a simple interval polynomial of third-order is given as (Bruyere, 2004):

$$p(s, \boldsymbol{q}) = q_0 + q_1 s + q_2 s^2 + s^3 \tag{5.3}$$

where $q_0 \in [1200, 1600]$, $q_1 \in [110, 130]$ and $q_2 \in [45, 55]$. It is Hurwitz since the roots of all polynomials are in left-hand plane by using the griding method, shown in Fig. 5.1. Instead of this computational checking method, the stability of Eq. (5.3)

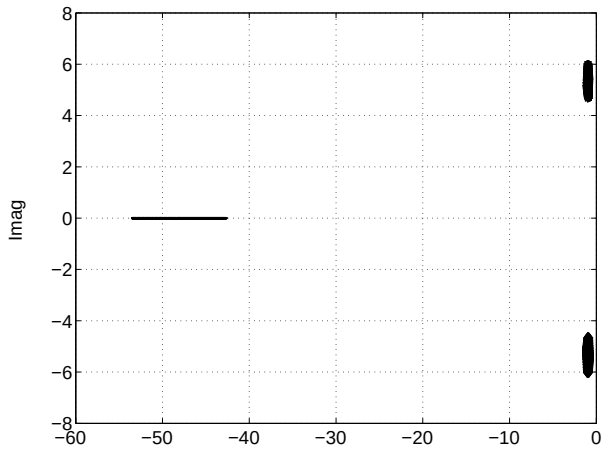

Figure 5.1: All the Roots of an Interval Polynomial Family

is simplified to assess the stability of the following four Kharitonov polynomials:

$$\begin{aligned} p_1(s) &= 1200 + 110s + 55s^2 + s^3 \\ p_2(s) &= 1200 + 130s + 55s^2 + s^3 \\ p_3(s) &= 1600 + 110s + 45s^2 + s^3 \\ p_4(s) &= 1600 + 130s + 45s^2 + s^3 \end{aligned} \tag{5.4}$$

whose stability can be checked by using the Routh criteria or solving their roots directly: the roots are -53.36, $-0.82 \pm 4.67i$, -52.97, $-1.01 \pm 4.65i$,-43.31, $-0.84 \pm 6.02i$, and -42.84, $-1.08 \pm 6.02i$, respectively. Therefore, using Kharitonov's theorem, the interval polynomial in Eq. (5.3) is Hurwitz since all of its four Kharitonov polynomials are Hurwitz.

From the example, one can observe that the essence of Kharitonov's theorem is to map the 2^m vertices in the box parameter space to a rectangular (4 vertices) image in the s-plane. Considering the imaginary axis ($j\omega$) is the border between the stable and unstable region, one can use the following theorem to check the stability of an interval polynomial family with four Kharitonov polynomials.

Theorem 2 (Zero Exclusion Condition) *If an interval polynomial family* $\Phi_i = p(s, \boldsymbol{q}), \boldsymbol{q} \in \Pi_b$ *has invariant degree and at least one stable member* $p(s, \boldsymbol{q}^0)$*, then* Φ_i *is robustly stable iff the origin is excluded from the Kharitonov rectangle at all* $\omega \geq 0$*; that is* $\forall \omega \geq 0$, $p(j\omega, \boldsymbol{q}) \neq 0$, $\boldsymbol{q} \in \Pi_b$.

For the example in Eq. (5.3), the interval polynomial family is Hurwitz since

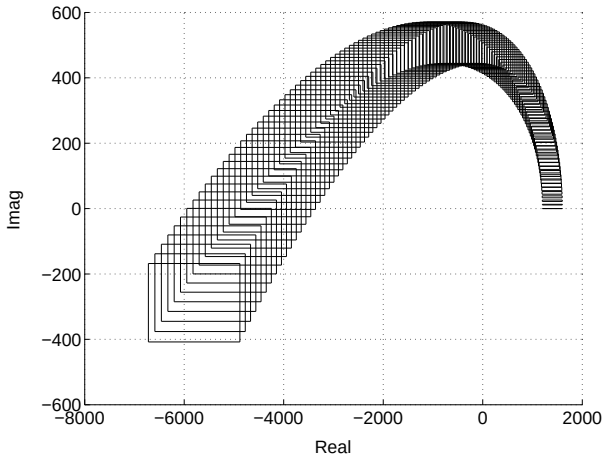

Figure 5.2: The Application of Kharitonov's Theorem for Interval Polynomial Family

the Zero Exclusion condition is satisfied for its Kharitonov rectangles shown in Fig. 5.2, which is generated by frequency sweeping along the $j\omega$ axis in the s-plane.

One point that should be noted is the that Zero Exclusion condition is not only suitable for testing Hurwitz stability but can also be used to test for $\mathcal{D}$-stability (Djaferis, 1995; Bruyere, 2004).

5.1.2 Affine Polynomial Family

Applications of Kharitonov's theorem have been developed widely for controller design of uncertain interval polynomials. However, its use is quite restrictive since the polynomial intervals should all be independent, which is quite restrictive and conservative. Fortunately by using edges instead of vertices of the uncertainty box, results have been developed for affine/polytopic uncertain polynomials.

Certain definitions are required to develop the theorems for the affine polynomial family.

Definition 4 (Convex polytopic parameter space) *A polytopic parameter space, Π_a, is a space which has the form $\Pi_a = \{\boldsymbol{q}^a | \boldsymbol{q}^a \in \mathbb{R}^n, \forall i \in \mathbb{N}_n^* \;\; q_i^a = \sum_{i,j \in \mathbb{N}_n^*} t_{i,j} q_j^b + b_i \;\; \boldsymbol{q}^b \in \Pi_b\}$, where $\boldsymbol{q}^a = [q_1^a, q_2^a, ..., q_n^a]^T$, and $\boldsymbol{q}^b = [q_1^b, q_2^b, ..., q_n^b]^T$, $\boldsymbol{b} = [b_1, b_2, ..., b_n]^T$ is a constant vector.*

Definition 5 (Affine/polytopic polynomial family) *An affine/polytopic polynomial*

family, $\Phi_a(s)$, is a family of polynomial in the form

$$p(s, \boldsymbol{q}) = \alpha_0(\boldsymbol{q}) + \alpha_1(\boldsymbol{q})s + \alpha_2(\boldsymbol{q})s^2 + \alpha_3(\boldsymbol{q})s^3 + ... + \alpha_n(\boldsymbol{q})s^n \tag{5.5}$$

where the coefficients $\alpha_i(\boldsymbol{q})$ are affine/linear functions of $\boldsymbol{q}$ such that the order n of $p(s)$ is preserved; that is $\boldsymbol{\alpha} \in \Pi_a$.

In a similar manner to Kharitonov's theorem for interval polynomial families, a theorem to check the stability of affine polynomial families is given by

Theorem 3 (Edge Theorem) *The affine polynomial family in Eq.* (5.5) *is Hurwitz iff all its edge polynomials of the space Π_a are Hurwitz.*

As one can see, the Edge Theorem requires checking all of the exposed edges of the affine polynomial family, which would be a high computational load. A simpler method, that of the Generalized Kharitonov's Theorem is stated in Bhattacharyya et al. (1995), which only requires the checking of a sum of interval polynomials which reduces the complexity of the computation significantly (Bruyere, 2004). For more detail, please refer to Bhattacharyya et al. (1995), page 300.

5.1.3 Multi-Affine Polynomial Family

The results reviewed so far are useful to assess the robustness of uncertain systems during the controller design. However, these methods are still very restricted since only one very special type of uncertainties is addressed. Noting that polynomial family value sets can be produced from its parameter space vertices, a different type of method, the Mapping Theorem (Bhattacharyya et al., 1995; Barmish, 1994) is developed by computing the value set of a multi-affine polynomial family as a convex hull which reduces the complexity to that of computing the convex hull of the parameter box vertices. This strategy is a quite powerful stability analysis for a much wider type of polynomial family, although it still introduces some conservatism.

The definitions of a multi-affine polynomial family, vertex polynomials and value sets are first given before presenting the Mapping Theorem.

Definition 6 (Multi-affine/Multi-linear polynomial family) *A multi-affine polynomial family, $\Phi_m(s)$, is a family of polynomials in the form*

$$p(s, \boldsymbol{q}) = \alpha_0(\boldsymbol{q}) + \alpha_1(\boldsymbol{q})s + \alpha_2(\boldsymbol{q})s^2 + \alpha_3(\boldsymbol{q})s^3 + ... + \alpha_n(\boldsymbol{q})s^n \tag{5.6}$$

where the coefficient $\alpha_i(\boldsymbol{q})$ are multi-affine/multi-linear functions of $\boldsymbol{q} \in \Pi_b$ such that the order n of $p(s)$ is preserved.

Definition 7 (Vertex polynomials) *The vertex polynomials, $\Phi_m^V(s)$, of the multi-affine polynomial family, $\Phi_m(s)$, is the family of polynomials described by the vertices of Π_b, Π_b^V, in the form*

$$\Phi_m^V(s) = \{p(s, \boldsymbol{q}) \in \Phi_m(s), \boldsymbol{q} \in \Pi_b^V\} \tag{5.7}$$

where $\Pi_b^V = \{\boldsymbol{q} \in \Pi_b, \forall j \in \mathbb{N}_m \quad q_j = q_j^- \vee q_j = q_j^+\}$.

Definition 8 (Value set) *The value set of a multi-linear polynomial $p(s, \Phi_b)$, $\Delta(s^*)$, is the image in the s-plane of its family at each specific generalized frequency s^*, in the form*

$$\Delta(s^*) = \{z \in \mathbb{C}, \quad \forall \boldsymbol{q} \in \Pi_b \quad z = p(s^*, \boldsymbol{q})\}. \tag{5.8}$$

Theorem 4 (Mapping theorem) *For a multi-linear polynomial family, $\Phi_m(s)$, on Pi_b, the value set at s^* of the polynomial family, $\Delta(s^*)$, is included in its convex hull, $co(\Delta(s^*))$, and in the convex hull of the value set of its vertex polynomials $\Phi_m^V(s)$, $co(\Delta^V(s^*))$, hence*

$$\forall s^* \in \mathbb{C}, \quad \Delta(s^*) \subset \Delta^V(s^*). \tag{5.9}$$

Therefore, the multi-affine uncertainty problem is reduced to examining an affine or interval value set which can be tested by the methods described so far. This over-bounding method provides an efficient way to reduce the computational load, but it introduces some conservatism which can be very large (see the examples in Bhattacharyya et al. (1995); Bruyere (2004)) since the convex hull can be much larger than the actual value set. To reduce this conservatism, the parameter space can be partitioned into subspaces which generate several overlapping convex hulls each of which can be tested. However, this approach will increase the computation load.

5.2 $\mathcal{D}$-Stability of Polynomic Polynomial Families

The approaches reviewed so far are very useful in reducing the complexity of testing a polynomial family, but the major drawback is that they still require a

frequency sweep to check the polynomial stability. These approaches are not easy to use to check the stability of polynomials for $\mathcal{D}$-regions which are used to define the range of damping ratio and natural frequency required for stability and performance assessment during controller design.

The following theorem from Djaferis (1995) can be used to determine the $\mathcal{D}$-stability of a polynomial family by using root checking within a specific $\mathcal{D}$-contour in the s plane. Unlike the method of frequency sweeping, the number of check using this approach only depends on the order of polynomial and the number of chosen sector angles. This theorem provides only a sufficient condition for robust $\mathcal{D}$-stability for polynomic polynomial families, but it provides a necessary condition as well for the important case of affine polynomial families.

Definition 9 (Polynomic polynomial family) *A polynomic polynomial family, $\Phi_p(s)$, is a family of polynomial in the form*

$$p(s, \boldsymbol{q}) = \alpha_0(\boldsymbol{q}) + \alpha_1(\boldsymbol{q})s + \alpha_2(\boldsymbol{q})s^2 + \alpha_3(\boldsymbol{q})s^3 + ... + \alpha_n(\boldsymbol{q})s^n \tag{5.10}$$

where the coefficients $\alpha_i(\boldsymbol{q})$, $i \in \mathbb{N}_n$, are polynomic functions of $\boldsymbol{q}$, such that the order n of $p(s)$ is preserved.

With these definitions, the following theorem can be proved.

Theorem 5 (Finite Inclusion Theorem, FIT) *For a polynomic polynomial family, $\Phi_p(s)$, Let $\Gamma \subset \mathbb{C}$ be a closed Jordan curve such that int(Γ) is convex. Then for all $\boldsymbol{q} \in \Pi_b$, $p(s, \boldsymbol{q}) \in \Phi_p(s)$ is of degree n and has all its roots in int(Γ) if there exists $m \geq 1$ intervals $(c_k, d_k) \subset \mathbb{R}$ and a counterclockwise sequence of points $s_k \in \Gamma$, $1 \leq k \leq m$, such that*

$$\forall 1 \leq k < m \quad max\{d_{k+1} - c_k, d_k - c_{k-1}\} \leq \pi \tag{5.11}$$

$$max\{d_m - (c_1 + 2n\pi), (d_1 + 2n\pi) - c_m\} \leq \pi \tag{5.12}$$

$$\forall 1 \leq k \leq m \quad p(s_k, \Pi_b) \subset \{re^{j\theta} | r > 0, \theta \in (c_k, d_k)\} \tag{5.13}$$

With this FIT theorem, the complexity of checking the $\mathcal{D}$-stability of a polynomial family is reduced to checking a finite number of value sets at some generalized frequencies. However, it can be very complex to calculate the value set of a polynomic polynomial family required in Eq. (5.13). Fortunately, the Mapping theorem shows that the value set of a polynomial family is always contained in the convex hull of its vertex polynomials. Therefore, the image set can

be overbounded by calculating the convex hull of the vertex polynomials. This method is conservative, but this can be reduced by subdividing the parameter space recursively if necessary. Another limitation is that the number of uncertain parameters should be less than 10 in general, as the number of vertex checks increases geometrically.

5.3 Robust Stability Analysis of SISO Systems

The control system shown in Eq. (2.58) is a MIMO system with three coupled control channels. However, the robust stability of a MIMO system with parametric uncertainties is still a complex and difficult problem to solve. As a compromise, the analysis methods used for SISO systems can be adopted to analyse the stability of systems with parametric uncertainties by assuming that all the coupling terms are treated as unstructured uncertainties. Such an assumption will give rise to some conservativeness, but it is not usually significant because the number of coupling terms are relative small with respect to the rest of the entries in matrix $\boldsymbol{A}(\boldsymbol{p})$. For the L_2 point formation problem, the robustness analysis for each of the three-axes is similar due to similar dynamics and controller in each axis. Therefore, only the x-axis system will be analysed here in detail.

5.3.1 X-axis Nominal Closed-Loop Model

The SISO closed-loop control system for the L_2 point formation problem can be obtained by substituting the control law in Eq. (4.21) into Eq. (2.58), neglecting the coupling effects. This yields the x-axis dynamic equations as:

$$\dot{\boldsymbol{x}}_x = \boldsymbol{A}_x(\boldsymbol{p})\boldsymbol{x}_x + \boldsymbol{B}_x\boldsymbol{K}_x\boldsymbol{x}_x \quad \boldsymbol{y}_x = \boldsymbol{C}_x\boldsymbol{x}_x \tag{5.14}$$

where $\boldsymbol{x}_x = [\int \delta x, \delta x, \delta \dot{x}]^T$, $\boldsymbol{B}_x = [0 \;\; 0 \;\; 1]^T$, $\boldsymbol{C} = \boldsymbol{I}_3$,

$$\boldsymbol{K}_x = \begin{bmatrix} -K_{ux}^{-1}K_{ax} & -K_{ux}^{-1}K_{cx} & -K_{ux}^{-1}K_{ix} \end{bmatrix},$$

$$\boldsymbol{A}_x(\boldsymbol{p}) = \begin{bmatrix} 0 & 1 & 0 \\ 0 & 0 & 1 \\ 0 & a_{41}(\boldsymbol{p}) & a_{44}(\boldsymbol{p}) \end{bmatrix} \tag{5.15}$$

where the controller gains are given in Eq. (4.68) ~ Eq. (4.70).

To carry out the robust stability analysis, the system shown in Eq. (5.74) is assumed to be an uncertain LTI system, whose uncertainties are caused by variations in $\boldsymbol{p}$. Then, the nominal transfer function from reference variable x_d to output x is:

$$G(s) = \boldsymbol{C}(\boldsymbol{I}s - \boldsymbol{A} - \boldsymbol{B}\boldsymbol{K})^{-1} = n(s)/d(s) \tag{5.16}$$

where the subscript x is dropped, $n(s) = K_a$,

$$d(s) = K_u s^3 + (K_i - a_{44}K_u)s^2 + (K_c - a_{41}K_u)s + K_a \tag{5.17}$$

5.3.2 Parametric Uncertain Closed-Loop Model

Two sources of parametric uncertainty are considered in this section to analyse the stability margins of the nominal closed-loop system.

The first source is uncertainty in the controller parameters K_u, K_i, K_c, and K_a, which not only denote the uncertainties of the actuators, but also include the variation of the spacecraft mass and the measurement error of the sensors.

The other source of uncertainty is in the dynamic parameters a_{41} and a_{44}, arising from variation in the system dynamic parameters.

5.3.2.1 Uncertainties in Controller Parameters

From Eq. (4.68) ~ Eq. (4.70), the nominal values of controller parameters are given by:

$$\hat{K}_u = 1/d_0, \quad \hat{K}_i = (a_{41} + d_1)/d_0, \quad \hat{K}_i = (a_{44} + d_2)/d_{x0}, \quad \hat{K}_a = 1 \tag{5.18}$$

Assuming an error model of the form:

$$K_u = \hat{K}_u + \Delta K_u, \quad K_i = \hat{K}_i + \Delta K_i, \quad K_c = \hat{K}_c + \Delta K_c, \quad K_a = \hat{K}_a + \Delta K_a \ , \tag{5.19}$$

then, the uncertainty in the characteristic polynomial Eq. (5.17) is:

$$\begin{aligned} d(s) = {} & (\hat{K}_u + \Delta K_u)s^3 + ((\hat{K}_i + \Delta K_i) - a_{44}(\hat{K}_u + \Delta K_u))s^2 \\ & + ((\hat{K}_c + \Delta K_c) - a_{41}(\hat{K}_u + \Delta K_u))s + (\hat{K}_a + \Delta K_a) \end{aligned} \tag{5.20}$$

Define the entries of the relative error vector $\boldsymbol{q}$ of the controller gains as $q_1 \triangleq \Delta K_u/\hat{K_u}$, $q_2 \triangleq \Delta K_i/\hat{K_i}$, $q_3 \triangleq \Delta K_c/\hat{K_c}$, $q_4 \triangleq \Delta K_a/\hat{K_a}$, Eq. (5.24) can be described by:

$$d(s) = \delta_0(s) + \sum_{i=1}^{4} \delta_i(s) q_i \tag{5.21}$$

where:

$\delta_0(s) = \hat{K_u}s^3 + (\hat{K_i} - a_{44}\hat{K_u})s^2 + (\hat{K_c} - a_{41}\hat{K_u})s + \hat{K_a} = (d_0 + d_1 s + d_2 s^2 + s^3)/d_0$,

$\delta_1(s) = \hat{K_u}s^3 - a_{44}\hat{K_u}s^2 - a_{41}\hat{K_u}s$,

$\delta_2(s) = \hat{K_i}s^2$,

$\delta_3(s) = \hat{K_c}s$,

$\delta_4(s) = \hat{K_a}$.

This can be rewritten in affine form as:

$$d(s) = \sum_{i=0}^{3} \alpha_i(\boldsymbol{q}) s^i \tag{5.22}$$

where:

$\alpha_0(\boldsymbol{q})) = 1 + \hat{K_a}q_4$,

$\alpha_1(\boldsymbol{q})) = d_1/d_0 - \hat{K_u}a_{41}q_1 + \hat{K_c}q_3$,

$\alpha_2(\boldsymbol{q})) = d_2/d_0 - \hat{K_u}a_{44}q_1 + \hat{K_i}q_2$,

$\alpha_3(\boldsymbol{q})) = 1/d_0 - \hat{K_u}q_1$,

and where the parameters in $\boldsymbol{q}$ lie in a parameter box Π_b, that is $q_i^- \le q_i \le q_i^+$, $i = 1, 2, 3, 4$, where q_i^- and q_i^+ are constants.

5.3.2.2 Uncertainties in Dynamic Derivatives

From Eq. (2.40), the nominal values of dynamic parameters can be defined as:

$$\hat{a_{41}} = n^2 + 2\sigma, \quad \hat{a_{44}} = 0 \tag{5.23}$$

Assuming an error model of the form:

$$a_{41} = \hat{a_{41}} + \Delta a_{41}, \quad a_{44} = \hat{a_{44}} + \Delta a_{44} \tag{5.24}$$

then, the uncertainty in the characteristic polynomial Eq. (5.17) is:

$$d(s) = \hat{K_u}s^3 + (\hat{K_i} - \hat{a_{44}} + \Delta a_{44}\hat{K_u})s^2 + (\hat{K_c} - \hat{a_{41}} + \Delta a_{41})\hat{K_u}s + \hat{K_a} \tag{5.25}$$

Define the entries of the error vector $\boldsymbol{q}$ of the dynamic parameters as $q_1 \triangleq \Delta a_{44}$, $q_2 \triangleq \Delta a_{41}$;, then Eq. (5.25) can be described by:

$$d(s) = \delta_0(s) + \sum_{i=1}^{2} \delta_i(s) q_i \tag{5.26}$$

where q_i are the errors, and:

$\delta_0(s) = \hat{K}_u s^3 + (\hat{K}_i - a_{44}\hat{K}_u)s^2 + (\hat{K}_c - a_{41}\hat{K}_u)s + \hat{K}_a = (d_0 + d_1 s + d_2 s^2 + s^3)/d_0$,

$\delta_1(s) = -\hat{K}_u s^2$,

$\delta_2(s) = -\hat{K}_u s$.

The affine form of this equation is:

$$d(s) = \sum_{i=0}^{3} \alpha_i(\boldsymbol{q}) s^i \tag{5.27}$$

where $\alpha_0(\boldsymbol{q})) = 1$,

$\alpha_1(\boldsymbol{q})) = d_1/d_0 - \hat{K}_u q_1$,

$\alpha_2(\boldsymbol{q})) = d_2/d_0 - \hat{K}_u q_2$,

$\alpha_3(\boldsymbol{q})) = 1/d_0$.

5.3.2.3 Uncertainties in both Control and Dynamic Parameters

The nominal values of controller parameters and dynamic parameters are defined in Eq. (5.23) and Eq. (5.18). Assuming an error model of the form:

$$\begin{aligned} &K_u = \hat{K}_u + \Delta K_u, \quad K_i = \hat{K}_i + \Delta K_i, \quad K_c = \hat{K}_c + \Delta K_c, \\ &K_a = \hat{K}_a + \Delta K_a, \quad a_{41} = \hat{a_{41}} + \Delta a_{41}, \quad a_{44} = \hat{a_{44}} + \Delta a_{44} \end{aligned}, \tag{5.28}$$

then, the uncertainty in the characteristic polynomial in Eq. (5.17) is:

$$\begin{aligned} d(s) = (\hat{K}_u + \Delta K_u)s^3 + ((\hat{K}_i + \Delta K_i) - (\hat{a_{44}} + \Delta a_{44})(\hat{K}_u + \Delta K_u))s^2 + \\ ((\hat{K}_c + \Delta K_c) - (\hat{a_{41}} + \Delta a_{41})(\hat{K}_u + \Delta K_u))s + (\hat{K}_a + \Delta K_a) \end{aligned} \tag{5.29}$$

Defining the entries of relative error vector $\boldsymbol{q}$ of uncertain parameters as:

$q_1 \triangleq \Delta K_u/\hat{K}_u$,

$q_2 \triangleq \Delta K_i/\hat{K}_i$,

$q_3 \triangleq \Delta K_c / \hat{K}_c$,

$q_4 \triangleq \Delta K_a / \hat{K}_a$,

$q_5 \triangleq \Delta a_{44} / n_c$, ($n_c$, the velocity of earth orbit, used instead of $\hat{a}_{44}$),

$q_6 \triangleq \Delta a_{41} / \hat{a}_{41}$.

then Eq. (5.81) can be written in the form:

$$d(s, \boldsymbol{q}) = \delta_0(s) + \sum_{i=1}^{2} \delta_i(s) q_i + \sum_{j=5}^{6} \delta_{1j}(s) q_1 q_j \tag{5.30}$$

where q_i are the errors, and:

$\delta_0(s) = \hat{K}_u s^3 + (\hat{K}_i - \hat{a_{44}} \hat{K}_u) s^2 + (\hat{K}_c - \hat{a_{41}} \hat{K}_u) s + \hat{K}_a = (d_0 + d_1 s + d_2 s^2 + s^3)/d_0$,

$\delta_1(s) = \hat{K}_u s^3 - \hat{a_{44}} \hat{K}_u s^2 - \hat{a_{41}} \hat{K}_u s$,

$\delta_2(s) = \hat{K}_i s^2$,

$\delta_3(s) = \hat{K}_c s$,

$\delta_4(s) = \hat{K}_a$,

$\delta_5(s) = -\hat{a_{41}} \hat{K}_u s$,

$\delta_6(s) = -n_c \hat{K}_u s^2$,

$\delta_{15}(s) = -\hat{a_{41}} \hat{K}_u s$,

$\delta_{16}(s) = -n_c \hat{K}_u s^2$.

This equation can be rewritten in multi-affine form as:

$$d(s, \boldsymbol{q}) = \sum_{i=0}^{3} \alpha_i(\boldsymbol{q}) s^i \tag{5.31}$$

where:

$\alpha_0(\boldsymbol{q}) = 1 + \hat{K}_a q_4$,

$\alpha_1(\boldsymbol{q}) = d_1/d_0 - \hat{K}_u \hat{a_{41}} q_1 + \hat{K}_c q_3 - \hat{a_{41}} \hat{k_u} q_5 - \hat{a_{41}} \hat{k_u} q_1 q_5$,

$\alpha_2(\boldsymbol{q}) = d_2/d_0 - \hat{K}_u a_{44} q_1 + \hat{K}_i q_2 - n_c \hat{k_u} q_6 - n_c \hat{k_u} q_1 q_6$,

$\alpha_3(\boldsymbol{q}) = 1/d_0 + \hat{K}_u q_1$,

and where the parameters $\boldsymbol{q}$ lie in a parameter box Π_b (Bruyere, 2004), that is $q_i^- \le q_i \le q_i^+$, $i = 1, ..., 6$, where q_i^- and q_i^+ are constants.

5.3.3 Hurwitz Stability Analysis

5.3.3.1 Hurwitz Stability Analysis for Uncertainties in Controller Parameters

To analyse the Hurwitz stability of the affine polynomial in Eq. (5.22), it is sufficient to check the polynomials on the exposed edges of Π_b with the Edge Theorem (Djaferis, 1995). However, the computational complexity is still the main obstacle associated with the application of the Edge Theorem because the number of edges can be excessively large with large degree n. Instead of working with the edge of Π_b, the Mapping Theorem (Bhattacharyya et al., 1995) only requires checking the convex hull vertex polynomials. Its keystone is to obtain the convex hull of mapped vertices in the image plot, and then utilize the Zero Exclusion Condition (Djaferis, 1995) to test for stability.

Using the Mapping Theorem, the convex hull of the mapped vertices across a grid of frequencies is shown in Fig. 5.3, where the Zero Exclusion Condition is satisfied for parameter variations of 30% for K_i and K_c, 60% for K_u and K_a. The greatest effect on stability is in the variation of K_i and K_c, which means they are more sensitive than the other two parameters K_u and K_a.

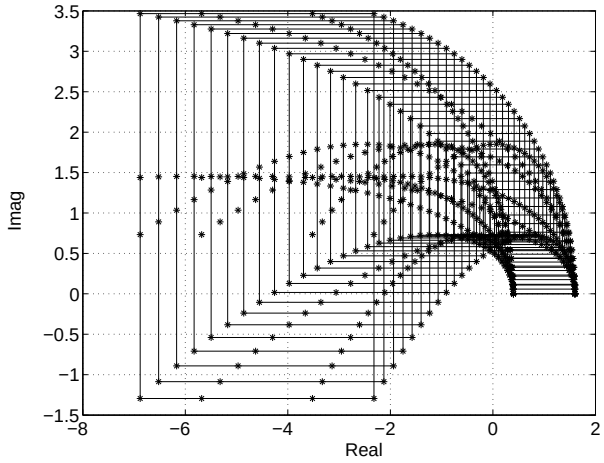

Figure 5.3: Hurwitz Stability Analysis with Mapping Theorem for Controller Parameters

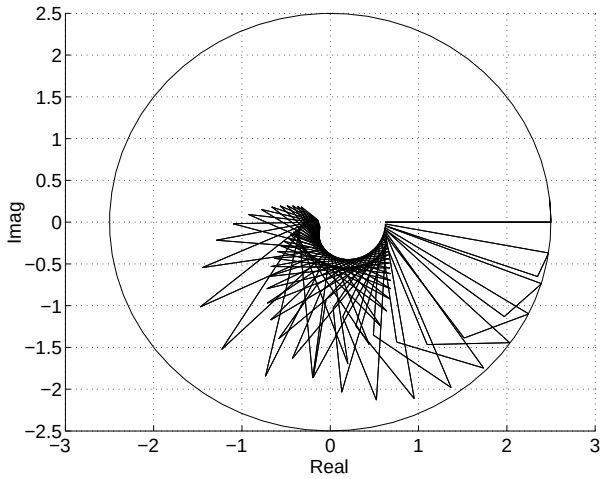

Figure 5.4: Frequency Template of G_k and H_∞ Stability Margin for Variations in Controller Parameters

5.3.3.2 Hurwitz Stability Analysis for Uncertainties in Dynamic Derivatives

Using the Mapping Theorem, the convex hull of the mapped vertices across a grid of frequencies is shown in Fig. 5.5, where the Zero Exclusion Condition is satisfied for parameter variations of 100 times a_{41} and a_{44} (while setting the angular velocity of earth n_c as its nominal values), which indicates the dynamic derivatives have negligible effect on the stability robustness of the system.

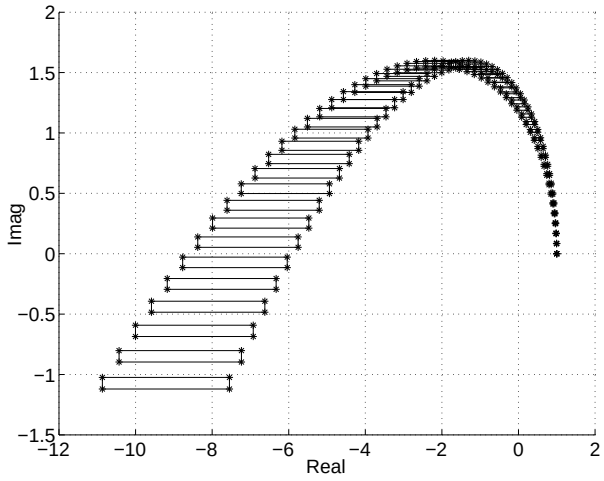

Figure 5.5: Hurwitz Stability Analysis with Mapping Theorem for Dynamic Derivatives

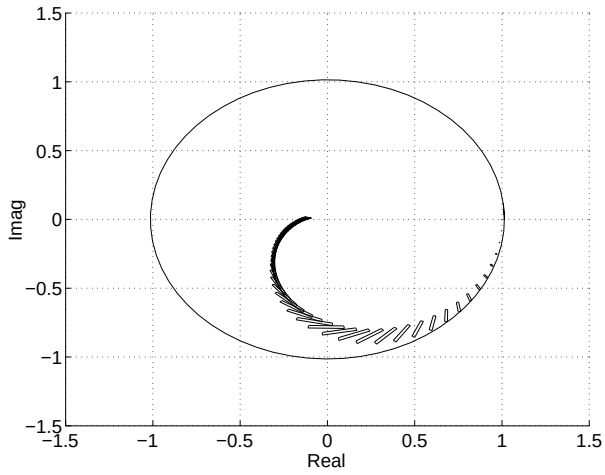

Figure 5.6: Frequency Template of G_k and H_∞ Stability Margin for Variations in Dynamic Derivatives

5.3.3.3 Worst-Case H_∞ Stability Margin

For unstructured uncertainties, the analysis usually uses the maximum tolerance of the unstructured perturbation that doesn't destroy the closed-loop system stability to measure the stability margin of the system. This maximum tolerance, specified as a ball of bounded norm, can be obtained by computing the maximum H_∞ norm of the Kharitonov polynomials using the following theorem (Bhattacharyya et al., 1995; Tsourdos et al., 2001).

Theorem 6: *Let $G(s) = N(s)/D(s)$ be an uncertain closed-loop system and $G_k(s) = \{K_N^i(s)/K_D^j(s) |\ i, j \in \{1, 2, 3, 4\}\}$ be the interval family of stable proper systems with $K_N^i(s)$ and $K_D^j(s)$ denoting the Kharitonov polynomials associated with $N(s)$ and $D(s)$, respectively. Then G is stable for all perturbations ΔG such that $\|\Delta G\|_\infty < \alpha$ iff $\alpha \leq 1/\max\|G_k\|_\infty$.*

This theorem can reduce the computation load significantly because the norms of an infinite family is studied by examining those of a finite set. To compute the worst-case H_∞ stability margin of the closed-loop system, two methods can be employed: one is to plot the frequency reponse $G(j\omega)$ and obtain the convex hull of its Kharitonov polynomials; the other one is to calculate the H_∞ norm of the Kharitonov polynomials directly.

Using the variation in controller parameters shown in Section 5.3.3.1, Fig.(5.4) shows the frequency response of G_k where the worst-case H_∞ stability margin is

$\alpha = 1/2.503 = 0.399$.

The transfer function $G(s)$ is shown in Eq. (5.16). The numerator of G can be set to its nominal value, so that G_k has the following four elements:

$$\begin{aligned} \|G_1\|_\infty &= 2.500 \quad \|G_2\|_\infty = 0.625 \\ \|G_3\|_\infty &= 1.991 \quad \|G_4\|_\infty = 2.500 \end{aligned} \tag{5.32}$$

Therefore, the system with respect to variation in controller parameters in Section 5.3.3.1 is still Hurwitz under any unstructured feedback perturbation of H_∞ norm less than $\alpha = 1/2.500 = 0.400$. This result is the same as that obtained from Fig. 5.4.

Using the variation of dynamic derivatives shown in Section 5.3.3.2, Fig. 5.6 shows the frequency response of G_k and the worst-case H_∞ stability margin is $\alpha = 1/1.016 = 0.984$.

Noting the transfer function $G(s)$, G_k then has following elements:

$$\begin{aligned} \|G_1\|_\infty &= 1.014 \quad \|G_2\|_\infty = 1.000 \\ \|G_3\|_\infty &= 1.000 \quad \|G_4\|_\infty = 1.003 \end{aligned} \tag{5.33}$$

Using Theorem 6, if the entire family of polynomials is Hurwitz, then the unstructured feedback perturbation of the H_∞ norm should less than $\alpha = 1/1.014 = 0.986$.

5.3.4 $\mathcal{D}$-Stability Analysis by Using the FIT Approach

Using the FIT theorem, the $\mathcal{D}$-stability analysis of each control channel for the L_2 point formation flying can be investigated using each parametric uncertain closed-loop model. For the uncertain characteristic polynomial in Eq. (5.30), the $\mathcal{D}$-stability region should surround the nominal poles defined with damping ratio and natural frequency bounds, which depend on the performance requirements of the closed loop system. So the minimum damping ratio is set to 0.7, the minimum $\xi\omega_n$ is set to 3/4 of the real part of the complex pair poles, and the maximum natural frequency is set to 4/3 of the third pole. Thus, the $\mathcal{D}$-stability region is a symmetrical cone shape with respect to real axis.

The sector angle used for the FIT theorem is chosen as $3\pi/4$, which leads to 25 sectors to cover the range for a third-order polynomial. To reduce the

complexity of evaluating the value set of the multi-affine polynomial family in Eq. (5.31), the Mapping Theorem is used to calculate the convex hull of the vertex polynomials. There are 6 uncertain parameters in Eq. (5.31), therefore $2^6 = 64$ vertex polynomials are required to be evaluated to obtain its convex hull. The results are shown in Fig. 5.7 ~ Fig. 5.10.

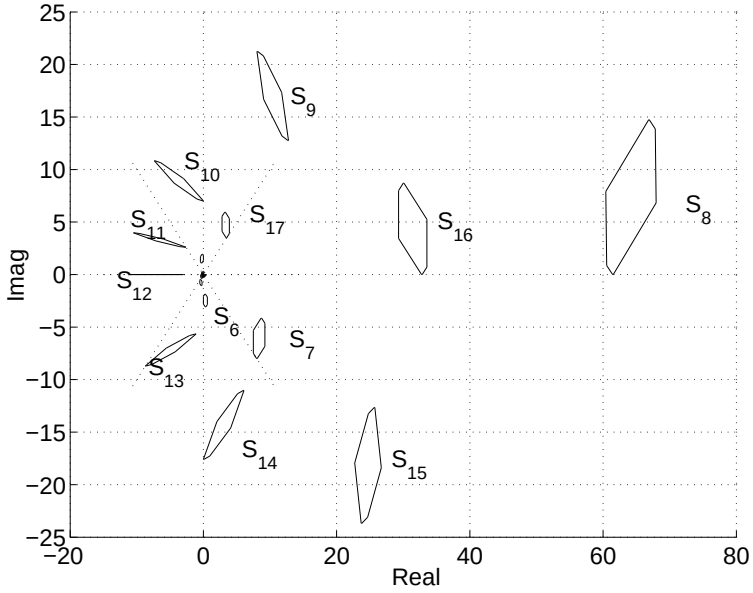

Figure 5.7: $\mathcal{D}$-stability for Uncertainty up to ±4.5% of the Six Independent Parameters for X-axis Control

For the analysis, all parameters are assumed to have a uniform percentage uncertainty. From Fig. 5.7 and Fig. 5.8, the maximum uncertainty of the system parameters is ±4.5% whilst satisfying the Zero Exclusion Theorem and remaining within the $\mathcal{D}$-stable region. This indicates that the QLPV PEA controller can ensure the robust $\mathcal{D}$-stability of the formation control system with up to ±4.5% uncertainty in the controller parameters and dynamic derivatives. From Fig. 5.9, it is shown that the poles of closed loop system are inside the $\mathcal{D}$-stability region with up to ±4.5% uncertainties. Using the convex hull shape and its corresponding values, shown in Fig. 5.10, one can examine the effect of every parameter uncertainty on the closed-loop system robustness as all six parameters have the uniform percentage variation. Obviously, the uncertainty of controller parameters, ΔK_c, ΔK_i, ΔK_a and ΔK_u, are the main factors in the value set size and the uncertainty of dynamic derivatives Δa_{41} and Δa_{44} have very little effect. Therefore, the controller parameters have much more sensitivity than dynamic derivatives

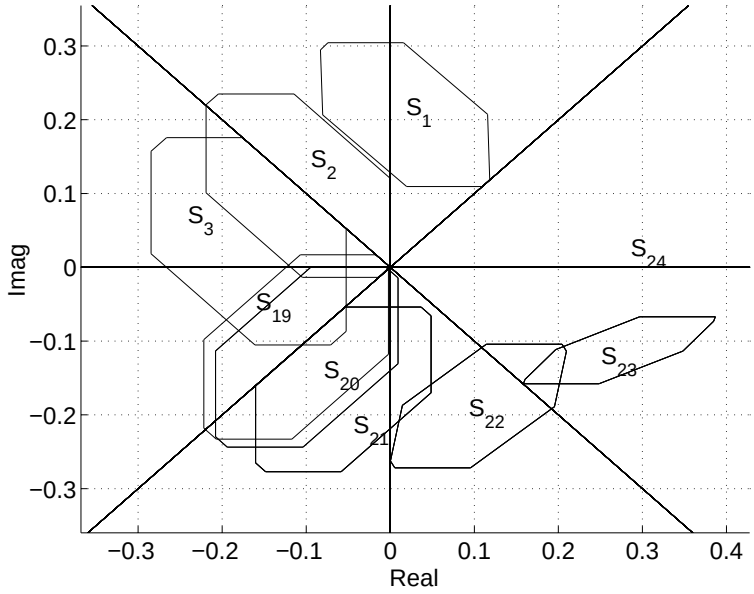

Figure 5.8: $\mathcal{D}$-stability for Uncertainty up to ±4.5% of the Six Independent Parameters for X-axis Control (zoom in of the previous figure)

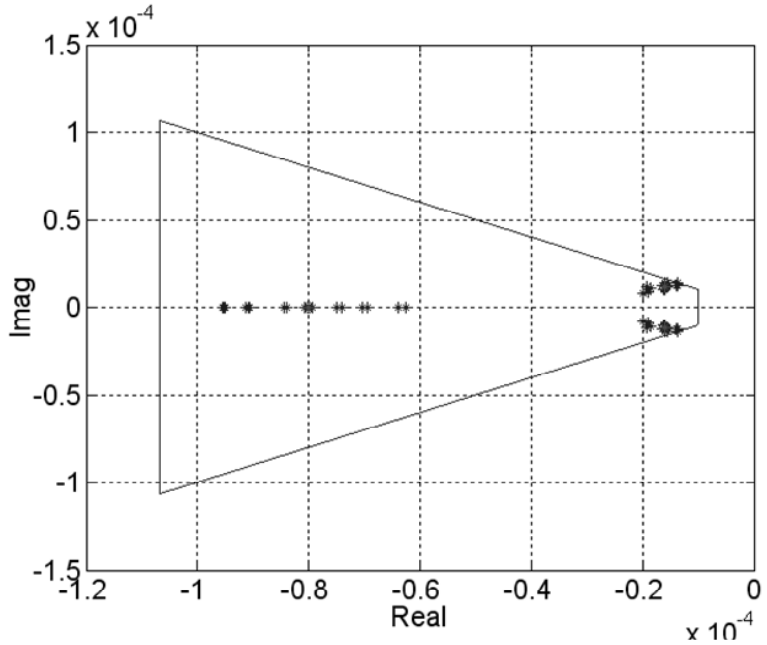

Figure 5.9: Poles of System with up to ±4.5% Uncertainty

for the $\mathcal{D}$-stability of x-axis control system.

Further, the shape of value set almost matches a polygon formed by ΔK_c, ΔK_i, ΔK_a and ΔK_u, which indicates that the multi-affine system is almost a linear uncertain system. Actually, since the dynamic derivatives have much less effect

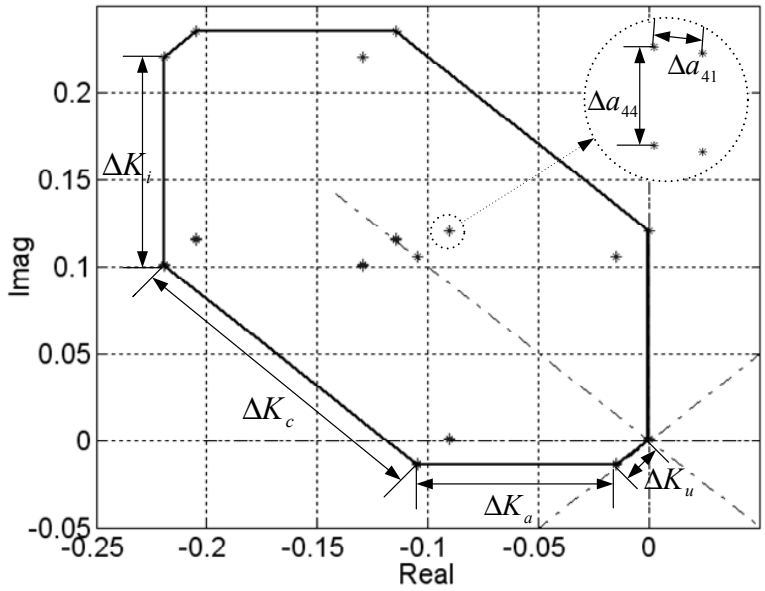

Figure 5.10: Convex Hull Induced by each Parameter with up to ±4.5% Uncertainty

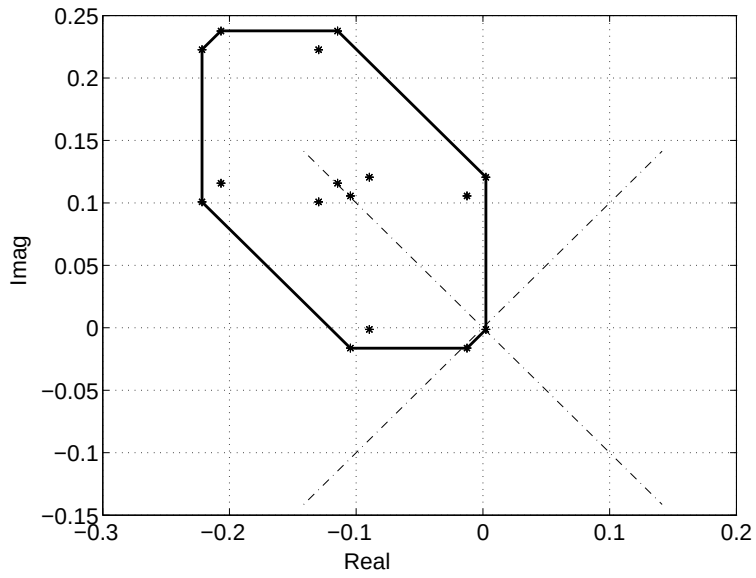

Figure 5.11: Convex Hull of Sector 2 of System with up to ±4.6% Uncertainty

than controller parameters for system $\mathcal{D}$-stability, it's not difficult to deduce that the multi-affine terms in Eq. (5.30)) can be neglected for the $\mathcal{D}$-stability analysis. This means the analysis of this system is not very conservative when using the FIT theorem which is sufficient and necessary for affine uncertain systems, which is illustrated in Fig. 5.11 and Fig. 5.12. Figure 5.11 is the convex hull of value set in sector 2 for uncertainty up to ±4.6% uncertainty. In the figure, the convex

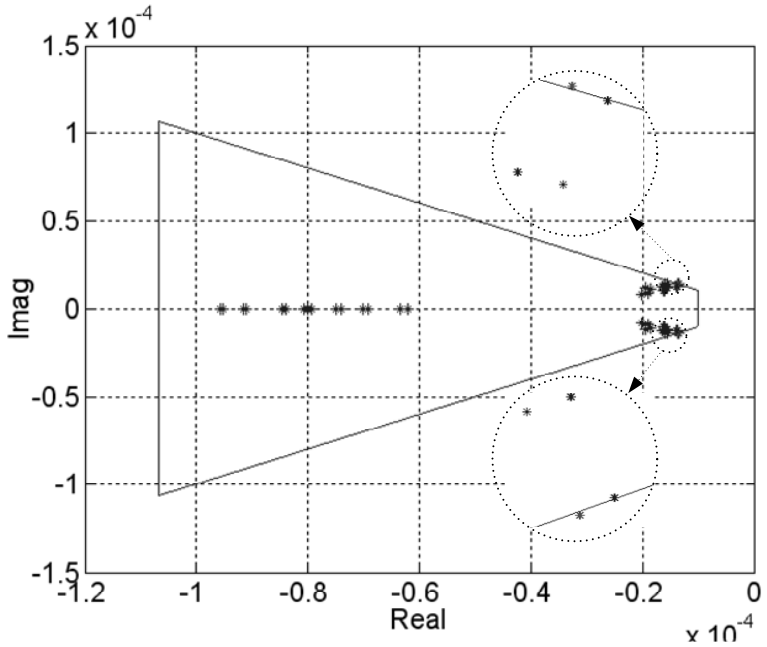

Figure 5.12: Poles of System by up to ±4.6% *Uncertainty*

hull includes the origin which violates the Zero Exclusion Theorem and means the system is D-unstable for this case. This conclusion is confirmed by examining the location of poles of the closed-loop system, shown in Fig. 5.12, where several poles are seem to be outside the $\mathcal{D}$-stability region.

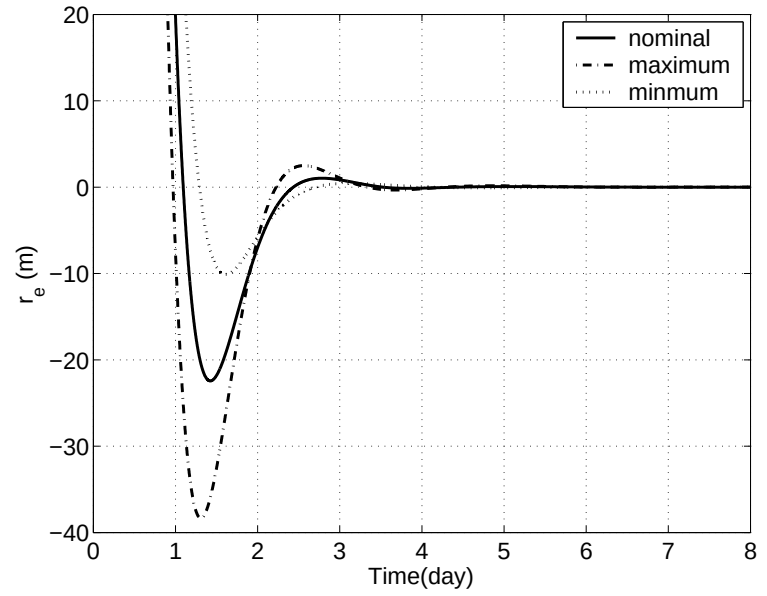

Figure 5.13: The Relative Position Errors of X-axis Control System with Uncertainties

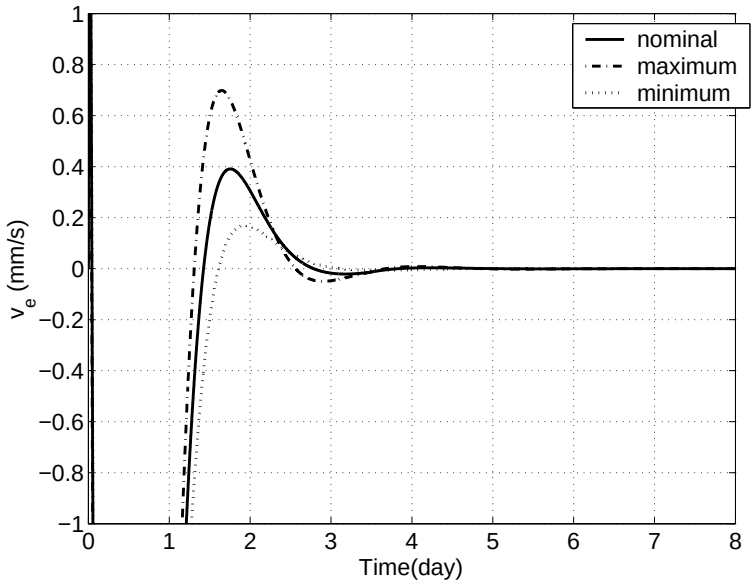

Figure 5.14: The Relative Velocity Errors of X-axis Control System with Uncertainties

Finally, a simulation with such uncertainties is carried out to confirm the performance and robustness of the system, and is shown in Fig. 5.13 and Fig. 5.14. The damping and rising time meet the system specifications and the results show that the system has good performance and robustness.

5.4 $\mathcal{D}$-Stability of Polynomial Matrices and Polynomial Matrix Polytopes

In order to study the effect of the coupling terms of the original MIMO system, this section will assess the robust stability of uncertain polynomial matrices and polynomial matrix polytopes by using Linear Matrix Inequalies.

Based on a general optimization methodology mixing quadratic and semidefinite programming, several more or less conservative LMI conditions are presented to determine the $\mathcal{D}$-stability of a polynomial matrix (Herion et al., 2001; Oliveira et al., 2002; Herion et al., 2001; Leite & Peres, 2003). These conditions are valid for checking stability of polynomial matrices and polynomial matrix polytopes in the subregion $\mathcal{D}$ in the complex plane. Apart from a convex region, this subregion may also be open, non-convex or even nonconnected, but cannot be an

intersecting region, for instance a conic sector, a typical clustering region in the left half-plane (Herion et al., 2001).

This section will present a sufficient and necessary LMI condition for polynomial matrices and a sufficient LMI condition for polynomial matrix polytopes to analyse robust stability in intersecting $\mathcal{D}$-regions. An intersecting region $\mathcal{D}$ is described by several disjoint regions. Therefore, the problem of analysing the stability of polynomial matrices and polytopes in an intersection $\mathcal{D}$-region can be transformed into that of analysing the stability of polynomial matrices and polytopes in each disjoint $\mathcal{D}$-region respectively. With this strategy, the performance of polynomial matrices and polytopes in many kinds of $\mathcal{D}$-regions, including both convex and non-convex regions, can be analysed easily and conveniently by using the LMI Control Toolbox in Matlab. Noting that the definition of an intersecting region usually includes complex values, but that the LMI solver in Matlab can only solve real-valued LMI problems, the real-valued LMI conditions associated with the complex-valued LMI conditions in Herion et al. (2001) and Herion et al. (2001) are developed as well.

5.4.1 $\mathcal{D}$-Stability of Uncertain Systems

Assuming a non-singular $n \times n$ complex polynomial matrix $\boldsymbol{A}(s)$ of degree d given as:

$$\boldsymbol{A}(s) = \boldsymbol{A}_0 + \boldsymbol{A}_1 s + ... + \boldsymbol{A}_d s^d \in \mathbb{C}^{n\times n}[s] \tag{5.34}$$

then a complex value $\xi \in \mathbb{C}$ is defined as a zero of $\boldsymbol{A}(s)$ if there is a loss of rank in $\boldsymbol{A}(s)$, that is $\text{Rank}\boldsymbol{A}(\xi) < \text{Rank}\boldsymbol{A}(s)$, and the set ξ can be computed from the determinant of $\boldsymbol{A}(s)$ (Kailath, 1980).

For a given subregion $\mathcal{D}$ in the complex plane, the problem of $\mathcal{D}$-stability of $\boldsymbol{A}(s)$ is to look for conditions that can ensure all the zeros of $\boldsymbol{A}(s)$ belong to $\mathcal{D}$. Given N $n \times n$ complex polynomials matrices $\boldsymbol{A}_1(s)$, $\boldsymbol{A}_2(s)$, ..., $\boldsymbol{A}_N(s)$ of degree d, the polynomial matrix polytope $\mathbb{P} \subset \mathbb{C}^{n\times n}[s]$ as the set of all polynomial matrices can be written as:

$$\boldsymbol{A}(s,\lambda) = \lambda_1 \boldsymbol{A}_1(s) + \lambda_2 \boldsymbol{A}_2(s) + ... + \lambda_N \boldsymbol{A}_N(s), \quad \lambda_i \geq 0, \quad \sum_{i=1}^{N} \lambda_i = 1. \tag{5.35}$$

The aim here is to know whether $\mathbb{P}$ is $\mathcal{D}$-stable, that is whether all polynomial matrices $\boldsymbol{A}(s,\lambda)$ are $\mathcal{D}$-stable. For simplicity and without loss of generality, it is supposed that no matrix has zeros at infinity in the polytope $\mathbb{P}$ (Herion et al., 2001).

5.4.2 Definition of the LMI $\mathcal{D}$-Region

Using the definition in Herion et al. (2001), a general LMI $\mathcal{D}$-region is given as:

$$\mathcal{D} = \{s \in \mathbb{C} : \boldsymbol{B}_{00} + \boldsymbol{B}_{01}s + \boldsymbol{B}_{10}s^* + \boldsymbol{B}_{11}ss^* < 0\} \tag{5.36}$$

where the star represents transpose conjugate. The choice of matrix:

$$\boldsymbol{B} = \boldsymbol{B}^* = \begin{bmatrix} \boldsymbol{B}_{00} & \boldsymbol{B}_{01} \\ \boldsymbol{B}_{10} & \boldsymbol{B}_{11} \end{bmatrix} \in \mathbb{C}^{2k\times 2k} \tag{5.37}$$

defines the $\mathcal{D}$-region to be tested, where k is the order of the region. Such stability regions, including first and second order regions, are introduced in a more general setting in Herion et al. (2001). In this thesis, only half-plane region, disc region, parabola region and their intersection are considered. For more details of other regions, see Herion et al. (2001). A half-plane region $\mathcal{D} = \{s = x + jy \in \mathbb{C} : ax + by + c < 0, a, b, c \in \mathbb{R}\}$, can be described in matrix form as:

$$\boldsymbol{B} = \begin{bmatrix} 2c & a + jb \\ a - jb & 0 \end{bmatrix}. \tag{5.38}$$

A disc region $\mathcal{D} = \{s \in \mathbb{C} : |s - s_0| < r, s_0 \in \mathbb{C}, r > 0 \in \mathbb{R}\}$, can be described in matrix form as:

$$\boldsymbol{B} = \begin{bmatrix} -r^2 + s_0 s_0^* & -s_0 \\ -s_0^* & 1 \end{bmatrix} \in \mathbb{C}^{2\times 2}. \tag{5.39}$$

Finally, a parabola region $\mathcal{D} = \{s = x + jy \in \mathbb{C} : x + x_0 + a^2y^2 < 0, x_0, a \in \mathbb{R}\}$, can be described in matrix form as:

$$\boldsymbol{B} = \begin{bmatrix} 4x_0 & 0 & 2 & a \\ 0 & 1 & a & 0 \\ 2 & a & 4a^2 & 0 \\ a & 0 & 0 & 0 \end{bmatrix} \in \mathbb{C}^{4\times 4}. \tag{5.40}$$

5.4.3 LMI Conditions for $\mathcal{D}$-Stability Analysis

Define a constant matrix $\mathcal{A}_i \in \mathbb{C}^{n\times(d+1)n}$ as:

$$\mathcal{A}_i = [\ \boldsymbol{A}_i^0,\ \ ...,\ \ \boldsymbol{A}_i^k,\ \ ...,\ \ \boldsymbol{A}_i^d\ ] \tag{5.41}$$

where $\boldsymbol{A}_i^k, k = 0, 1, ..., d$, are the coefficient matrices associated with the polynomial matrix $\boldsymbol{A}_i(s)$ defined in Eq. (5.34).

Denoting a solution for the right null-space of matrix $\mathcal{A}_i$ as $\mathcal{N}_{\mathcal{A}_i}$, that is $\mathcal{A}_i\mathcal{N}_{\mathcal{A}_i} = 0$, one has:

$$\mathcal{N}_{\mathcal{A}_i} = \begin{bmatrix} \boldsymbol{I}_{dn} \\ -(\boldsymbol{A}_i^d)^{-1}\left[\boldsymbol{A}_i^0,\ \ \boldsymbol{A}_i^1,\ \ ...,\ \ \boldsymbol{A}_i^{d-1}\right] \end{bmatrix} \tag{5.42}$$

Likewise, define a constant matrix $\mathcal{A}(\lambda) \in \mathbb{C}^{n\times(d+1)n}$ associated with the polynomial matrix polytope $\mathbb{P}$ as:

$$\mathcal{A}(\lambda) = \sum_{i=1}^{N}\lambda_i\mathcal{A}_i = \left[\ \sum_{i=1}^{N}\lambda_i\boldsymbol{A}_i^0,\ \ \sum_{i=1}^{N}\lambda_i\boldsymbol{A}_i^1,\ \ ...,\ \ \sum_{i=1}^{N}\lambda_i\boldsymbol{A}_i^{d-1}\ \right] \tag{5.43}$$

Thus, $\mathcal{N}_{\mathcal{A}(\lambda)}$, a solution for the right null-space of matrix $\mathcal{A}(\lambda)$ can be determined as:

$$\mathcal{N}_{\mathcal{A}(\lambda)} = \sum_{i=1}^{N}\lambda_i\mathcal{N}_{\mathcal{A}_i} = \begin{bmatrix} \boldsymbol{I}_{dn} \\ -\boldsymbol{n}a_0,\ \ -\boldsymbol{n}a_1,\ \ ...,-\boldsymbol{n}a_{d-1} \end{bmatrix} \tag{5.44}$$

where $\boldsymbol{n}a_1 = \sum_{i=1}^{N}\lambda_i(\boldsymbol{A}_i^d)^{-1}\boldsymbol{A}_i^0$, $\boldsymbol{n}a_1 = \sum_{i=1}^{N}\lambda_i(\boldsymbol{A}_i^d)^{-1}\boldsymbol{A}_i^1$, $\boldsymbol{n}a_{d-1} = \sum_{i=1}^{N}\lambda_i(\boldsymbol{A}_i^d)^{-1}\boldsymbol{A}_i^{d-1}$.

Finally, Let $\otimes$ denote the Kronecker product (Kailath, 1980) and define the projection matrix $\mathcal{R} \in \mathbb{C}^{2dn\times(d+1)n}$ (Herion et al., 2001; Oliveira et al., 2002) as:

$$\mathcal{R} = \begin{bmatrix} \boldsymbol{I}_{dn} & \boldsymbol{0}_{dn\times n} \\ \boldsymbol{0}_{dn\times n} & \boldsymbol{I}_{dn} \end{bmatrix}. \tag{5.45}$$

With this notation, the mains results are presented to determine the $\mathcal{D}$-stability of polynomial matrices and polynomial matrix polytopes.

Lemma 1: *The Polynomial matrix $\boldsymbol{A}_i(s)$ is $\mathcal{D}$-stable if and only if there exists a positive definite matrix $\boldsymbol{P}_i \in \mathbb{C}^{dn\times dn}$, solving the LMI feasibility problem*

$$\mathcal{N}_{\mathcal{A}_i}^*\mathcal{R}^*(\boldsymbol{B}\otimes\boldsymbol{P}_i)\mathcal{R}\mathcal{N}_{\mathcal{A}_i} < 0. \tag{5.46}$$

Proof: See Herion et al. (2001).

Lemma 2: *The Polynomial matrix polytope* $\mathbb{P} \subset \mathbb{C}^{n\times n}[s]$ *is robustly* $\mathcal{D}$*-stable if there exist* N *positive definite matrices* $\boldsymbol{P}_i \in \mathbb{C}^{dn\times dn}, i = 1, ..., N$, *and a matrix* $\boldsymbol{Q} \in \mathbb{C}^{2dn\times n}$, *solving the LMI feasibility problem*

$$\begin{bmatrix} \mathcal{R} \\ \mathcal{A}_i \end{bmatrix}^* \begin{bmatrix} \boldsymbol{B} \otimes \boldsymbol{P}_i & \boldsymbol{Q} \\ \boldsymbol{Q}^* & \boldsymbol{0} \end{bmatrix} \begin{bmatrix} \mathcal{R} \\ \mathcal{A}_i \end{bmatrix} < 0. \tag{5.47}$$

Proof: See Herion et al. (2001).

Theoretically, Lemma 1 and Lemma 2 are suitable for handling the $\mathcal{D}$-stability of polynomial matrices and polynomial matrix polytopes in the complex plane. However, complex-valued LMI feasibility problems cannot be solved by the LMI solvers in Matlab directly at the present time (Gahinet et al., 1995). Fortunately, complex-valued LMIs can be turned into real-valued LMIs by noting that a complex Hermitian matrix $\boldsymbol{L}$ which satisfies $\boldsymbol{L} < 0$ if only if (Gahinet et al., 1995):

$$\begin{bmatrix} Re(\boldsymbol{L}) & Im(\boldsymbol{L}) \\ -Im(\boldsymbol{L}) & Re(\boldsymbol{L}) \end{bmatrix} < 0, \tag{5.48}$$

where $Re(\boldsymbol{L})$ is the real part of matrix $\boldsymbol{L}$ and $Im(\boldsymbol{L})$ is the imaginary part, that is $\boldsymbol{L} = Re(\boldsymbol{L}) + jIm(\boldsymbol{L})$. Using Eq. (5.48), the complex-valued LMIs in Lemma 1 and Lemma 2 are extended to real-valued LMIs in Theorem 7 and Theorem 8, respectively.

Theorem 7: *Polynomial matrix* $\boldsymbol{A}_i(s)$ *is* $\mathcal{D}$*-stable if and only if there exists a positive definite matrix* $\boldsymbol{P}_i \in \mathbb{C}^{dn\times dn}$, *solving the LMI feasibility problem*

$$\mathcal{N}^*_{\mathcal{A}_i RI}\mathcal{R}^*_{RI}\Xi_i\mathcal{R}_{RI}\mathcal{N}_{\mathcal{A}_i RI} < 0, \tag{5.49}$$

where $\Xi_i = \boldsymbol{B}_{RI} \otimes Re(\boldsymbol{P}_i) + \boldsymbol{B}_{IR} \otimes Im(\boldsymbol{P}_i)$,

$$\mathcal{N}_{\mathcal{A}_i RI} = \begin{bmatrix} Re(\mathcal{N}_{\mathcal{A}_i}) & Im(\mathcal{N}_{\mathcal{A}_i}) \\ -Im(\mathcal{N}_{\mathcal{A}_i}) & Re(\mathcal{N}_{\mathcal{A}_i}) \end{bmatrix}, \mathcal{R}_{RI} = \begin{bmatrix} \mathcal{R} & \boldsymbol{0} \\ \boldsymbol{0} & \mathcal{R} \end{bmatrix},$$

$$\boldsymbol{B}_{RI} = \begin{bmatrix} Re(\boldsymbol{B}) & Im(\boldsymbol{B}) \\ -Im(\boldsymbol{B}) & Re(\boldsymbol{B}) \end{bmatrix}, \boldsymbol{B}_{IR} = \begin{bmatrix} -Im(\boldsymbol{B}) & Re(\boldsymbol{B}) \\ -Re(\boldsymbol{B}) & -Im(\boldsymbol{B}) \end{bmatrix}.$$

Proof: Using the method in Gahinet et al. (1995), the real matrices $\mathcal{N}_{\mathcal{A}_i RI}$ and $\mathcal{R}_{RI}$ can be obtained directly. For the term $\boldsymbol{B} \otimes \boldsymbol{P}_i$ in Eq. (5.46), one has:

$$\boldsymbol{B} \otimes \boldsymbol{P}_i = \begin{bmatrix} b_{11}\boldsymbol{P}_i & \cdots & b_{12k}\boldsymbol{P}_i \\ \vdots & b_{ef}\boldsymbol{P}_i & \vdots \\ b_{2k1}\boldsymbol{P}_i & \cdots & b_{2k2k}\boldsymbol{P}_i \end{bmatrix} \tag{5.50}$$

Noting that:

$$b_{ef}\boldsymbol{P}_i = Re(b_{ef})Re(\boldsymbol{P}_i) - Im(b_{ef})Im(\boldsymbol{P}_i) + j(Re(b_{ef})Im(\boldsymbol{P}_i) + Im(b_{ef})Re(\boldsymbol{P}_i)) \ , \quad (5.51)$$

Eq. (5.53) yields:

$$\begin{aligned}\boldsymbol{B} \otimes \boldsymbol{P}_i &= Re(\boldsymbol{B}) \otimes Re(\boldsymbol{P}_i) - Im(\boldsymbol{B})\otimes)Im(\boldsymbol{P}_i) + j(Re(\boldsymbol{B}) \otimes Im(\boldsymbol{P}_i) + Im(\boldsymbol{B}) \otimes Re(\boldsymbol{P}_i)) \\ &\triangleq Re\boldsymbol{BP} + jIm\boldsymbol{BP}\end{aligned} \ . \quad (5.52)$$

Thus, the term used instead of $\boldsymbol{B} \otimes \boldsymbol{P}_i$ is:

$$\begin{aligned}\begin{bmatrix} Re\boldsymbol{BP} & Im\boldsymbol{BP} \\ -Im\boldsymbol{BP} & Re\boldsymbol{BP} \end{bmatrix} &= \begin{bmatrix} Re(\boldsymbol{B}) & Im(\boldsymbol{B}) \\ -Im(\boldsymbol{B}) & Re(\boldsymbol{B}) \end{bmatrix} \otimes Re(\boldsymbol{P}_i) + \begin{bmatrix} -Im(\boldsymbol{B}) & Re(\boldsymbol{B}) \\ -Re(\boldsymbol{B}) & -Im(\boldsymbol{B}) \end{bmatrix} \otimes Im(\boldsymbol{P}_i) \\ &= \boldsymbol{B}_{RI} \otimes Re(\boldsymbol{P}_i) + \boldsymbol{B}_{IR} \otimes Im(\boldsymbol{P}_i)\end{aligned} \ . \quad (5.53)$$

□

It is interesting to note that Eq. (5.49) reduces to Eq. (5.46) if $\boldsymbol{B}$ and $\boldsymbol{P}$ are real matrices.

Theorem 8: *The Polynomial matrix polytope* $\mathbb{P} \subset \mathbb{C}^{n\times n}[s]$ *is robustly* $\mathcal{D}$*-stable if there exist N positive definite matrices* $\boldsymbol{P}_i \in \mathbb{C}^{dn\times dn}, i = 1, ..., N, \boldsymbol{Q} \in \mathbb{R}^{4dn\times 2n}$*, solving the LMI feasibility problem*

$$\begin{bmatrix} \mathcal{R}_{RI} \\ \mathcal{A}_{iRI} \end{bmatrix}^* \begin{bmatrix} \boldsymbol{\Xi}_i & \boldsymbol{Q} \\ \boldsymbol{Q}^* & \boldsymbol{0} \end{bmatrix} \begin{bmatrix} \mathcal{R}_{RI} \\ \mathcal{A}_{iRI} \end{bmatrix} < 0, \quad (5.54)$$

where $\boldsymbol{\Xi}_i$, $\mathcal{R}_{RI}$, $\boldsymbol{B}_{RI}$ *and* $\boldsymbol{B}_{IR}$ *are defined as the same as that in Theorem 1,*

$$\mathcal{A}_{iRI} = \begin{bmatrix} Re(\mathcal{A}_i) & Im(\mathcal{A}_i) \\ -Im(\mathcal{A}_i) & Re(\mathcal{A}_i) \end{bmatrix}.$$

Proof: Expanding Eq. (5.54) leads to:

$$\mathcal{R}_{RI}^*\boldsymbol{\Xi}_i\mathcal{R}_{RI} + \mathcal{A}_{iRI}^*\boldsymbol{Q}^*\mathcal{R}_{RI} + \mathcal{R}_{RI}^*\boldsymbol{Q}\mathcal{A}_{iRI} < 0. \quad (5.55)$$

Multiplying Eq. (5.55) by λ_i and summing, one has

$$\mathcal{R}_{RI}^*\boldsymbol{\Xi}(\lambda)\mathcal{R}_{RI} + \mathcal{A}_{RI}(\lambda)^*\boldsymbol{Q}^*\mathcal{R}_{RI} + \mathcal{R}_{RI}^*\boldsymbol{Q}\mathcal{A}_{RI}(\lambda) < 0. \quad (5.56)$$

where $\boldsymbol{\Xi}(\lambda) = \boldsymbol{B}_{RI} \otimes Re(\boldsymbol{P}(\lambda)) + \boldsymbol{B}_{IR} \otimes Im(\boldsymbol{P}(\lambda))$, $\boldsymbol{P}(\lambda) = \sum_{i=1}^{N} \lambda_i \boldsymbol{P}_i$, $\mathcal{A}_{RI}(\lambda)$

Define:

$$\mathcal{N}_{\mathcal{A}_{RI}(\lambda)} = \begin{bmatrix} Re(\mathcal{N}_{\mathcal{A}(\lambda)}) & Im(\mathcal{N}_{\mathcal{A}(\lambda)}) \\ -Im(\mathcal{N}_{\mathcal{A}(\lambda)}) & Re(\mathcal{N}_{\mathcal{A}(\lambda)}) \end{bmatrix}, \tag{5.57}$$

where $\mathcal{N}_{\mathcal{A}(\lambda)}$ is given in Eq. (5.44). Multiplying Eq. (5.58) by $\mathcal{N}^*_{\mathcal{A}_{RI}(\lambda)}$ and $\mathcal{N}_{\mathcal{A}_{RI}(\lambda)}$ each side and noting that $\mathcal{N}_{\mathcal{A}_{RI}(\lambda)}\mathcal{A}_{RI}(\lambda) = 0$, yields:

$$\mathcal{N}^*_{\mathcal{A}_{RI}(\lambda)}\mathcal{R}^*_{RI}\Xi(\lambda)\mathcal{R}_{RI}\mathcal{N}_{\mathcal{A}_{RI}(\lambda)} < 0. \tag{5.58}$$

Recalling the result of Theorem 7, the polynomial matrix $\mathcal{A}(s,\lambda)$ associated with $\mathcal{A}(\lambda)$ is $\mathcal{D}$-stable for all admissible λ and as a result, the Polynomial matrix polytope $\mathbb{P}$ is robustly $\mathcal{D}$-stable.

□

Theorem 7 and Theorem 8 are used to handle the stability of polynomial matrices and polynomial matrix polytopes in $\mathcal{D}$-regions defined in Eq.(5.36) and their unions. However, they are not suitable to cope with intersecting $\mathcal{D}$-regions since Lemma 1 and Lemma 2 cannot easily handle intersection of these regions (Herion et al., 2001). An intersecting region $\mathcal{D}_I$ can be defined as

$$\mathcal{D}_I = \mathcal{D}_1 \cap \mathcal{D}_2 \cap ... \cap \mathcal{D}_M \tag{5.59}$$

where all $\mathcal{D}_l$-regions are defined in Eq. (5.36) for $l = 1, 2, ..., M$. Actually for such a region $\mathcal{D}_I$, one can use the following theorem 9 to determine the stability of the polynomial matrix polytope $\mathbb{P}$. For clarity, set $M = 2$ in theorem 9.

Theorem 9: *Polynomial matrix polytope $\mathbb{P} \subset \mathbb{C}^{n\times n}[s]$ is robustly stable in an intersection $\mathcal{D}_I$, $\mathcal{D}_I = \mathcal{D}_1 \cap \mathcal{D}_2$, if the following holds:*

1) In region $\mathcal{D}_1$, there exist N positive definite matrices $\boldsymbol{P}_{1i} \in \mathbb{C}^{dn\times dn}, i = 1, ..., N$, $\boldsymbol{Q}_1 \in \mathbb{R}^{4dn\times 2n}$, solving the LMI feasibility problem

$$\begin{bmatrix} \mathcal{R}_{RI} \\ \mathcal{A}_{iRI} \end{bmatrix}^* \begin{bmatrix} \Xi_{1i} & \boldsymbol{Q}_1 \\ \boldsymbol{Q}_1^* & \mathbf{0} \end{bmatrix} \begin{bmatrix} \mathcal{R}_{RI} \\ \mathcal{A}_{iRI} \end{bmatrix} < 0, \tag{5.60}$$

2) In region $\mathcal{D}_2$, there exist N positive definite matrices $\boldsymbol{P}_{2i} \in \mathbb{C}^{dn\times dn}, i = 1, ..., N$, $\boldsymbol{Q}_2 \in \mathbb{R}^{4dn\times 2n}$, solving the LMI feasibility problem

$$\begin{bmatrix} \mathcal{R}_{RI} \\ \mathcal{A}_{iRI} \end{bmatrix}^* \begin{bmatrix} \Xi_{2i} & \boldsymbol{Q}_2 \\ \boldsymbol{Q}_2^* & \mathbf{0} \end{bmatrix} \begin{bmatrix} \mathcal{R}_{RI} \\ \mathcal{A}_{iRI} \end{bmatrix} < 0, \tag{5.61}$$

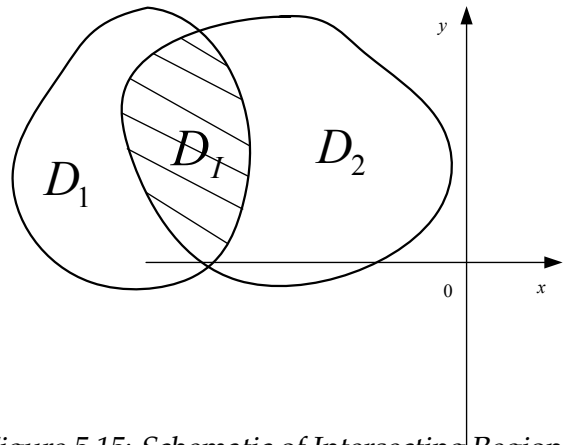

Figure 5.15: Schematic of Intersecting Region $\mathcal{D}_I$

where $\mathcal{A}_{iRI}$, $\mathcal{R}_{RI}$ are defined as the same as that in Theorem 8,

$$\Xi_{1i} = \boldsymbol{B}_{1RI} \otimes Re(\boldsymbol{P}_{1i}) + \boldsymbol{B}_{1IR} \otimes Im(\boldsymbol{P}_{1i}),$$

$$\Xi_{2i} = \boldsymbol{B}_{2RI} \otimes Re(\boldsymbol{P}_{2i}) + \boldsymbol{B}_{2IR} \otimes Im(\boldsymbol{P}_{2i}),$$

$$\boldsymbol{B}_{1RI} = \begin{bmatrix} Re(\boldsymbol{B}_1) & Im(\boldsymbol{B}_1) \\ -Im(\boldsymbol{B}_1) & Re(\boldsymbol{B}_1) \end{bmatrix}, \quad \boldsymbol{B}_{1IR} = \begin{bmatrix} -Im(\boldsymbol{B}_1) & Re(\boldsymbol{B}_1) \\ -Re(\boldsymbol{B}_1) & -Im(\boldsymbol{B}_1) \end{bmatrix},$$

$$\boldsymbol{B}_{2RI} = \begin{bmatrix} Re(\boldsymbol{B}_2) & Im(\boldsymbol{B}_2) \\ -Im(\boldsymbol{B}_2) & Re(\boldsymbol{B}_2) \end{bmatrix}, \quad \boldsymbol{B}_{2IR} = \begin{bmatrix} -Im(\boldsymbol{B}_2) & Re(\boldsymbol{B}_2) \\ -Re(\boldsymbol{B}_2) & -Im(\boldsymbol{B}_2) \end{bmatrix}.$$

Proof: Using the result of Theorem 8, all the zeros of any polynomial matrix in polytope $\mathbb{P}$ belong to region $\mathcal{D}_1$ if all the LMI feasibility problems in Eq. (5.60) are feasible. Likewise, all the zeros of any polynomial matrix in polytope $\mathbb{P}$ belong to region $\mathcal{D}_2$ if all the LMI feasibility problems in Eq. (5.61) are feasible. Therefore, as shown in Fig. 5.15, all the zeros of any polynomial matrix in polytope $\mathbb{P}$ belong to region $\mathcal{D}_I$ if the LMI feasibility problems in Eq. (5.60) and Eq. (5.61) are both feasible.

□

Using complex-valued LMIs, Theorem 3 can be simplified to Theorem 10.

Theorem 10: *Polynomial matrix polytope $\mathbb{P} \subset \mathbb{C}^{n\times n}[s]$ is robustly stable in an intersection $\mathcal{D}_I$, $\mathcal{D}_I = \mathcal{D}_1 \cap \mathcal{D}_2$, if the following holds:*

1) In region $\mathcal{D}_1$, there exist N positive definite matrices $\boldsymbol{P}_{1i} \in \mathbb{C}^{dn\times dn}, i = 1, ..., N$, $\boldsymbol{Q}_1 \in \mathbb{R}^{2dn\times n}$, solving the LMI feasibility problem

$$\begin{bmatrix} \mathcal{R} \\ \mathcal{A}_i \end{bmatrix}^* \begin{bmatrix} \boldsymbol{B} \otimes \boldsymbol{P}_{1i} & \boldsymbol{Q}_1 \\ \boldsymbol{Q}_1^* & \boldsymbol{0} \end{bmatrix} \begin{bmatrix} \mathcal{R} \\ \mathcal{A}_i \end{bmatrix} < 0. \tag{5.62}$$

2) In region $\mathcal{D}_2$, there exist N positive definite matrices $\boldsymbol{P}_{2i} \in \mathbb{C}^{dn\times dn}, i = 1,...,N$, $\boldsymbol{Q}_2 \in \mathbb{R}^{2dn\times n}$, solving the LMI feasibility problem

$$\begin{bmatrix} \mathcal{R} \\ \mathcal{A}_i \end{bmatrix}^* \begin{bmatrix} \boldsymbol{B}\otimes\boldsymbol{P}_{2i} & \boldsymbol{Q}_2 \\ \boldsymbol{Q}_2^* & \boldsymbol{0} \end{bmatrix} \begin{bmatrix} \mathcal{R} \\ \mathcal{A}_i \end{bmatrix} < 0. \tag{5.63}$$

Proof: The proof is similar to that of theorem 9.

Using the similar strategy, a necessary and sufficient complex-value LMI condition for the stability of a polynomial matrix in an intersecting region $\mathcal{D}_I$ can be obtained in Theorem 11 using the result of Lemma 1.

Theorem 11: *Polynomial matrix $\boldsymbol{A}_i(s)$ is stable in an intersection $\mathcal{D}_I$, $\mathcal{D}_I = \mathcal{D}_1 \cap \mathcal{D}_2$, if and only if the following holds:*

1) In region $\mathcal{D}_1$, there exists a positive definite matrix $\boldsymbol{P}_{1i} \in \mathbb{C}^{dn\times dn}$, solving the LMI feasibility problem

$$\mathcal{N}_{\mathcal{A}_i}^* \mathcal{R}^* (\boldsymbol{B}\otimes\boldsymbol{P}_{1i}) \mathcal{R} \mathcal{N}_{\mathcal{A}_i} < 0. \tag{5.64}$$

2) In region $\mathcal{D}_2$, there exists a positive definite matrix $\boldsymbol{P}_{2i} \in \mathbb{C}^{dn\times dn}$, solving the LMI feasibility problem

$$\mathcal{N}_{\mathcal{A}_i}^* \mathcal{R}^* (\boldsymbol{B}\otimes\boldsymbol{P}_{2i}) \mathcal{R} \mathcal{N}_{\mathcal{A}_i} < 0. \tag{5.65}$$

Proof: The sufficiency proof is the same as that of Theorem 9. Here we only prove the necessity condition. For an intersection $\mathcal{D}_I$ shown in Fig. 5.15, $\boldsymbol{A}_i(s)$ is stable in $\mathcal{D}_I$ if all of its roots are inside $\mathcal{D}_I$. Since $\mathcal{D}_I \subset \mathcal{D}_1$, hence all the roots of $\boldsymbol{A}_i(s)$ are inside $\mathcal{D}_1$. Using the results of Lemma 1, one has the LMI condition for part 1). The LMI condition in part 2) has an identical proof.

□

Noting the result in Theorem 7, it is easy to develop the corresponding real-value LMI condition but not provide here to keep the length of this thesis.

5.4.4 Examples

In this section, numerical examples are carried out to analyse $\mathcal{D}$-region stability of polynomial matrices and polynomial matrix polytopes. During the analysis, the LMI Control Toolbox in Matlab is used to solve the LMI feasibility problems.

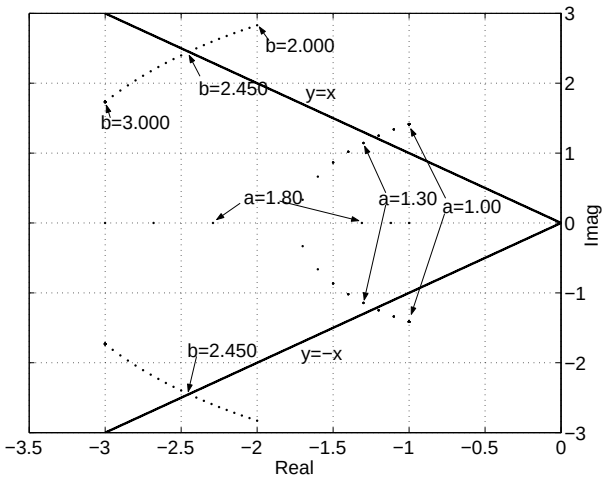

Figure 5.16: Root Locus of the Polynomial and $\mathcal{D}$-region

5.4.4.1 Scalar Polynomial and Polynomial Polytope

As an illustrative example to check the effect of Theorem 7, consider a polynomial of degree 4 with two parameters a and b given by

$$A(s) = (s^2 + 2a + 3)(s^2 + 2bs + 12). \tag{5.66}$$

Choose a half-plane region $\mathcal{D}_1$ as $\mathcal{D}_1 = \{s = x + jy \in \mathbb{C} : x - y < 0\}$. Thus its matrix $\boldsymbol{B}$ in Eq. (5.37) is

$$\boldsymbol{B} = \begin{bmatrix} 0 & 1-j \\ 1+j & 0 \end{bmatrix}. \tag{5.67}$$

The problem is to determine the ranges of a and b which can guarantee the polynomial $A(s)$ in Eq. (5.66) is stable in half-plane region $\mathcal{D}_1$ in Eq. (5.67), that is all the roots of $A(s)$ belong to region $\mathcal{D}_1$.

Solving the LMI problem in Theorem 7, feasible solutions exist for $a > 1.225$ and $b > 2.450$. Therefore, the polynomial $A(s)$ is stable in region $\mathcal{D}_1$ if $a > 1.225$ and $b > 2.450$.

Actually, the roots of of $A(s)$ can be solved directly by sweeping a from 1 to 2 and b from 2 to 3, as shown in Fig. 5.16. The root locus of $A(s)$ in this figure indicates all the roots of $A(s)$ belong to region $\mathcal{D}_1$ if $a > 1.225$ and $b > 2.450$. Noting that the roots of the polynomial are symmetric with respect to the real axis, one can have if $a > 1.225$ and $b > 2.450$, that all of the roots of $A(s)$ belong to

$\mathcal{D}_2 = \{s = x + jy \in \mathbb{C} : x + y < 0\}$, the symmetric region of $\mathcal{D}_1$. This LMI problem is also feasible.

As an illustrative example of Theorem 8, a polynomial polytope $\mathbb{P}$ of degree 3 whose 3 vertices are given by(Herion et al., 2001):

$$\begin{aligned} A_1(s) &= 28.3820 + 34.7667s + 8.3273s^2 + s^3, \\ A_2(s) &= 0.2985 + 1.6491s + 2.6567s^2 + s^3, \\ A_3(s) &= 4.0421 + 9.3039s + 5.5741s^2 + s^3. \end{aligned} \tag{5.68}$$

A half-plane region is chosen as $\mathcal{D}_3 = \{s = x + jy \in \mathbb{C} : ax + y < 0, a < 0\}$. The $\boldsymbol{B}$ matrix can be expressed as:

$$\boldsymbol{B} = \begin{bmatrix} 0 & a + j \\ a - j & 0 \end{bmatrix}. \tag{5.69}$$

The problem is to determine the range of a which can guarantee the polytope $\mathbb{P}$ is stable in the region $\mathcal{D}_3$.

Solving the LMI problem in Theorem 8, it is found feasible if $a > 1.420$ and infeasible if $a = 1.418$. Therefore, the polytope $\mathbb{P}$ is stable in the region $\mathcal{D}_3$ if $a > 1.420$.

The conservativeness of Theorem 8 for this problem is very small if one can solve all of the roots of any polynomial in the polytope $\mathbb{P}$ by using the sweeping method. Figure 5.17 and Figure 5.18 are the root locus of this polytope $\mathbb{P}$. As one can see in Fig. 5.18, several roots are over the line defined by $a = -1.418$ but not the line defined by $a = -1.420$.

5.4.4.2 Polynomial Matrix and Polynomial Matrix Polytope

To test Theorem 11, a matrix polynomial of degree $d = 2$ and dimension $n = 2$ is given by

$$\boldsymbol{A}(s) = \begin{bmatrix} s^2 + 2a + 3 & 1 \\ 2 & s^2 + 2bs + 12 \end{bmatrix}. \tag{5.70}$$

where a and b are two unknown parameters. An intersecting region $\mathcal{D}_I$ is used, consisted of four disjoint regions $\mathcal{D}_1$, $\mathcal{D}_2$, $\mathcal{D}_3$, and $\mathcal{D}_4$, as shown in Fig. 5.19. The

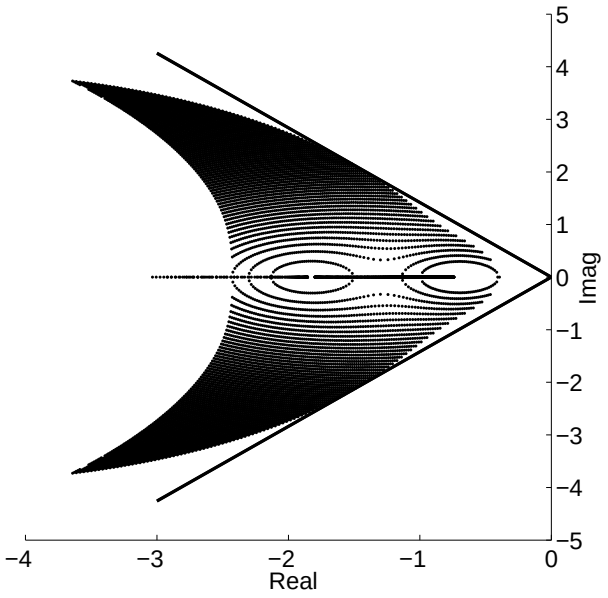

Figure 5.17: Root Locus of the Polynomial Polytope and $\mathcal{D}$-region

corresponding $\boldsymbol{B}$ matrices are given as:

$$\begin{aligned} \boldsymbol{B}_1 &= \begin{bmatrix} 2*1.4 & 1 \\ 1 & 0 \end{bmatrix}, \quad \boldsymbol{B}_2 = \begin{bmatrix} 0 & 1+j \\ a-j & 0 \end{bmatrix}, \\ \boldsymbol{B}_3 &= \begin{bmatrix} -3.5^2 & 0 \\ 0 & 1 \end{bmatrix}, \quad \boldsymbol{B}_4 = \begin{bmatrix} 0 & 1-j \\ a+j & 0 \end{bmatrix}. \end{aligned} \tag{5.71}$$

The problem is to determine the stability of polynomial matrix in Eq. (5.70) for the region $\mathcal{D}_I$ for different values of a and b. The values of a and b are chosen as $(1.5, 2.8)$, $(1.3, 2.8)$, $(1.3, 3.5)$, and $(1.5, 2.3)$.

Solving the LMI problems in Theorem 11, the results are listed in Table 5.1 for different choices of a and b. For the case $(1.5, 2.8)$, the polynomial matrix is stable in $\mathcal{D}_I$ since all LMI problems are feasible ($tmin < 0$). While for other cases, the matrix is unstable in $\mathcal{D}_I$. Furthermore, each infeasible result in Table 5.1 means at least one root of the polynomial matrix is outside of that relevant region. This can be verified by solving the roots of polynomial matrix directly, as shown in Fig. 5.19.

To illustrate Theorem 9, a interval polynomial matrix is given by:

$$\boldsymbol{A}(s) = \begin{bmatrix} 4.3s^2 + 2.3s + [3.7, 7.7] & -2.2s^2 - 7s - [3.1, 4.1] \\ 4.3s^s + 6.4s + 3.6 & 8.2s^2 + 12s + [3.2, 16] \end{bmatrix}. \tag{5.72}$$

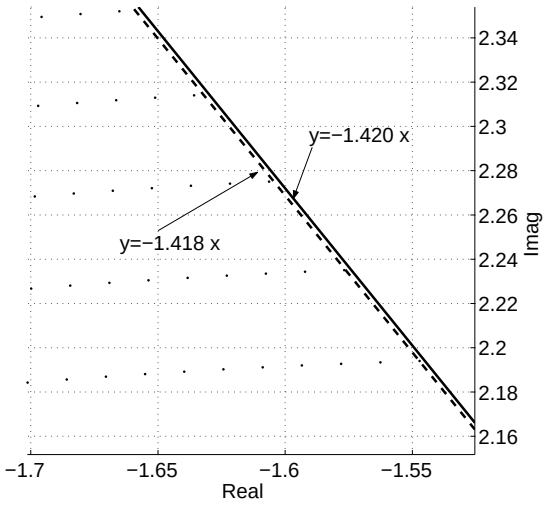

Figure 5.18: Part of Root Locus of the Polynomial Polytope

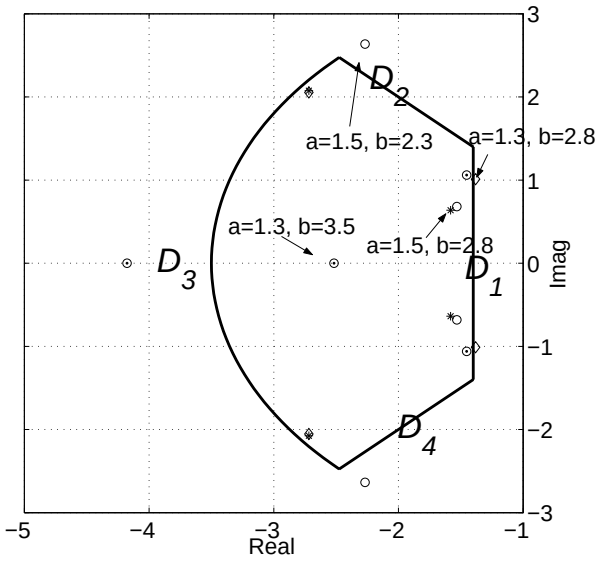

Figure 5.19: Root Locus of the Polynomial Matrix and $\mathcal{D}$-region

Table 5.1: The Analysis Results of LMI Feasibility Problem (tmin)

(a, b)	$\mathcal{D}_1$	$\mathcal{D}_2$	$\mathcal{D}_3$	$\mathcal{D}_4$	Roots
(1.5, 2.8)	-0.2614	-0.0066	-1.1131	-0.0066	*
(1.3, 2.8)	**-0.0000**	-0.0091	-0.0011	-0.0091	△
(1.3, 3.5)	-0.0026	-0.0305	**-0.0000**	-0.0305	◎
(1.5, 2.3)	-0.2792	**-0.0000**	-0.1860	**-0.0000**	*o*

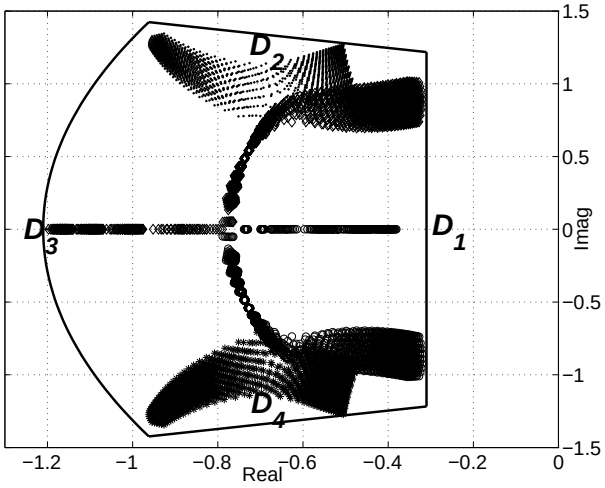

Figure 5.20: Root Locus of the Interval Polynomial Matrix and $\mathcal{D}$-region

Choose an intersecting region $\mathcal{D}_I = \mathcal{D}_1 \cap \mathcal{D}_2 \cap \mathcal{D}_3 \cap \mathcal{D}_4$, where the corresponding $\boldsymbol{B}$ matrices are given as:

$$\begin{aligned} \boldsymbol{B}_1 &= \begin{bmatrix} 2*0.31 & 1 \\ 1 & 0 \end{bmatrix}, \quad \boldsymbol{B}_2 = \begin{bmatrix} -2\times 1.12 & 0.3158 + j \\ a - j & 0 \end{bmatrix}, \\ \boldsymbol{B}_3 &= \begin{bmatrix} -4.21^2 + 3^2 & -3 \\ -3 & 1 \end{bmatrix}, \quad \boldsymbol{B}_4 = \begin{bmatrix} -2\times 1.12 & 0.3158 - j \\ 0.3158 + j & 0 \end{bmatrix}. \end{aligned} \tag{5.73}$$

The problem is to determine the $\mathcal{D}$ stability of the interval polynomial matrix in Eq. (5.70) in $\mathcal{D}_I$. Associated with the interval polynomial matrix, there is a polynomial matrix polytope with $2^3 = 8$ vertices.

Solving the LMI problems in Theorem 9, the analysis results *tmin* for $\mathcal{D}_1$, $\mathcal{D}_2$, $\mathcal{D}_3$ and $\mathcal{D}_4$ are -0.0101, -0.0006, -0.0065 and -0.0006, respectively. Using these results, the interval polynomial matrix in Eq. (5.70) is stable in the intersection region $\mathcal{D}_I$ since all *tmin* are negative.

Once again, the root locus of the interval polynomial matrix can be obtained by using three-dimensional sweeping, as shown in Fig. 5.20, which shows that all the roots are inside the $\mathcal{D}_I$ region, and so implies the interval polynomial matrix is stable in $\mathcal{D}_I$.

Thus, a new necessary and sufficient LMI condition of polynomial matrices and a new sufficient LMI condition of polynomial matrix polytopes have been developed to analyse the robust stability of an intersecting region $\mathcal{D}$, and the

numerical examples illustrate that using these LMI conditions, the stability of polynomial matrices and polytopes for an intersecting region $\mathcal{D}$ can be checked successfully and conveniently.

5.5 Robust Stability Analysis of MIMO Systems

The major contribution in this section is to develop an effective $\mathcal{D}$-stability performance analysis method for QLPV MIMO closed-loop control systems. During $\mathcal{D}$-stability analysis, the QLPV system is assumed to be an uncertain LTI system and its uncertainties are caused by the variations of specific parameters. To use the LMI approach, the dynamics of the MIMO system is expressed in a polynomial matrix fraction description and a polynomial matrix polytope of the uncertain system is computed by defining parametric uncertainties. With this polynomial matrix polytope, the parametric $\mathcal{D}$-stability margins for uncertainties in the controller parameters and dynamic derivatives are assessed by solving the LMI conditions described in last section. The results show that such an LMI approach is efficient and convenient in analysing the $\mathcal{D}$-stability of uncertain MIMO systems, and hence the performance of the uncertain closed-loop system can be tested over an intersecting $\mathcal{D}$-region.

5.5.1 Nominal MIMO Closed-Loop Model

The formation flying closed-loop control system is obtained by substituting the control law in Eq. (4.21) into Eq. (2.58). This yields the closed-loop system in the form:

$$\dot{\boldsymbol{x}} = \boldsymbol{A}(\boldsymbol{p})\boldsymbol{x} + \boldsymbol{B}\boldsymbol{K}(\boldsymbol{p})\boldsymbol{x} \tag{5.74}$$

where: $\boldsymbol{K}(\boldsymbol{p}) = \left[-\boldsymbol{K}_u^{-1}(\boldsymbol{p})\boldsymbol{K}_a(\boldsymbol{p}) \quad -\boldsymbol{K}_u^{-1}(\boldsymbol{p})\boldsymbol{K}_c(\boldsymbol{p}) \quad -\boldsymbol{K}_u^{-1}(\boldsymbol{p})\boldsymbol{K}_i(\boldsymbol{p})\right]$,

$\boldsymbol{x} = [\int \delta\boldsymbol{r}, \delta\boldsymbol{r}, \delta\dot{\boldsymbol{r}}]^T$, and $\boldsymbol{A}(\boldsymbol{p}) = \begin{bmatrix} 0 & \boldsymbol{I}_3 & 0 \\ 0 & 0 & I_3 \\ 0 & \boldsymbol{A}_{\delta\boldsymbol{r}} & \boldsymbol{A}_{\delta\dot{\boldsymbol{r}}} \end{bmatrix}$.

To explore the robustness of the control system design using PEA, a $\mathcal{D}$-stability analysis can be performed on Eq. (5.74), which is an uncertain LTI system, whose uncertainties are caused by the variations in $\boldsymbol{p}$. With this assumption, the nominal denominator polynomial matrix description of the closed-loop system, can be obtained from Eq. (5.74) as:

$$\boldsymbol{D}(s) = \boldsymbol{K}_u s^3 + (\boldsymbol{K}_i - \boldsymbol{K}_u \boldsymbol{A}_{\delta\dot{\boldsymbol{r}}})s^2 + (\boldsymbol{K}_c - \boldsymbol{K}_u \boldsymbol{A}_{\delta\boldsymbol{r}})s + \boldsymbol{K}_a, \tag{5.75}$$

where: $\boldsymbol{A}_{\delta\dot{\boldsymbol{r}}}$ and $\boldsymbol{A}_{\delta\boldsymbol{r}}$ are the dynamic derivatives of system in Eq. (5.74).

5.5.2 Uncertain MIMO Closed-Loop Model

To analyse the $\mathcal{D}$-stability performance of the nominal closed-loop system, two sources of parametric uncertainty are taken into account: one is the varying controller parameters $\boldsymbol{K}_u$, $\boldsymbol{K}_i$, $\boldsymbol{K}_c$, and $\boldsymbol{K}_a$, which not only denote the uncertainties of the actuator, but also include the variation of spacecraft mass, the measured error of the sensors and the other source of uncertainty is the varying dynamic derivatives $\boldsymbol{A}_{\delta\dot{\boldsymbol{r}}}$ and $\boldsymbol{A}_{\delta\boldsymbol{r}}$, which describe the variations of system dynamic parameters.

As shown in Eq. (2.40), the nominal values of dynamic parameter are given as:

$$\hat{\boldsymbol{A}}_{\delta\boldsymbol{r}} = \begin{bmatrix} n^2 + 2\sigma & 0 & 0 \\ 0 & n^2 - \sigma & 0 \\ 0 & 0 & -\sigma \end{bmatrix}, \quad \hat{\boldsymbol{A}}_{\delta\dot{\boldsymbol{r}}} = \begin{bmatrix} 0 & 2n & 0 \\ -2n & 0 & 0 \\ 0 & 0 & 0 \end{bmatrix}. \tag{5.76}$$

Using the nominal values of the dynamic parameters, the nominal values of the controller parameters are computed using Eq. (4.68) ~ Eq. (4.70) as:

$$\hat{\boldsymbol{K}}_u = diag\{ \ \tfrac{1}{d_{x0}} \quad \tfrac{1}{d_{y0}} \quad \tfrac{1}{d_{z0}} \ \} \tag{5.77}$$

$$\hat{\boldsymbol{K}}_c = \begin{bmatrix} \frac{n^2+2\sigma+d_{x1}}{d_{x0}} & 0 & 0 \\ 0 & \frac{n^2-\sigma+d_{y1}}{d_{y0}} & 0 \\ 0 & 0 & \frac{-\sigma+d_{z1}}{d_{z0}} \end{bmatrix} \tag{5.78}$$

$$\hat{\boldsymbol{K}}_i = \begin{bmatrix} \frac{d_{x2}}{d_{x0}} & \frac{2n}{d_{x0}} & 0 \\ \frac{-2n}{d_{y0}} & \frac{d_{y2}}{d_{y0}} & 0 \\ 0 & 0 & \frac{d_{z2}}{d_{z0}} \end{bmatrix} \tag{5.79}$$

$$\hat{\boldsymbol{K}}_a = \boldsymbol{I}_{3\times 3} \tag{5.80}$$

Assuming an error model of the form:

$$\begin{array}{l} \boldsymbol{K}_u = \hat{\boldsymbol{K}}_u + \Delta\boldsymbol{K}_u, \quad \boldsymbol{K}_i = \hat{\boldsymbol{K}}_i + \Delta\boldsymbol{K}_i, \quad \boldsymbol{K}_c = \hat{\boldsymbol{K}}_c + \Delta\boldsymbol{K}_c, \\ \boldsymbol{K}_a = \hat{\boldsymbol{K}}_a + \Delta\boldsymbol{K}_a, \quad \boldsymbol{A}_{\delta\boldsymbol{r}} = \hat{\boldsymbol{A}}_{\delta\boldsymbol{r}} + \Delta\boldsymbol{A}_{\delta\boldsymbol{r}}, \quad \boldsymbol{A}_{\delta\dot{\boldsymbol{r}}} = \hat{\boldsymbol{A}}_{\delta\dot{\boldsymbol{r}}} + \Delta A_{\delta\dot{\boldsymbol{r}}} \end{array}, \tag{5.81}$$

then the uncertainty in polynomial matrix Eq. (5.75) is given by:

$$\begin{array}{c} \boldsymbol{D}(s) = (\hat{\boldsymbol{K}}_u + \Delta\boldsymbol{K}_u)s^3 + ((\hat{\boldsymbol{K}}_i + \Delta\boldsymbol{K}_i) - (\hat{\boldsymbol{K}}_u + \Delta\boldsymbol{K}_u)(\hat{\boldsymbol{A}}_{\delta\dot{\boldsymbol{r}}} + \Delta\boldsymbol{A}_{\delta\dot{\boldsymbol{r}}}))s^2 + \\ ((\hat{\boldsymbol{K}}_c + \Delta\boldsymbol{K}_c) - (\hat{\boldsymbol{K}}_u + \Delta\boldsymbol{K}_u)(\hat{\boldsymbol{A}}_{\delta\boldsymbol{r}} + \Delta\boldsymbol{A}_{\delta\boldsymbol{r}}))s + (\hat{\boldsymbol{K}}_a + \Delta\boldsymbol{K}_a) \end{array} \tag{5.82}$$

Assuming the entries in each parameter have the same percentage uncertainty, then the entries of the relative error vector $\boldsymbol{q}$ of uncertainty parameters can be defined as: $q_1 \triangleq \Delta\boldsymbol{K}_u(\hat{\boldsymbol{K}}_u)^{-1}$, $q_2 \triangleq \Delta\boldsymbol{K}_i(\hat{\boldsymbol{K}}_i)^{-1}$, $q_3 \triangleq \Delta\boldsymbol{K}_c(\hat{\boldsymbol{K}}_c)^{-1}$, $q_4 \triangleq \Delta\boldsymbol{K}_a(\hat{\boldsymbol{K}}_a)^{-1}$, $q_5 \triangleq \Delta\boldsymbol{A}_{\delta\boldsymbol{r}}(\hat{\boldsymbol{A}}_{\delta\boldsymbol{r}})^{-1}$, $q_6 \triangleq \Delta\boldsymbol{A}_{\delta\dot{\boldsymbol{r}}}(\hat{\boldsymbol{A}}_{\delta\dot{\boldsymbol{r}}})^{-1}$. Using this definition of the error vector, the polynomial matrix in Eq. (5.82) can be written as:

$$\boldsymbol{D}(s, \boldsymbol{q}) = \boldsymbol{d}_0(\boldsymbol{q}) + \boldsymbol{d}_1(\boldsymbol{q})s + \boldsymbol{d}_2(\boldsymbol{q})s^2 + \boldsymbol{d}_3(\boldsymbol{q})s^3 \tag{5.83}$$

where: $\boldsymbol{d}_0(\boldsymbol{q}) = (1 + q_4)\hat{\boldsymbol{K}}_a$, $\boldsymbol{d}_1(\boldsymbol{q}) = (1 + q_2)\hat{\boldsymbol{K}}_i - (1 + q_1)\hat{\boldsymbol{K}}_u(1 + q_6)\hat{\boldsymbol{A}}_{\delta\dot{\boldsymbol{r}}}$, $\boldsymbol{d}_2(\boldsymbol{q}) = (1 + q_3)\hat{\boldsymbol{K}}_c - (1 + q_1)\hat{\boldsymbol{K}}_u(1 + q_5)\hat{\boldsymbol{A}}_{\delta\boldsymbol{r}}$, $\boldsymbol{d}_3(\boldsymbol{q}) = (1 + q_1)\hat{\boldsymbol{K}}_u$, and where the error vector $\boldsymbol{q}$ is in a parameter box Π_b (Bruyere, 2004), that is $q_i^- \leq q_i \leq q_i^+$, $i = 1, ..., 6$, where q_i^- and q_i^+ are constants. For the 6 uncertainties, there are 64 polynomial matrix vertices in Eq. (5.83). If the uncertainties associated with each coefficient matrix is treated as independent, the solution will be slightly conservative, but the resulting form can be used in LMI analysis. Therefore the polynomial matrix polytope $\mathbb{D}$ required for the $\mathcal{D}$-stability analysis can be expressed as:

$$\boldsymbol{D}(s, \lambda) = \lambda_1\boldsymbol{D}_1(s) + \lambda_2\boldsymbol{D}_2(s) + ... + \lambda_{64}\boldsymbol{D}_{64}(s), \quad \lambda_i \geq 0, \quad \sum_{i=1}^{64}\lambda_i = 1. \tag{5.84}$$

where $\boldsymbol{D}_i(s)$ are the vertices of uncertain polynomial matrix in Eq. (5.83).

5.5.3 $\mathcal{D}$-Stability Analysis by Using LMI Approach

With the polynomial matrix polytope in Eq. (5.84), the $\mathcal{D}$-stability analysis of the uncertain formation flying control system can now be investigated using Theorem 9 in Section 5.4. The basic performance of the closed-loop system can be assessed using the results of this $\mathcal{D}$-stability analysis. The polynomial matrix polytope in Eq. (5.84) is third order with poles chosen to lie within the desired $\mathcal{D}$-stability

region. Using the PEA approach, the desired transfer function for each axis nominal closed-loop system is selected as a combination of a second-order plant and an integrator. Therefore, the desired characteristic polynomial of the nominal model is given as $D^d(s) = (s + p_t)(s^2 + 2\xi\omega_n s + \omega_n^2)$, where ξ is the damping ratio, set at 0.8, ω_n is the natural frequency for the system, set at 2×10^{-5}rad/s, $p_t = 5\xi\omega_n$ is the third pole, set at 8×10^{-5}. This results in a nominal rise time of 2 days and a settling time of less than 10 days.

To guarantee the performance of the system, the desired $\mathcal{D}$-stability region should surround the nominal poles within damping ratio and natural frequency bounds. Noting the requirements of the system, the $\mathcal{D}$-stability region is defined as a symmetrical cone shape with respect to real axis, shown in Fig. 5.21, where the maximum damping ratio is 0.7, the minimum natural frequency is $\frac{3}{4}$ of the natural frequency ($\frac{3}{4}\omega_n$), and the maximum natural frequency is $\frac{4}{3}$ of the third pole ($\frac{20}{3}\omega_n$).Thus, the maximum rise time is 2.2 days and settling time is no more than 12 days. Using the definition in Eq. (5.36), the resulting $\mathcal{D}$-stability region can be described as an intersection of the following 4 half-plane regions:

$$\begin{aligned} \boldsymbol{B}_1 &= \begin{bmatrix} \frac{3}{2}\xi\omega_n & 1 \\ 1 & 0 \end{bmatrix}, \boldsymbol{B}_2 = \begin{bmatrix} 0 & 1+j \\ 1-j & 0 \end{bmatrix}, \\ \boldsymbol{B}_3 &= \begin{bmatrix} 0 & 1-j \\ 1+j & 0 \end{bmatrix}, \boldsymbol{B}_4 = \begin{bmatrix} \frac{40}{3}\xi\omega_n & -1 \\ -1 & 0 \end{bmatrix}. \end{aligned} \tag{5.85}$$

5.5.4 Robustness Results

To measure the effect of uncertainty of every parameter for the closed-loop system, only one parameter at a time is varied. Table 5.2 shows the analysis results. From the table, the variations of the dynamic parameters have very little effect on the system $\mathcal{D}$-stability. Both $\Delta\boldsymbol{A}_{\delta r}$ and $\Delta\boldsymbol{A}_{\delta \dot{r}}$ can vary more than 5 times their nominal values. However, the controller parameters are much more sensitive than the dynamic derivatives and to ensure the $\mathcal{D}$-stability performance, all of the uncertainties of the controller parameter must be less than ±20%. In detail, $\Delta\boldsymbol{K}_u$, $\Delta\boldsymbol{K}_c$, and $\Delta\boldsymbol{K}_a$ can vary up to ±17.5%, while $\Delta\boldsymbol{K}_i$ can only vary by ±8.4%. This indicates that the variation of $\Delta\boldsymbol{K}_i$ has more effect than the other controller parameters on the system $\mathcal{D}$-stability performance.

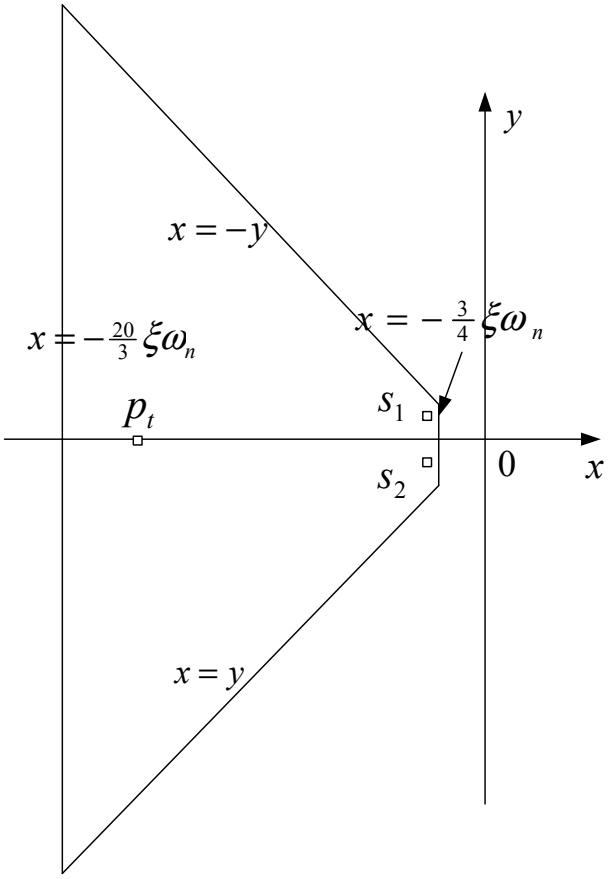

Figure 5.21: $\mathcal{D}$-stability Region for Uncertain Formation Control System

In order to compare the analysis result in Section 5.3, all parameters are assumed to have uniform percentage variation. Using the LMI conditions in Theorem 9, the maximum uncertainty in parameters is ±4.4% to ensure the LMI feasibility problem is feasible. This value is less than the one (±4.5%) obtained using FIT approach in Section 5.3. The reason is the effect of the coupling term among three control channels, which is assumed as negligible for the FIT approach since the analysis tools in Section 5.3 can only cope with SISO systems.

Table 5.2: $\mathcal{D}$-Stability Analysis Results for Each Uncertain Parameter

Uncertainty	Maximum	Uncertainty	Maximum
q_1	±18.3%	q_4	±18.5%
q_2	±8.4%	q_5	±500%
q_3	±17.5%	q_6	±500%

Actually neglecting the coupling term, one can obtain the same result by using LMI conditions in Theorem 9. This further indicates that the coupling term affects the $\mathcal{D}$-stability of the close-loop system. These analysis results illustrate that the QLPV PEA controller can ensure the robust $\mathcal{D}$-stability of the MIMO control system since the system can tolerate ±4.4% uncertainty in the both controller parameters and the dynamic derivatives.

5.5.5 Simulation

In this section, two simulation scenarios are simulated for the closed-loop L_2 point formation flying system described in Section 3.4.1 to confirm the performance and robustness of the design. Both simulations drive the initial relative position error $\delta \boldsymbol{r}$ from $[450\sqrt{2} \;\; -450\sqrt{2} \;\; 0]^T$ m to zero, starting at 1 day and finishing after 11 days (scenario 1, without rate limitation) or 65 days (scenario 2, with rate limitation).

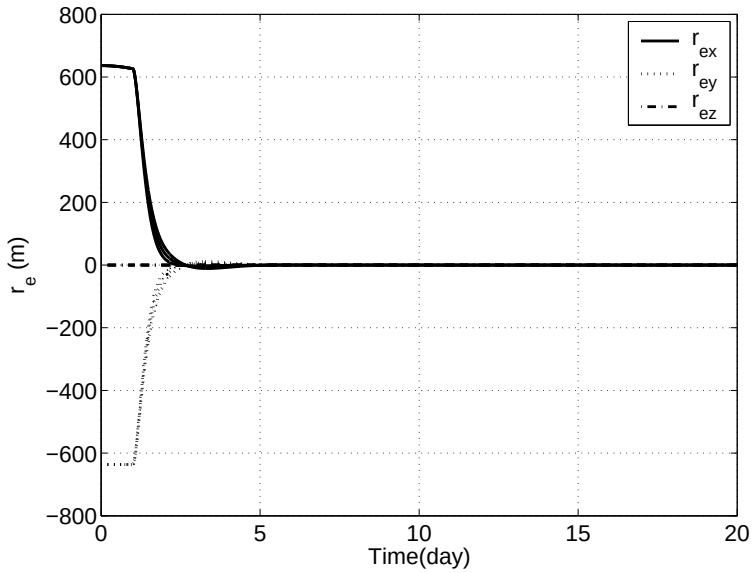

Figure 5.22: The Relative Position Errors of Uncertain Formation Control System over 20 days without Rate Limitation

In the first scenario, the closed-loop control system tolerates up to ±4.4% parametric uncertainties without rate limitation. Figure 5.22 ~ Figure 5.25 show the simulation results over 20 days (the results after 20 days are the same as those in Section 4.4.2). From the results in Fig. 5.22 and Fig. 5.23, that the desired damping and rise time are attained according to the design requirements within

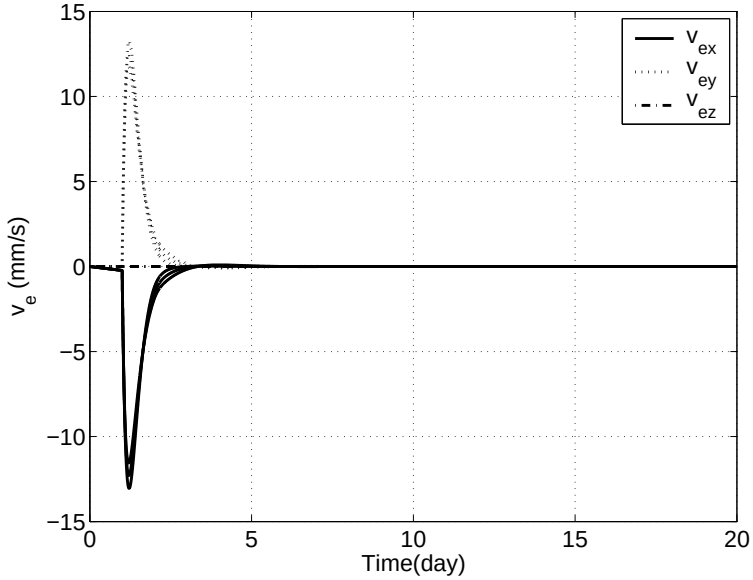

Figure 5.23: The Relative Velocity Errors of Uncertain Formation Control System over 20 days without Rate Limitation

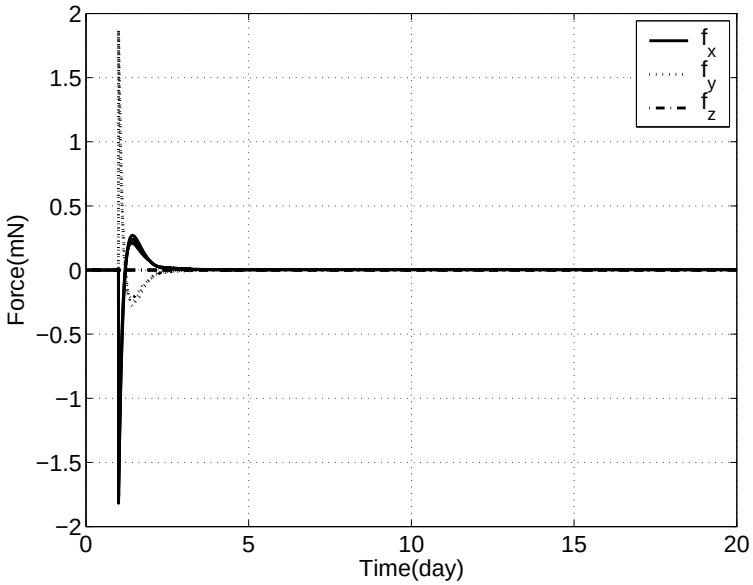

Figure 5.24: The Control Forces of Uncertain Formation Control System over 20 days without Rate Limitation

the range of parametric uncertainties. The maximums rise time and settling time are less than 2.2 days (case 1) and 12 days (case 2), respectively. From Fig. 5.25, the fuel cost of the system varies from 0.037 m/s (case 1) to 0.041 m/s (case 2) due to the uncertainties. Actually after the initial manoeuvre, the fuel costs are very similar

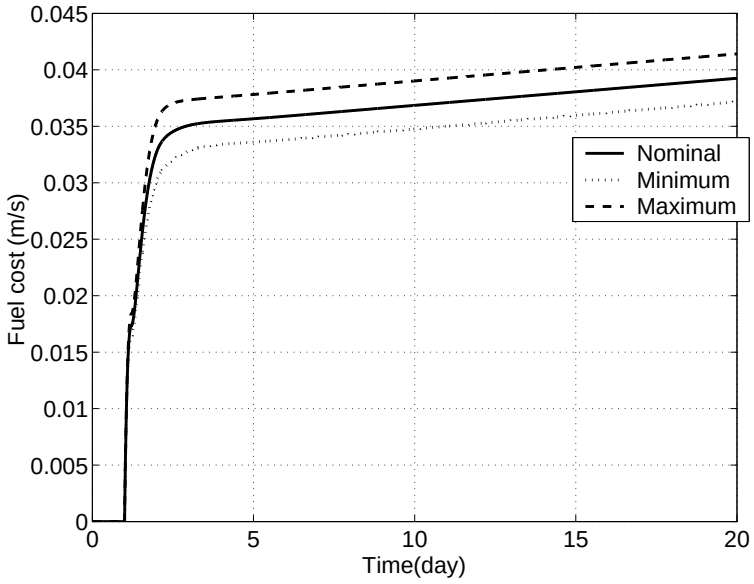

Figure 5.25: The Fuel Cost of Uncertain Formation Control System over 20 days without Rate Limitation

(0.024 $m/s/day$) because the disturbance of each uncertain system is almost the same. Once system reaches steady state, the error is less than 0.1 mm (the same as the nominal performance, Fig. 4.15) and maintains this accuracy over the rest of simulation time. This indicates that, using the PEA approach, the closed-loop system with uncertainty achieves the desired $\mathcal{D}$-stability performance during the process of formation flying.

The second scenario is used to evaluate the performance and robustness of the uncertain closed-loop system with rate limits. Although the approach developed in this chapter cannot cope with parameter limitation, the simulation results can still be used to partially check robustness. In this scenario, the PEA controller tolerates up to ±4.4% parametric uncertainties and the manoeuvre rates are limited in 10 m/day during the simulation. Therefore for 637 m position error, the nominal manoeuvre should complete around 65 days.

Figure 5.26 ~ Figure 5.29 show the simulation results over 100 days . Due to the uncertainties, Fig. 5.26 indicates that the number of manoeuvre days is uncertain, varying from 60 days (case 1) to 74 days (case 2), which can be observed from the control forces in Fig. 5.28 as well. Figure 5.23 depicts the variation of the the maximum manoeuvre rate, which varies between 0.106 mm/s and 0.127 mm/s (9.16 m/day and 10.97 m/day). From Fig. 5.29, the fuel cost of each case over

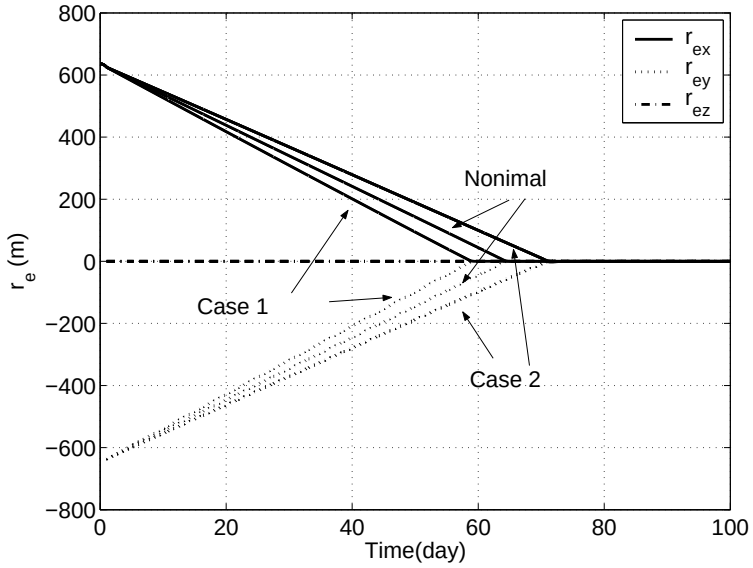

Figure 5.26: The Relative Position Errors of Uncertain Formation Control System over 100 days with Rate Limitation

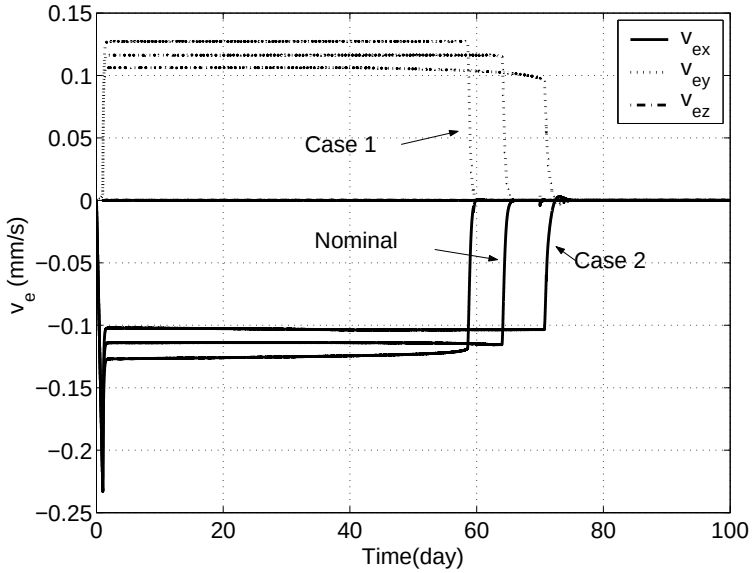

Figure 5.27: The Relative Velocity Errors of Uncertain Formation Control System over 100 days with Rate Limitation

100 days is very similar, 0.0235 m/s (0.024 $m/s/day$, which is the same as that of position keeping in the scenario 1), in which the factor which affects the fuel cost is not the uncertainties but the others, for example disturbances and noise.

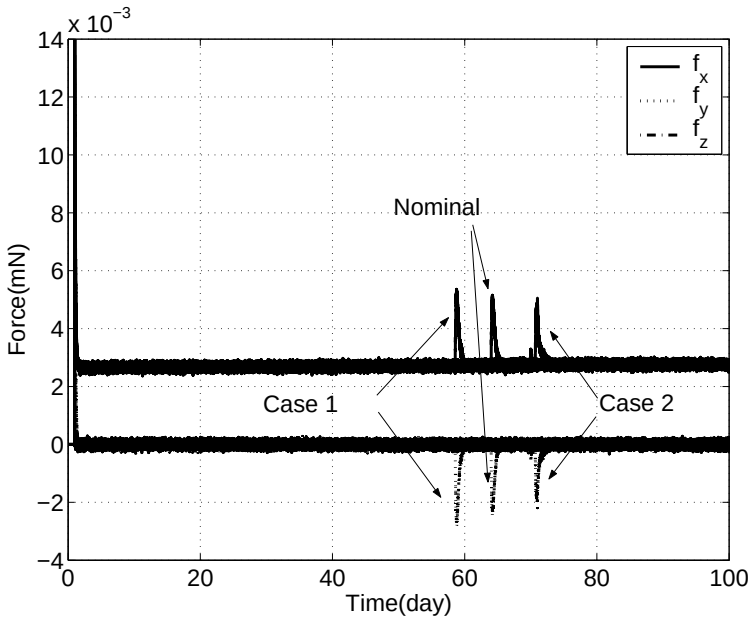

Figure 5.28: The Control Forces of Uncertain Formation Control System over 100 days with Rate Limitation

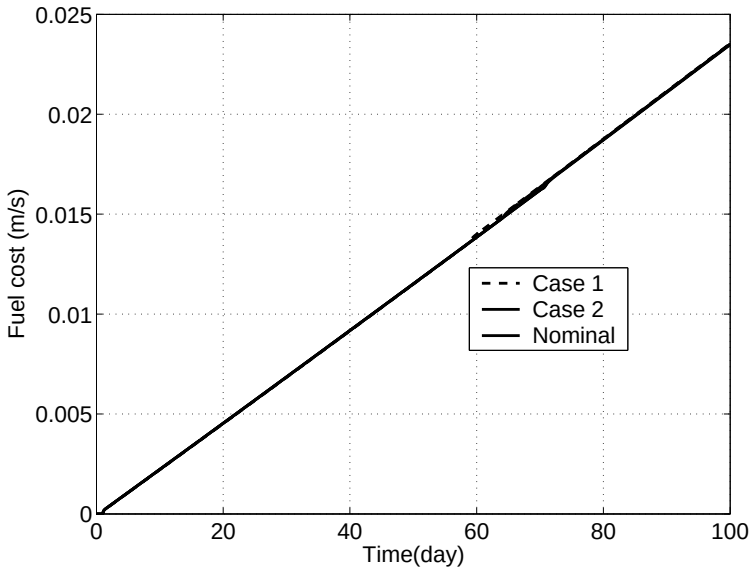

Figure 5.29: The Fuel Cost of Uncertain Formation Control System over 100 days with Rate Limitation

5.6 Conclusion

As the first contribution, the robust stability analysis of the uncertain L_2 point formation flying SISO system is accomplished by using a polynomial approach.

In detail, the Hurwitz robustness stability of parametric uncertainty is carried out by using Kharitonov's theorem and the Mapping Theorem, in which two sources of parametric uncertainty, controller parameter uncertainty and dynamic derivative uncertainty are taken into account during the analysis. Then in order to avoid frequency sweeping, the Finite Inclusion Theorem is applied to analyse the robust $\mathcal{D}$-stability of the SISO closed-loop system. The analysis results indicate that good performance and robustness are attained for the uncertain PEA control system in Chapter 4.

To analyse the robust stability of MIMO systems in an arbitrary intersecting region $\mathcal{D}$, a new necessary and sufficient LMI condition for polynomial matrices and a new sufficient LMI condition for polynomial matrix polytopes are developed in Section 5.4, which is the third major contribution in this thesis. During the robustness analysis of the MIMO L_2 point formation flying problem in Section 5.5, the $\mathcal{D}$-stability performance with controller parameter uncertainty and dynamic derivative uncertainty are assessed by solving an LMI feasibility problem of a polynomial matrix polytope of the uncertain system. The analysis results indicate the controller parameters have much more sensitivity than the dynamic parameters, and the simulation results indicate that the performance of the uncertain system can be ensured to maintain the system eigenvalues within a $\mathcal{D}$-region. Comparing the results attained by the SISO system approach developed in Section 5.3 (maximum uncertainty for each parameter is up to 4.5 %), this LMI approach can achieve more accurate results for MIMO systems (maximum uncertainty is only up to 4.4 %) since it takes the effect of coupling terms into account. This is another contribution in this chapter.

All the polynomial approaches developed in this chapter can only handle the robustness of uncertain time-invariant systems, which means for the uncertain time-varying systems, a new approach and new theory are required to analyse the robust stability. This is the motivation in Chapter 6: robust stability analysis via Lyapunov functions.

Chapter 6

Robust Stability Analysis via Lyapunov Functions

In Chapter 4, the PEA design algorithm produces a closed-loop system almost independent of the operating point and thus is similar to that of dynamic inversion while encompassing a broader class of systems. The control performance can be ensured by this approach for a nonlinear system. However, during the calculation of controller gains, the technique only defines the desired transfer function as a coprime factorization, and does not indicate how to choose the roots of the characteristic equation to guarantee the stability of the closed-loop system. This can be a problem, especially for a QLPV system and its stability should be analysed carefully since the states matrix $\boldsymbol{A}(\boldsymbol{p})$ and input matrix $\boldsymbol{B}(\boldsymbol{p})$ both vary with the system states and with time. Therefore, for the application of PEA design approach to an QLPV system, the closed-loop system stability should be analysed to ensure that this approach still produces a stable response that meets the performance requirements, and due to the variation of parameters, the system robustness to parameter uncertainties should be studied as well.

In this chapter, the Lyapunov method is used to analyse the stability of the nominal and uncertain QLPV system, respectively. For the nominal QLPV system, a theorem is presented with the assumption that the close-loop eigenvalues should be distinct to guarantee stability (Section 6.1). To assess the stability of the uncertain QLPV system with bounded uncertainties, a quadratic Lyapunov function is defined to ensure that the uncertain system is stable (Section 6.2). To test the performance of the uncertain system, an affine parameter-dependent Lyapunov function is implemented to develop an LMI approach to check the $\mathcal{D}$-stability of the matrix polytopes (Section 6.3). Furthermore, two different methods are presented to reduce the conservatism of this new LMI approach (Section 6.4). Finally, Section 6.5 presents the analysis results by using these new LMI approaches to analyse the $\mathcal{D}$-stability performance of the QLPV PEA L_2 point formation control system.

6.1 Stability Analysis for Nominal QLPV Systems

Using the QLPV PEA control design in Section 4.4, and substituting Eq. (4.21) into Eq. (4.18), the closed-loop system can be expressed as:

$$\dot{\boldsymbol{x}} = (\boldsymbol{A}(\boldsymbol{x},t) - \boldsymbol{B}(\boldsymbol{x},t)\boldsymbol{K}(\boldsymbol{x},t))\boldsymbol{x} = \boldsymbol{A}_c(\boldsymbol{x},t)\boldsymbol{x} \tag{6.1}$$

where $\boldsymbol{A}_c(\boldsymbol{x},t)$ is the state matrix for the closed-loop system, which is bounded since matrix $\boldsymbol{A}(\boldsymbol{x},t)$ and $\boldsymbol{B}(\boldsymbol{x},t)$ are bounded. In this chapter, the parameter $\boldsymbol{p}$ in Chapter 4 is replaced by the state $\boldsymbol{x}$ and time t. Thus, the model shown in Eq. (6.1) denotes a much more general case, resulting in a Quasi-Linear Time-Varying model. For the desired characteristic equation of the PEA controller, one has:

$$D_d(s,\boldsymbol{p}) = \prod_{i=1}^{n}(s - \lambda_i(\boldsymbol{x},t)) \tag{6.2}$$

where $\lambda_i(\boldsymbol{x},t)$ are desired eigenvalues, and where $-\rho \leq Re(\lambda_i(\boldsymbol{x},t)) \leq -\varepsilon < 0$, $\varepsilon, \rho > 0$ for all $\lambda_i(\boldsymbol{x},t)$. So for the PEA approach for QLPV systems, one has:

$$|\boldsymbol{I}s - \boldsymbol{A}_c| = |\boldsymbol{I}s - \boldsymbol{A}(\boldsymbol{x},t) + \boldsymbol{B}(\boldsymbol{x},t)\boldsymbol{K}(\boldsymbol{x},t)| = D_d(s,\boldsymbol{p}) \tag{6.3}$$

where $\boldsymbol{I}$ is an identity matrix. If the system is LTI, its stability can be determined easily. However for a QLPV system, it is required to choose a Lyapunov function to prove that the designed controller can ensure the stability of closed-loop system.

In Gaiduk (1993, 2003) and Solodovnik et al. (2004), a Lyapunov function is developed to prove the stability of QLPV systems, given as:

$$V(\boldsymbol{x},t) = \boldsymbol{x}^*\boldsymbol{M}(\boldsymbol{x},t)\boldsymbol{x}e^{h(\boldsymbol{x},t)}. \tag{6.4}$$

Using this function, several conditions to ensure the stability of QLPV systems are developed in Gaiduk (1993, 2003) and Solodovnik et al. (2004). But, the expression of $\boldsymbol{M}(\boldsymbol{x},t)$ in their methods is very complex because it is constructed using a Vandermonde matrix composed of system eigenvalues and two matrices related to the coefficients of the polynomial $D_d(s,\boldsymbol{p})$ in Eq. (6.2) and the system matrices $\boldsymbol{A}(\boldsymbol{x},t)$ and $\boldsymbol{B}(\boldsymbol{x},t)$ in Eq. (6.1), which results in a tedious calculation for this application. In this section, the same Lyapunov function is used but with a

simpler expression of $\boldsymbol{M}(\boldsymbol{x},t)$ to guarantee the stability of QLPV systems. This is detailed in Theorem 12 below.

Theorem 12 *The solution* $\boldsymbol{x}(\boldsymbol{x}_0,t)$ *of system Eq.* (6.1) *for each initial condition* $\boldsymbol{x}_0=\boldsymbol{x}(0)$ *is globally asymptotically stable if the following conditions are satisfied: the eigenvalues of the system matrix are distinct and their real parts are negative, that is,* $\lambda_i(\boldsymbol{x},t)\neq\lambda_j(\boldsymbol{x},t)$, $i\neq j$ *and* $-\rho\leq Re(\lambda_i(\boldsymbol{x},t))\leq-\varepsilon<0$, $\varepsilon>0$, $\rho>0$.

Proof: Consider the same Lyapunov function as in Gaiduk (1993, 2003) and Solodovnik et al. (2004):

$$V(\boldsymbol{x},t)=\boldsymbol{x}^*\boldsymbol{M}(\boldsymbol{x},t)\boldsymbol{x}e^{h(\boldsymbol{x},t)} \tag{6.5}$$

where the asterisk denotes complex conjugation, $h(\boldsymbol{x},t)$ is a scalar function and the functional matrix $\boldsymbol{M}(\boldsymbol{x},t)$ is simpler than the one in Gaiduk (1993, 2003) and Solodovnik et al. (2004) and is defined as:

$$\boldsymbol{M}(\boldsymbol{x},t)=(\boldsymbol{L}^{-1}(\boldsymbol{x},t))^*\boldsymbol{L}^{-1}(\boldsymbol{x},t) \tag{6.6}$$

where $\boldsymbol{L}(\boldsymbol{x},t)$ is the matrix consisting of all of the eigenvectors of $\boldsymbol{A}_c(\boldsymbol{x},t)$, and its inverse, $\boldsymbol{L}^{-1}(\boldsymbol{x},t)$, is guaranteed since $\boldsymbol{A}_c(\boldsymbol{x},t)$ and all its eigenvalues are bounded.

Noting that all the eigenvalues of $\boldsymbol{A}_c(\boldsymbol{x},t)$ are distinct, e.g., $\lambda_i(\boldsymbol{x},t)\neq\lambda_j(\boldsymbol{x},t)$, the system can be decomposed into modes:

$$\boldsymbol{L}^{-1}(\boldsymbol{x},t)\boldsymbol{A}_c(\boldsymbol{x},t)\boldsymbol{L}(\boldsymbol{x},t)=\boldsymbol{\Lambda}(\boldsymbol{x},t)=diag\{\lambda_1,...,\lambda_n\} \tag{6.7}$$

Substituting Eq. (6.6) into Eq. (6.5), one has:

$$V(\boldsymbol{x},t)=\boldsymbol{x}^*\boldsymbol{M}(\boldsymbol{x},t)\boldsymbol{x}e^{h(\boldsymbol{x},t)}=(\boldsymbol{L}^{-1}(\boldsymbol{x},t)x)^*(\boldsymbol{L}^{-1}(\boldsymbol{x},t)\boldsymbol{x})e^{h(\boldsymbol{x},t)}=\left\|\boldsymbol{L}^{-1}(\boldsymbol{x},t)\boldsymbol{x}\right\|^2e^{h(\boldsymbol{x},t)} \tag{6.8}$$

With the properties of the norm and the exponential function, we have for all $x\in\mathbb{C}^n$:

$$V(\boldsymbol{x},t)=\left\|\boldsymbol{L}^{-1}(\boldsymbol{x},t)\boldsymbol{x}\right\|^2e^{h(\boldsymbol{x},t)}\geq0 \tag{6.9}$$

where the equality holds if and only if $\boldsymbol{x}=0$. For the case when $\boldsymbol{x}=0$, one has $\dot{\boldsymbol{x}}=0$ from Eq. (6.1) hence $\boldsymbol{A}_c(\boldsymbol{x},t)$ is bounded and the system is stable. The following is the proof for the case when $\boldsymbol{x}\neq0$.

Taking the derivative of the function $V(\boldsymbol{x},t)$ in Eq. (6.5) with respect to time and accounting for Eq. (6.1), the following expression can be inferred:

$$\dot{V}(\boldsymbol{x},t) = [\boldsymbol{x}^* \boldsymbol{A}_c^*(\boldsymbol{x},t)\boldsymbol{M}(\boldsymbol{x},t)\boldsymbol{x}+\boldsymbol{x}^* \boldsymbol{M}(\boldsymbol{x},t)\boldsymbol{A}_c(\boldsymbol{x},t)\boldsymbol{x} + \boldsymbol{x}^* \dot{\boldsymbol{M}}(\boldsymbol{x},t)x+\dot{h}(\boldsymbol{x},t)\boldsymbol{x}^* \boldsymbol{M}(\boldsymbol{x},t)\boldsymbol{x}]e^{h(\boldsymbol{x},t)} \tag{6.10}$$

where $\dot{\boldsymbol{M}}(\boldsymbol{x},t)$ is the derivative of $\boldsymbol{M}(\boldsymbol{x},t)$ with respect to time. Choosing the function $h(\boldsymbol{x},t)$ as the following form:

$$\dot{h}(\boldsymbol{x},t) = -(\boldsymbol{x}^* \dot{\boldsymbol{M}}(\boldsymbol{x},t)x)\Big/(\boldsymbol{x}^* \boldsymbol{M}(\boldsymbol{x},t)\boldsymbol{x}) \tag{6.11}$$

then, Eq.(6.10) can be rewritten as:

$$\dot{V}(\boldsymbol{x},t) = \boldsymbol{x}^*(\boldsymbol{A}_c^*(\boldsymbol{x},t)\boldsymbol{M}(\boldsymbol{x},t) + \boldsymbol{M}(\boldsymbol{x},t)\boldsymbol{A}_c(\boldsymbol{x},t))\boldsymbol{x}e^{h(\boldsymbol{x},t)} \tag{6.12}$$

Using Eq. (6.5) and Eq. (6.6), Eq. (6.12) can be modified to give:

$$\begin{aligned}\dot{V}(\boldsymbol{x},t)&= \boldsymbol{x}^*(\boldsymbol{L}(\boldsymbol{x},t)\Lambda(\boldsymbol{x},t)\boldsymbol{L}^{-1}(\boldsymbol{x},t))^*(\boldsymbol{L}^{-1}(\boldsymbol{x},t))^*\boldsymbol{L}^{-1}(\boldsymbol{x},t)+\\ &(\boldsymbol{L}^{-1}(\boldsymbol{x},t))^*\boldsymbol{L}^{-1}(\boldsymbol{x},t)\boldsymbol{L}(\boldsymbol{x},t)\boldsymbol{\Lambda}(\boldsymbol{x},t)\boldsymbol{L}^{-1}(\boldsymbol{x},t))\boldsymbol{x}e^{h(\boldsymbol{x},t)}\\ &= (\boldsymbol{L}^{-1}(\boldsymbol{x},t)\boldsymbol{x})^*((\boldsymbol{\Lambda}(\boldsymbol{x},t))^* + \boldsymbol{\Lambda}(\boldsymbol{x},t))(\boldsymbol{L}^{-1}(\boldsymbol{x},t)\boldsymbol{x})e^{h(\boldsymbol{x},t)}\end{aligned} \tag{6.13}$$

We note that $(\boldsymbol{\Lambda}^* + \boldsymbol{\Lambda}) = \text{diag}\{2Re[\lambda_1], \cdots, 2Re[\lambda_n]\}$ and all the eigenvalues satisfy $-\rho \leq Re(\lambda_i(\boldsymbol{x},t)) \leq -\varepsilon < 0$, thus Eq. (6.13) satisfies the following inequality for all nonzero vectors $x \in \mathbb{C}^n$:

$$-2\rho V(\boldsymbol{x},t) \leq \dot{V}(\boldsymbol{x},t) \leq -2\varepsilon V(\boldsymbol{x},t) < 0 \tag{6.14}$$

This completes the proof.

Theorem 12 indicates that during the PEA design approach for QLPV systems, if all the desired eigenvalues are distinct and their real parts are negative, the closed-loop system is globally asymptotically stable.

6.2 Stability Analysis for Uncertain QLPV Systems

Using the Barbashin method, any generalized uncertain dynamic system can be transformed into the following QLPV form:

$$\dot{x} = (\boldsymbol{A}(\boldsymbol{x},t) + \delta\boldsymbol{A}(\boldsymbol{x},t))x + (\boldsymbol{b}(\boldsymbol{x},t) + \delta\boldsymbol{b}(\boldsymbol{x},t))\boldsymbol{u} \tag{6.15}$$

in which the unknown matrices $\delta \boldsymbol{A}(\boldsymbol{x}, t) \in \mathbb{R}^{n \times n}$ and $\delta \boldsymbol{b}(\boldsymbol{x}, t) \in \mathbb{R}^{n \times m}$ represent system and input uncertainties respectively. Assume that the upper bounds on these uncertainties are known, which means there are two known symmetric positive definite constant matrices: $\boldsymbol{Q} \in \mathbb{R}^{n \times n}$, $\boldsymbol{R} \in \mathbb{R}^{m \times m}$ and constants $\gamma_a, \gamma_b \geq 0$ such that:

$$\delta \boldsymbol{A}^T(\boldsymbol{x}, t) \delta \boldsymbol{A}(\boldsymbol{x}, t) \leq \gamma_a \boldsymbol{Q} \qquad \delta \boldsymbol{b}^T(\boldsymbol{x}, t) \delta \boldsymbol{b}(\boldsymbol{x}, t) \leq \gamma_b R \tag{6.16}$$

Without uncertainties in Eq. (6.15), the close-loop system is the nominal model, as shown in Eq. (4.18). Substituting the state feedback controller in Eq. (4.21) into Eq. (6.15), the closed-loop uncertain system can be expressed as:

$$\dot{\boldsymbol{x}} = (\boldsymbol{A}(\boldsymbol{x}, t) - \boldsymbol{b}(\boldsymbol{x}, t)\boldsymbol{K}(\boldsymbol{x}, t))\boldsymbol{x} + (\delta \boldsymbol{A} - \delta \boldsymbol{b}(\boldsymbol{x}, t)\boldsymbol{K}(\boldsymbol{x}, t))x = \boldsymbol{A}_c(\boldsymbol{x}, t)\boldsymbol{x} + \delta \boldsymbol{A}_c(\boldsymbol{x}, t)\boldsymbol{x} \tag{6.17}$$

In the following, a Lyapunov function is chosen to prove that the controller designed using the PEA design approach can ensure the stability of the closed-loop system in Eq. (6.17). Before the choice and proof of the Lyapunov function is described, the following preliminaries presented in Vesely & Rosinova (1998) are reviewed.

Definition 10. The uncertain closed-loop system in Eq. (6.17) is said to be robustly exponentially stable with a decay rate $\alpha > 0$ if there exists a Lyapunov function $V(\boldsymbol{x}, t)$, for all initial conditions $\boldsymbol{x}_0 = \boldsymbol{x}(0)$ and for all admissible uncertainties given by Eq. (6.16), such that the following inequality holds along the solution $\boldsymbol{x}(\boldsymbol{x}_0, t)$ of system Eq. (6.17):

$$dV(\boldsymbol{x}, t)/dt \leq -\alpha V(\boldsymbol{x}, t) \tag{6.18}$$

with:

$$c_1 \|\boldsymbol{x}\|^2 \leq V(\boldsymbol{x}, t) \leq c_2 \|\boldsymbol{x}\|^2, \dot{V}(\boldsymbol{x}, t) \leq -c_3 \|\boldsymbol{x}\|^2 \tag{6.19}$$

where $c_1, c_2, c_3 > 0$.

Remark: A solution of Eq. (6.18) is:

$$V(\boldsymbol{x}, t) \leq V(\boldsymbol{x}_0, t_0) e^{-\alpha t} \tag{6.20}$$

Using the inequality in Eq. (6.19), one can obtain:

$$\| \boldsymbol{x} \| \leq \sqrt{c_2/c_1} V \| \boldsymbol{x}_0 \| e^{-\frac{\alpha}{2}t} \tag{6.21}$$

for all $\boldsymbol{x} \in \mathbb{R}^n$. Equation (6.21) shows that if the closed-loop system in Eq. (38) is exponentially stable with a decay rate $\alpha > 0$, then x exponentially converges with a decay rate $\frac{\alpha}{2}$ for all $\boldsymbol{x} \in \mathbb{R}^n$.

Now, a possible Lyapunov function can be defined to provide sufficient conditions to guarantee the exponential stability of the uncertain closed-loop system in Eq. (6.17) with uncertainty bounds Eq. (6.16).

Theorem 13: *The uncertain dynamic system in Eq.* (6.17) *with bounded uncertainties in Eq.* (6.16) *and all* $\boldsymbol{x} \in \mathbb{R}^n$*, is exponentially stable with a decay rate* $\alpha > 0$ *if the following conditions are satisfied:*

1) *The eigenvalues of the closed-loop nominal system in Eq.* (6.1) *are distinct and their real parts are negative, that is,* $\lambda_i(\boldsymbol{x}, t) \neq \lambda_j(\boldsymbol{x}, t)$*,* $i \neq j$ *and* $-\rho \leq Re(\lambda_i(\boldsymbol{x}, t)) \leq -\varepsilon < 0$*,* $\varepsilon > 0$*,* $\rho > 0$*;*

2) *There exists a positive definite solution of the following Lyapunov equation:*

$$\boldsymbol{A}_c^* \boldsymbol{M} + \boldsymbol{M} \boldsymbol{A}_c = -(2\alpha_m \boldsymbol{M} + \alpha_i I) \tag{6.22}$$

and the matrix N satisfies:

$$\boldsymbol{N} = \boldsymbol{N}^* = \xi_1^{-1}\sigma_1^{-1}\boldsymbol{M}^*\boldsymbol{M} + \xi_1\sigma_1((1 + \xi_2\sigma_2)\gamma_a \boldsymbol{Q} + (1 + \xi_2^{-1}\sigma_2^{-1})\gamma_b \boldsymbol{K}^* \boldsymbol{R} \boldsymbol{K}) \leq (2\alpha_n \boldsymbol{M} + \alpha_i \boldsymbol{I}) \tag{6.23}$$

where α_m*,* α_i*,* $\xi_1, \sigma_1, \xi_2, \sigma_2 > 0$*,* $\alpha_n < \alpha_m$*.*

Proof:

From Theorem 12, the control algorithm in Eq. (4.21) can ensure global stability for the nominal system in Eq. (6.1).

For the uncertaint system, consider a possible Lyapunov function of the form:

$$V(\boldsymbol{x}, t) = \boldsymbol{x}^* \boldsymbol{M}(\boldsymbol{x}, t) \boldsymbol{x} e^{h(\boldsymbol{x}, t)} \tag{6.24}$$

where the scalar function $h(\boldsymbol{x}, t)$ is defined in Eq. (6.11) and matrix $\boldsymbol{M}(\boldsymbol{x}, t)$ is obtained from the solution of Eq. (6.22). Therefore:

$$V(\boldsymbol{x}, t) \geq 0 \tag{6.25}$$

where the equality holds if and only if $\boldsymbol{x} = 0$.

Taking the derivative of function $V(\boldsymbol{x}, t)$ in Eq. (6.24) with respect to time and taking into account the system defined in Eq. (6.17), $\dot{V}(\boldsymbol{x}, t)$ can be expressed as:

$$\dot{V}(\boldsymbol{x}, t) = \dot{V}_1(\boldsymbol{x}, t) + \dot{V}_2(\boldsymbol{x}, t) \tag{6.26}$$

where $\dot{V}_1(\boldsymbol{x}, t) = (\boldsymbol{x}^* \boldsymbol{A}_c^* \boldsymbol{M}(\boldsymbol{x}, t)\boldsymbol{x} + \boldsymbol{x}^* \boldsymbol{M}(\boldsymbol{x}, t)\boldsymbol{A}_c \boldsymbol{x})e^{h(\boldsymbol{x},t)}$, and:

$$\dot{V}_2(\boldsymbol{x}, t) = (\boldsymbol{x}^* \delta \boldsymbol{A}_c^* \boldsymbol{M}(\boldsymbol{x}, t)\boldsymbol{x} + \boldsymbol{x}^* \boldsymbol{M}(\boldsymbol{x}, t)\delta \boldsymbol{A}_c \boldsymbol{x} + \boldsymbol{x}^* \dot{\boldsymbol{M}}(\boldsymbol{x}, t)\boldsymbol{x} + \dot{h}(\boldsymbol{x}, t)\boldsymbol{x}^* \boldsymbol{M}(\boldsymbol{x}, t)\boldsymbol{x})e^{h(\boldsymbol{x},t)} \tag{6.27}$$

For $\dot{V}_1(\boldsymbol{x}, t)$, with Eq. (6.22), one has:

$$\dot{V}_1(\boldsymbol{x}, t) = -2\alpha_m V(\boldsymbol{x}, t) - \alpha_i \|\boldsymbol{x}\|^2 < 0 \tag{6.28}$$

and $\dot{V}_2(\boldsymbol{x}, t)$, can be rewritten as:

$$\dot{V}_2(\boldsymbol{x}, t) = (\dot{V}_{21}(\boldsymbol{x}, t) + \dot{V}_{22}(\boldsymbol{x}, t))e^{h(\boldsymbol{x},t)} = (\boldsymbol{x}^*(\delta \boldsymbol{A}_c^* \boldsymbol{M} + \boldsymbol{M}\delta \boldsymbol{A}_c)\boldsymbol{x} + \boldsymbol{x}^*(\dot{\boldsymbol{M}} + \dot{h}(\boldsymbol{x}, t)\boldsymbol{M})\boldsymbol{x})e^{h(\boldsymbol{x},t)} \tag{6.29}$$

Now, for any two vectors $\boldsymbol{X}, \boldsymbol{Y} \in \mathbb{C}^n$, the following equality and inequality hold (Vesely & Rosinova, 1998):

$$\boldsymbol{X}^*\boldsymbol{Y} + \boldsymbol{Y}^*\boldsymbol{X} = (\boldsymbol{Y}\sigma_\gamma^{-\frac{1}{2}} + \boldsymbol{X}\sigma_\gamma^{\frac{1}{2}})^*(\boldsymbol{Y}\sigma_\gamma^{-\frac{1}{2}} + \boldsymbol{X}\sigma_\gamma^{\frac{1}{2}}) - \| \boldsymbol{Y} \|^2 \sigma_\gamma^{-1} - \| \boldsymbol{X} \|^2 \sigma_\gamma, \quad \sigma_\gamma \geq 0 \tag{6.30}$$

$$0 \leq \| \boldsymbol{X} + \boldsymbol{Y} \|^2 \leq \| \boldsymbol{X} \|^2 + \| \boldsymbol{Y} \|^2 + 2 \| \boldsymbol{X} \| \| \boldsymbol{Y} \| \leq (1 + \xi_\gamma) \| \boldsymbol{X} \|^2 + (1 + \xi_\gamma^{-1}) \| \boldsymbol{Y} \|^2, \quad \xi_\gamma \geq 0 \tag{6.31}$$

Using Eq. (6.30) and Eq. (6.31), one has:

$$\begin{aligned} &-\sigma_1 \|\delta \boldsymbol{A}_c \boldsymbol{x}\|^2 - \sigma_1^{-1} \|\boldsymbol{M}\boldsymbol{x}\|^2 \leq \dot{V}_{21}(\boldsymbol{x}, t) \\ &= (\delta \boldsymbol{A}_c \boldsymbol{x})^*(\boldsymbol{M}\boldsymbol{x}) + (\delta \boldsymbol{A}_c \boldsymbol{x})^*(\boldsymbol{M}\boldsymbol{x}) \leq \xi_1 \sigma_1 \|\delta \boldsymbol{A}_c \boldsymbol{x}\|^2 + \xi_1^{-1} \sigma_1^{-1} \|\boldsymbol{M}\boldsymbol{x}\|^2 \end{aligned} \tag{6.32}$$

Now $\delta A_c(\boldsymbol{x}, t) = \delta A(\boldsymbol{x}, t) - \delta b(\boldsymbol{x}, t)K(\boldsymbol{x}, t)$, thus:

$$\begin{aligned} &-\sigma_2 \|\delta \boldsymbol{A}\boldsymbol{x}\|^2 - \sigma_2^{-1} \|\delta \boldsymbol{b}\boldsymbol{K}\boldsymbol{x}\|^2 \leq \boldsymbol{x}^*(\delta \boldsymbol{A}^* \delta \boldsymbol{b}\boldsymbol{K} + \boldsymbol{K}^* \delta \boldsymbol{b}^* \delta \boldsymbol{A})\boldsymbol{x} \\ &= (\delta \boldsymbol{A}\boldsymbol{x})^*(\delta \boldsymbol{b}\boldsymbol{K}\boldsymbol{x}) + (\delta \boldsymbol{b}\boldsymbol{K}\boldsymbol{x})^*(\delta \boldsymbol{A}\boldsymbol{x}) \leq \xi_2 \sigma_2 \|\delta \boldsymbol{A}\boldsymbol{x}\|^2 + \xi_2^{-1} \sigma_2^{-1} \|\delta \boldsymbol{b}\boldsymbol{K}\boldsymbol{x}\|^2 \end{aligned} \tag{6.33}$$

Using Eq. (6.30) and Eq. (6.31) again, then one has:

$$\begin{aligned} &-\sigma_2 \|\delta \boldsymbol{A}\boldsymbol{x}\|^2 - \sigma_2^{-1} \|\delta \boldsymbol{b}\boldsymbol{K}\boldsymbol{x}\|^2 \leq (\delta \boldsymbol{A}\boldsymbol{x})^*(\delta \boldsymbol{b}\boldsymbol{K}\boldsymbol{x}) + (\delta \boldsymbol{A}\boldsymbol{x})^*(\delta \boldsymbol{b}\boldsymbol{K}\boldsymbol{x}) \\ &\leq \xi_2\sigma_2 \|\delta \boldsymbol{A}\boldsymbol{x}\|^2 + \xi_2^{-1}\sigma_2^{-1} \|\delta \boldsymbol{b}\boldsymbol{K}\boldsymbol{x}\|^2 \end{aligned} \tag{6.34}$$

With Eq. (6.34), from Eq. (6.33), one has:

$$\begin{aligned} &\|\delta \boldsymbol{A}_c\boldsymbol{x}\|^2 \leq \boldsymbol{x}^*((1+\xi_2\sigma_2)\|\delta \boldsymbol{A}\|^2 + (1+\xi_2^{-1}\sigma_2^{-1})\boldsymbol{K}^* \|\delta \boldsymbol{b}\|^2 \boldsymbol{K})\boldsymbol{x} \\ &\leq \boldsymbol{x}^*((1+\xi_2\sigma_2)\gamma_a \boldsymbol{Q} + (1+\xi_2^{-1}\sigma_2^{-1})\gamma_b \boldsymbol{K}^* \boldsymbol{R}\boldsymbol{K})\boldsymbol{x} \end{aligned} \tag{6.35}$$

Therefore $\dot{V}_{21}(\boldsymbol{x},t)$ has following inequality:

$$\begin{aligned} &-\sigma_1^{-1} \|\boldsymbol{M}\boldsymbol{x}\|^2 - \boldsymbol{x}^*(\sigma_1((1+\xi_2\sigma_2)\gamma_a \boldsymbol{Q} + (1+\xi_2^{-1}\sigma_2^{-1})\gamma_b \boldsymbol{K}^* \boldsymbol{R}\boldsymbol{K}))\boldsymbol{x} \leq \dot{V}_{21}(\boldsymbol{x},t) \\ &\leq \boldsymbol{x}^*(\xi_1\sigma_1((1+\xi_2\sigma_2)\gamma_a \boldsymbol{Q} + (1+\xi_2^{-1}\sigma_2^{-1})\gamma_b \boldsymbol{K}^* \boldsymbol{R}\boldsymbol{K}))\boldsymbol{x} + \xi_1^{-1}\sigma_1^{-1} \|\boldsymbol{M}\boldsymbol{x}\|^2 \end{aligned} \tag{6.36}$$

Defining $\boldsymbol{N} = \boldsymbol{N}^* = \xi_1^{-1}\sigma_1^{-1}\boldsymbol{M}^*\boldsymbol{M} + \xi_1\sigma_1((1+\xi_2\sigma_2)\gamma_a \boldsymbol{Q} + (1+\xi_2^{-1}\sigma_2^{-1})\gamma_b \boldsymbol{K}^* \boldsymbol{R}\boldsymbol{K}) > 0$, Eq. (6.36) can be simplified to give:

$$\dot{V}_{21}(\boldsymbol{x},t) \leq \boldsymbol{x}^* \boldsymbol{N}\boldsymbol{x} \tag{6.37}$$

Using Eq.(6.37) and Eq.(6.29), and choosing function $h(\boldsymbol{x},t)$ as the form in Eq. (6.11), $\dot{V}_2(\boldsymbol{x},t)$ becomes:

$$\dot{V}_2(\boldsymbol{x},t) \leq \boldsymbol{x}^* \boldsymbol{N}\boldsymbol{x} e^{h(\boldsymbol{x},t)} \tag{6.38}$$

From Eq. (6.28) and Eq. (6.23), we have:

$$\dot{V}(\boldsymbol{x},t) \leq -2(\alpha_m - \alpha_n)V(\boldsymbol{x},t) < 0 \tag{6.39}$$

Therefore, choosing $\alpha = 2(\alpha_m - \alpha_n)$, one has:

$$\dot{V}(\boldsymbol{x},t) \leq -\alpha V(\boldsymbol{x},t) \tag{6.40}$$

For a nonnegative definite matrix, all the eigenvalues are nonnegative real, therefore the eigenvalues of $\boldsymbol{M}(\boldsymbol{x},t)e^{h(\boldsymbol{x},t)}$ can be denoted as:

$$0 < \rho_M \leq \lambda_{M1}(\boldsymbol{x},t) \leq \cdots \leq \lambda_{Mn}(\boldsymbol{x},t) \leq \varepsilon_M \tag{6.41}$$

With Rayleigh's principle (Barnett & Storey, 1970), it is easy to obtain:

$$c_1 \|\boldsymbol{x}\|^2 \leq V(\boldsymbol{x},t) \leq c_2 \|\boldsymbol{x}\|^2 \tag{6.42}$$

where $c_1 = \rho_M, c_2 = \varepsilon_M$. From Eq.(6.40) and Eq.(6.42), it is also easy to show that:

$$\dot{V}(\boldsymbol{x}, t) \leq -c_3 \|\boldsymbol{x}\|^2 \tag{6.43}$$

where $c_3 = \alpha c_1$. Equation (6.40), Eq. (6.42) and Eq.(6.43) satisfy the conditions in definition 10, thus the uncertain closed-loop system Eq. (6.17) is robustly exponentially stable with a decay rate $\alpha > 0$ for all initial condition $x_0 = x(0)$ and for all admissible uncertainties given by Eq.(6.16).

This completes the proof.

6.3 $\mathcal{D}$-Stability Analysis based on a Parameter-dependent Lyapunov Function

The quadratic Lyapunov function can be used to study the stability of time-varying uncertain systems. However, it may lead to very conservative solutions sometimes when the uncertainties are time-invariant since only one single function is used for the entire uncertain system set.

To reduce the conservatism, a new function, known as a parameter-dependent Lyapunov function, has been developed in recent years from the quadratic function. The affine parameter-dependent Lyapunov function (Ramos & Peres, 2002; Peaucelle et al., 2000; Ramos & Peres, 2001; Oliveira et al., 2002; Oliveira & Peres, 2005) and the homogeneous parameter-dependent Lyapunov function (Chesi et al., 2003; Oliveira & Peres, 2005; Chesi et al., 2003; Oliveira & Geromel, 2006) have been applied successfully to achieve several different sufficient LMI conditions for robustness analysis.

The LMI conditions are only suitable in assessing the robust stability of either hurwitz stability or Schur stability, but cannot be used to analyse the $\mathcal{D}$-stability of matrix polytopes. Noting the relation between hurwitz stability and positive realness, Geromel et al. (1998) proposed a LMI method to test a given matrix for $\mathcal{D}$-stability using parameter-dependent Lyapunov function. Based on the key idea of this paper, Peaucelle et al. (2000) developed robust $\mathcal{D}$-stability LMI conditions for uncertain systems. Using this approach, the performance robustness of the system can be assessed by solving for LMI conditions of a matrix polytope. However, the

theory only establishes a sufficient condition, and the particular approach using ES described in Oliveira et al. (2002), cannot solve for all matrix polytopes which can be solved by the QS approach described in Ramos & Peres (2002). Therefore, it is necessary to develop a new $\mathcal{D}$-stability approach based QS as an extension of the approach in Peaucelle et al. (2000). This is the main idea of the new robust stability developed in this section.

Using the same strategy as that described in Gahinet et al. (1996), this new approach is based on the use of scalar multi-convex functions. For continuous systems, this LMI approach can lead to the identical result of the Robust Stability (RS) approach in Ramos & Peres (2002) and it leads to similar results for discrete systems and has less complexity than the RS approach in Ramos & Peres (2001). Several examples are illustrated to prove that this new approach is less conservative than the approach in Peaucelle et al. (2000), including checking for $\mathcal{D}$-stability of uncertain systems. Therefore, this new approach complements the approach developed in Peaucelle et al. (2000).

The rest of this section is organized as follows. Section 6.3.1 states the $\mathcal{D}$-stability problem. In Section 6.3.2, the LMI approach to analyse the $\mathcal{D}$-stability of matrix polytopes is developed for uncertain systems. Section 6.3.3 gives examples to illustrate the approach.

6.3.1 $\mathcal{D}$-Stability of Uncertain Systems

Suppose an uncertain LTI system is given by:

$$\delta(\boldsymbol{x}(t)) = \boldsymbol{A}\boldsymbol{x}(t) \tag{6.44}$$

with $\boldsymbol{x} \in \mathbb{R}^n$, $\boldsymbol{A} \in \mathbb{R}^{n\times n}$. The symbol $\delta(\cdot)$ denotes the forward operator for discrete-time and the derivative operator for continuous-time systems.

Definition 11 (Peaucelle et al., 2000): *A matrix $\boldsymbol{A} \in \mathbb{R}^{n\times n}$ is said to be $\mathcal{D}$-stabile for a given subregion $\mathcal{D}$ defined in Eq.* (5.36) *if and only if all of its eigenvalues lie in this region $\mathcal{D}$.*

One can easily check the $\mathcal{D}$-stability of A by using Lemma 1 (Peaucelle et al., 2000; Chilali & Gahinet, 1996).

Lemma 3: *$\boldsymbol{A} \in \mathbb{R}^{n\times n}$ is $\mathcal{D}$-stable if and only if there exists a positive definite matrix $\boldsymbol{P} \in \mathbb{R}^{n\times n}$, solving the LMI feasibility problem*

$$\boldsymbol{B}_{00} \otimes \boldsymbol{P} + \boldsymbol{B}_{01} \otimes (\boldsymbol{P}\boldsymbol{A}) + \boldsymbol{B}_{10} \otimes (\boldsymbol{A}^T\boldsymbol{P}) + \boldsymbol{B}_{11} \otimes (\boldsymbol{A}^T\boldsymbol{P}\boldsymbol{A}) < 0 \tag{6.45}$$

For an uncertain system, $\boldsymbol{A}$ is not precisely known but belongs to a polytopic uncertainty domain $\mathcal{A}$. Therefore, any matrix $\boldsymbol{A}$ in the domain $\mathcal{A}$ can be expressed as a convex combination of the N polytope vertices $\boldsymbol{A}_i, i = 1, \cdots, N$, that is $\boldsymbol{A}(\lambda) \in \mathcal{A}$ with:

$$\mathcal{A} = \{\boldsymbol{A}(\lambda) = \sum_{i=1}^{N} \lambda_i \boldsymbol{A}_i; \lambda \in \Delta_N\} \tag{6.46}$$

where Δ_N stands for the unit simplex, defined as:

$$\Delta_N = \{\lambda \in \mathbb{R}^N; \sum_{i=1}^{N} \lambda_i = 1; \lambda_i \geq 0\} \tag{6.47}$$

Definition 12 (Peaucelle et al., 2000): *A Matrix polytope $\mathcal{A}$ is robustly $\mathcal{D}$-stable if and only if, for each $\boldsymbol{A} \in \mathcal{A}$, there exists a positive definite matrix $\boldsymbol{P} \in \mathbb{R}^{n\times n}$ such that Eq.* (6.45) *holds.*

Definition 13 (Peaucelle et al., 2000): *A Matrix polytope $\mathcal{A}$ is quadratically $\mathcal{D}$-stable if and only if, for all $\boldsymbol{A} \in \mathcal{A}$, there exists a positive definite matrix $\boldsymbol{P} \in \mathbb{R}^{n\times n}$ such that Eq.* (6.48) *holds.*

$$\begin{aligned} &\boldsymbol{B}_{00} \otimes \boldsymbol{P}(\lambda) + \boldsymbol{B}_{01} \otimes (\boldsymbol{P}(\lambda)\boldsymbol{A}(\lambda)) + \\ &\boldsymbol{B}_{10} \otimes (\boldsymbol{A}(\lambda)^T\boldsymbol{P}(\lambda)) + \boldsymbol{B}_{11} \otimes (\boldsymbol{A}(\lambda)^T\boldsymbol{P}(\lambda)\boldsymbol{A}(\lambda)) < 0 \end{aligned} \tag{6.48}$$

Applying the Schur complement argument, Eq. (6.48) is equivalent to:

$$\begin{bmatrix} \boldsymbol{B}_{00} \otimes \boldsymbol{P}(\lambda) + \boldsymbol{B}_{01} \otimes (\boldsymbol{P}(\lambda)\boldsymbol{A}(\lambda)) + \boldsymbol{B}_{10} \otimes (\boldsymbol{A}(\lambda)^T\boldsymbol{P}(\lambda)) & \boldsymbol{L} \otimes (\boldsymbol{A}(\lambda)\boldsymbol{P}(\lambda)) \\ \boldsymbol{L}^T \otimes (\boldsymbol{A}(\lambda)^T\boldsymbol{P}(\lambda)) & -\boldsymbol{I}_k \otimes \boldsymbol{P}(\lambda) \end{bmatrix} < 0 \tag{6.49}$$

where $\boldsymbol{B}_{11} = \boldsymbol{L}\boldsymbol{L}^T$ and $\boldsymbol{I}_k$ is identity matrix.

The aim in this thesis is to assess the robust $\mathcal{D}$-stability of $\boldsymbol{A}(\lambda) \in \mathcal{A}$ by using an affine parameter-dependent quadratic Lyapunov function, that is $v(\boldsymbol{x}) = \boldsymbol{x}'\boldsymbol{P}(\lambda)\boldsymbol{x}$, where $\boldsymbol{P}(\lambda)$ is given by:

$$\boldsymbol{P}(\lambda) = \sum_{i=1}^{N} \lambda_i \boldsymbol{P}_i \tag{6.50}$$

6.3.2 New LMI Approach of $\mathcal{D}$-Stability Analysis

In this section, a new LMI approach will be developed using the property of the multi-convex scalar quadratic function shown in Lemma 3. Compared to other LMI approaches (Peaucelle et al., 2000; Ramos & Peres, 2002, 2001; Oliveira et al., 2002), this approach has less conservative.

Lemma 4: *Consider a multi-convex scalar quadratic function of $\lambda \in \Delta_N$*

$$f(\lambda_1, \cdots, \lambda_N) = -\sum_{i=1}^{N} \|\boldsymbol{\alpha}_i\|^2 \lambda_i^2 + \sum_{1=i<j}^{N} \alpha_{ij} \lambda_i \lambda_j \tag{6.51}$$

where $\boldsymbol{\alpha}_i \in \mathbb{R}^n$. Then $f(\cdot) < 0$ if

$$\alpha_{ij} < \frac{2}{N-1} \boldsymbol{\alpha}_i^T \boldsymbol{\alpha}_j \quad for \;\; 1 \le i < j \le N. \tag{6.52}$$

Proof: Note that $\boldsymbol{a}^T \boldsymbol{b} = \boldsymbol{b}^T \boldsymbol{a}$ for any vector $\boldsymbol{a} \in \mathbb{R}^n$ and $\boldsymbol{b} \in \mathbb{R}^n$. Therefore, using Eq. (6.52), one has

$$\begin{aligned} f(\cdot) &< -\sum_{i=1}^{N} \boldsymbol{\alpha}_i^T \boldsymbol{\alpha}_i \lambda_i^2 + \sum_{1 \le i<j}^{N} \frac{2}{N-1} \boldsymbol{\alpha}_i^T \boldsymbol{\alpha}_j \lambda_i \lambda_j \\ &= -\sum_{1=i<j}^{N} \frac{1}{N-1} (\boldsymbol{\alpha}_i \lambda_i - \boldsymbol{\alpha}_j \lambda_j)^T (\boldsymbol{\alpha}_i \lambda_i - \boldsymbol{\alpha}_j \lambda_j) \\ &= -\sum_{1=i<j}^{N} \frac{1}{N-1} \|\boldsymbol{\alpha}_i \lambda_i - \boldsymbol{\alpha}_j \lambda_j\| \le 0 \end{aligned} \tag{6.53}$$

□

The next theorem is the main result of this section which gives a tractable approach to assess the $\mathcal{D}$-stability of matrix polytopes.

Theorem 14: *The Matrix polytope $\mathcal{A}$ is robustly $\mathcal{D}$-stable if there exists N positive definite matrices $\boldsymbol{P}_i \in \mathbb{R}^{n \times n}$ and N positive definite matrices $\boldsymbol{Q}_i \in \mathbb{R}^{2n \times 2n}$ such that*

$$\begin{bmatrix} \boldsymbol{B}_{00} \otimes \boldsymbol{P}_i + \boldsymbol{B}_{01} \otimes \boldsymbol{H}_i + \boldsymbol{B}_{10} \otimes \boldsymbol{H}_i^T & \boldsymbol{L} \otimes \boldsymbol{H}_i \\ \boldsymbol{L}^T \otimes \boldsymbol{H}_i^T & -\boldsymbol{I}_k \otimes \boldsymbol{P}_i \end{bmatrix} < -\boldsymbol{Q}_i < 0, \quad i = 1, \cdots, N \tag{6.54}$$

$$\begin{bmatrix} \boldsymbol{B}_{00} \otimes (\boldsymbol{P}_i + \boldsymbol{P}_j) + \boldsymbol{B}_{01} \otimes \boldsymbol{H}_{ij} + \boldsymbol{B}_{10} \otimes \boldsymbol{H}_{ij}^T & \boldsymbol{L} \otimes \boldsymbol{H}_{ij} \\ \boldsymbol{L}^T \otimes \boldsymbol{H}_{ij}^T & -\boldsymbol{I}_k \otimes (\boldsymbol{P}_i + \boldsymbol{P}_j) \end{bmatrix} < \tfrac{1}{N-1} (\boldsymbol{Q}_i^{\frac{1}{2}} \boldsymbol{Q}_j^{\frac{1}{2}} + \boldsymbol{Q}_j^{\frac{1}{2}} \boldsymbol{Q}_i^{\frac{1}{2}}), \quad 1 = i < j, \cdots, N \tag{6.55}$$

where $\boldsymbol{H}_i = \boldsymbol{P}_i\boldsymbol{A}_i$ *and* $\boldsymbol{H}_{ij} = \boldsymbol{P}_i\boldsymbol{A}_j + \boldsymbol{P}_j\boldsymbol{A}_i$.

proof: $\mathcal{A}$ is robustly $\mathcal{D}$-stable if Eq. (6.49) holds with a parameter-dependent positive definite matrix $P(\lambda)$ given by Eq. (6.50). Denote the left term in Eq. (6.49) as $\boldsymbol{F}(\lambda)$ and noting Eq. (6.47) and by using $\boldsymbol{P}(\lambda)$ given in Eq. (6.50), $\boldsymbol{F}(\lambda)$ can be written in the form:

$$\begin{aligned}\boldsymbol{F}(\lambda) = \sum_{i=1}^{N}\lambda_i^2\begin{bmatrix}\boldsymbol{B}_{00}\otimes\boldsymbol{P}_i + \boldsymbol{B}_{01}\otimes\boldsymbol{H}_i + \boldsymbol{B}_{10}\otimes\boldsymbol{H}_i^T & \boldsymbol{L}\otimes\boldsymbol{H}_i\\ \boldsymbol{L}^T\otimes\boldsymbol{H}_i^T & -\boldsymbol{I}_k\otimes\boldsymbol{P}_i\end{bmatrix} +\\ \sum_{1=i<j}^{N}\lambda_i\lambda_j\begin{bmatrix}\boldsymbol{B}_{00}\otimes(\boldsymbol{P}_i+\boldsymbol{P}_j) + \boldsymbol{B}_{01}\otimes\boldsymbol{H}_{ij} + \boldsymbol{B}_{10}\otimes\boldsymbol{H}_{ij}^T & \boldsymbol{L}\otimes\boldsymbol{H}_{ij}\\ \boldsymbol{L}^T\otimes\boldsymbol{H}_{ij}^T & -\boldsymbol{I}_k\otimes(\boldsymbol{P}_i+\boldsymbol{P}_j)\end{bmatrix}\\ \triangleq \sum_{i=1}^{N}\lambda_i^2\ \boldsymbol{F}_i + \sum_{1=i<j}^{N}\lambda_i\lambda_j\boldsymbol{F}_{ij}\end{aligned} \tag{6.56}$$

Take any nonzero vector $x \in \mathbb{R}$ and define:

$$f(\lambda) = \boldsymbol{x}^T\boldsymbol{F}(\lambda)\boldsymbol{x} = \sum_{i=1}^{N}\lambda_i^2\ \boldsymbol{x}^T\boldsymbol{F}_i\boldsymbol{x} + \sum_{1=i<j}^{N}\lambda_i\lambda_j\boldsymbol{x}^T\boldsymbol{F}_{ij}\boldsymbol{x} \tag{6.57}$$

In general, it is difficuly to guarantee that $f(\lambda) < 0$. However, using Eq. (6.54), one can define:

$$-\boldsymbol{x}^T\boldsymbol{F}_i\boldsymbol{x} > \boldsymbol{x}^T\boldsymbol{Q}_i\boldsymbol{x} = (\boldsymbol{Q}_i^{\frac{1}{2}}\boldsymbol{x})^T(\boldsymbol{Q}_i^{\frac{1}{2}}\boldsymbol{x}) = \boldsymbol{\alpha}_i^T\boldsymbol{\alpha}_i > 0, \tag{6.58}$$

which indicates $f(\lambda)$ is multi-convex. Using Eq. (6.55), α_{ij} is defined as

$$\begin{aligned}\alpha_{ij} = \boldsymbol{x}^T\boldsymbol{F}_{ij}\boldsymbol{x} < \tfrac{1}{N-1}\boldsymbol{x}^T(\boldsymbol{Q}_i^{\frac{1}{2}}\boldsymbol{Q}_j^{\frac{1}{2}} + \boldsymbol{Q}_j^{\frac{1}{2}}\boldsymbol{Q}_i^{\frac{1}{2}})\boldsymbol{x}\\ = \tfrac{1}{N-1}((\boldsymbol{Q}_i^{\frac{1}{2}}\boldsymbol{x})^T(\boldsymbol{Q}_j^{\frac{1}{2}}\boldsymbol{x}) + (\boldsymbol{Q}_j^{\frac{1}{2}}\boldsymbol{x})^2(\boldsymbol{Q}_i^{\frac{1}{2}}\boldsymbol{x}) = \tfrac{2}{N-1}\boldsymbol{\alpha}_i^T\boldsymbol{\alpha}_j\end{aligned} \tag{6.59}$$

Using the result in Lemma 4, it is enough to ensure that $f(\lambda) < 0$, that is $\boldsymbol{F}(\lambda) < 0$.

□

The condition shown in Eq. (6.55) in Theorem 14 ensure that $\mathcal{A}$ is robustly $\mathcal{D}$-stable if all of its matrix vertices are $\mathcal{D}$-stable. However, it can not be solved by using the LMI toolbox in Matlab since they are not LMIs. To assess $\mathcal{D}$-stability by using the LMI toolbox, Theorem 14 can be simplified by assuming $\boldsymbol{Q}_1 = \boldsymbol{Q}_2 = ,\cdots, = \boldsymbol{Q}_N$. This might introduce some conservatism, but a solution is now possible.

Corollary 1: *The Matrix polytope $\mathcal{A}$ is robustly $\mathcal{D}$-stable if there exists a positive definite matrix $\boldsymbol{Q} \in \mathbb{R}^{2n\times 2n}$ and N positive definite matrices $\boldsymbol{P}_i \in \mathbb{R}^{n\times n}$, solving the LMI feasibility problem*

$$\left[\begin{array}{cc} \boldsymbol{B}_{00}\otimes\boldsymbol{P}_i + \boldsymbol{B}_{01}\otimes\boldsymbol{H}_i + \boldsymbol{B}_{10}\otimes\boldsymbol{H}_i^T & \boldsymbol{L}\otimes\boldsymbol{H}_i \\ \boldsymbol{L}^T\otimes\boldsymbol{H}_i^T & -\boldsymbol{I}_k\otimes\boldsymbol{P}_i \end{array}\right] < -\boldsymbol{Q}, \quad i = 1,\cdots,N \tag{6.60}$$

$$\left[\begin{array}{cc} \boldsymbol{B}_{00}\otimes(\boldsymbol{P}_i+\boldsymbol{P}_j) + \boldsymbol{B}_{01}\otimes\boldsymbol{H}_{ij} + \boldsymbol{B}_{10}\otimes\boldsymbol{H}_{ij}^T & \boldsymbol{L}\otimes\boldsymbol{H}_{ij} \\ \boldsymbol{L}^T\otimes\boldsymbol{H}_{ij}^T & -\boldsymbol{I}_k\otimes(\boldsymbol{P}_i+\boldsymbol{P}_j) \end{array}\right] < \tfrac{2}{N-1}\boldsymbol{Q}, \quad 1 = i < j,\cdots,N \tag{6.61}$$

where $\boldsymbol{H}_i = \boldsymbol{P}_i\boldsymbol{A}_i$ and $\boldsymbol{H}_{ij} = \boldsymbol{P}_i\boldsymbol{A}_j + \boldsymbol{P}_j\boldsymbol{A}_i$.

Remark1: If $\boldsymbol{P}_1 = \boldsymbol{P}_2 =, \cdots, = \boldsymbol{P}_N = \boldsymbol{P}$, the condition in Eq. (6.60) become the quadratical $\mathcal{D}$-stable condition of $\mathcal{A}$ in Peaucelle et al. (2000). In this case, the condition in Eq. (6.61) can be satisfied using simple computation.

Remark2: For continuous systems, one has $\boldsymbol{B}_{00} = \boldsymbol{B}_{11} = 0$ and $\boldsymbol{B}_{10} = \boldsymbol{B}_{01} = 1$. Therefore Eq. (6.60) and Eq. (6.61) can be simplified to:

$$\left[\begin{array}{cc} \boldsymbol{P}_i\boldsymbol{A}_i + \boldsymbol{A}_i^T\boldsymbol{P}_i & 0 \\ 0 & -\boldsymbol{P}_i \end{array}\right] < -\boldsymbol{Q}, \quad i = 1,\cdots,N \tag{6.62}$$

$$\left[\begin{array}{cc} \boldsymbol{P}_i\boldsymbol{A}_j + \boldsymbol{P}_j\boldsymbol{A}_i + \boldsymbol{A}_j^T\boldsymbol{P}_i + \boldsymbol{A}_i^T\boldsymbol{P}_j & 0 \\ 0 & -(\boldsymbol{P}_i+\boldsymbol{P}_j) \end{array}\right] < \tfrac{2}{N-1}\boldsymbol{Q}, \quad 1 = i < j,\cdots,N \tag{6.63}$$

By choosing $\boldsymbol{Q} = diag(\boldsymbol{I}, \varepsilon\boldsymbol{I}), \varepsilon > 0$ in these equations, the same conditions in Peaucelle et al. (2000) can be obtained easily, which indicates this new approach has less conservatism.

Remark3: For discrete systems, one has $\boldsymbol{B}_{00} = -1, \boldsymbol{B}_{11} = 1$ and $\boldsymbol{B}_{10} = \boldsymbol{B}_{01} = 0$, which simplifies Eq. (6.60) and Eq. (6.61) to:

$$\left[\begin{array}{cc} -\boldsymbol{P}_i & \boldsymbol{P}_i\boldsymbol{A}_i \\ \boldsymbol{A}_i^T\boldsymbol{P}_i & -\boldsymbol{P}_i \end{array}\right] < -\boldsymbol{Q}, \quad i = 1,\cdots,N \tag{6.64}$$

$$\left[\begin{array}{cc} -(\boldsymbol{P}_i+\boldsymbol{P}_j) & \boldsymbol{P}_i\boldsymbol{A}_j + \boldsymbol{P}_j\boldsymbol{A}_i \\ \boldsymbol{A}_j^T\boldsymbol{P}_i + \boldsymbol{A}_i^T\boldsymbol{P}_j & -(\boldsymbol{P}_i+\boldsymbol{P}_j) \end{array}\right] < \tfrac{2}{N-1}\boldsymbol{Q}, \quad 1 = i < j,\cdots,N \tag{6.65}$$

6.3.3 Examples

In this section, numerical examples are carried out to analyse the $\mathcal{D}$-region stability of matrix polytopes and the LMI Control Toolbox in Matlab is used to solve the LMI feasibility problems. The performance of most existing stability analysis approaches via affine parameter-dependent Lyapunov function, including QS approach (Oliveira et al., 2002), ES approach (Peaucelle et al., 2000; Oliveira et al., 2002) and RS approach (Ramos & Peres, 2002, 2001; Oliveira et al., 2002) have been compared by using exhaustive numerical examples in Oliveira et al. (2002) for continuous and discrete systems respectively. This thesis only presents a few stable matrix polytopes whose stability can only be determined by the New Robust Stability (NRS) approach to illustrate the reduced conservatism of this new result. To illustrate the performance of NRS in different cases, the examples are listed for the stability conditions of continuous, discrete and $\mathcal{D}$-stable systems respectively. All of the polytopes are obtained following the method described in Oliveira et al. (2002).

Table 6.1: Numerical Complexity of each Stability Test for Continuous and Discrete Systems

Approach	K	L, continuous	L, discrete
QS	$\frac{n(n+1)}{2}$	$(N+1)n$	$(N+1)n$
ES	$\frac{Nn(n+1)}{2}+2n^2$	$3Nn$	$3Nn$
RS	$\frac{Nn(n+1)}{2}$	$\frac{Nn(N+3)}{2}$	$\frac{n(N^3+3N^2+8N)}{6}$
NRS	$\frac{Nn(n+1)+4n^2}{2}$	$Nn(N+3)$	$Nn(N+3)$

The complexity of each approach, including the number of scalar variables K and the number of LMI rows L, is compared and shown in Table 6.1, which is an extension of Table 1 in Oliveira et al. (2002) by the addition of the NRS approach. Note that the time required to test the feasibility of the LMIs is proportional to K^3L (Boyd et al., 1994; Oliveira et al., 2002; Gahinet et al., 1996). If n is large, the required time for each approach is $O(N)$ for the QS, $O(N^4)$ for the ES, $O(N^5)$ for the RS, and $O(N^5)$ for the NRS of continuous systems and $O(N)$ for the QS, $O(N^4)$ for the ES, $O(N^6)$ for the RS, and $O(N^5)$ for the NRS of discrete systems respectively. Therefore one can conclude that the QS is the simplest, the ES is the second, the RS and NRS have the same complexity for the continuous case, but RS is more

complex than NRS in the discrete case. The reason is that RS in Ramos & Peres (2001) for continuous system and RS in Ramos & Peres (2002) for discrete system are separate conditions, developed for each case individually, as opposed to the ES case developed in Peaucelle et al. (2000) which uses a common condition.

6.3.3.1 Continuous Systems

To illustrate the use of the NRS approach, a matrix polytope $\mathcal{A}_1$ is described by $N = 3$ vertex matrices $\boldsymbol{A}_i \in \mathbb{R}^{3\times3}$:

$$\boldsymbol{A}_1 = \begin{bmatrix} -0.0106 & 1.4461 & -0.2565 \\ -1.3455 & -0.0376 & 0.2026 \\ -0.3511 & -0.7088 & -1.7676 \end{bmatrix}, \tag{6.66}$$

$$\boldsymbol{A}_2 = \begin{bmatrix} -0.9160 & 0.2320 & -0.9314 \\ -0.3671 & 0.4784 & 1.2272 \\ 0.2448 & -0.3041 & -0.7564 \end{bmatrix}, \tag{6.67}$$

$$\boldsymbol{A}_3 = \begin{bmatrix} -1.1496 & -0.8188 & 0.5634 \\ -0.8700 & -0.6244 & 0.3854 \\ -0.0008 & -0.0248 & -0.2185 \end{bmatrix}. \tag{6.68}$$

The roots locus of all of the matrices in this polytope are computed using three-dimensional sweeping, as shown in Fig. 6.1, where the roots do not cross the imaginary axis, which means this polytope is stable.

However for this stable polytope, apart from the NRS and the RS approaches, the LMI feasibility problems of both QS and ES cannot be solved by using the LMI toolbox. Therefore with this result one can conclude that the NRS has less conservatism than the other approaches for this example, since the RS is included by using the NRS approach.

To show that the RS condition is a special case of the NRS condition for continues system, an example which can be assessed by NRS but not RS is presented here. It can be shown that using the NRS approach that it is a stable matrix. The marix polytope $\mathcal{A}_2$ has 2 vertex matrices $\boldsymbol{A}_i \in \mathbb{R}^{3\times3}$ given by:

$$\boldsymbol{A}_1 = \begin{bmatrix} -2.7761 & 0.1472 & 0.9774 \\ 2.1187 & -0.7513 & -0.2740 \\ 0.0170 & 0.2906 & -0.2214 \end{bmatrix}, \tag{6.69}$$

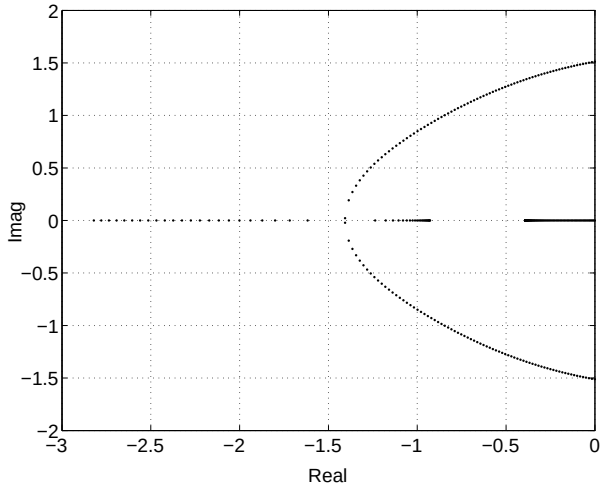

Figure 6.1: Root Locus of Matrix Polytope $\mathcal{A}_1$

$$A_2 = \begin{bmatrix} -0.9297 - 2.35870.3901 \\ 1.29260.8448 - 0.1353 \\ -0.1835 - 0.5372 - 0.3042 \end{bmatrix}. \tag{6.70}$$

6.3.3.2 Discrete Systems

For discrete systems, a stable matrix polytope $\mathcal{A}_3$ is expressed by the following 3 vertex matrices:

$$\boldsymbol{A}_1 = \begin{bmatrix} 0.5628 & 0.0183 & 0.2422 \\ -0.1100 & -0.3761 & -0.6371 \\ 0.1536 & -0.6730 & 0.5770 \end{bmatrix} \tag{6.71}$$

$$\boldsymbol{A}_2 = \begin{bmatrix} -0.3812 & -0.6846 & -0.4208 \\ 0.4609 & -0.0983 & 0.7447 \\ 0.5755 & -0.6302 & -0.9932 \end{bmatrix} \tag{6.72}$$

$$\boldsymbol{A}_3 = \begin{bmatrix} 0.5628 & 0.0183 & 0.2422 \\ -0.1100 & -0.3761 & -0.6371 \\ 0.1536 & -0.6730 & 0.5770 \end{bmatrix} \tag{6.73}$$

The roots locus of all of the matrices in this polytope are computed by using the same sweeping method, and are shown in Fig. 6.2, where all the roots are inside the unit circle. Therefore this polytope is stable.

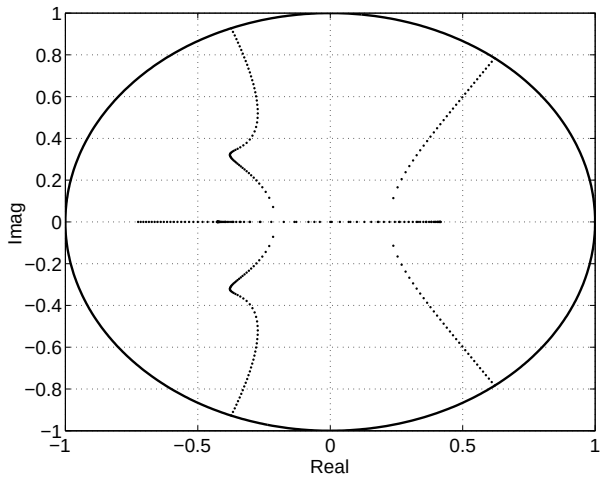

Figure 6.2: Root Locus of Matrix Polytope $\mathcal{A}_3$

Again, the stability of this polytope cannot be checked by QS and ES. However, it can be determined by RS and NRS.

6.3.3.3 $\mathcal{D}$-stable Systems

For the $\mathcal{D}$-stable case, one can choose an intersecting region as $\mathcal{D}_I = \mathcal{D}_1 \cap \mathcal{D}_2 \cap \mathcal{D}_3 \cap \mathcal{D}_4$, as shown in Fig. 6.3, where the corresponding $\boldsymbol{B}$ matrices are given as:

$$\begin{aligned}
\boldsymbol{B}_1 &= \begin{bmatrix} 2\times 0.5 & 1 \\ 1 & 0 \end{bmatrix}, \\
\boldsymbol{B}_2 &= \begin{bmatrix} -0.25\times 2 & 0.5+j \\ 0.5-j & 0 \end{bmatrix}, \\
\boldsymbol{B}_3 &= \begin{bmatrix} -2.7^2 & 0 \\ 0 & 1 \end{bmatrix}, \\
\boldsymbol{B}_4 &= \begin{bmatrix} -0.25\times 2 & 0.5-j \\ 0.5+j & 0 \end{bmatrix}.
\end{aligned} \tag{6.74}$$

Likewise, an example to show the reduced conservatism of NRS for this $\mathcal{D}$-stable case is for the polytope $\mathcal{A}_3$:

$$\boldsymbol{A}_1 = \begin{bmatrix} -1.2539 & -1.1088 & 0.9025 \\ 0.4802 & -1.1928 & 0.0746 \\ -0.1523 & 1.5034 & -1.1209 \end{bmatrix} \tag{6.75}$$

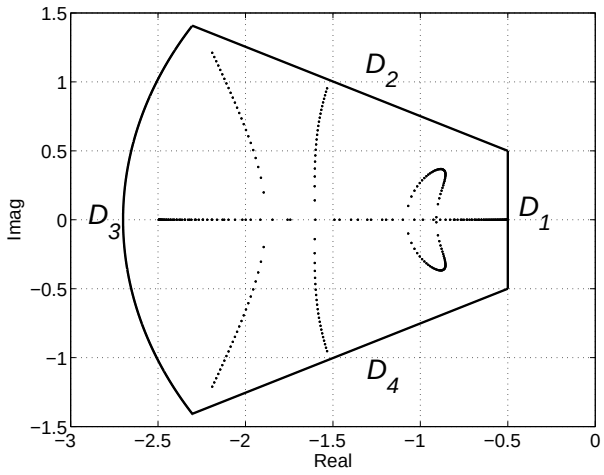

Figure 6.3: Root Locus of Matrix Polytope $\mathcal{A}_4$ and $\mathcal{D}_l$-region

$$\boldsymbol{A}_2 = \begin{bmatrix} -0.5983 & 1.0381 & 1.1078 \\ 0.0575 & -0.6949 & -0.0770 \\ -0.7075 & 0.2169 & -2.5633 \end{bmatrix} \tag{6.76}$$

$$\boldsymbol{A}_3 = \begin{bmatrix} -2.2093 & 1.1497 & 1.2537 \\ -1.7462 & -2.0698 & 0.8724 \\ 0.2595 & 0.4277 & -0.6015 \end{bmatrix} \tag{6.77}$$

For this example the LMI feasibility using NRS is solvable but is not solvable using ES. The locus of this polytope shown in Fig. 5.19 indicates that all the roots of this polytope are inside the intersecting region $\mathcal{D}_l$ confirming the stability.

In this section, three examples have been presented to indicate that NRS has less conservatism than ES developed in Peaucelle et al. (2000) to assess the $\mathcal{D}$-stability of matrix polytopes. However as stressed in Oliveira et al. (2002), one should be aware that both ES and NRS are only sufficient conditions for robust $\mathcal{D}$-stability.

6.4 An Improved LMI Approach for $\mathcal{D}$-Stability Analysis

A new LMI approach (NRS) to assess the $\mathcal{D}$-stability of matrix polytopes has been developed in the last section. However, the numerical results show that

conservatism still exists since only a sufficient condition for robust $\mathcal{D}$-stability has been given.

Actually, reviewing the deduction of this new approach, one can note that the major factor which introduces the conservatism is the assumption in Eq.(6.59), which can be modified to reduce the conservatism of this approach. This is the main idea for the research in this section to seek less conservatism or necessary and sufficient LMI conditions.

6.4.1 Problem Statement

Suppose an uncertain matrix $\boldsymbol{A} \in \mathbb{R}^{n\times n}$ given by:

$$\boldsymbol{A} = \boldsymbol{A}_0 + \theta \boldsymbol{A}_m \tag{6.78}$$

with one uncertain parameter $\theta \in [-\theta_m \quad \theta_m]$ and two constant matrices $\boldsymbol{A}_0$ and $\boldsymbol{A}_m$. Therefore a matrix polytope $\mathcal{A}$ related to this uncertain matrix can be defined as:

$$\mathcal{A} \triangleq \{\boldsymbol{A}(\tau) = \tau_1 \boldsymbol{A}_1 + \tau_2 \boldsymbol{A}_2, \quad \tau_1 + \tau_2 = 1, \tau_1 \in [0, \quad 1]\} \tag{6.79}$$

with two matrix vertices $\boldsymbol{A}_1 = \boldsymbol{A}_0 + \theta_m \boldsymbol{A}_m$ and $\boldsymbol{A}_2 = \boldsymbol{A}_0 - \theta_m \boldsymbol{A}_m$. Using the method in Section6.3, an affine parameter-dependent Lyapunov matrix for this matrix polytope $\mathcal{A}$ can be expressed as:

$$\boldsymbol{P}(\tau) = \tau_1 \boldsymbol{P}_1 + \tau_2 \boldsymbol{P}_2 \tag{6.80}$$

where $\boldsymbol{P}_1 > 0$ and $\boldsymbol{P}_2 > 0$ are the Lyapunov matrices for $\boldsymbol{A}_1$ and $\boldsymbol{A}_2$, respectively, that is:

$$\begin{aligned} \boldsymbol{A}_1^T \boldsymbol{P}_1 + \boldsymbol{P}_1 \boldsymbol{A}_1 = -\boldsymbol{Q}_1, \quad \boldsymbol{Q}_1 > 0, \\ \boldsymbol{A}_2^T \boldsymbol{P}_2 + \boldsymbol{P}_2 \boldsymbol{A}_2 = -\boldsymbol{Q}_2, \quad \boldsymbol{Q}_2 > 0. \end{aligned} \tag{6.81}$$

Thus, the problem here is to check whether $\boldsymbol{P}(\tau)$ is the Lyapunov matrix for $\boldsymbol{A}(\tau)$, that is:

$$\boldsymbol{F}(\tau) \triangleq \boldsymbol{A}(\tau)^T \boldsymbol{P}(\tau) + \boldsymbol{P}(\tau)\boldsymbol{A}(\tau) < 0, \tag{6.82}$$

So that for all nonzero vector $\boldsymbol{x} \in \mathbb{R}^n$, one has equivalently:

$$\begin{aligned} f(\tau) &\triangleq \boldsymbol{x}^T \boldsymbol{F}(\tau)\boldsymbol{x} \\ &= -\tau_1^2 \boldsymbol{x}^T \boldsymbol{Q}_1 \boldsymbol{x} - \tau_2^2 \boldsymbol{x}^T \boldsymbol{Q}_2 \boldsymbol{x} + \tau_1\tau_2 \boldsymbol{x}^T (\boldsymbol{A}_1^T \boldsymbol{P}_2 + \boldsymbol{P}_2 \boldsymbol{A}_1 + \boldsymbol{A}_2^T \boldsymbol{P}_1 + \boldsymbol{P}_1 \boldsymbol{A}_2)\boldsymbol{x} \\ &\triangleq -(\tau_1^2 \alpha_1^2 + \tau_2^2 \alpha_2^2) + \tau_1\tau_2 \alpha_{12} < 0. \end{aligned}$$

(6.83)

where $\alpha_2^2 = \boldsymbol{x}^T\boldsymbol{Q}_1\boldsymbol{x}$, $\alpha_2^2 = \boldsymbol{x}^T\boldsymbol{Q}_2\boldsymbol{x}$, $\alpha_{12} = \boldsymbol{x}^T(\boldsymbol{A}_1^T\boldsymbol{P}_2 + \boldsymbol{P}_2\boldsymbol{A}_1 + \boldsymbol{A}_2^T\boldsymbol{P}_1 + \boldsymbol{P}_1\boldsymbol{A}_2)\boldsymbol{x}$.

For the case when $\tau_1\tau_2 = 0$, the inequality in Eq. (6.83) is fulfilled using the result in Eq. (6.81). For the case when $\tau_1\tau_2 \neq 0$, Eq. (6.83) is equivalent to:

$$g(\tau) \triangleq \frac{\tau_1^2\alpha_1^2 + \tau_2^2\alpha_2^2}{\tau_1\tau_2} > \alpha_{12}, \tag{6.84}$$

6.4.2 Conservatism Analysis for New LMI approach

For $g(\tau)$, one has:

$$g(\tau) = \alpha_1^2\frac{\tau_1}{\tau_2} + \alpha_2^2\frac{\tau_2}{\tau_1} \geq 2\sqrt{\alpha_1\alpha_2}, \tag{6.85}$$

where the equality holds if and only if $\alpha_1 = \frac{\tau_2}{\tau_1}\alpha_2$. Noting that $\tau_2 + \tau_1 = 1$, $g(\tau)$ can be rewritten as:

$$g(\tau_1) = \alpha_1^2\frac{\tau_1}{1-\tau_1} + \alpha_2^2\frac{1-\tau_1}{\tau_1} \geq 2\sqrt{\alpha_1\alpha_2}, \tag{6.86}$$

where the equality holds if and only if $\tau_1 = \frac{\alpha_2}{\alpha_1+\alpha_2}$. As shown in Fig. 6.4, the monotonicity of function $g(\tau_1)$ can be described as:

1. For $\tau_1 \in [0, \tau_{10}]$, $g(\tau_1)$ is monotonically decreasing, that is $g(\tau_1) \leq g(\tau_{10})$;
2. For $\tau_1 \in [\tau_{10}, 1]$, $g(\tau_1)$ is monotonically increasing, that is $g(\tau_1) \geq g(\tau_{10})$.

where $\tau_{10} \triangleq \frac{\alpha_2}{\alpha_1+\alpha_2}$. By choosing $\alpha_{12} < 2\sqrt{\alpha_1\alpha_2}$, the LMI conditions from Theorem 14 in Section 6.3 to assess the stability of continuous uncertain system can be obtained as:

$$\begin{aligned} \boldsymbol{A}_1^T\boldsymbol{P}_1 + \boldsymbol{P}_1\boldsymbol{A}_1 &< -\boldsymbol{Q}, \\ \boldsymbol{A}_2^T\boldsymbol{P}_2 + \boldsymbol{P}_2\boldsymbol{A}_2 &< -\boldsymbol{Q}, \\ \boldsymbol{A}_1^T\boldsymbol{P}_2 + \boldsymbol{P}_2\boldsymbol{A}_1 + \boldsymbol{A}_2^T\boldsymbol{P}_1 + \boldsymbol{P}_1\boldsymbol{A}_2 &< 2\boldsymbol{Q} \\ \boldsymbol{P}_1 > 0, \quad \boldsymbol{P}_2 > 0, \quad \boldsymbol{Q} &> 0 \end{aligned} \tag{6.87}$$

Using the monotonicity of function $g(\tau_1)$ in Fig. 6.4, the conservatism of this LMI approach can be reduced since it only requires $\alpha_{12} < g(\tau_{10}) = 2\sqrt{\alpha_1\alpha_2}$ as opposed to $g(\tau_1)$ in Eq. (6.84). Therefore, how to choose a suitable parameter γ to satisfy the condition:

$$g(\tau) \geq \gamma > \alpha_{12} \tag{6.88}$$

is the keystone to reduce the conservatism of this approach.

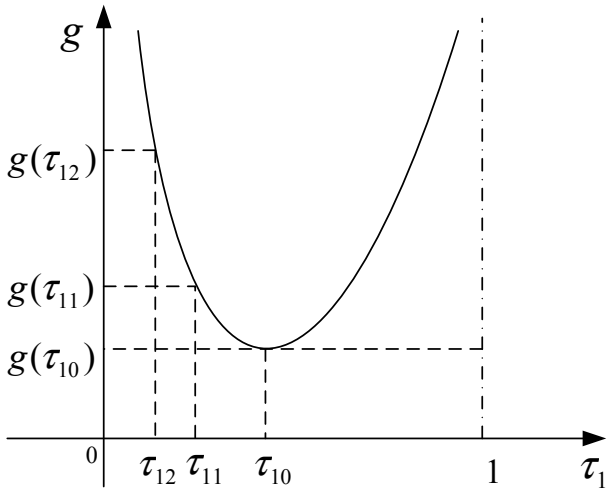

Figure 6.4: The Monotonicity of Function $g(\tau_1)$

6.4.3 Improved New LMI approach

In this section, to reduce the conservatism of the approach, a series of variables $g(\tau_{10})$, $g(\tau_{11})$, $g(\tau_{12})$, $\cdots$ or other parameters as opposed to the single variable $g(\tau_{10})$ are chosen as γ to fulfil the condition in Eq. (6.88).

Choosing $\gamma = g(\tau_{10})$ and using the new LMI approach for the uncertain matrix $\boldsymbol{A}$ in Eq. (6.78), one can obtain a region $[-\theta_{\varepsilon 0} \quad \theta_{\varepsilon 0}]$ which can ensure the LMI conditions in Eq. (6.87) are feasible. Thus, for all $\theta \in [-\theta_{\varepsilon 0} \quad \theta_{\varepsilon 0}]$, $\boldsymbol{A}$ is stable, which indicates that its corresponding matrix polytope $\mathcal{A}_{\varepsilon 0}$ is stable, expressed in the form of Eq. (6.79) as:

$$\mathcal{A}_{\varepsilon 0} = \{\boldsymbol{A}_0 + (\tau_2 - \tau_1)\theta_{\varepsilon 0}\boldsymbol{A}_m, \quad \tau_1 + \tau_2 = 1, \tau_1 \in [0, \quad 1]\} \tag{6.89}$$

Defining $\Delta t = (\tau_2 - \tau_1)\theta_{\varepsilon 0}$, one has $\Delta t \in [-\theta_{\varepsilon 0} \quad \theta_{\varepsilon 0}]$ which can be rewritten as:

$$[-\theta_{\varepsilon 0} \quad \theta_{\varepsilon 0}] = [-\frac{\theta_{\varepsilon 0}}{\theta_m} \quad \frac{\theta_{\varepsilon 0}}{\theta_m}]\theta_m, \tag{6.90}$$

Thus, the matrix polytope $\mathcal{A}_{\varepsilon 0}$ can be rewritten as:

$$\mathcal{A}_{\varepsilon 0} = \{\boldsymbol{A}_0 + (\tau_2 - \tau_1)\theta_m\boldsymbol{A}_m, \quad \tau_1 + \tau_2 = 1, \tau_1 \in [\tau_{111}, \quad \tau_{121}]\}. \tag{6.91}$$

where $[\tau_{111}, \quad \tau_{121}] = [\frac{1}{2}(1 - \frac{\theta_{\varepsilon 0}}{\theta_m}), \quad \frac{1}{2}(1 + \frac{\theta_{\varepsilon 0}}{\theta_m})]$. If $\theta_{\varepsilon 0} \geq \theta_m$, then $[\tau_{111}, \quad \tau_{121}] \supseteq [0, \quad 1]$. Thus the polytope $\mathcal{A}$ in Eq. (6.79) is stable. However due to the conservatism of new LMI approach, $\theta_{\varepsilon 0}$ could be less than θ_m in certain cases. Thus, in order to

complete the stability analysis of $\mathcal{A}$, the following two polytopes $\mathcal{A}_{\varepsilon 111}$ and $\mathcal{A}_{\varepsilon 121}$ have to be assessed:

$$\begin{aligned}\mathcal{A}_{\varepsilon 111} &= \{\boldsymbol{A}_0 + (\tau_2 - \tau_1)\theta_m \boldsymbol{A}_m, \quad \tau_1 + \tau_2 = 1, \tau_1 \in [0, \quad \tau_{111}]\} \\ \mathcal{A}_{\varepsilon 121} &= \{\boldsymbol{A}_0 + (\tau_2 - \tau_1)\theta_m \boldsymbol{A}_m, \quad \tau_1 + \tau_2 = 1, \tau_1 \in [\tau_{121}, \quad 1]\}.\end{aligned} \tag{6.92}$$

Two methods can be implemented to assess the stability of $\mathcal{A}_{\varepsilon 111}$ and $\mathcal{A}_{\varepsilon 121}$. The first is to choose $\gamma = g(\tau_{111})$ (for $\mathcal{A}_{\varepsilon 111}$) and $\gamma = g(\tau_{121})$(for $\mathcal{A}_{\varepsilon 121}$), which can satisfy the LMI condition in Eq. (6.87) as ($\tau_1 < \tau_{10}$) to give:

$$\begin{aligned} \boldsymbol{A}_1^T \boldsymbol{P}_1 + \boldsymbol{P}_1 \boldsymbol{A}_1 &< -\boldsymbol{Q}_1, \\ \boldsymbol{A}_2^T \boldsymbol{P}_2 + \boldsymbol{P}_2 \boldsymbol{A}_2 &< -\boldsymbol{Q}_2, \\ \boldsymbol{A}_1^T \boldsymbol{P}_2 + \boldsymbol{P}_2 \boldsymbol{A}_1 + \boldsymbol{A}_2^T \boldsymbol{P}_1 + \boldsymbol{P}_1 \boldsymbol{A}_2 &< \boldsymbol{Q}_1 \tfrac{\tau_{111}}{1-\tau_{111}} + \boldsymbol{Q}_2 \tfrac{1-\tau_{111}}{\tau_{111}} \\ \boldsymbol{Q}_1 &< (\tfrac{1-\tau_{111}}{\tau_{111}})^2 \boldsymbol{Q}_2 \\ \boldsymbol{P}_1 > 0, \quad \boldsymbol{P}_2 > 0, \quad \boldsymbol{Q}_1 > 0, \quad \boldsymbol{Q}_2 > 0, \end{aligned} \tag{6.93}$$

and for $\tau_1 > \tau_{10}$:

$$\begin{aligned} \boldsymbol{A}_1^T \boldsymbol{P}_1 + \boldsymbol{P}_1 \boldsymbol{A}_1 &< -\boldsymbol{Q}_1, \\ \boldsymbol{A}_2^T \boldsymbol{P}_2 + \boldsymbol{P}_2 \boldsymbol{A}_2 &< -\boldsymbol{Q}_2, \\ \boldsymbol{A}_1^T \boldsymbol{P}_2 + \boldsymbol{P}_2 \boldsymbol{A}_1 + \boldsymbol{A}_2^T \boldsymbol{P}_1 + \boldsymbol{P}_1 \boldsymbol{A}_2 &< \boldsymbol{Q}_1 \tfrac{\tau_{121}}{1-\tau_{121}} + \boldsymbol{Q}_2 \tfrac{1-\tau_{121}}{\tau_{121}} \\ (\tfrac{1-\tau_{121}}{\tau_{121}})^2 \boldsymbol{Q}_2 &< Q_1 \\ \boldsymbol{P}_1 > 0, \quad \boldsymbol{P}_2 > 0, \quad \boldsymbol{Q}_1 > 0, \quad \boldsymbol{Q}_2 > 0. \end{aligned} \tag{6.94}$$

Using the LMI solver in Matlab, a region $[-\theta_{\varepsilon 111} \quad \theta_{\varepsilon 111}]$ can be obtained to ensure that all the LMI conditions in Eq. (6.93) and Eq. (6.94) are feasible. As $g(\tau_{111}) > g(\tau_0)$, one has $\theta_{\varepsilon 111} > \theta_{\varepsilon 0}$. Thus, for all $\theta \in [-\theta_{\varepsilon 111} \quad -\theta_{\varepsilon 0}] \cup [\theta_{\varepsilon 0} \quad \theta_{\varepsilon 111}]$, $\boldsymbol{A}$ is stable, which indicates that the following corresponding matrix polytopes $\mathcal{A}_{\varepsilon 10}$ and $\mathcal{A}_{\varepsilon 01}$ are stable:

$$\begin{aligned}\mathcal{A}_{\varepsilon 10} &= \{\boldsymbol{A}_0 - (\tau_1 \theta_{\varepsilon 111} + \tau_2 \theta_{\varepsilon 0})\boldsymbol{A}_m, \quad \tau_1 + \tau_2 = 1, \tau_1 \in [0, \quad 1]\} \\ \mathcal{A}_{\varepsilon 01} &= \{\boldsymbol{A}_0 + (\tau_1 \theta_{\varepsilon 0} + \tau_2 \theta_{\varepsilon 111})\boldsymbol{A}_m, \quad \tau_1 + \tau_2 = 1, \tau_1 \in [0, \quad 1]\}\end{aligned} \tag{6.95}$$

Using the same approach as in Eq. (6.90), the matrix polytopes in Eq. (6.95) can be rewritten in the form:

$$\begin{aligned}\mathcal{A}_{\varepsilon 10} &= \{\boldsymbol{A}_0 + (\tau_2 - \tau_1)\theta_m \boldsymbol{A}_m, \quad \tau_1 + \tau_2 = 1, \tau_1 \in [\tau_{112}, \quad \tau_{111}]\} \\ \mathcal{A}_{\varepsilon 01} &= \{\boldsymbol{A}_0 + (\tau_2 - \tau_1)\theta_m \boldsymbol{A}_m, \quad \tau_1 + \tau_2 = 1, \tau_1 \in [\tau_{121}, \quad \tau_{122}]\}\end{aligned} \tag{6.96}$$

where $\tau_{112} = \frac{1}{2}(1 - \frac{\theta_{\varepsilon 111}}{\theta_m})$, and $\tau_{122} = \frac{1}{2}(1 + \frac{\theta_{\varepsilon 111}}{\theta_m})$. Once again if $\theta_{\varepsilon 111} \geq \theta_m$, then $[\tau_{112} \quad \tau_{111}] \supseteq [0 \quad \tau_{111}]$, and $[\tau_{121} \quad \tau_{122}] \supseteq [\tau_{121} \quad 1]$. Thus the polytopes $\mathcal{A}_{\varepsilon 111}$ and

$\mathcal{A}_{\varepsilon 121}$ in Eq. (6.92) are stable. Again due to the conservatism, $\theta_{\varepsilon 0}$ could be less than θ_m in certain cases, then a larger value of γ is chosen, that is $\Upsilon = g(\tau_{112}) = g(\tau_{122})$, to check the stability of the rest polytope. Repeating this method, the stability of $\mathcal{A}$ can be assessed successfully.

To apply the improved LMI approach 1 (IM1) in Matlab, the stability analysis for the matrix polytope $\mathcal{A}$ is carried out for τ_1 in the region $[0 \quad \tau_0]$ and the region $[\tau_0 \quad 1]$, respectively. The flow charts are shown in Fig. 6.5. Figure 6.5(a) is the flow chart to analyse the stability in region $[0 \quad \tau_0]$. Suppose h is the minimum computing step size. The code is built as follows:

1. $h = 0.01$, $\theta_1 = 0$, $\theta_2 = -h$, $\tau = \tau_{10} = \frac{\alpha_2}{\alpha_1+\alpha_2}$
2. $\gamma = g(\tau) = \alpha_1^2 \frac{\tau}{1-\tau} + \alpha_2^2 \frac{1-\tau}{\tau}$
3. if $\theta_2 > -(\theta_m + h)$, then $A_1 = A_0 + \theta_1 A_m$ and $A_2 = A_0 + \theta_2 A_m$; else goto 6
4. if $\alpha_{12} < g(\tau)$, $\alpha_1 < \alpha_2 \frac{1-\tau}{\tau}$ and the LMIs in Eq. (6.93) are feasible, then $\theta_2 = \theta_2 - h$, and goto 2; else
5. if $\theta_1 - \theta_2 = h$, goto 7; else $\theta_1 = \theta_2$, $\theta_2 = \theta_2 - h$, $\tau = \frac{1}{2}(1 - \frac{\theta_1}{\theta_m})$, goto 2
6. $\mathcal{A}$ is stable
7. $\mathcal{A}$ is unstable (depends on the precision of h)

Meanwhile, Fig. 6.5(b) shows the flow chart to analyse the stability in the region $[\tau_0 \quad 1]$. Suppose h is the minimum computing step size. The code is then built as follows:

1. Initial: $h = 0.01$, $\theta_1 = 0$, $\theta_2 = h$, $\tau = \tau_{10} = \frac{\alpha_2}{\alpha_1+\alpha_2}$
2. $\gamma = g(\tau) = \alpha_1^2 \frac{\tau}{1-\tau} + \alpha_2^2 \frac{1-\tau}{\tau}$
3. if $\theta_2 < (\theta_m + h)$, then $A_1 = A_0 + \theta_1 A_m$ and $A_2 = A_0 + \theta_2 A_m$; else goto 6
4. if $\alpha_{12} < g(\tau)$, $\alpha_1 > \alpha_2 \frac{1-\tau}{\tau}$ and the LMIs in Eq. (6.94) are feasible, then $\theta_2 = \theta_2 + h$, and goto 2; else
5. if $\theta_1 - \theta_2 = h$, goto 7; else $\theta_1 = \theta_2$, $\theta_2 = \theta_2 + h$, $\tau = \frac{1}{2}(1 - \frac{\theta_1}{\theta_m})$, goto 2
6. $\mathcal{A}$ is stable

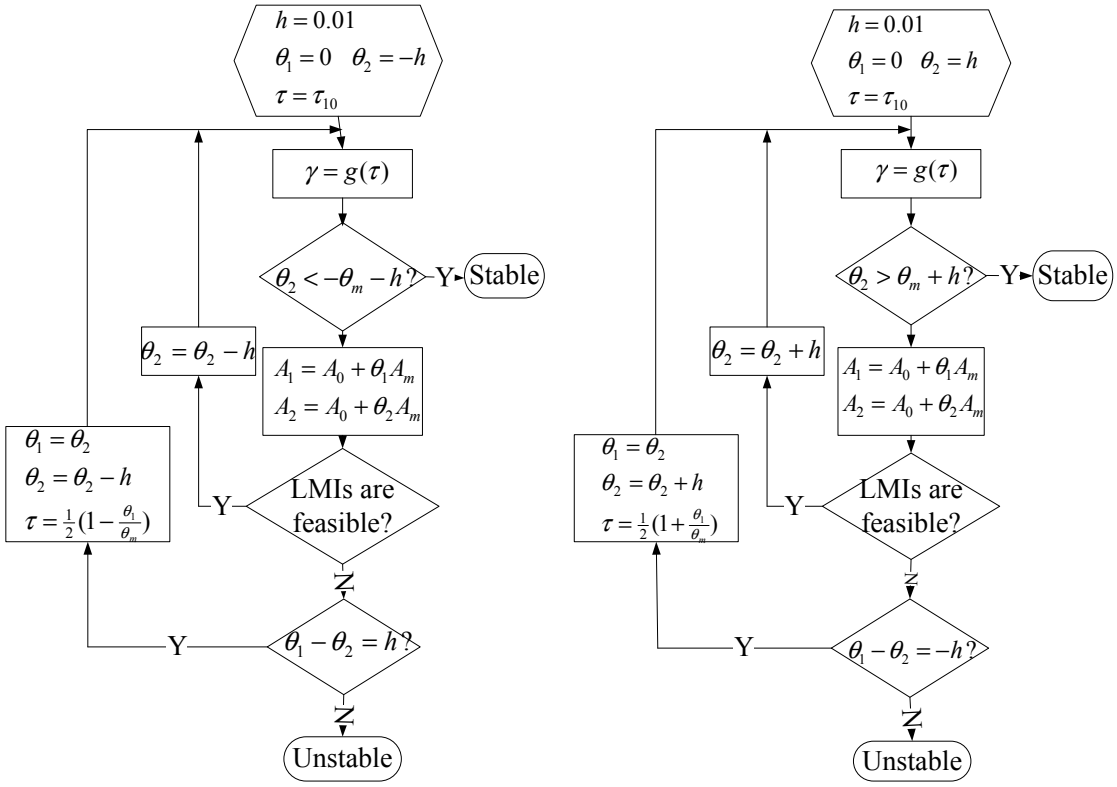

(a) The case of $0 \le \tau_1 \le \tau_{10}$ *(b) The case of* $\tau_{10} \le \tau_1 \le 1$

Figure 6.5: The Flow Chart of Improved LMI Approach 1

7. $\mathcal{A}$ is unstable (depends on the precision of h)

The second method to improved conservatism is to keep $\gamma = g(\tau_{10})$, that is the LMI conditions in Eq. (6.87) are not changed but the matrix vertices are replaced by new vertices during the analysis.

With the same transformation in Eq. (6.90), the polytopes in Eq. (6.92) can be rewritten as:

$$\begin{aligned}\mathcal{A}_{\varepsilon 111} &= \{\tau_1(\boldsymbol{A}_0 + \theta_{\varepsilon 0}\boldsymbol{A}_m) + \tau_1(\boldsymbol{A}_0 + \theta_m\boldsymbol{A}_m), \quad \tau_1 + \tau_2 = 1, \tau_1 \in [0, \quad 1]\} \\ \mathcal{A}_{\varepsilon 121} &= \{\tau_1(\boldsymbol{A}_0 - \theta_{\varepsilon 0}\boldsymbol{A}_m) + \tau_1(\boldsymbol{A}_0 - \theta_m\boldsymbol{A}_m), \quad \tau_1 + \tau_2 = 1, \tau_1 \in [0, \quad 1]\}.\end{aligned} \tag{6.97}$$

Meanwhile, solving the LMI conditions in Eq. (6.87), two parameters θ_{m11} and θ_{m21} can be obtained to ensure the following two polytopes are stable:

$$\begin{aligned}\mathcal{A}_{\varepsilon 111} &= \{\tau_1(\boldsymbol{A}_0 + \theta_{\varepsilon 0}\boldsymbol{A}_m) + \tau_1(\boldsymbol{A}_0 + \theta_{m11}\boldsymbol{A}_m), \quad \tau_1 + \tau_2 = 1, \tau_1 \in [0, \quad 1]\} \\ \mathcal{A}_{\varepsilon 121} &= \{\tau_1(\boldsymbol{A}_0 - \theta_{\varepsilon 0}\boldsymbol{A}_m) + \tau_1(\boldsymbol{A}_0 - \theta_{m21}\boldsymbol{A}_m), \quad \tau_1 + \tau_2 = 1, \tau_1 \in [0, \quad 1]\}.\end{aligned} \tag{6.98}$$

Thus if $\theta_{m11} \ge \theta_m$ and $\theta_{m21} \ge \theta_m$, then $\mathcal{A}$ is stable. Again due to the conservatism, θ_{m11} and θ_{m21} could be less than θ_m in certain cases, then new matrix

vertices are chosen to check the stability of the rest of the polytopes. Repeating this method, the stability of $\mathcal{A}$ can be assessed successfully.

To apply this improved method (IM2) in Matlab, Fig. 6.6(a) and Fig. 6.6(b) provide the procedure to analyse the stability of $\mathcal{A}_{\varepsilon 111}$ and $\mathcal{A}_{\varepsilon 121}$, respectively. Suppose h is the minimum computing step size. For $\tau_1 \in [0 \quad \tau_{10}]$, the code is given as:

1. $h = 0.01$, $\theta_1 = 0$, $\theta_2 = -h$,
2. $\gamma = 2\sqrt{\alpha_1 \alpha_2}$
3. if $\theta_2 > -(\theta_m + h)$, then $A_1 = A_0 + \theta_1 A_m$ and $A_2 = A_0 + \theta_2 A_m$; else goto 6
4. if the LMIs in Eq. (6.87) are feasible, then $\theta_2 = \theta_2 - h$, and goto 2; else
5. if $\theta_2 - \theta_1 = h$, goto 7; else $\theta_1 = \theta_2$, $\theta_2 = \theta_2 - h$, goto 2
6. $\mathcal{A}$ is stable
7. $\mathcal{A}$ is unstable (depends on the precision of h)

For $\tau_1 \in [\tau_{10} \quad 1]$, the code is given as:

1. $h = 0.01$, $\theta_1 = 0$, $\theta_2 = h$,
2. $\gamma = 2\sqrt{\alpha_1 \alpha_2}$
3. if $\theta_2 < (\theta_m + h)$, then $A_1 = A_0 + \theta_1 A_m$ and $A_2 = A_0 + \theta_2 A_m$; else goto 6
4. if the LMIs in Eq. (6.87) are feasible, then $\theta_2 = \theta_2 + h$, and goto 2; else
5. if $\theta_2 - \theta_1 = h$, goto 7; else $\theta_1 = \theta_2$, $\theta_2 = \theta_2 + h$, goto 2
6. $\mathcal{A}$ is stable
7. $\mathcal{A}$ is unstable (depends on the precision of h)

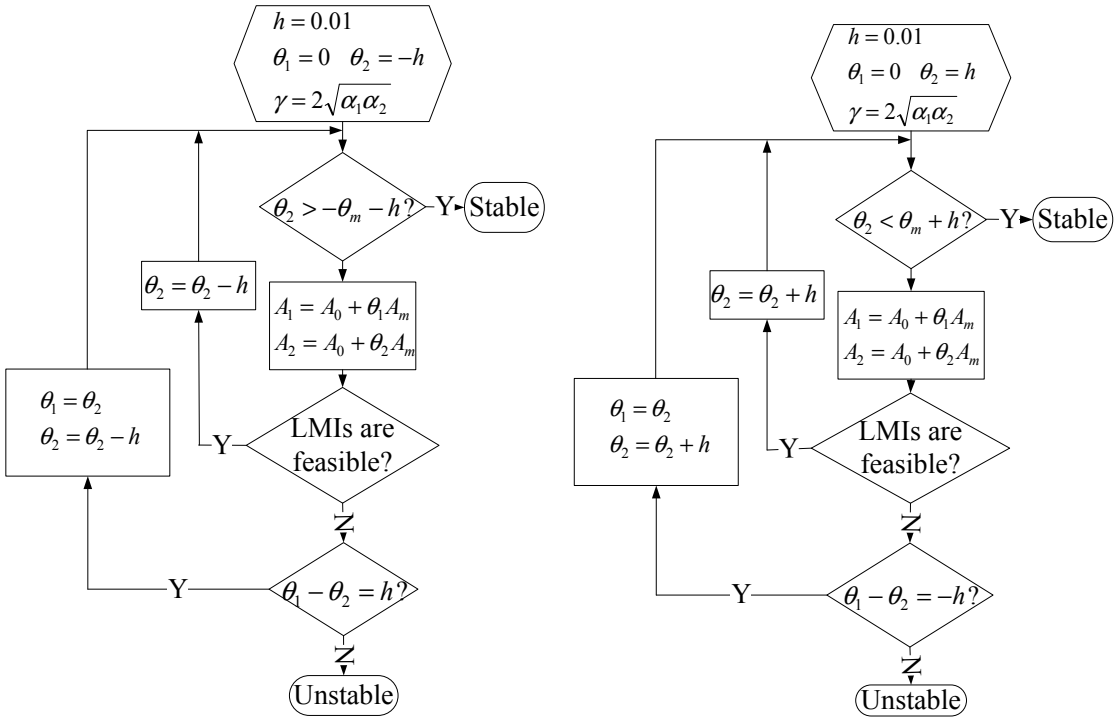

(a) The case of $0 \le \tau_1 \le \tau_{10}$ *(b) The case of* $\tau_{10} \le \tau_1 \le 1$

Figure 6.6: The Flow Chart of Improved LMI Approach 2

6.4.4 Examples

In this section, the efficiency of the improved LMI approach is validated through several numerical examples.

The first example is taken from Ebihara & Hagiwara (2006), which is scaled and approximated appropriately from Example 2 in Chesi et al. (2003). The uncertain matrix $\boldsymbol{A}$ is given in Eq. (6.78), with an uncertain parameter $\theta \in [-\theta_m \quad \theta_m]$ and two related stable matrices $\boldsymbol{A}_0$ and $\boldsymbol{A}_m$, given by:

$$\boldsymbol{A}_0 = \begin{bmatrix} -4 & 2 & -2 \\ 5 & 6 & 1 \\ -2 & 2 & -7 \end{bmatrix} \quad \boldsymbol{A}_m = \begin{bmatrix} -5 & -3 & -13 \\ -5 & 0 & 0 \\ 10 & 13 & 16 \end{bmatrix} \tag{6.99}$$

The problem is to determine the maximum θ_m which can still ensure that the uncertain matrix $\boldsymbol{A}$ is stable.

Four LMI approaches, the ES method in (Peaucelle et al., 2000), the NRS method, and two improved methods based on NRS (IM1 and IM2), are applied to solve this problem. The results are summarized in Table 6.2. From the table, it can

Table 6.2: The Maximum θ_m Obtained Using Different Methods

Method	ES	NRS	IM1	IM2
θ_m	0.895	0.843	1.105	1.105

be seen that the maximum θ_m for the ES method and the NRS method are both less than that of the improved methods due to their conservatism. Indeed, the result obtained by the improved methods has small conservatism since the result in Ebihara & Hagiwara (2006) indicates that the uncertain matrix $\boldsymbol{A}$ is stable for all $\theta \in [-1.105 \;\; 1.105]$ but unstable for all $\theta \in [-1.106 \;\; 1.106]$.

Although the results of IM1 and IM2 are the same, the iteration numbers (4 for IM1 and 3 for IM2) are different, which implies that IM2 converges faster than IM1. To confirm this conclusion, 9 stable matrix polytopes which would not be solved by ES and NRS are consideredy using the two improved methods. The first matrix vertex of the polytope is:

$$\boldsymbol{A}_1 = \begin{bmatrix} 0.4343 & 0.0305 & -0.3063 \\ 0.2586 & -0.6254 & -0.3267 \\ 1.0138 & 0.8446 & -0.1434 \end{bmatrix}, \tag{6.100}$$

and the second vertex $\boldsymbol{A}_2$ for each polytope is:

$$\begin{bmatrix} 0.5029 & -0.1317 & -1.0111 \\ -2.1900 & -0.9528 & 0.4366 \\ 0.6757 & -1.5562 & -1.5569 \end{bmatrix} \begin{bmatrix} -0.8953 & -0.5042 & -0.6468 \\ -0.0591 & -0.0563 & -1.0881 \\ -0.0129 & 0.5578 & 0.0406 \end{bmatrix}$$
$$\begin{bmatrix} -0.6419 & 0.9022 & -0.3350 \\ -0.6952 & 0.0206 & -0.2100 \\ -0.2988 & -0.1456 & -0.0664 \end{bmatrix} \begin{bmatrix} -0.5994 & 1.2490 & 0.0165 \\ -1.2531 & 0.5500 & 0.1377 \\ -0.6699 & 0.1902 & -1.0317 \end{bmatrix}$$
$$\begin{bmatrix} -1.1323 & -2.3796 & -0.1296 \\ 1.5693 & 0.7055 & 0.7713 \\ 0.9370 & 0.4415 & -0.7008 \end{bmatrix} \begin{bmatrix} -0.8189 & 1.2073 & -0.0926 \\ 0.2285 & 0.1939 & -0.9763 \\ 0.5387 & -0.2090 & -0.9731 \end{bmatrix} \tag{6.101}$$
$$\begin{bmatrix} -1.4837 & -1.1219 & -0.6732 \\ 1.6381 & 1.2838 & 0.0369 \\ 1.1897 & 0.9519 & -0.2685 \end{bmatrix} \begin{bmatrix} 0.3205 & 1.1568 & -0.3469 \\ -1.8145 & -0.4519 & 0.0133 \\ 0.2001 & -1.0087 & -1.3903 \end{bmatrix}$$
$$\begin{bmatrix} 0.1332 & -0.5138 & -0.9938 \\ 1.4632 & 0.0079 & -1.3457 \\ 0.7207 & 0.2970 & -0.1686 \end{bmatrix}$$

Table 6.3: The Iteration Number Comparison between IM1 and IM2

Polytopes	$\mathcal{A}_1$	$\mathcal{A}_2$	$\mathcal{A}_3$	$\mathcal{A}_4$	$\mathcal{A}_5$	$\mathcal{A}_6$	$\mathcal{A}_7$	$\mathcal{A}_8$	$\mathcal{A}_9$
IM1	> 10	3	3	> 10	> 10	7	3	> 10	3
IM2	3	3	3	3	3	3	3	3	3

Table 6.2 shows the iteration number for each improved method. As one can see, the iteration number for IM2 is very small (3 for each polytope). However, only four cases for IM1 have the same number as that of IM2, and the remaining cases have more iterations than 3, some greater than 10. These results indicate that the efficiency of IM2 is much better than IM1 in analysing the stability of these polytopes.

6.5 $\mathcal{D}$-Stability Analysis for QLPV PEA Formation Control System

In Section 6.3 and Section 6.4, a new LMI approach with an improved approach using affine parameter-dependent Lyapunov functions have been developed to analysis the $\mathcal{D}$-stability of uncertain systems, and numerical examples have illustratd that using these LMI conditions, the $\mathcal{D}$-stability of matrices and matrix polytopes can be successfully assessed with less conservatism than with other approaches.

The major work in this section is to use these new LMI approaches to assess the $\mathcal{D}$-stability performance of the QLPV PEA L_2 point formation control system. In the same manner as that in Chapter 5.4 for the $\mathcal{D}$-stability analysis, the QLPV system is assumed to be an uncertain LTI system and its uncertainties are caused by the variation of specific system parameters.

The dynamics of the uncertain control system is expressed as a matrix polytope with parametric uncertainties. With this matrix polytope, the parametric $\mathcal{D}$-stability margins for the controller gain and dynamic derivative uncertainties are assessed using the new LMI approach. The results show that this LMI approach using affine parameter-dependent Lyapunov functions is efficient when checking the $\mathcal{D}$-stability of uncertain systems. Compared with the approach in Section 5.4,

it has less conservatism and more application regions since it can be extended to cope with a time-varying uncertain systems.

6.5.1 Nominal and Uncertain Models

Equation (5.74) is the nominal model of the formation flying PEA control system, which is reproduced here for clarity:

$$\dot{\boldsymbol{x}} = \boldsymbol{A}(\boldsymbol{p})\boldsymbol{x} + \boldsymbol{B}\boldsymbol{K}(\boldsymbol{p})\boldsymbol{x} \tag{6.102}$$

To carry out the robust $\mathcal{D}$-stability analysis, it is assumed that the system in Eq. (6.102) is an uncertain LTI system, with uncertainties caused by the variations in $\boldsymbol{p}$.

Considering two sources of parametric uncertainty (varying controller parameters $\boldsymbol{K}_u$, $\boldsymbol{K}_i$, $\boldsymbol{K}_c$, and $\boldsymbol{K}_a$ and varying dynamic derivatives $\boldsymbol{A}_{\delta\dot{\boldsymbol{r}}}$ and $\boldsymbol{A}_{\delta\boldsymbol{r}}$), the uncertain state matrix of Eq. (6.102) $\boldsymbol{A}$ can be described by:

$$\boldsymbol{A} = \boldsymbol{A}_0 + \sum_{i=1}^{6} \theta_i \boldsymbol{A}_{mi} \tag{6.103}$$

where $\boldsymbol{A}_0$ is the nominal state matrix, θ_i are the uncertain parameters, $\theta_i \in [-\theta_{mi} \;\; \theta_{mi}]$, and $\boldsymbol{A}_{mi}$ are constant matrices for each uncertain parameter. $\boldsymbol{A}_0$ and $\boldsymbol{A}_{mi}$ can be expressed as:

$$\boldsymbol{A}_0 = \begin{bmatrix} 0 & \boldsymbol{I}_3 & 0 \\ 0 & 0 & I_3 \\ -\hat{\boldsymbol{K}}_u^{-1}\hat{\boldsymbol{K}}_a & -\hat{\boldsymbol{K}}_u^{-1}\hat{\boldsymbol{K}}_c + \hat{\boldsymbol{A}}_{\delta\boldsymbol{r}} & -\hat{\boldsymbol{K}}_u^{-1}\hat{\boldsymbol{K}}_i + \hat{\boldsymbol{A}}_{\delta\dot{\boldsymbol{r}}} \end{bmatrix} \tag{6.104}$$

$$\boldsymbol{A}_{m1} = \begin{bmatrix} 0 & 0 & 0 \\ 0 & 0 & 0 \\ -\hat{\boldsymbol{K}}_u^{-1}\hat{\boldsymbol{K}}_a & -\hat{\boldsymbol{K}}_u^{-1}\hat{\boldsymbol{K}}_c & -\hat{\boldsymbol{K}}_u^{-1}\hat{\boldsymbol{K}}_i \end{bmatrix} \quad \boldsymbol{A}_{m2} = \begin{bmatrix} 0 & 0 & 0 \\ 0 & 0 & 0 \\ -\hat{\boldsymbol{K}}_u^{-1}\hat{\boldsymbol{K}}_a & 0 & 0 \end{bmatrix}$$

$$\boldsymbol{A}_{m3} = \begin{bmatrix} 0 & 0 & 0 \\ 0 & 0 & 0 \\ 0 & -\hat{\boldsymbol{K}}_u^{-1}\hat{\boldsymbol{K}}_c & 0 \end{bmatrix} \quad \boldsymbol{A}_{m4} = \begin{bmatrix} 0 & 0 & 0 \\ 0 & 0 & 0 \\ 0 & 0 & -\hat{\boldsymbol{K}}_u^{-1}\hat{\boldsymbol{K}}_i \end{bmatrix} \tag{6.105}$$

$$\boldsymbol{A}_{m5} = \begin{bmatrix} 0 & 0 & 0 \\ 0 & 0 & 0 \\ 0 & \hat{\boldsymbol{A}}_{\delta\boldsymbol{r}} & 0 \end{bmatrix} \quad \boldsymbol{A}_{m6} = \begin{bmatrix} 0 & 0 & 0 \\ 0 & 0 & 0 \\ 0 & 0 & \hat{\boldsymbol{A}}_{\delta\dot{\boldsymbol{r}}} \end{bmatrix}$$

where $\hat{\boldsymbol{K}}_u$, $\hat{\boldsymbol{K}}_i$, $\hat{\boldsymbol{K}}_c$, $\hat{\boldsymbol{K}}_a$, $\hat{\boldsymbol{A}}_{\delta\dot{\boldsymbol{r}}}$, and $\hat{\boldsymbol{A}}_{\delta\boldsymbol{r}}$ are the nominal values of uncertain parameters, given in Eq. (5.23) ~ Eq. (5.80).

Therefore, the matrix polytope $\mathcal{A}$ related to this uncertain matrix $\boldsymbol{A}$ can be defined as:

$$\mathcal{A} \triangleq \{\boldsymbol{A}(\tau) = \sum_{i=1}^{64} \tau_j \boldsymbol{A}_j, \quad \sum_{j=1}^{64} \tau_j = 1, \tau_i \geq 0\} \tag{6.106}$$

where $\boldsymbol{A}_j$ are the matrix vertices determined by $\boldsymbol{A}_0$, θ_{mi} and $\boldsymbol{A}_{mi}$.

6.5.2 $\mathcal{D}$-stability Analysis Results

With the matrix polytope in Eq. (6.106), the $\mathcal{D}$-stability analysis of the uncertain L_2 point formation flying control system can now be performed by using the three LMI approaches (NRS, IM1, and IM2) presented in last two sections.

The nominal system performance and the $\mathcal{D}$-region are the same as in Section 5.5. Therefore, the robust stability analysis problem is to assess the maximum θ_{mi} for each uncertain parameter to guarantee that the polytope $\mathcal{A}$ is stable within region $\mathcal{D}$, defined in Fig 5.21.

To check the effect of each uncertain parameter, only one parameter is varied at a time during the analysis. The analysis results are summarized in Table 6.4, from which one can see that the results obtained by the three approaches are the same, which implies that there is little conservatism using NRS method for this uncertain L_2 point formation flying system. Regarding the results in Table 6.1, one can notice that the variation of each uncertain parameter obtained by using Lyapunov functions is the same as that achieved by using their polynomial matrix polytopes.

Table 6.4: $\mathcal{D}$-Stability Analysis Results for each Uncertain Parameter

Approach	θ_{m1}	θ_{m2}	θ_{m3}	θ_{m4}	θ_{m5}	θ_{m6}
NRS	18.3%	8.4%	17.5%	18.5%	500%	500%
IM1	18.3%	8.4%	17.5%	18.5%	500%	500%
IM2	18.3%	8.4%	17.5%	18.5%	500%	500%

Assuming now that all parameters have a uniform percentage variation and using the NRS method, the uncertainty of all parameters can vary up to ±4.4%, which is exactly the same as the result achieved in Section 5.5 .

These results indicate that the uncertain system $\mathcal{D}$-stability is assessed successfully by using the different approaches, as expectation since the same uncertain model is applied for both approaches, but we should note that the approach based on Lyapunov function (NRS) has a much greater application region than the one based on polynomial polytopes (Section 5.4), since the Lyapunov theory can cope with the robust stability of a time-varying uncertain system. Therefore, the more powerful LMI approaches based parameter-dependent Lyapunov function should be studied for the robust analysis of a time-varying uncertain system in the future.

6.6 Conclusions

In this chapter, a quadratic Lyapunov function is developed to analyse the stability of QLPV nominal and uncertain systems, respectively. In detail, a quadratic Lyapunov function is presented in Section 6.1, which is used to prove that a QLPV PEA closed-loop system is stable if all its eigenvalues are in the left half plane and distinct. To analyse the stability of uncertain QLPV systems with bounded uncertainties, one more condition is obtained via the use of a quadratic Lyapunov function. This completes the first contribution in this chapter.

To analyse the $\mathcal{D}$-stability of uncertain systems, an LMI approach using affine parameter-dependent Lyapunov functions is developed successfully by using the property of a multi-convex scalar quadratic function, and moreover, two improved methods are presented to reduce conservatism. The numerical examples indicate that this new LMI approach has less conservatism than the previous results. This is also a major contribution in this thesis.

Considering the controller parameter and dynamic derivative uncertainties, the $\mathcal{D}$-stability analysis of the the QLPV PEA MIMO L_2 point formation control system is performed in Section 6.5, and the results shown to be the same as those in Section 5.5, which indicates that the performance of closed-loop system can

be restricted within an intersecting $\mathcal{D}$-region with up to ±4.4 % variation of each parameter. This is another contribution.

During the robustness analysis in Section 6.5, the approach cannot take the rate limitation and actuator saturation of spacecraft into account since the LMI toolbox can only deal with linear constraints. In order to solve these nonlinear constraints, new optimization method (moments and LMI relaxations, semidefinite programming, polynomial optimization and sum-of-squares relaxation) should be the focus of future research.

Chapter 7

Conclusions and Future Work

7.1 Conclusions

The main aim of the thesis was to design a high precision control system for the Sun-Earth L_2 point formation flying problem. The system was required to attain an invariant stringent performance over a wide range of conditions and to be robust in the presence of parametric uncertainties. The other important aim was to develop robustness analysis approaches for uncertainties in formation flying control system, which will handle the analysis of the robust stability of the uncertain MIMO system efficiently with less conservativeness in current approaches. An advanced optimisation method, using LMI theory was applied to determine the maximum variation range of the uncertain parameters.

For a nonlinear control system, using approximated models (an LTI model or an LPV model) rather than the nonlinear model is the traditional strategy to design control systems. An LTI model expressed by Eq. (2.37) is the simplest form for system design, which is derived using Taylor linearization about a single equilibrium point of the nonlinear model. Such a model has limited applicability for the whole system control envelope. As a solution to satisfy the requirement across the control envelope, gain scheduling is required to produce a global controller. The controller is a collection of LTI controllers designed using an LTI model obtained from the nonlinear model for different equilibrium points. During operation, an appropriate LTI controller from the collection is switched on when the current operating point of the control envelope coincides with one of the relaxant equilibrium points. An external scheduling variable is required to control this switching schedule.

An LPV model is a more precise mathematical description of the resulting control system, expressing in Eq. (2.41). With such a form, the LPV model preserves the transparency of linear controller design while reflecting the rapidly varying system dynamics. However, the LPV model is still a collection of linear designs, and in each of those it is impossible to distinguish between real disturbances and

normal manifestations of nonlinearity (Tsourdos et al., 2001). Hence, it is better to use the system nonlinearity rather than the linear models to improve the system performance and robustness.

The QLPV model given in Eq. (2.49) is one of the mathematical description which incorporates the nonlinear dynamics explicitly. With this QLPV form, the transparency of linear controller design is preserved while reflecting the nonlinearity of the system dynamics.

For the formation flying around the L_2 point of the Sun-Earth system, an exact nonlinear model, including the effects of solar radiation pressure and lunar gravity, has been modeled successfully in Chapter 2. To obtain models for linear control system design, the LTI and LPV models of the relative motion have been attained by keeping some truncation in the gravitational force equations. To improve the modeling accuracy for the high precision formation control system of the interferometry mission, a QLPV model has been developed from the exact nonlinear model without any approximation using Barbashin's method. A simple QLPV model of the flexible spacecraft formation has been built as the foundation stone for checking the effect of spacecraft flexibility for the system control performance in Chapter 4.

As a benchmark to evaluate the nonlinear control performance designed in the thesis, LQR control theory was applied in Chapter 2 to design a linear controller based on the LTI model, of which the robustness has been analysed in brief as well. In order to analyse the accuracy of metrology in the DARWIN mission, we have estimated the system full state using Kalman Filters. In the end, a formation scenario has been defined to assess the performance of each LQR closed-loop system. The results indicate that in contrast to the traditional LQR controller, one including an integrator improves the system performance to the level of 1 *mm* with only a small increase in fuel cost.

However, due to the modeling error between the linearised and full nonlinear model, the LQR design requires gain scheduling (Tsourdos et al., 2001). Therefore, the control system will involve obtaining linearised models for the plant a finite number of equilibrium points, designing an LQR controller to satisfy the local performance objectives of each equilibrium point, and then adjusting the controller gains in real time as the operating conditions vary. Furthermore, a crucial problem requiring a solution is to determine the optimal scheduling routine for

this strategy. An ad hoc approach, such as linear interpolation and curve fitting may be sufficient for simple static-gain controllers, but it will be a tedious process for multi-variable controllers (Bruye're et al., 2002).

To achieve control performance and avoid gain scheduling, more precise models such as LPV and QLPV models need to be taken into account for the design of a gain-varying controller. In Chapter 4, a high precise control system has been developed using PEA techniques for the Sun-Earth L_2 point formation flying problem. The PEA approach used with the LTI and LPV models is extended to QLPV models, in which the formulation allows the polynomial eigenstructure to be used to compute the algebraic structure of the controller and naturally leads to a nonlinear controller without interpolation. The resulting controller renders the closed-loop system almost independent of the operating point, and thus performs a type of dynamic inversion while encompassing a broader class of LPV and QLPV systems to ensure that specific system performance can be achieved.

Using the LPV and QLPV models obtained in Chapter 2, the PEA controllers for the Sun-Earth L_2 point formation flying are designed in Chapter 4. In detail, the PEA approach has been applied to relative position control and attitude control to produce a closed-loop system with invariant performance over a wide range of conditions. To consider the coupling effect caused by thrusters, a combination method for relative position and attitude controllers is described, which is further modified by a cascade-saturation control logic to limit the maximum maneuver rates and actuator limits. Simulations are carried out to validate the performance of the controllers and compared with the results for the LQR controller in Chapter 3, they indicate that both the LPV PEA and the QLPV PEA controllers improve the control performance significantly as well as save fuel. The QLPV PEA controller has the best performance (0.1 mm) because its controller gains vary by virtue of the QLPV model used in the design, which has less modeling error than the LPV and LTI models since it contains all the effects of solar radiation pressure, lunar gravity and other nonlinear terms. To investigate the effect of spacecraft flexibility on the closed-loop system, the PEA controller is enhanced by the addition of a compensation term to suppress vibration, and the simulation results indicate that this PEA controller suppresses the vibration of the spacecraft.

The controllers designed in Chapter 3 and Chapter 4 are based on the nominal models. But for implementation, most systems are subject to uncertainties due to

the variation of system parameters. Such uncertainties will degrade the closed-loop system performance and even destroy its stability. The formation flying control system has uncertainties, and thus it is necessary to analyse the robust performance and stability of the uncertain PEA control system.

In Chapter 5, the robust stability analysis of the SISO uncertain formation flying system is accomplished by using Kharitonov's theorem and Mapping Theorem, in which two sources of parametric uncertainty, controller parameter uncertainty and dynamic derivative uncertainty are taken into account during the analysis. In order to avoid frequency sweeping, the Finite Inclusion Theorem is applied to analyse the robust $\mathcal{D}$-stability of the SISO closed-loop system. The analysis results indicate that good performance and robustness are attained for the uncertain PEA control system in Chapter 4.

Furthermore, a new necessary and sufficient LMI condition for polynomial matrices and a new sufficient LMI condition for polynomial matrix polytopes is developed to analyse robust stability of MIMO systems in an intersecting region $\mathcal{D}$. During the robustness analysis of the MIMO formation flying system, the $\mathcal{D}$-stability performance with controller parameter uncertainty and dynamic derivative uncertainty is assessed by solving a LMI feasibility problem for a polynomial matrix polytope of the uncertain system. The analysis results indicate that the controller parameters are more sensitive than the dynamic parameters, and the simulation results indicate that the performance of the uncertain system maintains the system eigenvalues within a $\mathcal{D}$-region. Comparing the results attained by the designs using the SISO system approach (maximum uncertainty for each parameter is up to 4.5 %), this LMI approach can achieve more accurate results using the MIMO system approach (maximum uncertainty up to 4.4 %) since it takes the effect of coupling terms into account.

All the polynomial approaches developed in this chapter can only handle the robustness of uncertain time-invariant systems, which means for the uncertain time-varying systems, new approachs and new theory are required to analyse the robust stability. Moreover, during the calculation of the PEA controller gains in Chapter 4, the desired transfer function as a coprime factorization has been defined, but how to choose the roots of its characteristic equation to guarantee the stability of the closed-loop system? This is very serious for the closed-loop control system, especially for a QLPV system, its stability should be analysed carefully

since the states matrix $\boldsymbol{A}(\boldsymbol{p})$ and input matrix $\boldsymbol{B}(\boldsymbol{p})$ both vary together with states and time. Therefore, for the design of PEA controllers using a QLPV system, the closed-loop system stability should be analysed.

In Chapter 6, a quadratic Lyapunov function is used to prove that a QLPV PEA closed-loop system is stable if all of its eigenvalues are in the left half plane and distinct. To analyse the stability of uncertain QLPV systems with bounded uncertainties, one more condition is obtained using quadratic Lyapunov functions.

Using the properties of a multi-convex scalar quadratic function, an LMI approach using an affine parameter-dependent Lyapunov function has been developed to analyse the $\mathcal{D}$-stability of uncertain systems. Moreover, two improved methods are presented to reduce conservatism. The numerical examples indicate this new LMI approach has less conservatism than the previous results reported in the literature.

Furthermore, the $\mathcal{D}$-stability analysis of the QLPV PEA MIMO formation control system is performed by taking the controller parameter and dynamic derivative uncertainties into account, and similar results to those obtained in Chapter 5, which indicates the performance of closed-loop system are restricted within an intersecting $\mathcal{D}$-region with up to ±4.4 % variation of each parameter. These results show the uncertain system $\mathcal{D}$-stability is assessed successfully by using this approach, which is to be expected since the same uncertain model is used for both approaches. But we should remember that the approach based on Lyapunov function has much wider application than those based on polynomial polytopes, since Lyapunov theory can cope with the robust stability of a time-varying uncertain systems.

7.2 Proposed Future Work

This thesis describes the feasibility of the robust control for high precision formation flying. Further study is required to check the controller performance with more realistic sensor models, estimation algorithms and enhanced robustness analysis approaches. The following highlights several recommendations for the future work.

All the controllers designed in this thesis assume that the full spacecraft states can be provided by the metrology system. However, the limitation or failure of sensors can result reduced state information, which requires the development of methods to extract the required full state information from the available measurements, or to design controllers with reduced state requirements (Luquette, 2006).

Using the Kalman Filter developed in Section 3.3 is one strategy which could provide full system state information for controller implementation. However, one would not guarantee the stability of a closed-loop system incorporating a convergent linear estimator and a stable nonlinear controller. Therefore, the stability of the integrated controller and estimator should be taken into account in the future study.

The second area is to design a partial feedback controller (Bruyere, 2004) to reduce the requirement of full system state information. This strategy not only can solve the problem of sensor limitations or failure, but also can cope with the case of an augmented system including actuator dynamics whose state is usually not available.

In Section 6.3, the affine parameter-dependent Lyapunov function is applied to develop a new LMI approach to analyse the robust stability of uncertain time-invariant systems. Actually, it can also be used to analyse the robust stability of uncertain time-varying systems (Gahinet et al., 1996; P. & Geromel, 2005; Chesi et al., 2004, 2007; Oliveira et al., 2007). Therefore, using the same strategy in this section, more new LMI approaches can be developed for uncertain time-varying systems.

In Section 6.4, two different improved methods are presented to reduce the conservatism of the LMI approach in the simplest case of a continuous system with one uncertain parameter. The LMI approach presented in Section 6.3 can be used to analyse the $\mathcal{D}$-stability of general uncertain systems. Therefore, using a similar idea, these approaches in Section 6.4 can be extended to the case of discrete systems and even $\mathcal{D}$-stabile systems with one or more uncertainties.

During the robustness analysis of the uncertain formation flying system, it was found that the LMI approaches cannot solve several important nonlinear constraints of spacecraft, such as rate limitation, actuator saturation, and so on.

Therefore, new optimization methods, including moments and LMI relaxation (Lasserre et al., 2005; Henrion et al., 2009), semi-definite programming (Henrion et al., 2009; Mevissen et al., 2010), polynomial optimization and sum-of-squares relaxation (Waki et al., 2006) should be investigated in order to solve these difficult but interesting problems.

References

References

Alazard, D., Cumer, C., & Tantawi, K. (2008). Linear dynamic modeling of spacecraft with various flexible appendages and on-board angular momentums. *7th International ESA Conference on Guidance, Navigation and Control Systems, 01-05 Jun 2008, Tralee, Ireland*.

Anskersen, F. (2008). Coordinate systems and rotations definitions for darwin and demonstration mission. *ESA report, IRSI-TN/FA-00/11 Issue 2.5*, 1–9.

Balch, T. & Arkin, R. C. (1998). Behavior-based formation control for multi-robot teams. *IEEE Trans. Robot. Automat.*, *14*(6), 926–939.

Barbashin, E. A. (1970). Lyapunov functions. *Nauka, Moscow*, 77–79.

Barden, B. T. & Howell, H. C. (1999). Dynamical issues associated with relative configurations of multiple spacecraft near the sun-earth/moon l1 point. *AAS meeting, AAS-99-450*.

Barmish, B. R. (1994). New tools for robustness of linear systems. *New York: Macmillan*.

Barnett, S. & Storey, C. (1970). Matrix methods in stability theory. *Richard Clay Ltd*.

Beard, R., Lawton, J., & Hadaegh, F. (2001). A coordination architecture for formation control. *IEEE Transactions on Control Systems Technology*, *9*(6), 777–790.

Beugnon, C., Calvel, B., & Ankersen, F. (2004). Design and modeling of the formation-flying gnc system for the darwin interferometer. *Modeling and Systems Engineering for Astronomy, Proc. Of SPIE, Vol. 5497*, 28–38.

Bhattacharyya, S. P., Chapellat, H., & Keel, L. H. (1995). Robust control, the parametirc approach. *Prentice-hall, Upper Saddle River, NJ*, 386–406.

Boyd, S., Ghaoui, L., Feron, E., & Balakrishnan, V. (1994). Linear matrix inequalities in systme and control theory. *SIAM Studies in Applied Mathematics, Philadelphia, USA*.

Bruyere, L. (2004). *Robust parametric autopilot for quasi-linear parameter-varying missile*. Phd thesis, Cranfield University.

Bruye're, L., Tsourdos, A., & White, B. A. (2005). Robust analysis for missile lateral acceleration control using finite inclusion theorem. *Journal of Guidance, Control, and Dynamics*, *28*(4), 679–685.

Bruye're, L., Tsourdos, A., & White, B. A. (2006). Quasilinear parameter-varying autopilot design using polynomial eigenstructure assignment with actuator constraints. *Journal of Guidance, Control, and Dynamics*, *29*(6), 1282–1294.

Bruye're, L., Tsourdos, A., Zbikowski, R., & White, B. A. (2002). Robust performance study for lateral autopilot of a quasi-linear parameter-varying missile. *In Proceedings of the American Control Conference*, *1*, 226–231.

Carpenter, K. (2011). Si: the stellar imager. `http://hires.gsfc.nasa.gov/si/`.

Chabot, T. (2005). *Integrated navigation architecture analysis for moon and mars exploration*. Thesis, Massachusetts Institute of Technology.

Chesi, G., Garulli, A., Tesi, A., & Vicino, A. (2003). Robust stability of polytopic systems via polynomially parameter-dependent lyapunov functions. *Proceedings of the 42nd IEEE Conferences o Decision and Control, Maui, HI, USA*, 4670–4675.

Chesi, G., Garulli, A., Tesi, A., & Vicino, A. (2004). Parameter-dependent lyapunov functions for robust stability of linear time-varying systems. *Proceedings of the 43nd IEEE Conferences o Decision and Control, Paradise Island, Bahamas*, 4095–4100.

Chesi, G., Garulli, A., Tesi, A., & Vicino, A. (2007). Robust stability of time-varying polytopic systems via parameter-dependent homogeneous lyapunov functions. *Automatica*, *43*, 309–316.

Chilali, M. & Gahinet, P. (1996). Hinf design with pole placement constraints: an lmi approach. *IEEE Transactions on Automatic Control*, *41*(3), 358–367.

Cockell, C. S., Herbst, T., Lĺęger, A., & et al. (2009). Darwinąłan experimental astronomy mission to search for extrasolar planets. *Experimental astronomy*, *23*, 435–461.

Collange, G. & Leitner, J. (2004). Spacecraft formation design near the sun-earth l2 point. *AIAA Guidance, Navigation, and Control Conference and Exhibit. 16-19, August 2004, Providence, Rhode Island*, AIAA 2004–4781.

Djaferis, T. E. (1995). Robust control design–a polynomial approach. *Kluwer Academic, Boston*, 79–82.

Ebihara, Y. & Hagiwara, T. (2006). Parameter-dependent lyapunov functions for. *Proceedings of the 17th International Symposium on Mathematical Theory of Networks and Systmes, Kyoto, Japan*, *FrP09.1*, 2763–2767.

ESA (2011a). Darwin: study ended, no further activities planned. `http://www.esa.int/science/darwin`.

ESA (2011b). Xeus overview. `http://www.esa.intscience/xeus`.

ESA-SciA (2007). Darwin mission summary status. *ESA report, REF: SCI/AM/DARWIN-SUMSTAT/06*.

Folta, D., Carpenter, J. R., & Wagner, C. (2000). Formation flying with decentralized control in libration point orbits. *International Symposium: Spaceflight Dynamics, Biarritz, France, June 2000.*

Fridlund, C. & Capaccioni, F. (2002). Infrafred space interferometry - the darwin mission. *Advance in Space Research*, *30*(9), 2135–2145.

Gahinet, P., Apkarian, P., & Chilali, M. (1996). Affine parameter-depent lyapunov functions and real parametric uncertainty. *IEEE Transactions on Automatic Control*, *41*(3), 436–442.

Gahinet, P., Nemirovski, A., Laub, A. J., & Chilali, M. (1995). Lmi control toolbox for use with matlab. *The MathWorks, Inc.*

Gaiduk, A. R. (1993). Analytical control synthesis for nonlinear objects in one class. *English trans. Automation and Remote Control*, *54*(2), 227–237.

Gaiduk, A. R. (2003). A polynomial design for nonlinear control systems. *Automation and Remote Control*, *64*(10), 1638–1642.

Gaulocher, S. (2005). Modeling the coupled translational and rotational relative dynamics for formation flying control. *AIAA Guidance, Navigation, and Control Conference and Exhibit 2005,San Francisco, California*, AIAA 2005–6091.

Gaulocher, S. L. & Chretien, J. P. (2006). Six-axis decentralized control design for spacecraft formation flying. *Proceedings of the 2006 IEEE International Conference on Control Applications Munich, Germany, October 4-6, 2006*, 2884–2889.

Gendreau, K. (2011). Vision mission: the black hole imager. `http://maxim.gsfc.nasa.gov/`.

Geromel, J., Oliveira, M. C., & Liu, H. (1998). Lmi characterization of structural and robust stability. *Linear Algebra and its Applications*, *285*, 69–80.

Gurfil, P., Idan, M., & Kasdin, N. J. (2003). Adaptive neural control of deep-space formation flying. *Journal of Guidance, Control, and Dynamics*, *26*(3), 491–501.

Hamilton, N. H., Folta, D., & Carpenter, R. (2002). Formation flying satellite control around the l2 sun-earth libration point. *AIAA-2002-4528*.

Henrion, D., Lasserre, J. B., & Lofberg, J. (2009). Gloptipoly 3: moments, optimization and semidefinite programming. *Optimization Methods and Software*, *24*(4-5), 761–779.

Herion, D., Arzelier, D., Peaucelle, D., & Sebek, M. (2001). An lmi condition for robust stability of polynomial matrix polytopes. *Automatica*, *37*, 461–468.

Herion, D., Bachelier, O., & Sebek, M. (2001). D-stability of polynomial matrices. *International Journal of Control*, *74*(8), 845–856.

Howell, K. & Marchand, B. G. (2005). Natural and non-natural spacecraft formations near the l 1and l2 libration points in the sun-earth/moon ephemeris system. *Dynamical Systems: An International Journal*, *20*(1), 149–173.

Howell, K. C. & Barden, B. T. (1999). Trajectory design and stationkeeping for multiple spacecraft in formation near the sun earth l1 point. *International Astronautical Federation/International Academy of Astronautics Congress,*, IAF/IAA Paper 99–A707.

Howell, K. C. & Marchand, B. G. (2003). Control strategies for formation flight in the vicinity of the libration points. *AIAA/AAS Space Flight Mechanics Conference, Ponce, Puerto Rico*, AAS Paper 03–113.

Hsiao, F. Y. & Scheeres, D. J. (2002). The dynamics of formation flight about a stable trajectory. *AAS meeting,AAS-02-189*.

Infeld, S. I., Josselyn, S. B., Murray, W., & Ross, I. M. (2007). Design and control of libration point spacecraft formations. *Journal of Guidance Control and Dynamics*, *30*(4), 899–909.

Kailath, T. (1980). Linear system. *Upper Saddle River, NJ: Prentice-Hall*.

Kimura, H. (1975). Pole assignment by gain output feedback. *IEEE Transactions on Automatic Control*, *20*(4), 509–516.

Lagadec, K., Lebas, J., & Ankersen, F. (2002). Precision formation flying for the darwin interferometer. *Proceedings of the 5th International ESA Conference on Spacecraft Guidance, Navigation and Control Systems, Frascati, Italy, Oct., 2002*, 201–207.

Lasserre, J. B., Prieur, C., & Henrion, D. (2005). Nonlinear optimal control: numerical approximation via moments and lmi relaxations. *Proceedings of the joint IEEE Conference on Decision and Control and European Control Conference, Sevilla, Spain, December 2005.*

Lawson, P., Lay, K., & Beichman, C. A. (2007). Terrestrial planet finder interferometer science working group report. *Jet Propulsion Laboratory Publication 07-1*.

Leger, A., Mariotti, J., Mennesson, B., & et al. (1996). Could we search for primitive life on extrasolar planets in the near future? the darwin poject. *Icarus*, *123*, 249–255.

Leite, V. J. S. & Peres, P. L. D. (2003). An improved lmi condition for robust d-stability of uncertain polytopic systems. *IEEE Transactions on Automatic Control*, *48*(3), 500–504.

Liu, G. P. & Patton, P. (1998). Eigenstructure assignment for control system design. *Wiley, Chichester*.

Luquette, R. (2006). *Nonlinear control design techniques for precision formation flying at lagrange points*. Phd thesis, University of Maryland, College Park, USA.

Luquette, R. & Sanner, R. (2004). Linear state-space representation of the dynamics of relative motion, based on restricted three body dynamics. *AIAA Guidance, Navigation, and Control Conference and Exhibit. 16-19, August 2004, Providence, Rhode Island*, AIAA 2004–4783.

Luquette, R. J. & Sanner, R. M. (2001). A nonlinear approach to spacecraft formation control in the vicinity of a collinear point. *Proceedings of the AAS/A IAA Astrodynamics Specialist Conference, July 2001*, AAS 01–330.

Marchand, B. & Howell, K. (2004). Aspherical formations near the libration points of the sunĺcearth/moon system. *AAS/AIAA Space Flight Mechanics Meeting, 7ĺC12 February 2004 (Maui, HI: AAS)*, AAS 04–157.

Marchand, B. G. & Howell, K. (2003). Formation flight near l1 and l2 in the sun-earth/moon system including solar radiation pressure. *AAS meeting, AAS-03-596*.

Martin, S., Rodriguez, J., Scharf, D., & et al. (2007). Tpf-emma: concept study of a planet finding space interferometer. *Technique and Instrumentation for Detection of Exoplanets III*.

Mevissen, M., Lasserre, J. B., & Henrion, D. (2010). Moment and sdp relaxation techniques for smooth approximations of problems involving nonlinear differential equations. *the IFAC World Congress on Automatic Control, Milan, Italy, 28 August - 2 September, 2011*.

NASA (2011). Terrestrial planet finder: a space telescope to find planets outside from our solar system as small as earth. `http://www.terrestrial-planet-finder.com/`.

Oliveira, C. R. L. F. & Geromel, J. C. (2006). Lmi conditions for robust stablity analysis based on polynomially parameter-dependent lyapunov functions. *Systems and Control Letters*, *55*, 52–61.

Oliveira, C. R. L. F., Oliveira, M. C., & Peres, P. L. D. (2007). Parameter-dependent lyapunov functions for robust stability analysis of time-varying systems in

polytopic domains. *Proceedings of the 2007 American Control Conference, New York City, USA, July, 2007*, 6079–6083.

Oliveira, P. J., Oliveira, R. C. L. F., & Peres, P. L. D. (2002). An new lmi condition for robust stability of polynomial matrix polytopes. *IEEE Transactions on Automatic Control*, *47*(10), 1775–1779.

Oliveira, P. J. d., Oliveira, R. C. L. F., Leite, V. J. S., Montagner, V. F., & Peres, P. L. D. (2002). Lmi based robust stability condtions for linear uncertain systems: a numerical comparison. *Proceedings of the 41st IEEE Conference on Decision and Control, Las Vegas, Nevada USA*, 644–649.

Oliveira, R. C. L. F. & Peres, P. L. D. (2005). Stability of polytopes of matrices via affine parameter-dependent lyapunov functions: asymptotically exact lmi condtions. *Linear Algebra and its Applications*, *405*, 209–228.

P., C. & Geromel, J. C. (2005). Parameter-dependent lyapunov functions for time varying polytopic systems. *Proceedings of the 2005 American Control Conference, Portland, OR, USA*, 604–608.

Pan, H. & Kapila, V. (2001). Adaptive nonlinear control for spacecraft formation flying with coupled translational and attitude dynamics. *Proceedings of the 40th IEEE Conference on Decision and Control, Orlando, Florida USA, Dec. 2001*, 2057–2062.

Peaucelle, D., Arzelier, D., Bachelier, O., & Bernussou, J. (2000). A new robust d-stability condition for real convex polytopic uncertainty. *Systems and Control Letters*, *40*(1), 21–30.

Penny, A. J., Mariotti, J., Schalinski, C., & et al. (1998). The darwin interferometer. *SPIE*, *3350*, 666–671.

Pernicka, H., Carlson, B., & Balakrishnan, S. (2005). Discrete maneuver formationkeeping at libration points l1 and l2. *AAS Paper 05-194*.

Pirson, L. & Christy, J. (2006). Icc2 study : Gnc development in formation flying. *IFAC paper*.

Ramos, D. C. W. & Peres, P. L. D. (2001). A less conservative lmi condition for the robust stability of discrete-time uncertain systems. *Systems and Control Letters*, *43*, 371–378.

Ramos, D. C. W. & Peres, P. L. D. (2002). An lmi approach to compute robust stability domains for uncertain linear systems. *IEEE Transactions on Automatic Control*, *47*(4), 675–678.

Ren, W. & Beard, R. (2002). Virtual structure based spacecraft formation control with formation feedback. *AIAA Guidance, Navigation, and Control Conference and Exhibit, 5-8 August 2002, Monterey, California.*, AIAA 2002–4963.

Ren, W. & Beard, R. (2004). Decentralized scheme for spacecraft formation flying via the virtual structure approach. *Journal of Guidance, Control and Dynamics*, *27*(1), 73–82.

Richardson, D. (1980). Analytic construction of periodic orbits about the collinear points. *Celestial mechanics*, *22*, 241–253.

Roberts, J. A. (2005). *Satellite formation flying for an interferometry mission*. Phd thesis, Cranfield University.

Ruilier, C., Sghedoni, M., & Krawczyk, R. (2007). Darwin system assessment study summary report. *Alcatle Alenia Space report, REF: DW-SAS-SAP-TN-457*,, 1–30.

Scharf, D. P., Hadaegh, F. Y., & Rahman, Z. H. (2004). An overview of the formation and attitude control system for the terrestrial planet finder formation flying interferometer. *IEEE Aerospace Conference Proceedings,Big Sky, MT*, *4*, 2667–2679.

Scheeres, D. J. & Vinh, N. X. (2000). Dynamics and control of relative motion in an unstable orbit. *AIAA 2000-4135*.

Segerman, A. & Zedd, M. (2003). Preliminary planar formation-flight dynamics near sun-earth l2 point. *AAS/AIAA Space Flight Mechanics Meeting, Ponce, Puerto Rico 2003*.

Shao, J., Xie, G., Yu, J., & Wang, L. (2005). Leader-following formation control of multiple mobile robots. *Intelligent Control, 2005. Proceedings of the 2005 IEEE*

International Symposium on, Mediterrean Conference on Control and Automation, 27-29 June 2005,, 808–813.

Smith, R. S. & Hadaegh, F. Y. (2005). Control of deep-space formation flying spacecraft: relative sensing and swithced information. *Journal of Guidance, Control and Dynamics*, *28*(1), 106–114.

Solodovnik, E., V., Liu, S., & Dougal, R. (2004). Power controller design for maximum power tracking in solar installations. *IEEE Transactions on power electronics*, *19*(5), 1295–1304.

Soylemez, M. T. (1999). Pole assignment for uncertain systems. *UMIST Control systems center series*.

Tanner, H., Pappas, G., & V., K. (2004). Leader-to-formation stability. *IEEE Trans. Robot. Automat.*, *20*(3), 443–454.

Tsourdos, A., Zbikowski, R., & White, B. A. (2001). Robust autopilot for a quasi-linear parametering-varying missile model. *Journal of Guidance, Control, and Dynamics*, *24*(2), 287–295.

Vadali, S., Bae, H. W., & Alfriend, K. T. (2004). Design and control of libration point satellite formations. *Advances in The Astronautical Sciences*, *119*, 897–912.

Vesely, V. & Rosinova, D. (1998). Robust expontial stability of a class of nonlinear systems. *Kyberbetika*, *34*(5), 579–594.

Waki, H., Kim, S., Kojima, M., & Muramatsu, M. (2006). Sums of squares and semidefinite program relaxations for polynomial optimization problems with structured sparsity. *SIAM J. on Optimization*, *17*, 218–242.

Wallner, O. (2007). Darwin system assessment study. *Astrium 2007 Darwin Summary Report*.

Wang, F., Cao, X., Chen, X., & Gao, D. (2006). Near eigenaxis maneuver for on-orbit-servicing spacecraft. *1st International Symposium on System and Control in Aerospace and Astronautics, Harbin, China*, 653–658.

Wang, F., Tsourdos, A., & White, B. A. (2009). Lpv polynomial eigenstructure assignment for formation flying control around sun-earth l2 point. *AIAA Guidance, Navigation, and Control Conference, Aug. 10-13, 2009, Chicago, Illinois*, AIAA 2009–6288.

Welch, G. & Bishop, G. (2001). An introduction to the kalman filter. *ACM Press, Addison-Wesley, Los Angeles, CA, USA, SIGGRAPH 2001 course pack edition*.

White, B. A. (1995). Eigenstructure assignment: A survey. *IMechE, Systems and Control Engineering*, *209*(I1), 1–11.

White, B. A. (1997). Robust polynomial eigenstructure assignment using dynamic feedback controllers. *IMechE, Systems and Control Engineering*, *211*(I1), 35–51.

White, B. A., Bruye're, L., & Tsourdos, A. (2007). Missile autopilot design using quasi-lpv polynomial eigenstructure assignment. *IEEE Transactions on Aerospace and Electronic Systems*, *43*(4), 1470–1482.

Wie, B. & Lu, J. (1995). Feedback control logic for spacecraft eigenaxis rotaions under slew rate and control contraints. *Journal of Guidance, Control, and Dynamics*, *18*(6), 1372–1379.

Xin, M., Balakrishnan, S. N., & Pernicak, H. J. (2007). Multiple spacecraft formation control with sita-d method. *IET Control Theory Application*, *1*(2), 485–493.

Young, B., Beard, R., & Kelsey, M. J. (2001). A control scheme for improving multi-vehicle formation maneuvers. *American Control Conference, Arlington, VA June. 25-27, 2001*, ACC01–IEEE1575.

Appendices

Appendix A

Definitions of Frames

The following coordinate systems are defined for the description and simulation in this thesis. All systems except the **ROF**system are the same as those in Anskersen (2008). Every system is right handed Cartesian orthogonal. The relationship of these frames is illustrated in Fig. A.1 and Fig. A.2.

IHE Inertial Heliocentric Ecliptic Frame.

Origin At the barycentre of the Sun-Earth system.

+X axis Towards the vernal equinox.

+Y axis In the ecliptic plane perpendicular to the X-axis, such that $Y = Z \times X$.

+Z axis Parallel to the angular momentum vector of the orbit of the Earth around the Sun.

ROF Rotating Orbital Frame. Usually, the dynamic equations are expressed in this frame. This frame defined here is different with that in Anskersen (2008).

Origin At the barycentre of the Sun-Earth system.

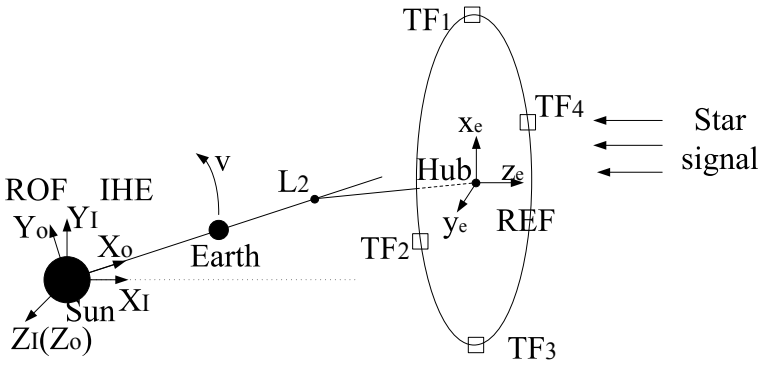

*Figure A.1: The Relationship of the Frames **IHE, ROF, REF***

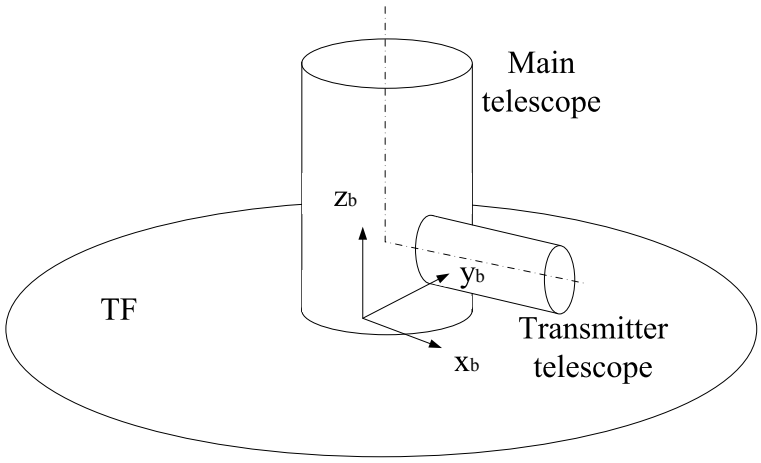

*Figure A.2: The Frame **RBF** Defined in the Telescope*

+X axis Radial to the orbit around the Sun and pointing from the Sun towards L_2. (-Z axis in Anskersen (2008))

+Y axis $Y = Z \times X$. (+X axis in Anskersen (2008))

+Z axis the angular momentum vector of the heliocentric orbit and parallel to IHE +Z-axis. (-Y axis in Anskersen (2008))

RBF Rotating Body Frame. This frame is fixed to each spacecraft and used for the GNC system. All the metrology sensors and actuators of every spacecraft are fixed and described in this frame (**HRBF** for the hub, **TRBF** for the telescope flyer, TF).

Origin Centre of Spacecraft mass.

+X axis Along the bore sight of the transmitter telescope towards the hub (for the TF) and along the bore sight of the receiver telescope towards TF 1 (for the hub).

+Y axis $Y = Z \times X$.

+Z axis Along the bore sight of the main telescope. For the hub, perpendicular to the plane of science-beams, and pointing away from the solar-panel.

REF Rotating Reference Frame. This frame usually can be used to describe desired position and attitude of the formation spacecraft.

Origin Centre of the hub mass.

+X axis Nominal direction of the science beam from TF 1 .

+Y axis Forming a right hand system.

+Z axis Towards the target star.

Appendix B

Expressions for Parameters in Eq. (2.11)

To describe the expressions, the following definitions should be presented firstly.

Denote the mass of the Sun and the Earth as M_1 and M_2, and define the constant μ as $\mu = \frac{M_1}{M_1+M_2}$. Also define n_1 as the mean motion of the Earth in its orbit about the Sun. Dimensionless quantity γ_L can be given by $\gamma_L = n_1^{2/3}$. Thus, the constants c_n can be expressed as:

$c_n = \frac{1}{\gamma_L^3}\left[(-1)^n(1-\mu) + (-1)^n \frac{\mu\gamma_L^{n+1}}{(1+\gamma_L)^{n+1}}\right]$

The linearized frequency λ can be calculated from the following equation:

$\lambda^4 + (c_2-2)\lambda^2 - (c_2-1)(1+2c_2) = 0.$

Define k as

$k = \frac{1}{2\lambda}(\lambda^2 + 1 + 2c_2) = \frac{2\lambda}{\lambda^2+1-c_2}.$

With these definitions, the parameters in Eq. (2.11) are expressed as:

$a_{21} = \frac{3c_3(k^2-2)}{4(1+2c_2)}$

$a_{22} = \frac{3c_3}{4(1+2c_2)}$

$a_{23} = -\frac{3c_3\lambda}{4kd_1}[3k^3\lambda - 6k(k-\lambda) + 4]$

$a_{24} = -\frac{3c_3\lambda}{4kd_1}(2 + 3k\lambda)$

$a_{31} = -\frac{9\lambda}{4d_2}[4c_3(ka_{23} - b_{21}) + kc_4(4+k^2)] + \frac{9\lambda^2+1-c_2}{2d_2}[3c_3(2a_{23} - kb_{21}) + c_4(2+3k^2)]$

$a_{32} = -\frac{1}{d_2}\{\frac{9\lambda}{4}[4c_3(ka_{24} - b_{22}) + kc_4] + \frac{3}{2}(9\lambda^2 + 1 - c_2)[c_3(kb_{22} + d_{21} - 2a_{24}) - c_4]\}$

$b_{21} = -\frac{3c_3\lambda}{2d_1}(3k\lambda - 4)$

$b_{22} = \frac{3c_3\lambda}{d_1}$

$b_{31} = \frac{3}{8d_2}\{8\lambda[3c_3(kb_{21} - 2a_{23} - c_4(2+3k^2))] + (9\lambda^2+1+2c_2)[4c_3(ka_{23} - b_{21}) + kc_4(4+k^2)]\}$

$b_{32} = \frac{1}{d_2}\{9\lambda[c_3(kb_{22} + d_{21} - 2a_{24}) - c_4] + \frac{3}{8}(9\lambda^2 + 1 + 2c_2)[4c_3(ka_{24} - b_{22}) + kc_4]\}$

$d_{21} = -\frac{c_3}{2\lambda^2}$

$d_{31} = \frac{3}{64\lambda^2}(4c_3a_{24} + c_4)$

$d_{32} = \frac{3}{64\lambda^2}[4c_3(a_{24} - d_{21}) + c_4(4 + k^2)]$

where

$d_1 = \frac{3\lambda^2}{k}[k(6\lambda^2 - 1) - 2\lambda]$,

$d_2 = \frac{8\lambda^2}{k}[k(11\lambda^2 - 1) - 2\lambda]$.

For the frequency correction:

$s_1 = \frac{1}{2\lambda[\lambda(1+k^2)-2k]}\{\frac{3}{2}c_3[2a_{21}(k^2 - 2) - a_{23}(k^2 + 2) - 2kb_{21}] - \frac{3}{8}c_4(3k^4 - 8k^2 + 8)\}$,

$s_2 = \frac{1}{2\lambda[\lambda(1+k^2)-2k]}\{\frac{3}{2}c_3[2a_{22}(k^2 - 2) + a_{24}(k^2 + 2) + 2kb_{22} + 5d_{21}] + \frac{3}{8}c_4(12 - k^2)\}$.

The amplitude-constraint relationship can be expressed as

$l_1A_x^2 + l_2A_z^2 + \Delta = 0$

where $\Delta = \lambda^2 - c_2$,

$l_1 = a_1 + 2\lambda^2 s_1$,

$l_2 = a_2 + 2\lambda^2 s_2$, and where

$a_1 = -\frac{3}{2}c_3(2a_{21} + a_{23} + 5d_{21}) - \frac{3}{8}c_4(12 - k^2)$,

$a_2 = \frac{3}{2}c_3(a_{24} - 2a_{22}) + \frac{9}{8}c_4$.